Precipitation measurements with polarimetric radio occultations

Ramon Padullés Rulló

PhD dissertation on

PRECIPITATION MEASUREMENTS WITH POLARIMETRIC RADIO OCCULTATIONS

RAMON PADULLÉS RULLÓ

Advisor: Estel Cardellach Galí

Tutor: Mª Rosa Soler

PROGRAMA DE DOCTORAT EN FÍSICA

Institut de Ciències de l'Espai
CSIC / IEEC

Departament de Física Aplicada
Universitat de Barcelona

2017

RESUM

CONTEXT

Al 2009, el ministeri Espanyol de Ciència i Innovació va aprovar una proposta per incorporar l'equipament necessari per capturar Radio Ocultacions Polarimètriques (Pol-RO) al satèl·lit d'observació de la Terra PAZ. El satèl·lit s'havia d'haver llençat al 2012, però finalment es va enraderir i a dia d'avui encara no s'ha fixat una data definitiva per al llançament. Incialment només estava pensat per portar un radar d'obertura sintètica (SAR), destinat a obtenir imatges de la superfície terrestre, i un equip de posicionament global per satèl·lit (GPS) per a determinar la seva posició en tot moment. Els canvis proposats, doncs, es van basar en l'instrument GPS i no van suposar una gran modificació de l'equipament incial.

PAZ va esdevinir una oportunitat per tal de posar a prova el nou concepte Pol-RO, dissenyat a l'Institut de Ciències de l'Espai (CSIC-IEEC). L'experiment dedicat a provar aquest concepte es va anomenar ROHP-PAZ, acrònim per Radio Ocultacions i precipitació extrema a bord del satèl·lit PAZ, en anglès. Aquest nou concepte de mesura es basa en identificar les petites diferències de fase que apareixen entre les components horitzontal (H) i vertical (V) de les ones electromagnètiques quan travessen pluja. Per tal d'obtenir aquesta mesura, es pretén seguir el senyal provinent dels satèl·lits GPS des d'un satèl·lit d'òrbita baixa (LEO) mitjançant una antena linealment polaritzada horitzontal i verticalment. Des de la prespectiva del LEO, el satèl·lit GPS s'amaga progressivament darrera de l'hortizó de la Terra, i per tant, el senyal que emet travessa cada cop més capes de l'atmosfera abans d'arribar al LEO. Abans d'amagar-se definitivament, el senyal ha creuat des de les capes més altes fins a les capes més baixes de l'atmosfera terrerestre. En les capes més baixes és on s'espera la precipitació.

Aquest tipus de mesura, anomenat Radio Ocultació (RO), que en la seva versió més estàndard no compta amb capacitat per obtenir mesures polaritzades horitzontal i verticalment, sinó que obté el senyal a través d'una antena polaritzada circularment a dretes (RHCP), és utilitzada rutinariament per sondejar l'atmosfera i obtenir perfils verticals de refractivitat, temperatura, pressió i vapor d'aigua. A mesura que el senyal penetra en l'atmosfera, aquest es corva degut als gradients de la densitat atmosfèrica. Aquest retard del senyal es pot mesurar estimant quan hauria d'arribar el senyal en cas que no hi haguès atmosfera, i comparant-ho amb quan arriba realment. A partir de la derivada d'aquesta diferència es pot obtenir l'angle de curvatura del raig, i aquest es pot invertir per obtenir els gradients de refractivitat atmosfèrica. A partir d'aquests es poden obtenir els perfils termodinàmics amb l'ajuda de models atmosfèrics. Afegint-hi la capacitat polarimètrica, l'objectiu és que a més a més d'aquests productes termodinàmics (anomenats productes estàndard), la tècnica pugui servir per obtenir perfils verticals de precipitació.

La difèrencia de fase introduïda per la pluja és deguda a que les gotes, en caure i notar la resistència de l'aire, adopten una forma aplanada, de manera que acaben sent més extenses en la dimensió paral·lela a la superfície que en la perpendicular. Degut a això, les ones electromagnètiques que viatgen tangencialment a la superfície travessen més medi de precipitació en la direcció hortizontal que en la vertical. Així, el senyal es veu més retardat en la seva component H que en la V, i s'espera que aquest efecte arribi a ser mesurable si la precipitació és prou extrema.

Obtenir mesures simultànies de l'estat termodinàmic de l'atmosfera i de precipitació ha esdevingut un repte per la comunitat científica. Les missions espacials dedicades a obtenir perfils termodinàmics de l'atmosfera tenen problemes amb la presència de núvols gruixuts, ja que el medi esdevé opac a la radiació infraroja (que és la banda de l'espectre electromagnètic en la qual operen). Alternativament, es poden utilitzar radiosondes. Les radiosondes obtenen perfils termodinàmics de l'atmosfera amb molt alta resolució vertical, però tenen l'inconvenient que el seu llençament necessita certa infraestructura, i per tant les zones més remotes en queden al marge. Això inclou pràcticament la totalitat dels mars i oceans, i moltes zones sub-desenvolupades. Per tant, moltes de les zones amb precipitació extrema no poden ser caracteritzades amb aquesta tècnica. A més a més, la resolució temporal acostuma a ser molt baixa, ja que no se'n poden llençar moltes al dia degut a l'elevat cost econòmic que suposaria. Per altra banda, els radars que mesuren les estructures en tres dimensions de la precipitació no tenen la capacitat d'obtenir perfils de temperatura o pressió. Les estacions meteorològiques, que poden ser molt nombroses en segons quins territoris, estan limitades a mesures en superfície, i altra vegada, mars, oceans i regions sub-desenvolupades en queden al marge.

Amb tot, les Radio Ocultacions Polarimètriques emergeixen com una tècnica a tenir en compte a l'hora de caracteritzar precipitació extrema. La seva cobertura global, alta resolució vertical i la capacitat de penetrar en núvols i precipitació la fa una tècnica molt atractiva en aquest sentit. Cada cop més estudis científics coincideixen en apuntar un augment en la frequència d'aquests fenòmens extrems, i una caracterització acurada és necessària per millorar els models de predicció.

METODOLOGIA

Els estudis realitzats per a aquesta tesis doctoral s'han basat en respondre a tres objectius bàsics previs al llançament del satèl·lit PAZ. El primer és el de descriure formalment tots els efectes que poden afectar al senyal en la seva propagació des del GPS fins al LEO, i en particular quantificar l'efecte degut als hidrometeors. El segon, determinar si la detecció de pluja és possible, en base a mesures existents que puguin servir com a referència de la mesura que farà PAZ. I tercer, proposar com les mesures obtingudes per PAZ es poden aplicar, o ser útils, per la comunitat científica. Paral·lelament, s'ha dut a terme una campanya experimental amb l'objectiu d'obtenir, per primer cop en geometria rasant, senyals provinents de satèl·lits GPS amb una antena linealment polaritzada horitzontal i verticalment, i començar la caracterització del senyal.

La campanya experimental es va dur a terme al Puigsesolles, al cim del Montseny. Allà s'hi va instal·lar un receptor GPS i una antena polarimètrica igual que la que portarà el satèl·lit PAZ. L'experiment va estar funcionant durant uns 8 mesos, durant els quals es van recollir dades durant 170 dies.

Per tal d'obtenir els objectius esmentats, s'ha combinat treball teòric, simulacions i l'anàlisi de dades de la campanya experimental. El treball més teòric ha consistit en descriure formalment la teoria de propagació i dispersió de les ones electromagnètiques a banda L, en el camí que segueixen des del GPS fins al LEO, i que són rellevants per la mesura polarimètrica. Això inclou la interacció amb la ionosfera i els efectes de dispersió induïts pels hidrometeors, a més a més dels efectes de l'emisor, receptor i les corresponents antenes.

Pel que fa a la ionosfera, aquesta indueix rotació de Faraday en l'ona electromagnètica. Aquesta rotació afecta per igual les components H i V de la ona en cas que aquesta estigui perfectament polaritzada circular. Es dona el cas, però, que els satèl·lits GPS no garanteixen que l'emisió electromagnètica sigui perfectament RHCP, sinó que s'hi espera una certa component ortogonal. A més a més, l'ona acabaria desviant-se del cas RHCP perfecte després de travessar la zona de precipitació. Per tant, la part de ionosfera que travessa el senyal en el seu camí cap al receptor indueix un efecte despolaritzador (afecta different les components H i V) en l'ona electromagnètica. Aquest efecte s'haurà de tenir en compte en les dades que obtindrà PAZ, ja que es barrejarà amb l'efecte que realment interessa, el dels hidrometeors.

L'efecte dels hidrometeors es pot modelar utilitzant la teoria de dispersió de les ones electromagnètiques. Aquesta teoria s'ha desenvolupat en gran part per la comunitat de radar meteorològic, ja que és la base de les seves observacions. L'efecte polarimètric degut a la dispersió causat pels hidrometors es pot descriure utilitzant la matriu d'amplitud de dispersió, **S**, que depèn de la composició, mida i forma de la partícula responsable de la dispersió. Les components d'aquesta matriu s'utilitzen per determinar la diferència de fase específica (K_{dp}) que indueix la pluja:

$$K_{\mathrm{dp}} = \int_D \Re \left\{ S_{\mathrm{hh}} - S_{\mathrm{vv}} \right\} N(D) \mathrm{d}D$$

on la D és el diàmetre de la partícula i $N(D)$ correspon a la distribució de mides. La K_{dp} quantifica la diferència de fase entre les components H i V de l'ona electromagnètica deguda a la dispersió soferta, en unitats de radiants per kilòmetre. En el cas que ens ocupa, la geometria és de propagació (*forward scattering*). L'efecte acomulat al llarg del camí recorregut s'anomena diferència de fase polarimètrica ($\Delta\Phi$), i és l'observable que obtindrà PAZ:

$$\Delta\Phi = \int_L K_{\mathrm{dp}} \mathrm{d}l$$

on L representa la longitud total de medi dispersiu que ha travessat la ona. Aquesta definició conté una ambigüitat implícita, i és que les contribucions de la intensitat de la pluja i de l'extensió d'aquesta són pràcticament impossible de separar.

Un cop s'ha descrit la teoria i per tant, l'efecte dels hidrometeors s'ha modelat, es poden fer simulacion per tal d'estudiar la magnitud de l'efecte en situacions realístiques. Per a fer unes simulacions el més reals possible, s'han utilitzat les mesures obtingues per la missió de radio ocultacions COSMIC i per les missions de mesura de núvols i precipitació TRMM, GPM i CloudSat. De la missió de radio ocultacions se n'obté les posicions dels GPS i els LEO, les mesures de fase estàndard (sense polarimetria) i els nivells de soroll. La geometria és equivalent a la que tindrà l'experiment de PAZ (només en canvia l'altura de l'òrbita, que en el cas dels satèl·lits COSMIC és 100 km més alta), i dels nivells de soroll se'n pot estimar els que obtindrà PAZ, ja que l'equipament que utilitza la missió COSMIC és similar.

De les missions de precipitiació se n'obté mesures realístiques dels seus radars. Simulant els observables de radar (concretament, la reflectivitat Z) que s'esperen del tipus de partícules per les quals es simula l'efecte polarimètric, es pot establir una relació entre la mesura de radar i la diferència de fase específica. Així és pot simular la $\Delta\Phi$ que haurien obtingut els satèl·lits de la missió COSMIC si tinguèssin capacitat polarimètrica. Si, a més a més, les mesures de COSMIC i TRMM, GPM o CloudSat coincideixen en l'espai i el temps, es poden avaluar els nivells de soroll i els perfils termodinàmics estàndard que ha obtingut COSMIC en presència de pluja.

RESULTATS

Utilitzant les simulacions i les coincidències entre diferents missions de radio ocultació i precipitació, es pot establir un llindar de detectabilitat basat en la precisió que es pot estimar fent servir la potència del senyal rebut. És a dir, avaluant la potència del senyal rebut en els receptors de COSMIC, en situacions on els raigs han travessat precipitació, es pot determinar quina precisió en la mesura de la fase es pot esperar per a PAZ. Per a això, és té en compte que les antenes de PAZ haurien de funcionar lleugerament millor que les de COSMIC, però que mesuren només polarització lineal, i per tant només reben la meitat de la potència. Fent servir les coincidències entre COSMIC i TRMM (l'exercici s'exlica en el següent paràgraf), s'ha establert que la precisió de PAZ serà de 1.4 mm (en la diferència de fase) en les capes més baixes, i que millorarà a mesura que augmenti l'alçada. Això vol dir que els fenòmens de precipitació que indueixin una despolarització en el senyal de més de 1.4 mm, seran detectables.

La pregunta que es deriva d'aquest resultat és si un fenòmen que indueixi una despolarització com aquesta és gaire freqüent. Per respondre-la s'han fet tres tipus diferents de simulacions. El primer tipus consisteix en utilitzar coincidències entre mesures de COSMIC i valors mitjans d'intensitat de precipitacio de TRMM, que permeten un anàlisi estadístic global, a l'engròs i en dos dimensions (en total, s'han analitzat uns $200,000$ casos). D'aquest exercici se n'ha extret el límit de detectabilitat, 1.4 mm a les capes més baixes en els raigs que han travessat precipitació. D'altra banda, s'ha realitzat un exercici on s'han utilitzat mesures reals de precipitació en tres dimensions, que s'han col·locat i interpolat en el pla de radio ocultacions generades artificialment. Aquestes radio ocultacions tenen la geometria real, i per tant es pot simular les trajectòria que han seguit els raigs de manera aproximada, però en manquen les mesures termodinàmiques. D'aquesta manera es pot analitzar el perfil vertical de l'efecte polarimètric de la precipitació, però no es pot analitzar el nivell de soroll i precisió (en aquest exercici s'han pogut analitzar uns $200,000$ casos de la missió GPM). Finalment, s'han fet simulacions molt detallades de casos concrets on les observacions entre COSMIC i TRMM, GPM o CloudSat han estat pràcticament simultànies en la mateixa regió. Per aquestes simulacions s'han utilitzat els productes de precipitació en tres dimensions, i s'han simulat les trajectòries dels raigs de la radio ocultació, per tal de col·locar i interpolar la precipitació en el pla de la radio ocultació. En aquestes simulacions és possible l'anàlisi raig a raig de la mesura polarimètrica esperada, soroll i precisió reals, i perfils termodinàmics reals (per aquest exercici s'han pogut analitzar uns $2,000$ casos)

Els tres anàlisis coincideixen en indicar que aproximadament un 40% dels casos on la intensitat de pluja mitjana al llarg del raig sigui superior a 1 mm/h seran detectables. Aquest nombre augmenta fins a un 85-90% en cas que la intensitat de pluja mitjana al llarg del raig sobrepassi els 5 mm/h. I pràcticament la totalitat dels casos amb una intensitat mitjana de pluja de més de 10 mm/h al llarg del raig seran detectables. D'aquest estudi també se n'extreuen patrons geogràfics i temporals (segons l'estació) on s'observen tendències d'on i quan és més probable que hi hagi fenòmens detectables.

Com ja s'ha dit, és pràcticament impossible distingir la contribució de la intensitat i l'extensió de la precipitació en l'observable $\Delta\Phi$. Per tant, no es pot establir una relació directa entre la mesura obtinguda i un paràmetre geofísic. És necessàri, però, establir una relació entre l'observable polarimètric i un sol paràmetre que contingui informació de la pluja. Amb aquest objectiu, s'han construït unes taules per tal de determinar quina intensitat de precipitació es pot correspondre a cada mesura de $\Delta\Phi$, de manera probabilística. Utilitzant els resultats de les simulacions en tres dimensions (tant les que contenen radio ocultacions reals com les que no), s'ha caclulat quina és la distribució d'intensitats de precipitació que han travessat els raigs que corresponen a una certa mesura $\Delta\Phi$ per a una certa alçada h_{tp}. En aquesta distribució es poden establir tres valors: el que conté el 50% de la distribució per damunt d'aquest valor (mediana), el que en conté el 75% i el que en conté el 95%.

Així, es pot afirmar, per exemple, que per una certa $\Delta\Phi(h_{\mathrm{tp}})$, la intensitat de pluja ha estat superior a un cert valor el 75% de les vegades. Aquest exercisi permet establir una relació entre la observació i el paràmetre geofísic de manera estadística. A més a més de per les distribucions de la intensitat mitjana al llarg del raig, s'ha fet el mateix per la intensitat màxima al llarg del raig.

També s'ha estudiat un mètode tomogràfic per tal de distingir entre la intensitat i l'extensió de la precipitació en l'observable polarimètric. Amb la tècnica que es proposa s'han obtingut bons resultats teòrics en intentar recuperar les estructures de precipitació en un pla de dos dimensions (distància hortizontal i alçada). El problema és que la tècnica requereix unes aproximacions bastant restrictives, que en limiten l'aplicació pràctica. De totes maneres, algunes d'aquestes aproximacions es podrien relaxar si s'utilitzessin prediccions de models meteorològics per restringir, per exemple, la zona on s'espera la precipitació. Altrament, amb aquesta tècnica tomogràfica s'ha pogut discriminar entre estructures de precipitació properes al punt tangent dels raigs de la radio ocultació, d'aquelles situades més lluny, informació que pot ser útil per la caracterització termodinàmica d'aquests fenòmens.

Pel que fa a la campanya experimental, els resultats es poden considerar molt positius. D'una banda, l'anàlisi de les dades obtingudes ha servit per identificar efectes sistemàtics que no s'havien tingut en compte fins llavors, com per exemple la diferència de fase arbitrària que introdueix el receptor entre el port H i V. Aquest efecte implica que la mesura de la diferència absoluta no serà possible en l'experiment, i que haurà de ser relativa a una regió on no s'hi esperi precipitació (en general, a les mesures més altes de 20 km). El tractament dels efectes de *multipath* també han suposat un repte i un aprenentage molt útil per al futur tractament de dades de la missió.

En quant a les mesures polarimètriques obtingudes en la campanya, es pot afirmar que s'han obtingut les primeres evidències de que la precipitació indueix efectes polarimètrics en el senyal GPS. Això ha quedat pal·lès en els resultats de l'anàlisi estadística de les observacions. Analitzant els casos concrets en dies de precipitació extrema, s'ha pogut explicar l'ordre de magnitud de les observacions utiltizant les simulacions i les dades meteorològiques del METEOCAT, AEMET i EUMETSAT, i s'ha conclòs que, a més a més de la pluja, altres hidrometeors com els cristalls de gel i les partícules en fase mixta (aigua líquida / gel) poden tenir una contribució important en la despolarització del senyal. Les simulacions i el modelatge que s'ha explicat anteriorment s'ha anat actualitzant i millorant amb les conclusions i troballes de la campanya experimental.

Per acabar, s'han realitzat dos exercisis aprofitant les observacions coincidents entre les missions de radio ocultació i precipitació, per tal de ressaltar el tipus d'anàlisis que es podran fer rutinariament quan existeixin les dades Pol-RO. Primer, s'han comparat els perfils termodinàmics provinents de models meteorològics amb les dades obtingudes amb les radio ocultacions. Aquestes comparacions s'han pogut separar entre els perfils que han travessat pluja, i els que no, i s'ha pogut veure com existeixen diferències en els perfils que han travessat pluja. Tot i que no se n'ha determinat l'origen, aquestes diferències demostren la necessitat de més investigació en aquesta línea, ja sigui per millorar el modelatge de la precipitació, o bé millorar el tractament de les dades de radio ocultació en presència de precipitació. D'altra banda, s'ha dut a terme un estudi similar, però comparant els perfils de refractivitat obtinguts amb les radio ocultacions entre els casos on hi havia precipitació i els que no. Aquest estudi s'ha basat en determinar el règim termodinàmic que es pot identificar dels gradients de refractivitat, i si aquests canvien amb la presència de pluja. Els resultats mostren una tendència dels perfils amb precipitació a seguir règims que es poden associar a atmosferes saturades, que s'acostumen a identificar amb la presència de núvols.

Per tant, queda demostrat el ventall de possiblitats que s'obrirà amb les radio ocultacions polarimètriques. Si tot va bé, el satèl·lit PAZ serà el primer en obtenir-les i confirmar, des d'observacions espacials, les teories formulades en aquesta tesi.

ABSTRACT

In 2009, the Spanish Ministry of Science and Innovation approved a proposal to modify the Global Positioning System (GPS) receiver and to allocate a Polarimetric (Pol) Radio Occultation (RO) antenna in the Spanish PAZ satellite. PAZ became an opportunity to test the new Pol-RO concept, which aims to capture ROs using a two orthogonal linear polarization antenna. The experiment has been named Radio Occultations and Heavy Precipitation with PAZ (ROHP-PAZ). The objective is to measure the phase difference between the horizontal and the vertical components of the incoming electromagnetic field that is induced by heavy precipitation flattened raindrops. This effect, widely studied in the weather radar community, will be measured from space using GNSS signals for the first time with PAZ, which is planned to be launched in 2017 (date yet to be confirmed).

The main objective of this new concept is to enhance the RO capabilities by providing vertical precipitation information along with the current standard RO thermodynamic products (i. e. temperature, pressure and moisture). Until now, no other observing system has been able to provide simultaneous thermodynamic and precipitation information under extreme conditions. The high vertical resolution, global coverage and all-weather capability properties of the RO observations combined with vertical indication of precipitation intensity can be of great value for heavy rain characterization, and therefore for climate and weather forecasting and research.

Within this context, the theoretical background for the technique, its feasibility and applications have been assessed in this dissertation. The theoretical basis has been developed combining electromagnetic propagation theory and cloud and precipitation microphysics. Very detailed forward scattering simulations at L-band have been obtained in order to relate the microphysical parameters with the expected Pol-RO observables. Feasibility has been addressed using coincident (in space and time) RO profiles and space-based precipitation observations. Such simultaneous observations allow for the characterization of actual RO measurements according to the coincident precipitation information, and allow us to obtain, for example, the noise level under precipitating scenarios. Finally, the applications have been investigated through realistic end-to-end simulations of the Pol-RO observations, which provide the anticipated Pol-RO products for different precipitation situations, regions, and seasons.

Before the launch of the satellite, a field campaign has been conducted with the aim of starting the characterization of the polarimetric measurements. The engineering model of the PAZ antenna was placed at the top of a mountain peak in order to capture, for the first time, linear polarimetric GNSS signals at low grazing angles. Although the geometry and the scenario are different from those that

PAZ will be studying from space, this campaign has been useful to start identifying the hardware internal effects and unexpected precipitation features that will affect the Pol-RO observations. These effects have been incorporated into the simulations, providing valuable feedback to obtain more realistic Pol-RO products.

These exercises yielded several relevant results. The noise level analysis from actual RO observations sensing precipitation scenarios has allowed us to set a detectability threshold for the technique, indicating that a high percentage of moderate to heavy precipitation events will be detected with PAZ. Nevertheless, the integrated nature of the Pol-RO observable does not allow us to distinguish between the contributions from the rain's intensity and extension, leaving an ambiguity in the provided product. In an attempt to solve such ambiguity, a tomographic approach has been proposed, which has yielded promising theoretical results. Moreover, it has been shown how the Pol-RO observables can be linked to physical precipitation parameters, such as the along-ray averaged rain rate, in a probabilistic way. The end-to-end simulation has also revealed that the ionosphere will induce a non-negligible depolarization that will require calibration.

Besides providing feedback for the simulations, the data from the field campaign have also shown the first observational evidence that precipitation and other hydrometeors have a noticeable effect on the GNSS polarimetric signals. These effects have been compared with the simulations, showing agreement within an order of magnitude.

The collocated data has also been used to show the potential applications of Pol-ROs products. Comparison of model outputs with RO retrievals, in the presence of heavy rain, has shown discrepancies that will need further investigation, and Pol-RO data appears to be a well-fitted dataset for such studies.

PUBLICATIONS

The contents of this thesis have been published in the following peer reviewed papers:

- [Cardellach et al., 2014] Cardellach, E., Tomás, S., Oliveras, S., Padullés, R., Rius, A., de la Torre-Juárez, M., Turk, F. J., Ao, C. O., Kursinski, E. R., Schreiner, W. S., Ector, D., and Cucurull, L.: SENSITIVITY OF PAZ LEO POLARIMETRIC GNSS RADIO-OCCULTATION EXPERIMENT TO PRECIPITATION EVENTS, *IEEE Transactions on Geoscience and Remote Sensing, 53, 1, 190-206*, **2015**. doi: 10.1109/TGRS.2014.2320309

- [Padullés et al., 2016a] Padullés, R., Cardellach, E., de la Torre-Juárez, M., Tomás, S., Turk, F. J., Oliveras, S., Ao, C. O., and Rius, A: ATMOSPHERIC POLARIMETRIC EFFECTS ON GNSS RADIO OCCULTATIONS: THE ROHP-PAZ FIELD CAMPAIGN, *Atmospheric Chemistry and Physics, 2, 16, 635-649*, **2016**. doi: 10.5194/acp-16-635-2016.

- [Padullés et al., 2016b] Padullés, R., Cardellach, E., and Rius, A: UNTANGLING RAIN STRUCTURE FROM POLARIMETRIC GNSS RADIO OCCULTATION OBSERVABLES: A 2D TOMOGRAPHIC APPROACH, *European Journal of Remote Sensing, 49, 571-585*, **2016**. doi: 10.5721/EuJRS20164930

There are also two papers that have been already submitted:

- de la Torre-Juárez, M., Padullés, R., Turk, F. J., and Cardellach, E.: THERMODYNAMIC PROPERTIES OF CLOUDS AND PRECIPITATION FROM SATELLITE RADIO OCCULTATION PROFILES, *submitted to Journal of Geophysical Research: Atmospheres*, **2017**.

- [Cardellach et al., 2017] Cardellach, E., Padullés, R., Tomás, S., Turk, F. J., Ao, C. O., de la Torre-Juárez, M. PROBABILITY OF INTENSE PRECIPITATION IN GNSS RADIO-OCCULTATION THERMODYNAMIC PROFILES DERIVED FROM THEIR POLARIMETRIC SIGNATURES, *submitted to QJRMS*, **2017**.

And two that are in preparation at the time of writing:

- [Tomás et al., 2017] Tomás, S., Cardellach, E., Padullés, R. SEPARABILITY OF SYSTEMATIC EFFECTS ON POLARIMETRIC GNSS-RO FOR PRECIPITATION SENSING, *in preparation*, **2017**.

- Padullés, R., Cardellach, E., Ao, C.O., Turk, F. J., de la Torre-Juárez, M., EFFECT OF CLOUDS AND PRECIPITATION INTO GNSS RO RETRIEVALS, *in preparation*, **2017**.

We have to remember that what we observe is not nature herself,
but nature exposed to our method of questioning.

Werner Karl Heisenberg

ACKNOWLEDGEMENTS

This thesis has been possible because many people have participated, in one way or another, to its construction. I am deeply grateful to all of them.

First of all, I would like to thank Estel, my advisor. Without any doubt, this thesis wouldn't have been possible without her. She gave me the opportunity to start this challenge, and her guidance full of insightful advises and enthusiastic attitude has been a very enriching experience for me. I also want to thank Toni, Sergio and Santi for their advises, comments, discussions and help within the PAZ adventure. And to the rest of the Earth's Observation ICE group: Serni, Fran, Weiqiang, Hilda, Oleguer and Juan Carlos, they have been always happy to help.

I want to thank Josep for solving all kind of computer related problems and for the meals he organizes; the ICE staff: Isabel, Guadalupe, Josefa, Angels and Fina, for their inestimable help with bureaucracy; and all the co-PhDs and postdocs with whom I shared all these 4 years, from the cyber to the new building.

I also want to thank Manuel de la Torre, Joe Turk, and Chi Ao for their guidance during my stays at the Jet Propulsion Laboratory; the rest of the JPL's GNSS group for the interesting meetings and discussions; the staff from the student's office and from the planetary science section for their kindness and support. Special thanks to Manuel and Joe for making my stays in Pasadena more than a simple research visit.

It's important to acknowledge the people that provided pieces of code: Josep Maria (Environment Canada) and Chi (JPL), for the ray tracers and the patience solving doubts; R. Honeyager and Dr. Liu (FSU) for the ice particle shapes; J. Leinonen (JPL) for the aggregates generator, the pyTmatrix and the lesson on how to use them; J. Haase and M. Murphy (SIO) for providing data and models from the airborne campaign. Also, to the institutions that provided data: the METEOCAT provided data from the weather radars and the radiosondes; the AEMET provided data from models, radars and from the SAF-NWC; the EUMETSAT provided data from satellite. Data from the COSMIC mission were acquired at the UCAR's CDAAC archive; data from TRMM and GPM were acquired at the NASA GES DISC; data from CloudSat was acquired in the CloudSat DPC, run by CIRA at Colorado State University.

The field campaign gathered contribution from many people. I want to thank Adriano Camps and his group at the Remote Sensing Lab (TSC-UPC) for their contribution to the assembly of the experiment; to the Spanish Ministry of Defence, Estado Mayor de la Defensa (EMAD) and the Parc Natural del Montseny office for the experimental site; and to the Helmholtz German Research Centre for Geosciences (GFZ Potsdam) for providing the Javad GPS receiver.

And finally, I want to thank my family, my friends and Núria for their unconditional support.

This work has been supported by the FPI BES-2012-059353 grant from the Spanish National Research AYA2011-29183-C02-02 and ESP2015-70014-C2-2-R. The stays at the Jet Propulsion Laboratory were supported by the JVSRP program, funded through the NASA ROSES Grants NNH14ZDA001 N-ESUSPI, NNH10ZDA001N-GEOIM, and NNH11ZDA001 N-ESI.

CONTENTS

LIST OF FIGURES

LIST OF TABLES

ACRONYMS

2DVD	2 Dimensional Video Disdrometer
ABL	Atmospheric Boundary Layer
AEMET	Agencia Estatal de Meteorología
AIRS	Atmospheric InfraRed Sounder
AMSR	Advanced Microwave Scanning Radiometer
AMSU	Advanced Microwave Sounding Unit
BOC	Binary Offset Carrier
C/A	Coarse Acquisition
CALIPSO	Cloud-Aerosol Lidar and Infrared Pathfinder Satellite Observation
CDAAC	COSMIC Data Analysis and Archive Center
CDMA	Code Division Multiple Access
CHAMP	CHAllenging Minisatellite Payload
COSMIC	Constellation Observing System for Meteorology, Ionosphere, and Climate
CP	Cloud Top Phase
CPM	Convective Permitting Models
CPR	Cloud Profiling Radar
CSIC	Consejo Superior de Investigaciones Científicas
CTY	Cloud Type
CTH	Cloud Top Height
DDA	Discrete Dipole Approximation
DLL	Delay Lock Loop
DPR	Dual-frequency Precipitation Radar
DSD	Drop Size Distribution
DSSS	Direct Sequence Spread Spectrum
ECMWF	European Centre for Medium-Range Weather Forecast
ENSO	El Niño-Southern Oscillation
EU	European Union

EUMETSAT European Organisation for the Exploitation of Meteorological Satellites

FORMOSAT-3 Formosa Satellite mission # 3

FSI Full Spectrum Inversion

GFS Global Forecast System

GOES Geostationary Operational Environmental Satellite

GLONASS Global'naya Navigatsionnaya Sputnikovaya Sistema

GMI GPM Microwave Imager

GNSS Global Navigation Satellite System

GNSS-RO GNSS Radio Occultation

GNSS-R GNSS Reflectometry

GPM Global Precipitation Mission

GPS Global Positioning System

GPS-MET GPS Meteorological experiment

GRACE Gravity Recovery And Climate Experiment

GRAS GNSS Receiver for Atmospheric Sounding

GTS Global Telecommunication System

IASI Infrared Atmospheric Sounder Interferometer

ICE Institut de Ciències de l'Espai

IEEC Institut d'Estudis Espacials de Catalunya

IGOR Integrated GPS and Occultation Receiver

IGRF International Geomagnetic Reference Field

IRI International Reference Ionosphere

IRNSS Indian Regional Navigational Satellite System

IWC Ice Water Content

JPL Jet Propulsion Laboratory

LEO Low Earth Orbiter

LHCP Left Hand Circularly Polarized

LUT Look Up Table

LWC Liquid Water Content

M Military

METEOCAT Servei Meteorològic de Catalunya

MSG	Meteosat Second Generation
NASA	National Aeronautics and Space Administration
NCEP	National Centers for Environmental Prediction
NOAA	National Oceanic and Atmospheric Administration
NRT	Near Real Time
NWC-SAF	nowcasting and very short-range forecasting
NWP	Numerical Weather Prediction
OAT	Occultation Analysis Tools
OL	Open Loop
P	Precise
PLL	Phase Lock Loop
POD	Precise Orbit Determination
Pol-RO	Polarimetric Radio Occultation
PR	Precipitation Radar
PRN	Pseudo Random Noise
PSD	Particle Size Distribution
QBO	Quasi-Biennial Oscillation
QPSK	Quadrature Phase Shift Keying
QZSS	Quasi-Zenith Satellite System
RHCP	Right Hand Circularly Polarized
RO	Radio Occultation
ROHP	Radio Occultations and Heavy Precipitation
ROHP-PAZ	Radio Occultations and Heavy Precipitation aboard PAZ
ROPP	Radio Occultation Processing Package
TMBOC	Time Multiplexed Binary Offset Carrier
TOA	Time Of Arrival
TRMM	Tropical Rainfall Measurement Mission
SAC-C	Satellite de Aplicaciones Cientificas - C
SAR	Synthetic Aperture Radar
SIO	Scripps Institution of Oceanography
SNR	Signal to Noise Ratio
SR	Super Refraction

STD Slant Total Delay

TEC Total Electron Content

TMI TRMM Microwave Imager

TSVD Truncated Single Value Decomposition

UCAR University Corporation for Atmospheric Research

USA United States of America

VIRS Visible and Infrared Radiometer System

WC Water Content

WMO World Meteorological Organization

WRF Weather Research and Forecasting

Z radar reflectivity factor

ZTD Zenith Total Delay

MOTIVATION

MOTIVATION

The motivation for this thesis goes back to 2009, when the Spanish Ministry for Science and Innovation approved a proposal to include a Polarimetric Radio Occultation (Pol-RO) payload in the PAZ satellite. PAZ was scheduled for launch by 2012 and became an opportunity to test the Pol-RO concept, a new technique devised at the Institut de Ciències de l'Espai (ICE-CSIC/IEEC) under the leadership of Dr. Estel Cardellach. The proof-of-concept experiment was called the Radio Occultation and Heavy Precipitation onboard PAZ (ROHP-PAZ), and is going to collect ROs with a double polarization antenna, with one port linearly polarized in the horizontal (H) direction and the other in the vertical (V). Never before has this approach been tested, except for the ground based experiment conducted during this PhD study. The launch of PAZ has been delayed several times, and it is now planned for 2017. The objective is to detect the depolarization effect that precipitation (especially the heaviest) might induce in the Global Navigation Satellite System (GNSS) signals propagating through the lower layers of the atmosphere, tangentially to the Earth surface. It is known thanks to the weather radar community that raindrops indeed induce depolarization in electromagnetic signals which is accounted for using the specific differential phase shift (K_{dp}). Its integral accumulation along the ray path is known as the differential phase shift, $\Delta\Phi$.

RO receivers can provide very precise measurements of the phase of incoming signals. Hence, the idea is to obtain the difference between the phase measured at the H port and the phase measured at the V port. This measurement is the differential phase shift between the horizontal and the vertical components of the incoming electromagnetic (EM) wave. The heavier the rain, the larger the phase shift expected. Thus, if successful, Polarimetric Radio Occultations could provide precipitation information along with the standard thermodynamic profiles that ROs already provide (refractivity, temperature, pressure and water vapour).

From the point of view of the ROs, this experiment could prove that information about precipitation can be provided, enhancing the possibilities that the technique already offers. ROs are routinely assimilated into Numerical Weather Prediction (NWP) models, and additional information could increase their impact. Additionally, and independently of the polarimetric experiment, PAZ collecting ROs will contribute to increasing the number of atmospheric profiles collected per day.

From the point of view of precipitation and weather, providing highly reliable and accurate thermodynamic profiles along with certain vertical profiles of precipitation information could have a large impact on the understanding of extreme precipitation events. Until now, no other observing system has been able to provide simultaneous thermodynamic and precipitation information under extreme conditions. The evolution of the temperature or the water vapour inside and outside precipitation events, and their interaction, is of great interest in the research of precipitation phenomena and ROHP-PAZ retrievals could therefore be much appreciated. Extreme weather events are believed to be increasing in frequency and severity due to climate change, hence interest in modelling them properly will increase in the coming decades.

Thus, many challenges and questions arise before the launch of the satellite, and this dissertation intends to answer them. Being a proof-of-concept mission, and being the first time that such observations will be acquired from space, this dissertation has the following main objectives:

- To set the basis of the technique and describe the observables.
- To describe in enough detail the different interactions, relevant to the observations, that signals undergo between emission and reception.
- To identify and characterize the potential systematic errors that will affect the signals.
- To anticipate the products that will be obtained and how to relate them to geophysical information.
- To explore the potential benefits of having such observations along with the standard RO products, by giving examples that show their impact.

These objectives can be addressed with a synthetic end-to-end simulation of the ROHP-PAZ mission using a forward model. First of all, the output of the simulation is defined by the observables that are going to be acquired. Then, the core of the simulation is based on the theory of EM wave propagation and scattering, as well as on precipitation and cloud microphysics. Scattering by precipitation droplets and ice cloud particles is the most important contribution to the observables, and the one that is intended to be quantified. However, modelling the interaction of EM waves with the ionosphere is needed as well, since it might affect the observables too. Therefore, the theory behind the simulations has to be understood and described in enough detail.

An experimental field campaign was scheduled before the launch of the satellite, with the aim to collect, for the first time, RO-like GNSS polarimetric signals. These data could be used to start identifying other phenomena that could be affecting the signals, besides precipitation. The results from the campaign can be used as valuable feedback, offering the possibility to account for unexpected effects in the polarimetric signal when performing the simulations.

Expected systematic errors, such as the biases that the antenna and the receiver might introduce, and the effect of the ionosphere on the signal propagation, must be included in the end-to-end simulation. This can be achieved using actual data from other RO missions to perform the polarimetric simulations on a realistic basis, in terms of the satellites geometry, noise, and phase measurements. In addition, inputs for precipitation and cloud particles can be obtained from actual weather radar measurements coincident with these RO observations. Long term missions such as COSMIC (for ROs), and TRMM, GPM and CloudSat (for precipitation and clouds) provide a large number of observations, and it is therefore possible to account for enough coincidences to perform such an exercise.

The outputs of the simulation can then be analysed as the retrievals of the polarimetric mission. The added value is that in this case, the source of the observables is known, so theoretical relationships between the observables and the source phenomena can be established. Geographical or seasonal patterns can be investigated, so that observations can be treated differently depending on the situation.

This technique has already raised interest in other research groups worldwide. The Jet Propulsion Laboratory has been involved since the beginning in the Pol-RO concept through two NASA funded grants, and they are currently applying for more ambitious projects using this technique. Also a Chinese group from the National Space Science Centre (NSSC) of the Chinese Academy of Science (CAS) has been performing theoretical analysis of the possibilities offered by Pol-ROs [An et al., 2016] and, attempting to conduct a field campaign. Finally, a group in the Scripps institution of Oceanography (SIO) in San Diego, led by Dr. J. Haase, has also shown interest and plans to collect Pol-ROs from an airplane. Therefore, one of the main aims of this dissertation is to describe the fundamentals of Pol-ROs, in views of the increasing interest in the technique.

OVERVIEW

This dissertation is divided into three main parts:

PART I The first part aims to give the reader the proper context.

First, the necessary *tools* are provided: a brief introduction to GNSS, how it works, and how it can be used for remote sensing; then, the Radio Occultation technique is introduced, with its history, the theoretical concept, and the products it provides. This occupies the first and second sections of Chapter 1. After the *tools*, the target that will be observed is presented: clouds and precipitation. A brief description, their modelling and current remote sensing techniques are provided in the third part of Chapter 1.

Right after that, in Chapter 2 the ROHP-PAZ mission is introduced. The PAZ satellite is described, and the objectives of the mission are stated. Finally, the expected performance of the technique is discussed.

PART II In the second part, a more theoretical and technical background is provided.

The EM wave propagation topics that are relevant to this dissertation are reviewed in the first part of Chapter 3. These are, for example, the forward scattering of GNSS signals by precipitation droplets and cloud ice crystals, and the propagation of GNSS signals through the ionosphere. In the second part of Chapter 3, a few topics on precipitation and cloud microphysics are addressed. At the end of the chapter, the expected systematic errors are discussed. This chapter sets the basis for the simulations.

The simulations are described in detail in the first part of Chapter 4. The rest of the chapter contains the collocation exercise between the RO and the precipitation missions, the description of the simulation of the ionosphere, and how all the information is combined and stored.

PART III The third part contains the results obtained from the simulations in Part II and the experimental field campaign.

The results are separated according whether they involve polarimetric measurements or not. In the first part of Chapter 5, the anticipated products of the polarimetric mission and how they should be treated are shown. In addition, simulations using weather model outputs are performed. Finally, a technique to disentangle the contribution to the polarimetric observable of the rain's intensity from the contribution of the rain's cell extension is proposed.

Chapter 6 shows the results that have been obtained that do not involve polarimetric measurements, but that are relevant to standard ROs. These are thermodynamic studies that combine measurements from actual RO missions coincident with those obtained by precipitation and cloud missions. These can be interpreted as anticipating of the kind of studies that it will be possible to perform with the ROHP-PAZ data.

In Chapter 7, the ROHP-PAZ field campaign is described, and the results are shown.

Finally, the main conclusions of the dissertation are discussed in Chapter 8.

Part I

INTRODUCTION

1

INTRODUCTION

This chapter aims to discuss the state of the art of several topics relevant to this thesis. First, basic notions of the Global Navigation Satellite System (GNSS) are provided. Then, a significant part of the chapter is dedicated to Radio Occultations, describing the concept and the technique, and its applications, especially those related to weather and climate. Finally, clouds and precipitation are also introduced, since they are going to be the targets of the observations for this work.

1.1 THE GLOBAL NAVIGATION SATELLITE SYSTEM

The GNSS is a space based technology intended for navigation purposes that provides global coverage. It comprises the Global Positioning System (GPS), owned by the United States of America (USA), and the Global'naya Navigatsionnaya Sputnikovaya Sistema (GLONASS), owned by Russia. Galileo, the European GNSS, and BeiDou, the Chinese one, are still in the deployment phase at the time of writing. There also exist a few regional navigation satellite systems, such as the Indian Regional Navigational Satellite System (IRNSS) and the Quasi-Zenith Satellite System (QZSS), owned by India and Japan, respectively, that do not provide global coverage. Among all the existing satellite systems, the most used is GPS. The work in this dissertation is based on GPS signals, although it could be easily adapted to be used on other systems.

The technique uses microwave signals emitted continuously from a satellite constellation, of which a minimum of 5 satellites are visible at any time from any place on Earth. It is highly precise, continuous and all-weather capable, so it can be used for positioning, timing, and therefore, navigation. Each satellite emits microwave signals at two or more frequencies in the L-band. These signals are emitted Right Hand Circularly Polarized (RHCP) to avoid polarization mismatches. The basics of the navigation technique rely on the one-way Time Of Arrival (TOA) ranging, applied to at least four visible satellites broadcasting a known signal from which their relative distance can be precisely derived.

Besides navigation, these signals can be used for many other purposes. When the signals are used for a purpose that they were not intended for, they are usually referred as signals of opportunity. Using these signals has no cost and they are therefore very attractive to explore and exploit. An example of this is the GNSS

Remote Sensing, which comprises most of the techniques that study the Earth's atmosphere and surface using GNSS signals. To understand how the atmosphere and surface states can be obtained from GNSS signals, one must first understand the signal itself, and how it is tracked.

1.1.1 *GPS signal*

The GPS satellites continuously broadcast signals in the L-band. The satellite transmissions are derived from the fundamental frequency of 10.23 MHz, driven by long-term stable atomic clocks. The three main carrier frequencies are $L1 = 1.57542$ GHz, $L2 = 1.22760$ GHz, and $L5 = 1.11765$ GHz. L5 is still considered pre-operational (see for example www.gps.gov).

The GPS signal is composed of different codes: the Coarse Acquisition (C/A) code, the Precise (P) code, and the navigation message. In addition, modern GPS satellites include the Military (M) code, and the civil signal L2C. However, L2C is still considered pre-operational and is not going to be discussed here. The C/A and the P codes are coded into the signal using the Direct Sequence Spread Spectrum (DSSS) technique, which is a form of phase shift modulation. The modulation is performed using a known Pseudo Random Noise (PRN) sequence (consisting of ± 1 rectangular pulses) that spreads the spectrum according to its chipping rate. The use of DSSS enables precise ranging by the receivers, enables different satellites to be transmitting at the same frequency with the possibility for the receiver to distinguish among them (Code Division Multiple Access (CDMA)), and it prevents narrowband interferences [Kaplan and Hegarty, 2006].

The C/A code is a pseudorandom sequence uniquely generated for each satellite. The sequences belongs to the *Gold* family of codes, implying low cross-correlation among the family members and thus making them rapidly distinguishable by the receiver. The C/A code sequence repeats every 1 ms. On the other hand, the P code sequence repeats every 266.4 days, and each 7-day segment is assigned to a PRN code which identifies a transmitting satellite. It has higher chipping rate than the C/A code, hence the distance between chip transitions is smaller. Due to its shorter chip transition, range measurements using the P code are more precise than those using the C/A code, but it takes longer to be distinguished. Moreover, since the bandwidth of the C/A code is smaller than that of the P code, it has a higher peak in the power spectrum.

The L1 carrier is modulated by both the C/A and the P codes, in addition to the navigation data message. The navigation message is modulated with a very low chipping rate. On top of it, the C/A and the P codes are modulated simultaneously using the Quadrature Phase Shift Keying (QPSK) method, where the two sequences are generated in phase quadrature (relative phase difference of 90°). Hence, the P code is encoded in the *quadrature* component of the L1 carrier, while the C/A code is modulated into the *in-phase* component. The L2 carrier phase used to have only

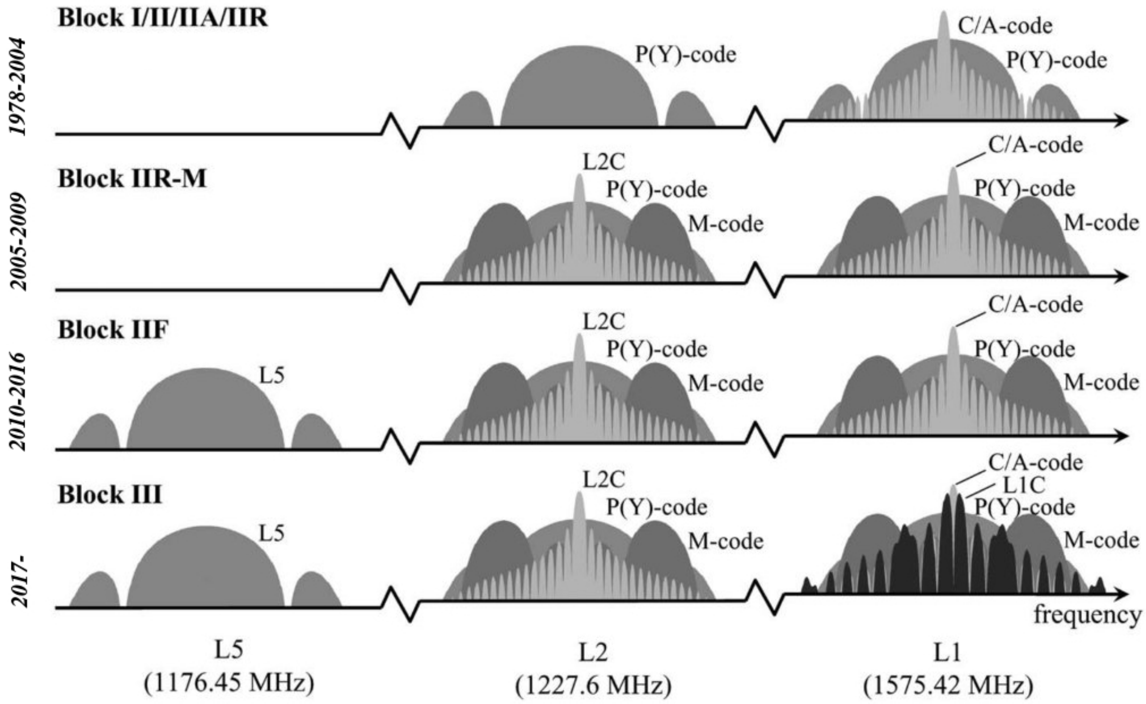

Figure 1.1: Schematic view of the GPS signals power spectrum, according to each satellite type. The years on the left indicate the launch year ranges for each satellite version. Image adapted from Hegarty and Chatre [2008].

the P code modulated on it, in addition to the navigation message. Therefore, the signal can be expressed as:

$$s_1(t) = \sqrt{2P_{C/A_1}}D(t)C(t)\cos(w_1 t + \phi_1) + \sqrt{2P_{P_1}}D(t)P(t)\sin(w_1 t + \phi_1) \quad (1.1)$$

$$s_2(t) = \sqrt{2P_{P_2}}D(t)P(t)\cos(w_2 t + \phi_2) \quad (1.2)$$

where $P_{C/A,P}$ is the received power of the C/A and P components of the signal for L1 (sub-index 1) and L2 (sub-index 2), $D(t)$ is the amplitude modulation containing the navigation data message, $C(t)$ is the pseudorandom sequence corresponding to the C/A code, and $P(t)$ is the pseudorandom sequence corresponding to the P code. The M code, not represented in these expressions, is modulated in both L1 and L2 using a variant of the DSSS technique called Binary Offset Carrier (BOC). This technique places the peak of the power spectrum at the edges of the bandwidth, avoiding interference with the existing codes [Hegarty and Chatre, 2008].

The structure of the power spectrum in each carrier phase is summarized in Figure 1.1. It shows the structure of each signal that is broadcast by each kind of satellite. The timeline of the different GPS satellite versions is summarized in Section 1.1.1.2.

1.1.1.1 *Pseudorange and phase observables*

GPS receivers also have a clock, which should be synchronized with the GPS clocks. If the clocks are perfectly synchronized, the receiver can create a replica of the GPS signal at the same time as the GPS satellite does. The replica is then delayed to account for the travel time of the signal generated by the satellite, and compared with the actual measured signals using cross-correlation techniques. Since the signals should look the same, it is actually an autocorrelation. Therefore, the objective is to find the time that the replica has to be delayed in order to maximize the autocorrelation. The time displacement between the two signals is multiplied by the speed of light (c), which leads to the pseudorange measurement P^S (*pseudo* because of other effects that affect the measurement besides the distance between the receiver and the satellite):

$$P^S = (T - T^S)c \tag{1.3}$$

where T is the receiver clock's time when the signal is received and T^S is the satellite clock's time when the signal was transmitted. Time measurements T and T^S can be related to the true time accounting for clock calibration errors, hence the pseudorange measurement is contaminated by small clock errors in addition to extra atmospheric and ionospheric delays, hardware errors, and noise.

The phase observable, Φ, is obtained by matching the phase of the received signal with the phase of the receiver's internal oscillator. Once the match has been performed (phase lock), what is measured is the adjustment of the oscillator's frequency to keep locked with the incoming phase. This adjustment is actually the delay to the replica that maximizes the autocorrelation, explained in the previous paragraph. This provides a measure of variation of the phase observable in time, equivalent to the integrated Doppler [Leick, 1995]. Even though this is a very precise measurement, the absolute number of full phase cycles is not obtained. Therefore, an accurate range measurement is not possible using the phase observable alone.

An example of this kind of technique is the Phase Lock Loop (PLL). Generally, when using these techniques, the receiver keeps track of the phase by anticipating a delay in the following measurement that is related to the previous measured one. However, under certain circumstances, the phase is varying too quickly for the receiver to keep track. The alternative tracking that aims to solve this issue is called Open Loop (OL) [e. g. Sokolovskiy, 2001]. This approach makes the receiver anticipate a Doppler shift based on a model (Doppler model), instead of relying on previous measurements. To build these models, real-time knowledge of the satellite and receiver positions is required. In addition, knowledge about the state of the atmosphere is usually needed.

1.1.1.2 *Evolution and modernization of GPS*

The first GPS satellites were developmental prototypes. They were called GPS Block I and a total of eleven satellites were launched between 1978 and 1985. These prototypes were followed by nine operational satellites, called Block II, that were launched between 1989 and 1999. Then, nineteen Block IIA satellites were launched between 1990 and 1997, and thirteen Block IIR satellites were launched between 1996 and 2004 [Hegarty and Chatre, 2008]. These satellites broadcast the L1 and L2 signals as explained in the previous section. Twelve of the Block IIR satellites are still operational.

In 2005, the first Block IIR-M (modernized IIR) satellite was launched, becoming the first to broadcast the M code on L1 and L2, and a civil signal on L2: the L2C. The L2C code has a similar power spectrum to the C/A, but it is generated in a different way. It combines two different PRN codes, with lower chipping rates than the C/A, and it contains a dataless component. The fact that one of the components of the L2C code is dataless allows for very robust tracking of the signal, and the fact that the data component is modulated with a lower rate than the C/A allows the L2C code to be demodulated in more challenging environments [Kaplan and Hegarty, 2006]. Between 2005 and 2009, a total of eight Block IIR-M satellites were launched.

After those, in 2010, the next generation of GPS, the Block IIF satellites, were ready. Block IIF satellites incorporated the capability to broadcast the L5 signal. It is broadcast using DSSS modulation, with the same chipping rate as the P code. The signal is composed of two components that are in quadrature, one of them being dataless (*quadrature*) and the other containing the navigation message (*in-phase*). Therefore, the GPS Block IIF satellites broadcast the C/A and P codes on L1, the L2C and P codes on L2, and the L5 signal. Twelve of these satellites have been launched until 2017.

At the time of writing, the new generation of GPS satellites, the GPS-III, is ready. The first one is scheduled for launch by the first quarter of 2017. The GPS-III satellites will incorporate the L1 civil signal (L1C). This signal arose from an agreement between different agencies, and is designed to allow interoperability with Galileo satellites and the regional QZSS, IRNSS and Beidou systems. The L1C signal is obtained through the Time Multiplexed Binary Offset Carrier (TMBOC) technique, broadcast at the same chip rate as the C/A code. The maximum of the power spectrum is displaced from the center, making the separation of the codes in the L1 carrier possible. Like L2C, L1C has a dataless component (called the data-less pilot signal, $L1C_P$) in quadrature with the component that has the navigation message coded onto it (called $L1C_D$) [Navstar GPS, 2013b].

At the time of writing, there are 12 Block IIR, 8 Block IIR-M, and 12 Block IIF satellites in operation. It is expected that L2C capability will reach 24 satellites by 2018, 24 satellites will have L5 capability by around 2024, and L1C will be available from 24 GPS satellites by the late 2020s. Currently, L2C and L5 are still considered pre-operational (see *www.gps.gov* for updated information).

1.1.2 *GNSS Remote Sensing*

When trying to obtain the range from the propagation time of the signal, one must take into account the possible sources of errors that are contaminating that signal. The main sources are satellite and receiver clock errors, satellite orbit and geometry errors, relativistic effects, receiver noise, atmospheric effects and multipath. While these effects introduce errors into the range determination, some of them can be used to infer the state of the propagation media. This is the case with atmospheric delays and multipath.

Signals propagating through the atmosphere are slightly delayed due to atmospheric refraction. On the one hand, refractivity gradients bend the signal, increasing its ray path. On the other hand, atmospheric refractivity changes the wave phase velocity due to the fact that the index of refraction is larger than 1. In addition, free electrons in the ionosphere affect the signal; this effect is notably different between the two GPS frequencies. Moreover, the signals can be reflected by the Earth's surface and reach the observer with the corresponding delay of a different travel path. These effects are considered noise in the range determination for navigation purposes, but can be a source of information about the Earth's atmosphere and surface.

The GNSS signals can be acquired from the ground (GNSS ground base stations) or from space (from a Low Earth Orbiter (LEO)). From the ground, the extra travel delay of the signal can be linked to the wet and the hydrostatic components of water vapour, which can be obtained through the Zenith Total Delay (ZTD) and the Slant Total Delay (STD) [e. g. Bevis et al., 1992]. These profiles are assimilated into weather prediction models [e. g. Cucurull, 2001]. Also from the ground, the reflected signals can be used to infer several properties of the surrounding soil, such as soil moisture, conductivity or roughness [e. g. Cardellach et al., 2011; Rodriguez-Alvarez et al., 2011]. Even multipath interferences can be used for inferring information about the surroundings, like moisture, or to locate reflective objects [e. g. Larson et al., 2010].

From a LEO, signals can be acquired using two different geometries. The first involves following the GPS satellite while it is occulting (or rising) behind the Earth. This is the GNSS Radio Occultation (GNSS-RO) technique, which is the main topic of this work and will be introduced in the following section. GNSS-RO provides vertical profiles of water vapour, temperature, pressure, refractivity and electron density. The other possible configuration is to collect the signals after they have been reflected by the Earth's surface. This technique is called GNSS Reflectometry (GNSS-R). With GNSS-R, altimetry and scatterometry studies can be performed, obtaining properties of the surface such as relative altitude and roughness [e. g. Garrison et al., 1998; Zavorotny and Voronovich, 2000; Martín-Neira et al., 2001; Cardellach, 2002]. Different configurations of GNSS-R are possible, like obtaining the reflected signals from other platforms such as airplanes or balloons, or obtaining the reflected signals at low grazing angle with a Radio Occultation (RO) configuration [e. g. Beyerle et al., 2002; Cardellach et al., 2004].

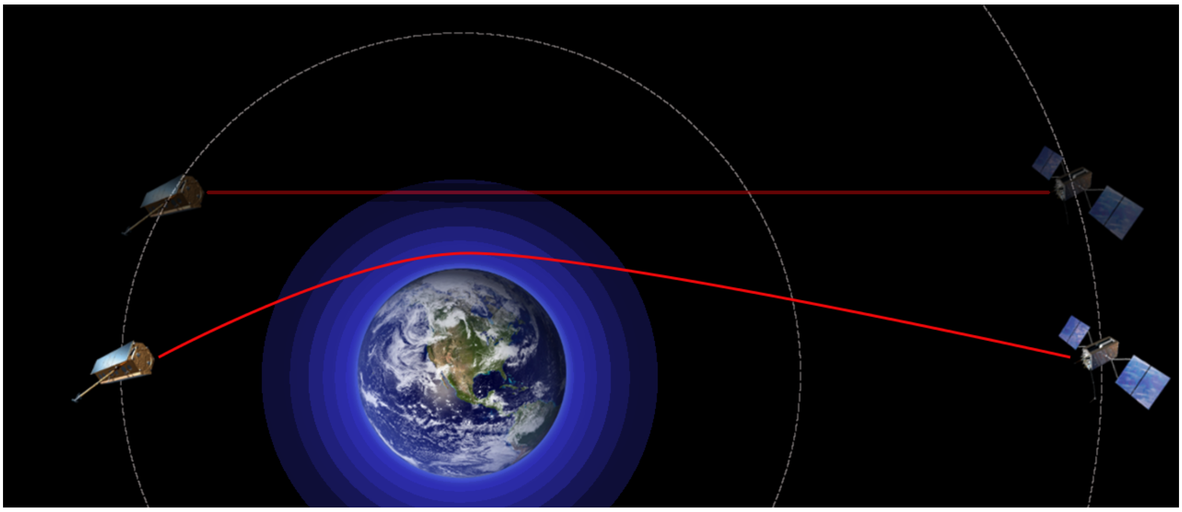

Figure 1.2: Schematic view of the Radio Occultation concept. Slightly faded, the RO configuration at the begining of the occultation, when the radio link (here represented as the red line) between the GPS (satellite in the right) and the LEO (satellite in the left) is in the upper layers of the atmosphere (here represented as a blue shadow). Below, the radio link when it is deep inside the atmosphere, and it is bent due to the refractivity gradients.

1.2 RADIO OCCULTATIONS

GNSS Radio Occultation (GNSS-RO) is a technique based on a LEO tracking the signal transmitted by a GPS satellite while it is occulting behind the Earth, so that from the point of view of the LEO, the GPS satellite is setting below the horizon. The emitted waves travel through the atmosphere before reaching the receiver, being delayed and bent by the atmospheric refractivity gradients. During the occultation, the LEO receives signals with different minimum heights, that approach the Earth's surface as the GPS sets. This results in a vertical scan of the atmosphere. Modern receivers are also able to collect rising occultations (in addition to setting). The retrievals that one can obtain from ROs are vertical profiles of refractivity, temperature, pressure, water vapour and geopotential height in the neutral atmosphere and free electron density in the ionosphere. It has a high vertical resolution of about 100 m, and a horizontal resolution of the order of 100 km. A schematic view of the technique is shown in Figure 1.2. The RO technique has also been successfully applied from aircraft [e. g. Healy et al., 2002; Haase et al., 2014], although the main applications come from spaceborne receivers.

1.2.1 *Brief history and missions*

The first time that RO measurements were used to infer properties about an atmosphere was in the 1960s, when the Mariner IV spacecraft occulted behind Mars. Then, researchers from the Jet Propulsion Laboratory (JPL) and Stanford University realized that the transmitted tracking and telemetry signals could be used to infer atmospheric and ionospheric parameters [Kliore et al., 1965; Fjeldbo and Eshleman, 1965; Fjeldbo et al., 1965]. The results of these first occultations where rapidly adapted to more general atmospheres [Phinney and Anderson, 1968], and soon after Mars, other atmospheres, such as those of Venus and Mercury, were sounded too [Fjeldbo and Eshleman, 1969; Howard et al., 1974]. After that, almost all the planets of the Solar System were studied using ROs, with the signals transmitted from the Pioneer project spacecraft and the Voyager 1 and 2. Moreover, a few of these planets' moons were sounded too. Since then, the exploratory missions travelling to solar system planets and moons have sounded their atmosphere using ROs. See a list of some of them in Jin et al. [2014].

Around the same time, it was suggested to apply the technique to the study of the Earth's atmosphere [Fischbach, 1965; Kliore, 1969]. However, it was not until 1976 that the first RO experiment was carried out to survey the Earth's atmosphere within the Apollo-Soyuz mission [Rangaswamy, 1976]. This first experiment showed reasonably good performance on the reconstruction of temperature and pressure profiles, and pointed out that the technique could be used as a source of meteorological information, if improvements to the retrievals and coverage were made. Two of the main problems noted were the lack of accuracy in the determination of the orbits and the lack of global capability. These problems disappeared with the emergence of the GNSS constellations around the 1980s.

The possibility of using GPS satellites as a source of radio frequency waves and LEO satellites as receivers was then proposed [Yunck et al., 1988; Ware, 1992; Gorbunov and Sokolovskiy, 1993; Melbourne et al., 1994], and the first proof of concept mission was designed by the mid-1990s. The proof of concept GPS Meteorological experiment (GPS-MET) was launched in 1995 and was the first satellite mission to sound the Earth's atmosphere using GNSS signals [Ware et al., 1996], lead by University Corporation for Atmospheric Research (UCAR). GPS-MET carried a receiver called Turbo Rogue GPS, that was built at JPL. The retrievals obtained by the mission agreed very closely with other measurements and models [Kursinski et al., 1996; Rocken et al., 1997]. The mission was a success and it became the precursor to several others.

After GPS-MET, National Aeronautics and Space Administration (NASA) contributed to two small international flight projects that would collect ROs as a secondary scientific objective. These were the Danish Ørsted mission [Larsen et al., 2005] and the South African Sunsat [Mostert and Koekemoer, 1997], between 1999 and 2000. In 2000, the next generation of JPL-built receivers, the *BlackJack*, were ready. They flew in the German satellite CHAllenging Minisatellite Payload (CHAMP) [Wickert et al., 2001] and in the Argentina spacecraft Satellite de Aplicaciones Cientificas - C (SAC-C) [Hajj et al., 2004]. Both satellites increased the number of RO per day, and served as a development test bed for GPS sounding. A *BlackJack* was also installed in the US-German Gravity Recovery And Climate Experiment (GRACE) mission [Wickert et al., 2005].

In 2006, a revolution in the RO community came with the launch of the Taiwan-US Formosa Satellite mission # 3 (FORMOSAT-3)/Constellation Observing System for Meteorology, Ionosphere, and Climate (COSMIC) constellation of six satellites. These were the first satellites fully dedicated to RO, with the ability to provide between 1500 and 2000 occultations per day distributed globally [Anthes et al., 2008]. They were equipped with the then newest receivers from JPL, the Integrated GPS and Occultation Receivers (IGORs), which offered Open Loop (OL) capability for better tracking of the lower troposphere and the ability to collect rising occultations [Ao et al., 2009]. COSMIC satellites are still providing observations at the present.

In addition to COSMIC, several other satellites have been equipped with RO receivers recently. This is the case with the Metop satellite (launched October 2006), the first European Organisation for the Exploitation of Meteorological Satellites (EUMETSAT) LEO for operational meteorology, that carries a GNSS Receiver for Atmospheric Sounding (GRAS) receiver [Luntama et al., 2008; Von Engeln et al., 2011]. TerraSAR-X, TanDEM-X, SAC-D/Aquarius and several other missions have also been equipped with RO receivers (see a list of several of them in Jin et al. [2014]), and are providing continuous observations.

To assimilate data provided by RO missions into Numerical Weather Prediction (NWP) was first proposed by Eyre [1994], and it has proven to be very useful using the data from GPS-MET and CHAMP [Liu et al., 2001; Healy et al., 2005]. The impact of these profiles on NWP increased with the rise in the number of daily observations produced since the launch of the COSMIC constellation [e. g. Cucurull et al., 2008; Rennie, 2010]. Nowadays, ROs are amongst the most valuable observing systems for data assimilation [Cardinali and Healy, 2014].

The next big step for the RO community will take place in 2017, when the first 6 satellites of the FORMOSAT 7 / COSMIC-2 mission are scheduled for launch. The FORMOSAT 7 / COSMIC-2 mission's aim is to advance the capabilities of global weather forecasting, space weather monitoring and climate research, by acquiring a large amount of RO thermodynamic profiles and ionospheric data. It will be comprised of 12 spacecraft, six orbiting at 24 deg of inclination and six at 72 deg of inclination. The second set of spacecraft do not have launches scheduled yet. The spacecraft will carry TriG GNSS-RO receivers (third generation), able to track Galileo and GLONASS satellites in addition to GPS. Due to the ability to track these three navigation systems, it will produce more than 8000 profiles per day when all the spacecraft are deployed, compared to the approximate 2000 profiles per day of COSMIC I.

1.2.2 *The concept*

The phase that a receiver would obtain from the GPS signal (Equation 1.1 and Equation 1.2) can be modelled as [Hajj et al., 2002]:

$$L_k^{ij} = -\frac{c}{f_k}\Phi_k^{ij} = \rho^{ij} + \gamma_k^{ij} + C^i + C^j + \nu_k \tag{1.4}$$

in units of distance, where Φ_k^{ij} is the recorded phase in cycles for the wave propagated from the transmitter i to the receiver j; c is the speed of light in a vacuum; k is the subindex indicating the frequency, i. e. 1 for L1 and 2 for L2; f_k is the frequency in Hz; ρ is the range corresponding to the time for light to travel in straight line between the transmitter and the receiver; γ_k^{ij} is the extra delay due to the neutral atmosphere and ionosphere; $C^{i,j}$ are the errors corresponding to the transmitter and receiver clocks; and ν_k is the measurement noise. Since this measurement uses the phase, there is an ambiguity in the absolute number of cycles that the wave has undergone before reaching the receiver. However, the interest here will recall in the derivative of the phase measurement, therefore there is no need to take it into account. Relative position derived errors and antenna patterns are not taken into account either, since they are assumed known and removed.

Hence, the objective here is to isolate the γ_k^{ij} term, which can be divided into two contributions:

$$\gamma_k^{ij} = \eta_k^{ij} + \mathrm{K}\frac{TEC_k^{ij}}{f_k^2} \tag{1.5}$$

where the first term, η_k^{ij}, is the contribution of the neutral atmosphere and the second term K TEC_k^{ij}/f_k^2 is the contribution of the ionosphere (to first order approximation), with K a constant and TEC_k^{ij} the integrated electron density along the ray path between the transmitter and the receiver.

First, one has to calibrate the signal, i. e. correct the clock errors in Equation 1.4. This can be achieved if: (1) the occulting LEO can simultaneously see an occulting GPS and a non-occulting one; (2) an additional receiver, e. g. a ground station, can also simultaneously see the occulting and the non-occulting GPSs. This configuration is shown in Figure 1.3. In addition, one needs to know very precisely the orbits of the GPS and LEO satellites, which is obtained using a network of GPS ground stations and all other GPS satellites. The detailed procedure and the effects of this correction are given in, e. g. Kursinski et al. [1997]; Hajj et al. [2002].

Once the signal is calibrated, the atmospheric bending angle (α) can be obtained using geometric optics and the Doppler shift. The Doppler shift is related to the transmitter and receiver velocities by [Hajj et al., 2002]:

$$\frac{\mathrm{d}\gamma}{\mathrm{d}t} = \lambda\Delta f = v_t \cdot \hat{k}_t - v_r \cdot \hat{k}_r - (v_t - v_r) \cdot \hat{k} \tag{1.6}$$

where $v_{t,r}$ is the transmitter or receiver's velocity; $\hat{k}_{t,r}$ is the unit vector in the direction of the transmitted or received signal; and $\hat{k}$ is the unit vector in the direction from the transmitter to the receiver. These are shown in the representation in Figure 1.3. Note that the Doppler shift is the difference between the actual Doppler effect and that which the signal would have suffered if the propagation had been in a straight line through a vacuum.

One approximation is needed to continue retrieving the bending angle: a spherically symmetric atmosphere. The Earth is an ellipsoid, therefore the center of sym-

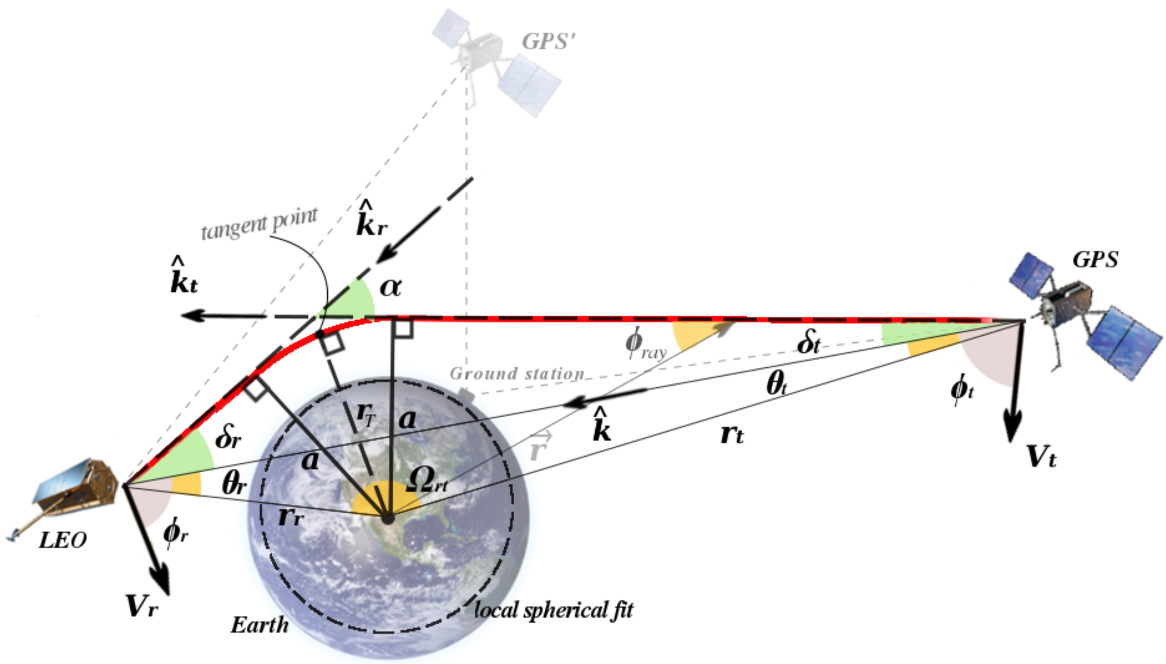

Figure 1.3: Geometry and definition of the angles and parameters involved in the RO technique concept.

metry is taken to be the center of the circle in the occultation plane which best fits the geoid near the tangent point. The occultation plane is defined as the plane that contains the transmitter, the receiver and the normal to the geoid at the tangent point of the lowest link of the RO. So, Equation 1.6 can be approximated as [Hajj et al., 2002]:

$$\frac{\mathrm{d}\gamma}{\mathrm{d}t} = (v_t \cos(\phi_t - \delta_t) - v_r \cos(\phi_r - \delta_r)) - (v_t \cos(\phi_t) - v_r \cos(\phi_r)) \tag{1.7}$$

where ϕ_t is the angle between $\hat{k}$ and $\vec{V}_t$, ϕ_r is the angle between $-\hat{k}$ and $\vec{V}_r$, δ_t is the angle between $\hat{k}$ and $\hat{k_t}$, and δ_r is the angle between $-\hat{k}$ and $-\hat{k_r}$. With these definitions, in the case sketched in Figure 1.3, both ϕ_t and ϕ_r are negative. In a spherically symmetric atmosphere, the refractivity index gradient only varies in the radial direction, i. e. $n = n(r)$. Then, all the rays are considered plane curves, and along each ray:

$$nr \sin(\phi_{\text{ray}}) = \text{const} = a \tag{1.8}$$

where r is the modulus of the position vector $\vec{r}$, ϕ_{ray} is the angle between the position vector and the tangent to the ray path at $\vec{r}$, and a is called the impact parameter, which is a constant for each ray. Hence, when $\phi_{\text{ray}} = 90°$ and $n = 1$, $a = r$, as is depicted in Figure 1.3.

By Bouguer's rule, it can be stated that:

$$a = r_t n_t \sin(\theta_t + \delta_t) = r_r n_r \sin(\theta_r + \delta_r) \tag{1.9}$$

where $r_{t,r}$ is the modulus of the vector from the center of curvature to the transmitter or the receiver, and n is the index of refraction, taken to be 1 at the height of the satellite. θ_t is the angle between $-\vec{r}_t$ and $\hat{k}$, and θ_r is the angle between $-\vec{r}_r$ and $-\hat{k}$. The bending angle can be expressed as a function of the δ angles, by:

$$\alpha = \delta_t + \delta_r, \tag{1.10}$$

therefore, the bending angle, as a function of the impact parameter, $\alpha(a)$, can be obtained by solving Equation 1.7, Equation 1.9, Equation 1.10 and knowing the Doppler shift.

The retrieved bending angle also includes a contribution from the ionosphere which can be removed with a combination of the bending angle for L1 and that for L2 [Vorob'ev and Krasil'nikova, 1994]:

$$\alpha_n(a) = \frac{f_1^2}{f_1^2 - f_2^2}\alpha_{L1}(a) - \frac{f_2^2}{f_1^2 - f_2^2}\alpha_{L2}(a). \tag{1.11}$$

When L2 measurements are too noisy, a large smoothing filter has to be applied to the L2 phase measurements to obtain $\alpha_{L2}(a)$, and Equation 1.11 has to be slightly modified [Rocken et al., 1997].

The geometric optics approach works well for most of the radio occultation event (the upper part). However, in the lower troposphere, where a significant amount of water vapour is present, the signal may undergo atmospheric multipath, whose effects are not well handled by geometric optics. This issue requires radio holographic techniques for retrieving the bending angle. Among the several approaches proposed, the most used are the canonical transformation [Gorbunov, 2002], the Full Spectrum Inversion (FSI) [Jensen et al., 2003] and phase screen matching [Jensen et al., 2004].

The basic principle of these techniques is to use the Fourier transform of the complex raw received signal to link the different frequencies that might be produced by the multipath with the corresponding impact parameters. Otherwise, using geometric optics in these regions would give a non-unique bending angle - impact parameter pair, inducing errors in the retrieval. Therefore, the use of this technique allows to keep a high vertical resolution in the lower troposphere. The main drawback of the application of the Fourier-based methods is the non-circularity of the orbits of GPSs and LEOs, which have to be solved using some approximations that require a priori values, usually obtained from the geometrical optics approach. Despite the approximations, the ability of these methods to retrieve the correct bending angle in the multipath regions has been demonstrated [e. g. Jensen et al., 2003].

1.2.3 *Refractivity and derived products*

The way to relate RO observations to geophysical quantities is to relate the bending angle to the refraction index. In a spherically symmetric atmosphere, the bending angle can be expressed as [e. g. Kursinski et al., 1997]:

$$\alpha(a) = -2a \int_{r_t}^{\infty} \frac{\mathrm{d}\ln(n)}{dr} \frac{\mathrm{d}r}{\sqrt{n^2r^2 - a^2}} \tag{1.12}$$

where r is the distance from the center of curvature of a ray path and the integral is over the portion of the atmosphere above the radius at the tangent altitude, r_t. Taking x to be nr, this equation can be inverted through the Abelian transformation and $n(r)$ can be expressed as [Fjeldbo et al., 1971]:

$$n(r) = \exp\left[\frac{1}{\pi}\int_a^{\infty} \frac{\alpha(x)\mathrm{d}x}{\sqrt{x^2 - a^2}}\right]. \tag{1.13}$$

Hence, given the refractive index profile, one can obtain the bending angle through Equation 1.12, and given a bending angle profile one can obtain the refractivity by solving Equation 1.13.

The deviations of the refractive index from unity are quantified using the term refractivity (N), defined as [Kursinski et al., 1997]:

$$N = (n-1) \times 10^6 = \mathrm{a}_1 \frac{P}{T} + \mathrm{a}_2 \frac{e}{T^2} - 40.3 \cdot 10^6 \frac{n_\mathrm{e}}{f^2} + \mathrm{a_w} W_\mathrm{w} + \mathrm{a_i} W_\mathrm{i} \tag{1.14}$$

where a_1, a_2, $\mathrm{a_w}$ and $\mathrm{a_i}$ are constants, P is the total pressure, e is the water vapour partial pressure, T is temperature, n_e is the electron density, and $W_\mathrm{w,i}$ are the liquid and ice water content, respectively. The values for a_1 and a_2 are commonly taken to be $\mathrm{a}_1 = 77.6\,\mathrm{K/hPa}$ and $\mathrm{a}_2 = 3.73 \times 10^5\,\mathrm{K^2/hPa}$, although there is some debate and alternatives are being proposed, accounting for the non-ideality behaviour of moist air [e. g. Aparicio et al., 2009; Healy, 2011; Aparicio and Laroche, 2014]. The constants $\mathrm{a_{w,i}}$ are taken to be $\mathrm{a_w} = 1.4$ and $\mathrm{a_i} = 0.6$, although in general these two terms are neglected. The convenience or not of neglecting them under heavy precipitation scenarios is discussed in Section 6.1.

In the neutral atmosphere, approximately below 50 - 60 km, the term that contains the electron density can be neglected if ionospheric correction has been performed (Equation 1.11). Hence Equation 1.14 in the neutral atmosphere is expressed as:

$$N = \mathrm{a}_1 \frac{P}{T} + \mathrm{a}_2 \frac{e}{T^2}. \tag{1.15}$$

To obtain P, T and e from this equation, additional constraints are needed. The hydrostatic equilibrium and the equation of state of the air leads to [Hajj et al., 2002]:

$$\frac{\partial P}{\partial r} = -\rho(r)g \tag{1.16}$$

$$\rho(r) = \rho_\mathrm{d} + \rho_\mathrm{m} = \frac{P(r)m_\mathrm{d}}{T(r)\mathrm{R}} + \frac{e(r)(m_\mathrm{w} - m_\mathrm{d})}{T(r)\mathrm{R}} \tag{1.17}$$

where g is gravitational acceleration, ρ is the total density, $\rho_{\mathrm{d,m}}$ is dry or moist air density respectively, and $m_{\mathrm{d,m}}$ is the mean molecular mass of dry or moist air. R is the universal gas constant.

In a dry atmosphere, where e can be neglected, the last term on the right side of Equation 1.15 and Equation 1.17 disappears, leading to a system of two equations and two unknowns: P and T. For a given N, T and P can be found, with only a boundary condition required. Usually this is taken to be the temperature at around 50 km (obtained from models).

When water vapour cannot be neglected, the system becomes under-determined, and ancillary information about one of the three parameters (P, e, T) is needed. Therefore, either temperature or moisture is obtained from in-situ observations, models or climatologies, and this is used to calculate the remaining parameters. Alternatively, variational approaches can also be used [Healy and Eyre, 2000], finding a statistically optimal solution that, based on a climatological first guess of the parameters, looks for the combination that fits the refractivity observations the best. Both approaches provide retrievals that can contain uncertainties stemming from the a priori information. Nevertheless, retrievals in the lower troposphere show very good agreement with other measurement techniques.

Above the neutral atmosphere, the excess phase delay is only due to the ionosphere, hence the electron density profile can be approximated, from Equation 1.14, as:

$$n_{\mathrm{e}}(r) = (1 - n(r)) \cdot \frac{f^2}{40.3}. \tag{1.18}$$

Then, the Total Electron Content (TEC) can be obtained through [Schreiner et al., 1999]:

$$TEC = \int n_{\mathrm{e}} \mathrm{d}l = -\frac{f^2}{40.3} \int (n-1) \mathrm{d}l = -\frac{f^2 L}{40.3} \tag{1.19}$$

where L is the phase (this expression provides the ionospheric term in Equation 1.4 and Equation 1.5). L1 and L2 signals travel on slightly different paths through the ionosphere, but this can be neglected when the bending angle is small, therefore:

$$TEC = -\frac{f_1^2 L_1}{40.3} = -\frac{f_2^2 L_2}{40.3} = \frac{(L_1 - L_2) f_1^2 f_2^2}{40.3 (f_1^2 - f_2^2)}. \tag{1.20}$$

This method can induce errors due to the assumptions made and the noisy L2 measurement. Alternatively, TEC can be obtained using only L_1 through an Abel transformation, but then calibration is required and the ionosphere above the LEO must be modelled. From TEC, the electron density can be obtained through an Abel transform [Schreiner et al., 1999]:

$$n_{\mathrm{e}}(r) = -\frac{1}{\pi} \int_{r_0}^{r_{\mathrm{LEO}}} \frac{\mathrm{d}(TEC)}{\mathrm{d}r_0} \frac{\mathrm{d}r_0}{\sqrt{r_0^2 - r^2}}. \tag{1.21}$$

1.2.4 *Characteristics and applications of ROs*

After many years of operation and development, the main characteristics of GNSS-RO can be summarized as [Anthes, 2011]:

- It provides profiles of the ionosphere, stratosphere and troposphere with global coverage. This is enhanced by the fact that the signals are weakly attenuated by clouds, precipitation and aerosols, therefore providing all-weather capability

- High accuracy, precision and vertical resolution for dry retrievals, in addition to the independence of first guess solutions. The temperature accuracy is assumed to be < 0.5 K, with a vertical resolution ranging from 0.1 to 1 km (troposphere to stratosphere). Wet retrievals for the lower troposphere, i.e. humidity, are assumed to have an accuracy of < 10 - 20% [Kursinski and Hajj, 2001], which is comparable to other satellite based sounders, and have a dependence on their first guess.

- Independent determination of height and pressure

- Self-calibrated, no instrumental drifts and no significant biases among processing centres, satellites or missions.

These characteristics make RO very suitable for the study of weather and climate. Weather phenomena can be well studied due to the fact that very precise retrievals can be obtained with a high vertical resolution, regardless of the cloud coverage or precipitation. An example of this would be tropical cyclones and atmospheric fronts, whose thermodynamic properties can be obtained where other sounders cannot penetrate them [e. g. Vergados et al., 2013, 2014; Biondi et al., 2013]. However, the density of RO near these weather systems is not very high (currently $\sim$ 1500 occultations per day around the whole globe) so the horizontal gradients are poorly obtained. Increasing the density would produce an enhancement of the capability of RO to study and forecast these phenomena [Liu et al., 2011]. It is also worth mentioning the capabilities of ROs in studying the processes related to the Atmospheric Boundary Layer (ABL) [e. g. Ao et al., 2012; Xie et al., 2012] and cloud top height and temperature detection [e. g. Peng et al., 2006; Biondi et al., 2013]

On the climate studies' side, the long-term stability of RO is very useful for climate monitoring. They have been shown to be equal or more relevant in climate trends detection than radiosondes [Ladstädter et al., 2015]. The global coverage increases the number of observations, especially in the regions where other kind of observations are less frequent, like over oceans and in less-developed regions. Climate change trends are observed using RO, such as upper tropospheric warming and lower stratospheric cooling, or tropopause heights e. g. Schmidt et al. [2010]; Steiner et al. [2011]; Rieckh et al. [2014]. Also, RO can be used for climate monitoring, since large scale signatures such as those of El Niño-Southern Oscillation (ENSO) and Quasi-Biennial Oscillation (QBO) are clearly seen in RO data [Lackner et al., 2011].

NWP have also benefited from RO through assimilating their retrievals. Most NWP centres have been operationally assimilating RO observations since 2006, for example, the Met Office [e. g. Buontempo et al., 2008], the European Centre for Medium-Range Weather Forecast (ECMWF) [e. g. Healy, 2008], the National Centers for Environmental Prediction (NCEP) [e. g. Cucurull and Derber, 2008], and Environment Canada [e. g. Aparicio and Deblonde, 2008]. The positive impact of ROs on forecasting has been widely proven [Cardinali and Healy, 2014], being the 5th largest contributor to decreasing forecast errors despite contributing only 3% of the total observations. An added value of ROs is that, in addition to assimilating their products, they can be used in helping to correct possible biases suffered by the microwave and infrared sounder radiances [Cucurull et al., 2014; Aparicio and Laroche, 2014], since they are unbiased. This skill is especially noticeable in the southern hemisphere, where the number of observations is reduced.

1.2.5 *Other atmospheric sounders*

Here, a few alternative atmospheric sounder systems are briefly described, to point out their differences with respect to RO. Radiosondes are the only atmospheric sounders that measure the thermodynamic state of the atmosphere in-situ. They are characterized by high vertical resolution and have been used to calibrate and validate other satellite-retrieved soundings. However, different types of radiosondes can have different performances, and it is known that they are affected by biases [Kuo et al., 2005; Sun et al., 2010; Wang et al., 2013]. The main drawback of radiosondes for climate studies is their irregularity in their coverage of space and time, being almost non-existent over ocean and remote areas. They are also very expensive compared to space-based RO.

The Atmospheric InfraRed Sounder (AIRS) instrument together with the Advanced Microwave Sounding Unit (AMSU) measures radiance in the infrared and microwave ranges. The AIRS measures the 3.7 - 15.4 μm spectral range with 2378 infrared spectral channels, and AMSU measures the 23 - 190 GHz range with a 19 channel radiometer [Aumann et al., 2003]. They provide temperatures and water vapour vertical profiles with an accuracy of 1 K and 10-20%, respectively, with a vertical resolution of 1 km for the temperature and 2 km for water vapour. The two instruments combined are mounted in the Aqua satellite, although different versions of the AMSU instrument are mounted on other meteorological satellites as well (such as the MetOp). The main drawbacks of these instruments is the vertical resolution (with respect to RO), their lower performance in the presence of thick clouds and their need of calibration, which is especially complicated over land.

Other similar sounders such as Infrared Atmospheric Sounder Interferometer (IASI), Advanced Microwave Scanning Radiometer (AMSR), and the instruments in the Geostationary Operational Environmental Satellite (GOES) and Meteosat satellites have similar characteristics to the instruments mentioned in the previous paragraph, and hence they have less vertical resolution than RO, need calibration and have low performance in the presence of clouds due to signal degradation [e. g. Susskind et al., 2003; Wulfmeyer et al., 2015]. On the other hand, these instruments provide a large amount of continuous measurements of the atmosphere, and are very valuable for data assimilation and weather forecasting.

1.3 CLOUDS AND PRECIPITATION

The existence of clouds is critical to the Earth's climate. They are one of the most important agents driving radiative interactions and radiation budget, and play an active part in the hydrological cycle. The study of the effects of clouds on Earth's radiation budget raised at the beginning of the 70s, when researchers started to realize that man's activities could have an impact on global climate [Schneider, 1972]. Since then, the effects of clouds on climate have been an active field of research (see e.g. Hartmann et al. [1986]; Wielicki et al. [1995]; Chen et al. [2000]; Stephens [2005]). A good understanding, characterization and modelling of these effects is still an open question, and more progress is needed in order to address one of the most challenging current issues: climate change. Nowadays, improvements in this direction are being achieved thanks to the increasing number of monitoring systems and the large number of observations that they provide (see e. g. Li et al. [2016] and references therein).

Clouds are formed by water vapour that has condensed in the form of water droplets and ice particles. One of the characteristics of water vapour is that it can condense into both liquid and solid phases in the conditions of the Earth atmosphere. It also varies a lot from one place to another. Water vapour is quantified through the mixing ratio (grams of water vapour per kilograms of dry air), but it is the relative humidity which is more important in determining if clouds are present or not. Relative humidity measures the degree of saturation of the atmosphere, and knowing it one can infer the probability of condensation of water vapour. Since water vapour is contained in the troposphere, most clouds occur entirely in this region of the atmosphere.

Clouds can be characterized according to many of their properties, like their vertical profiles, optical depth, liquid or ice water content, particle sizes, etc. All these properties have an effect on the radiation budget, and therefore have to be characterized. This effect or interaction between clouds and the global environment is called feedback, and it can happen in many ways. For example, water in the condensed phase is able to absorb more heat than water in its gaseous phase, thus clouds are better thermal absorbers than water vapour. Therefore, the presence of clouds in the atmosphere changes how temperature evolves with height. On the other hand, cloud coverage and cloud top height and temperature can change the

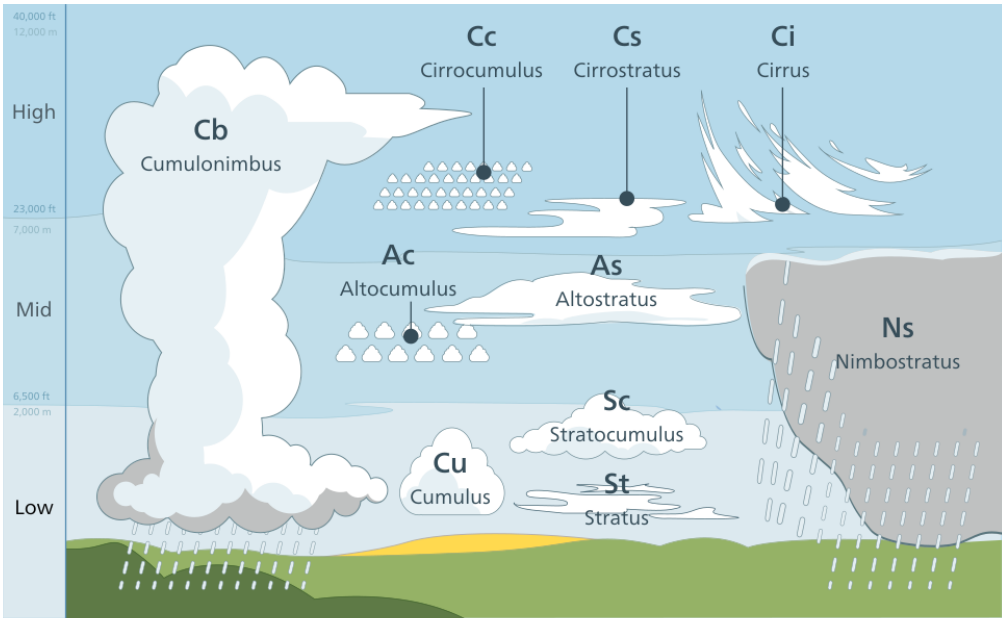

Figure 1.4: Classification of clouds according to their base height. Image credit: Valentin de Bruyn.

cloud's albedo[1] and emittance, and have an impact on the temperature above the clouds, i.e. the stratosphere. The balance between the cooling and the heating effects of clouds is very sensitive to cloud microphysics.

By convention, clouds are distinguished by their base height or by their phase, although they can be classified in any other arbitrary way. A classification by base height is shown in Figure 1.4, where clouds are separated into high clouds, middle clouds, and low clouds. Generally, high clouds are formed entirely of ice particles and low clouds are formed of water particles, but both alternatives can be found in rare scenarios under, for example, supercooled conditions. Detailed characteristics of the different clouds are shown in Figure 1.4 and nice pictures of them can be found in e. g. Wang [2013].

If clouds are distinguished by their phase, they can be formed of ice particles (ice clouds), water particles (water clouds), or a combination of both, called mixed-phase clouds. Water clouds are often called warm clouds, while ice clouds are usually referred as cold clouds, regardless of their temperature. There also exist clouds that are formed of both ice and water particles, located according to the vertical dimension, usually with the liquid phase particles at the bottom and ice particles in the top. This is often observed in *cumulonimbus* clouds, which can extend from a base at around surface altitude up to more than 10 km.

The phase of the particles is important with regards to the radiative properties of the cloud. For example, water droplets can absorb more solar radiation than ice

1 Cloud albedo is the fraction of solar energy (shortwave radiation) reflected from the top of the cloud back into space. It depends on the type, size and orientation of the particles that form the cloud. Thus, it is higher if the particles are ice than if they are water.

crystals, while ice is more reflective than water. Also, their scattering properties are quite different. Therefore, a good characterization of their properties is important. Globally, ice clouds make up 53% of all those observed, although they are not uniformly spatially distributed, but closely related to climate regimes [Hong and Liu, 2015]. Besides cloud feedback, the phase of the cloud particles, especially at the top of the clouds, is of great interest to the aviation industry. Several incidents of engine power loss have been linked to glaciated deep convective events [Fridlind et al., 2015].

1.3.1 *Hydrometeors*

Condensed particles in clouds are called *hydrometeors*, and are referred to as cloud particles if they are not falling thanks to updraft vertical currents inside the cloud. Hydrometeors that are falling are called *precipitation* particles. Again, this classification is rather arbitrary, but is adopted here by convention. According to Wang [2013], six types of particles or hydrometeors can be distinguished within clouds: cloud drops, raindrops, ice crystals, snowflakes, graupel, and hail. They are distinguished by their phase and their size. Cloud droplets are liquid phase drops, suspended by updraft and with a typical diameter of a few microns. Raindrops are falling liquid water particles, nearly spherical in shape, with diameters that range from $\simeq 1$ mm up to $\simeq 8$ mm. These eventually reach the ground in the form of rain. Ice crystals are crystalline ice particles, with a diameter of hundreds of microns and which are highly asymmetric in shape. They are suspended in the air, but if they are large or they aggregate with other crystals, they become snowflakes and start to fall. Snowflakes can reach a diameter of a few centimetres. Graupel and hail is formed when snowflakes collide with supercooled droplets, which freeze on the surface. When the rimming has formed an unrecognisable particle, graupel has formed. Graupel has a diameter of about 5 mm, and when the particles grow beyond that diameter they are called hail. Hailstones can reach diameters larger than 20 cm.

Each kind of particle is distributed differently within the cloud. The distribution of sizes and concentrations is determined by the particle size distribution, which will be carefully examined in Section 3.2. The concrete shape of each hydrometeor will be treated in Section 4.1.2. Phase, shape, and size distributions are the most important hydrometeor features for the scope of this work, since they govern the scattering properties and the derived quantities. Figure 1.5 shows all the types of hydrometeors and physical processes that they can undergo.

1.3.2 *Precipitation*

As has been defined above, precipitation can be understood as all liquid or solid phase aqueous particles that fall from clouds and eventually reach the surface. It can have also a more general meaning, such as the total amount of water that has

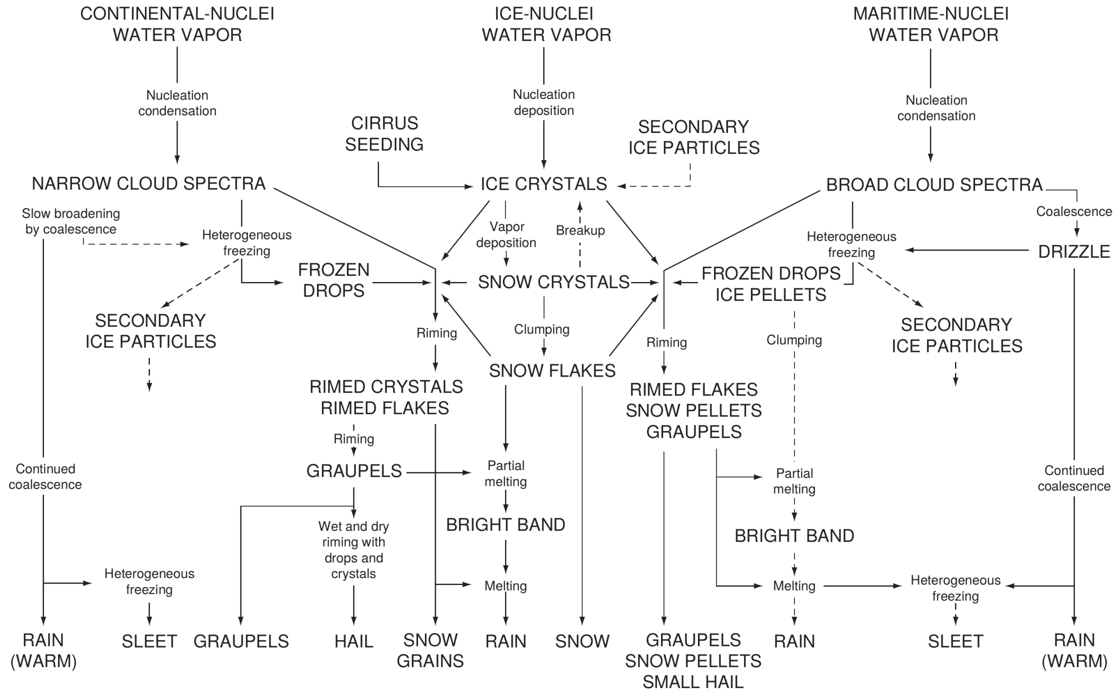

Figure 1.5: Flow diagram of all particle types and physical processes that they undergo. Adapted from Straka [2009].

fallen at a given point over a specific period of time[2]. Regardless of the definition used, the difference between clouds and precipitation is that the latter has a direct impact on people's lives. It is a crucial agent in the hydrological cycle, being the last step in bringing water from sea to land. For this reason, precipitation has always been a topic of interest for humans. In Strangeways [2006] there is a nice review of how ancient cultures saw and interacted with precipitation. A recurrent example through history is the importance of precipitation in agriculture, as a source of crop irrigation.

On the other hand, precipitation can be a destructive agent, for example, in the form of extreme events like hurricanes and typhoons, severe convective storms, extreme precipitation and snow and ice blizzards, which usually come accompanied by flooding. These events cause a lot of damage to the population, both in terms of social (e. g. Ashley and Ashley [2008]) and economic (e. g. Smith and Katz [2013]; Smith and Matthews [2015]) costs. In addition, an upward trend in the frequency and intensity of extreme precipitation has been observed (e. g. Kunkel et al. [2013]). It is worth saying that extreme events are regionally dependent. The same quantity of rain affects distinct regions differently, and therefore an absolute threshold value of accumulated rain cannot be defined. Thus, extreme events are better characterized when accounting for the top tail of the rain events distribution (e. g. Ralph et al. [2010]; Sukovich et al. [2014]).

2 Definitions from the Meteorology glossary of the American Meteorological Society.

The impact of these events has made modelling and prediction of precipitation a major goal over the last decades, and it still remains a challenge. NWP have been used for more than 50 years to produce weather forecasts, while the initial concepts date to the beginning of the 20th century [Richardson, 1920]. Although NWP has been very successful in weather forecasting, it has historically suffered from issues derived from lack of resolution. Computer power has always limited models to larger scales than desired. The main problem of the limited resolution (until around 2000, the finest achieved resolution was of the order of 15 km) is that processes occurring at smaller scales have to be parametrized, specially convection. Convective parametrization is identified as one of the major source of errors in precipitation forecasting (e. g. Kendon et al. [2012] and references therein). This approach intends to describe an average of the properties and characteristics of the unresolved convection over a grid box and distribute the increments of temperature, moisture and momentum.

More recently, and thanks to increasing computer resources, the so-called Convective Permitting Models (CPM) have appeared. These are high resolution models (less than 4 km resolution) that allow the explicit simulation of convection, therefore parametrization is no longer required [Clark et al., 2016]. Although Lilly [1990] attempted high resolution forecasts for a very small area, it was not until around 2000 that these techniques were applied to regional models (i. e. by the Met Office in 2003 [Davies et al., 2005]). CPM have revolutionized weather forecasting, and other related techniques, such as data assimilation, which has had to be adapted for high resolution purposes.

Also, climate models[3] have become convection-permitting [Prein et al., 2015], showing great improvements in rainfall prediction (e. g. Kendon et al. [2012]; Clark et al. [2016]). The truth is that neither NWP nor climate models can be used at high resolution at a global scale, and some degree of parametrization is still needed. In addition, the explicit simulation of convection processes requires a high understanding of cloud and precipitation microphysics, and how this can affect the simulations is one of the active fields of study in this area (e. g. Van Weverberg et al. [2014]).

One way towards achieving improvements in convective parametrization would be to better understand the interaction between the vertical structure of water vapour, temperature and heavy precipitation. Several investigations have studied the relationship between the water vapour and other thermodynamic quantities, and the amount of precipitation, and its interaction with the environment [e. g. Neelin et al., 2009; Holloway and Neelin, 2009; Schiro et al., 2016]. However, most of the studies are only regional, or they rely on atmospheric sounders that have performance problems in the presence of heavy precipitation (see e. g. Section 1.2.5).

3 Climate models differ from numerical weather prediction models in the time scales that they are intended to describe. NWP needs to forecast the near future, i.e. from a few to tens of hours, while climate models are intended to be extended from days to several years. Therefore, NWP models are very sensitive to the initial conditions, while climate models are more sensitive to the boundary conditions.

Therefore, more global thermodynamic measurements under extreme rain conditions are needed in order to improve the modelling of these events.

1.3.3 *Remote sensing of clouds and precipitation*

In the field of climate and weather, remote sensing is vital since in-situ measurements are difficult to achieve, and if they are achieved, they are limited to local events. Examples of in-situ measurements are ground-based meteorological stations and radiosondes, which are widely used by most of the national and regional meteorological agencies, and airborne campaigns to collect, for example, ice crystals (e. g. Heymsfield et al. [2002b]; Delanoë et al. [2005]; Carey et al. [2008]). In support of these measurements, meteorological stations can give local information with great temporal resolution, so they can be used for weather and climate research, in addition to provide the state of the weather locally. Radiosondes give a very precise picture of the state of the atmosphere, although the time resolution is usually low. Airborne in-situ measurements can provide an actual measurement of the distributions of particles and shapes within clouds. However, these distributions vary a lot from cloud to cloud and depend on the event.

Usually, for climate science, a more global coverage is needed, especially if the data has to be used for assimilation. Here some of the most widely used remote sensing techniques for precipitation and cloud measurements are briefly reviewed. They can be classified into active or passive, depending on whether they are *illuminating* the target and measuring the returned radiation, or they are only measuring radiation emitted or reflected by the target.

1.3.3.1 *Weather radars*

Weather radar science started during the World War II, when the British reached the Gigahertz range by methods of radio-frequency (RF) power generation. These frequencies were then widely used (mainly for aircraft detection and warning), but they noticed strong echoes from rainstorms that were not there when much lower frequencies were used [Fletcher, 1990]. The basic principles of weather radar recall measuring the backscattered radiation from an emitted pulse, from which the range, position and intensity of a precipitation cell can be estimated. Most of weather radars also include Doppler capabilities, so they can measure wind speeds from the horizontal velocity of precipitation. More recently, polarimetric capabilities have been included in many modern radars.

Usually, when talking about weather radar, one tends to think about ground meteorological radars. These typically have a range of about 200 km, reach heights ranging from 0 to 15 km, and are included in regional networks with several other radars. If they are not polarimetric, they generally emit linear polarized electromagnetic pulses, scanning 360° and all elevations. Ground weather radars typically operate at S (2 - 4 GHz / 15 - 7.5 cm), C (4 - 8 GHz / 7.5 - 3.75 cm) or X (8 - 12

GHz / 3.75 - 2.5 cm) frequency bands. The greater the frequency, the greater the attenuation and therefore the shorter the range. On the other hand, the shorter the frequency, the larger the range, but the fewer small particles detected. The choice of the frequency depends then on the desired range and kind of precipitation that is to be detected. Radars are widely used for short-range precipitation forecast, and for weather and climate research. Besides ground radars, weather radar technology is also used by some weather observing satellites.

The main observable from the radars is the radar reflectivity factor (Z), which depends on the particles' shapes and sizes. If the radar is polarimetric, additional information can be retrieved. Polarimetric radars emit two linear polarized electromagnetic pulses, one polarized in the horizontal (H) direction and other in the vertical (V). This allows to account for differences in the shape of the hydrometeors, especially for asymmetries between the horizontal and vertical components. Differences in the horizontal and vertical reflectivities are quantified by the differential reflectivity (Z_{dr}), and differences in phase, i.e. how much one of the signal component's phases (H or V) is delayed with respect to the other due to the shape's asymmetry, is quantified by the specific differential phase shift (K_{dp}) [Bringi and Chandrasekar, 2001]. With these observables and some assumptions on the distribution of sizes and shapes of hydrometeors, physical quantities like the rain's intensity or the water content can be estimated. This will be detailed in Chapter 3.

1.3.3.2 *Spaceborne measurements*

Precipitation and clouds can be remotely sensed from space as well. The main advantage of satellite-based monitoring is that it can provide global and homogeneous estimates of precipitation. The observation of precipitation and clouds is performed using passive (radiometers working in the infrared and microwave ranges) and active (radars working in the microwave range) methods. Passive infrared methods give direct information about the tops of the clouds, without the ability to look into them. From this information, precipitation intensity is inferred indirectly under the assumption that cold cloud top temperatures indicate larger development of the clouds and that this implies more precipitation. While this technique provides wide coverage and high temporal resolution, some problems arise from this method: time dependence (day / night capability of the observing systems), location dependence (the relationship between cloud top temperature and rain intensity may depend on the region and the season), and all the problems that can arise from multi-layered clouds [Tapiador et al., 2012].

Passive methods working in the microwave bands use the variations in the microwave radiation from the Earth's surface to determine if it is interacting with something (e. g. water vapour or clouds). Therefore, depending on the frequency and intensity of the signal measured by the sensor, the scattering and emissivity that dominate the signal can be inferred. Unlike infrared techniques, radiances measured from the scattering of melted particles can be more easily linked to rainfall

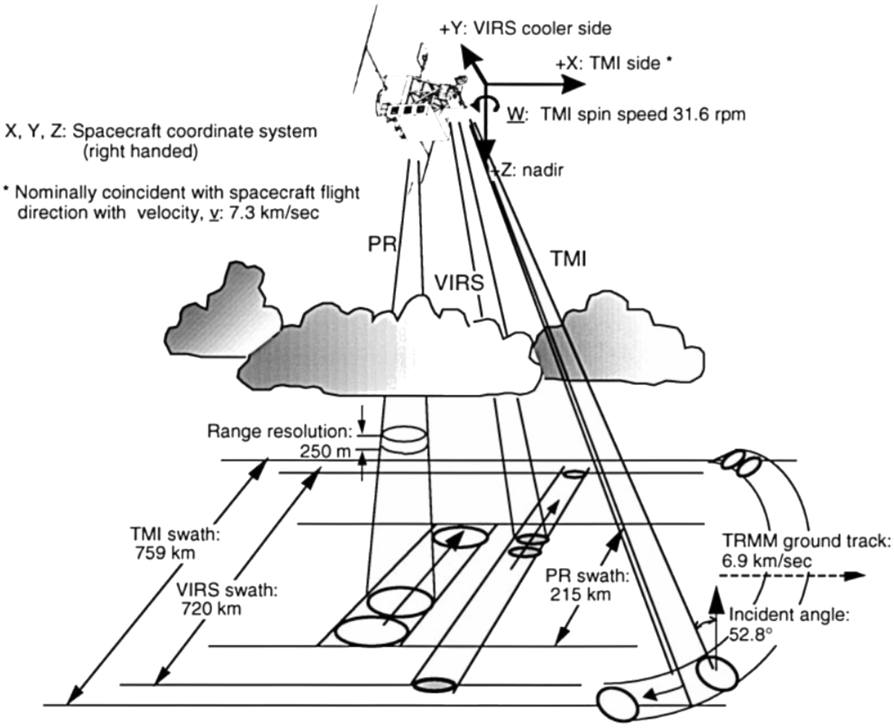

Figure 1.6: Schematic view of TRMM's instruments and their scanning geometry. Image adapted from Kummerow et al. [1998].

processes. Nonetheless, indirect scattering-based approaches are also needed, and Bayesian and probabilistic methods are used to select the best fits to the measured radiances [Tapiador et al., 2012].

The most direct measurements of clouds and precipitation are the active microwave sensors. There are three radar-based satellites for precipitation and cloud observation: the Tropical Rainfall Measurement Mission (TRMM), the Global Precipitation Mission (GPM), and CloudSat. The TRMM [Simpson et al., 1996; Kummerow et al., 1998] was the first mission to sense precipitation from space using a radar. It was launched in 1997 and was operational until 2015. The TRMM radar (Precipitation Radar (PR)) worked at the K_u frequency band (13.8 GHz / 2.2 cm), providing three-dimensional products distributed globally within $\pm 35°$ of latitude. It had a 215 km swath, a horizontal footprint diameter of 4.3 km and a vertical resolution of 250 m. Like ground radars, it provided the measured Z, and one then had to derive the rain rate using relationships where the parameters depend on the rain type, temperature and cloud top. TRMM satellite also carried a multi-frequency radiometer TRMM Microwave Imager (TMI), and an infrared sounder Visible and Infrared Radiometer System (VIRS) and their measurements were combined with the radar in order to produce more robust products. A schematic view of the instruments can be seen in Figure 1.6.

In 2014, the GPM core satellite (the TRMM's successor) was launched [Hou et al., 2014]. As an advanced version of the TRMM satellite, the GPM satellite

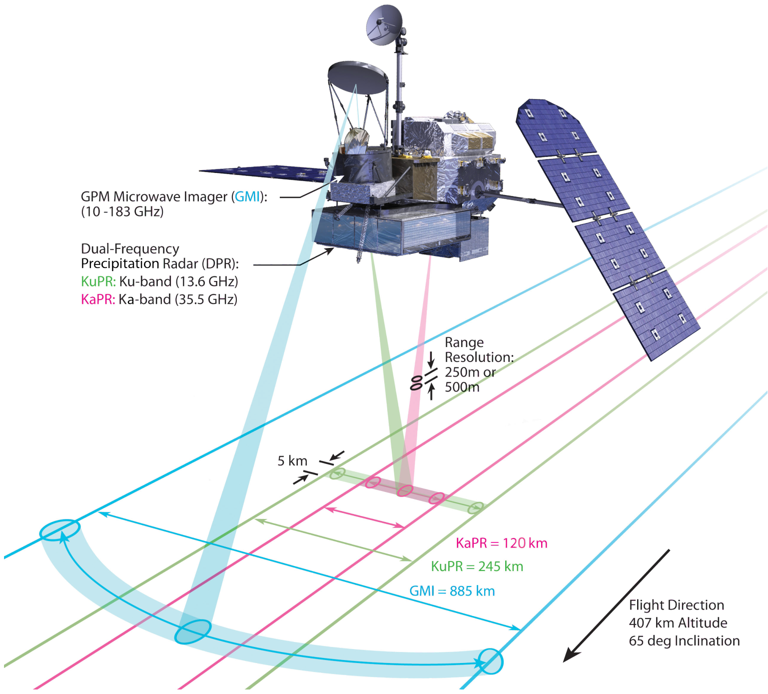

Figure 1.7: Schematic of the GPM's instruments and its scanning geometry. Image from *https://pmm.nasa.gov*. Image credit: NASA.

carries a dual frequency (13.6 and 35.5 GHz / 2.2 and 0.84 cm) radar called Dual-frequency Precipitation Radar (DPR) and a multi-frequency radiometer called GPM Microwave Imager (GMI) with 4 more channels than its predecessor. With a new radar working at a higher frequency band, GPM is able to detect lighter rain and smaller particles than TRMM. The DPR has a swath of 245 km, a horizontal footprint diameter of 5 km and a vertical resolution of 250 or 500 m. A schematic of the GPM instruments can be seen in Figure 1.7. The GPM satellite, like TRMM, provides measurements of Z, for both the K_u and K_a bands, and precipitation products from the radar alone and from a combination of the dual-frequency radar and the radiometer.

The third satellite that uses a radar to sense clouds and precipitation is CloudSat [Stephens et al., 2002, 2008]. It was launched in 2006 and it carries a W-band (94 GHz / 0.32 cm) radar Cloud Profiling Radar (CPR). The high frequency is intended for the detection of small particles, so clouds can be characterized. It flies in the A-train constellation [L'Ecuyer and Jiang, 2010], and it can be used to calibrate other satellites in the constellation. The radar is not scanning, therefore only nadir information is available, with a 1.4 km footprint resolution and a vertical resolution of 485 m. While CloudSat is very successful at cloud characterization, when heavy rain is present it suffers from strong attenuation (due to the short wavelength of its radar), so its products can be unreliable under a certain altitude.

From the three spaceborne radars described above (main characteristics summarized in Table 1.1), one can obtain precipitation and cloud information such as the

Satellite	TRMM	GPM		CloudSat
Frequency (GHz)	13.6	13.6	35.5	94
Wavelength (cm)	2.2	2.2	0.84	0.32
Horizontal resolution (km)	4.3	5		n/a
Vertical resolution (m)	250	250	250/500	485

Table 1.1: Summary of the spaceborne radars characteristics.

rain rate and the liquid and ice water content. This information comes from the Z observable, treated with algorithms that account for effects that disturb the signal, such as attenuation. In the combined products, the microwave information is also taken into account. However, most of the algorithms that relate Z to water content or rain rates rely on the temperature (among many other parameters), so they can distinguish between frozen and melted particles. One of the problems and sources of uncertainty is that temperature and other thermodynamic quantities are obtained from models, and can introduce errors into the retrievals.

2 POLARIMETRIC RADIO OCCULTATIONS

Once an overview of the GNSS-RO technique has been given, in this chapter the new concept of Polarimetric Radio Occultation (Pol-RO) is introduced. Afterwards, the proof-of-concept Radio Occultations and Heavy Precipitation aboard PAZ (ROHP-PAZ) mission is described in detail, and the results of the noise level assessment are discussed. This chapter is based on Cardellach et al. [2014].

2.1 POL-RO CONCEPT

Since GPS satellites emit RHCP waves, the antennas used to collect ROs are usually circularly polarized too. At L-band, no significant attenuation is expected from clouds and precipitation. However, it can be learned from the weather radar community that precipitation and cloud particles induce differential phase delays between the horizontal and the vertical components of the electromagnetic field. These differential phase delays arise from the fact that heavy precipitation raindrops become flattened due to air dragging, so that the vertical component of the wave is less affected by the propagation media than the horizontal component. Therefore, a differential phase delay between both components appears. The same effect can be produced by asymmetric ice crystals that are horizontally oriented. This effect is quantified locally by the specific differential phase shift (K_{dp}).

If, instead of a circularly polarized antenna, a double linearly polarized (H and V) one is used to collect GNSS-ROs signals, this effect can be potentially measured. Due to the RO geometry, the precipitation occurs at the region where the RO rays travel nearly tangentially to the local horizon, that is, the electromagnetic propagation is essentially parallel to the hydrometeors horizontal direction. Under the RO geometry is also true that the depolarization is cumulated along the ray path so that when the signal arrives at the receiver, the total differential phase delay caused by hydrometeors can be defined as:

$$\Delta\Phi^{\mathrm{trop}} = \int_L K_{\mathrm{dp}}\,\mathrm{d}l, \tag{2.1}$$

where trop refers to troposphere, L is the path length and the phase difference is defined in the linear polarization basis. A proper derivation of the quantities involved here is given in Chapter 3.

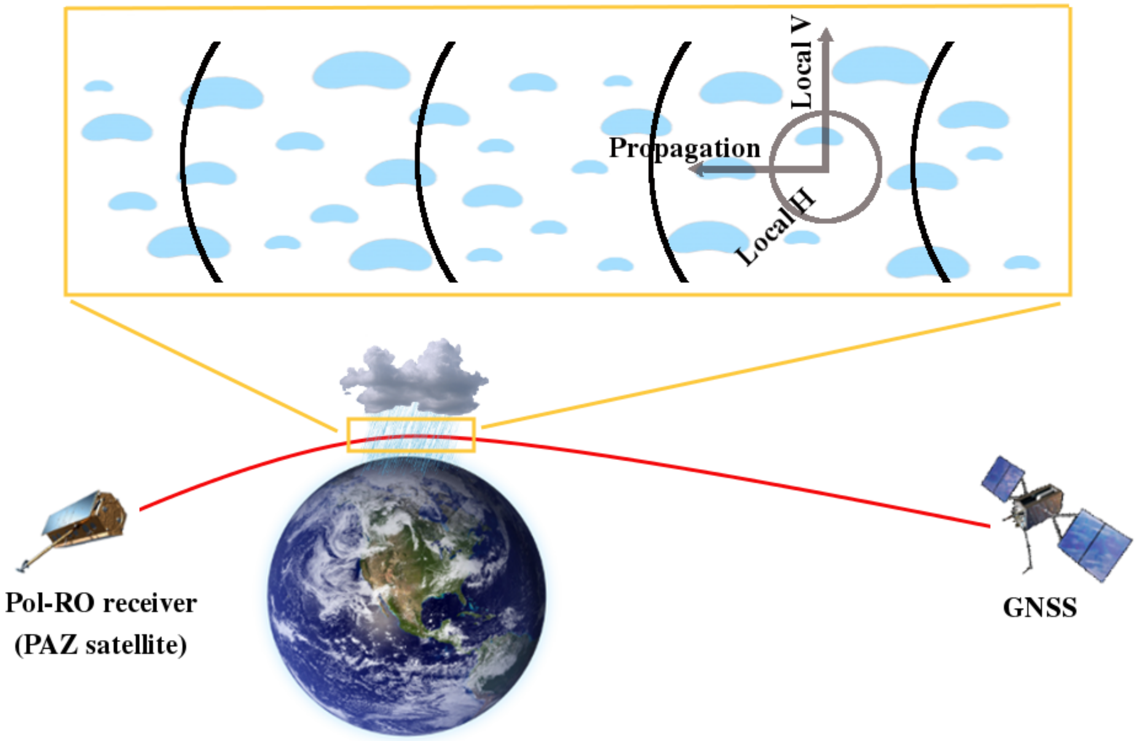

Figure 2.1: Schematic view of the Polarimetric Radio Occultation concept.

Weather radars measure the phase delay in backscattering geometry to infer K_{dp}. Differently, in a RO the signals are scanning the lower troposphere in forward scattering geometry. This situation is sketched in Figure 2.1. The phase measured in the V port is subtracted from the one measured in the H port to obtain $\Delta\Phi$. Theoretically, in a clear sky situation the phase difference between the two ports should be $\pi/2$, which would correspond to a purely RHCP wave. Therefore, hydrometeors would make $\Delta\Phi$ to differ from $\pi/2$. Such a difference is what is intended to be measured with Pol-ROs.

The two port measurements can be recombined to obtain the *standard* measurement of a RO, therefore the typical bending angle, refractivity and thermodynamic retrievals are equally provided. Hereafter, these are going to be called the *standard* RO products. The novelty and uniqueness of the Pol-RO technique is that it would be able to provide precipitation information along with the standard retrievals. To provide simultaneous precipitation information and thermodynamic vertical profiles is something that is not currently being done by any other measurement technique.

Since the observable is a differenced measurement, all the effects that are not polarimetric dependent cancel out. The phase measurement at each port is:

$$L_p = \rho + \gamma_p + C + \nu_p \tag{2.2}$$

where the subindex p indicates the port (H or V), and the terms are defined in Equation 1.4. Therefore, all the effects that should be common for both ports are cancelled in the differentiation, like the clock errors and the geometric range:

$$\Delta\Phi = L_{\mathrm{H}} - L_{\mathrm{V}} = \Delta\gamma + \Delta\nu. \tag{2.3}$$

Here, the term $\Delta\gamma$ includes polarimetric phase differences induced in the troposphere and in the ionosphere, while $\Delta\nu$ includes the thermal, instrumental and multipath errors that are induced into the phase observable. Then,

$$\Delta\gamma = \Delta\Phi^{\mathrm{trop}} + \Delta\Phi^{\mathrm{iono}}. \tag{2.4}$$

The tropospheric contribution is assumed to come solely from hydrometeors (Equation 2.1). The ionospheric term accounts for the phase delay that can be induced by the ionosphere. In an ideal situation, with perfect emission and no hydrometeors in the ray path, this term could be neglected. However, when the emission is not perfect (i. e. the signal is not purely RHCP) or the signal has crossed an hydrometeor's layer, some contribution from the ionosphere may be expected. This issue is further discussed in Chapter 3.

2.2 ROHP-PAZ MISSION

The Pol-RO concept will be tested from space for the first time in a proof of concept experiment onboard the Spanish PAZ satellite. The experiment is called Radio Occultations and Heavy Precipitation aboard PAZ (ROHP-PAZ). The PAZ satellite, owned by the company HISDESAT, was initially scheduled for launch by 2012. Its main payload is a Synthetic Aperture Radar (SAR), and it included an IGOR receiver for Precise Orbit Determination (POD). In 2009, the Spanish Ministry for Science and Innovation (MICINN) approved a proposal to include also a polarimetric GNSS-RO payload to test the Pol-RO concept. The Pol-RO concept and ROHP-PAZ experiment were devised and is under the responsibility of the Institut de Ciències de l'Espai (ICE) - Consejo Superior de Investigaciones Científicas (CSIC) / Institut d'Estudis Espacials de Catalunya (IEEC). The launch was delayed and at the time of writing, it is scheduled for 2017.

For the ground segment and processing chain, complementary agreements have been signed between ICE and National Oceanic and Atmospheric Administration (NOAA) and UCAR. UCAR will provide, under a best effort basis, the standard thermodynamic products that will be obtained from the recombination of the polarimetric signal, preferably in Near Real Time (NRT), and will disseminate them to worldwide meteorological services through the World Meteorological Organization (WMO)'s Global Telecommunication System (GTS). The polarimetric data will be stored and analysed at the ICE, where a dedicated server will make the data available.

The spacecraft was equipped with and IGOR receiver, that has been modified to collect ROs. Usually, in spacecraft dedicated to RO, there are two antennas placed

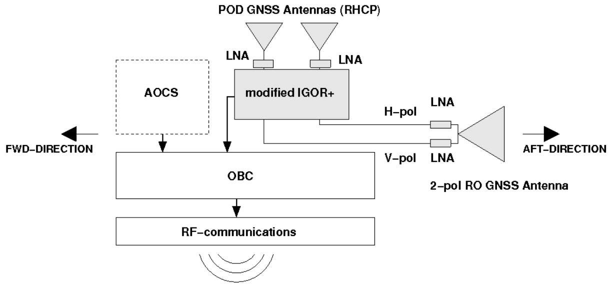

Figure 2.2: (Left): Artistic view of PAZ satellite (image courtesy of HISDESAT. (Right): Block diagram of the PAZ's payload components relevant to the ROHP-PAZ experiment. Figures from Cardellach et al. [2014], Figs. 2 and 3.

in the front and in the back of the satellite (with respect to the travel direction). These two antennas are connected to the IGOR independently, and the one in the front collects rising ROs while the one in the back collects setting ROs. In this case, the two IGOR ports are fed by the H and V channels of the polarimetric antenna installed in the back of the PAZ satellite. In consequence, only setting ROs will be collected. Figure 2.2 left shows an artistic view of PAZ satellite and in Figure 2.2 right there is sketched a block diagram of the ROHP-PAZ payload components. In Table 2.1 there are listed the most important characteristics of the satellite and its orbit.

The polarimetric RO antenna has been manufactured by Haigh-Farr under contract with the IGOR's manufacturing company, Broadreach Engineering, and following the ICE's system requirements. The design is based on COSMIC and TerraSAR-X GNSS-RO antennas, which were also provided by Haigh-Farr. The receiver and antenna can be seen in Figure 2.3. The Pol-RO antenna is a 5-element array with a nominal gain of 13 dB at L1 (12.95-dB H-pol and 12.66-dB V-pol, measured in an anechoic chamber) and 11.5 dB at L2 (11.67-dB H-pol and 11.12-dB V-pol). The cross-polar isolation at the Earth limb direction is around 27 dB at L1. There also exists a differential phase pattern that has also been measured in the anechoic chamber. These antenna patterns are shown in Figure 2.4.

2.3 NOISE LEVEL ASSESSMENT

The GNSS-RO technique allows a very precise measurement of the phase observable. The precision of each measurement depends on the received Signal to Noise Ratio (SNR) as:

$$\sigma_\phi = \frac{\lambda}{2\pi}\arctan\left(\frac{1}{\mathrm{SNR}}\right), \tag{2.5}$$

in units of delay length.

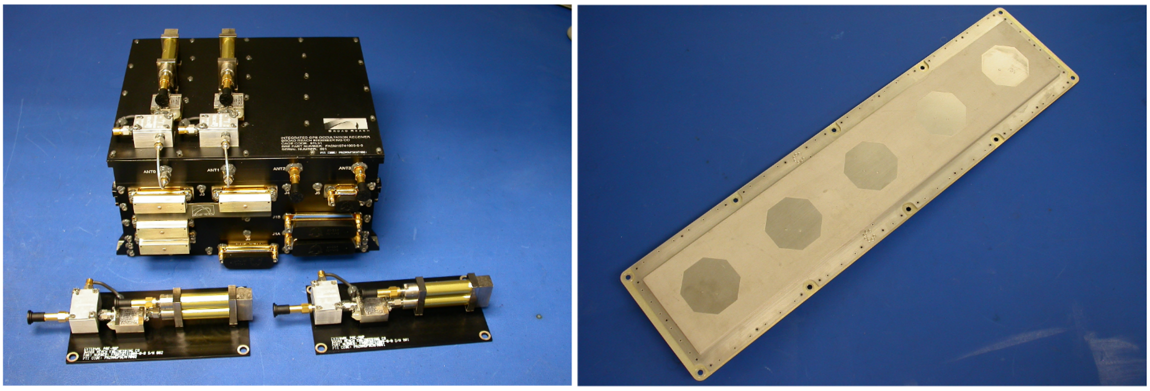

Figure 2.3: (Left): PAZ's IGOR receiver and the RHCP antennas for POD (flight units). (Right): PAZ's Polarimetric RO antenna (flight unit). Figure from Cardellach et al. [2014], Fig. 4.

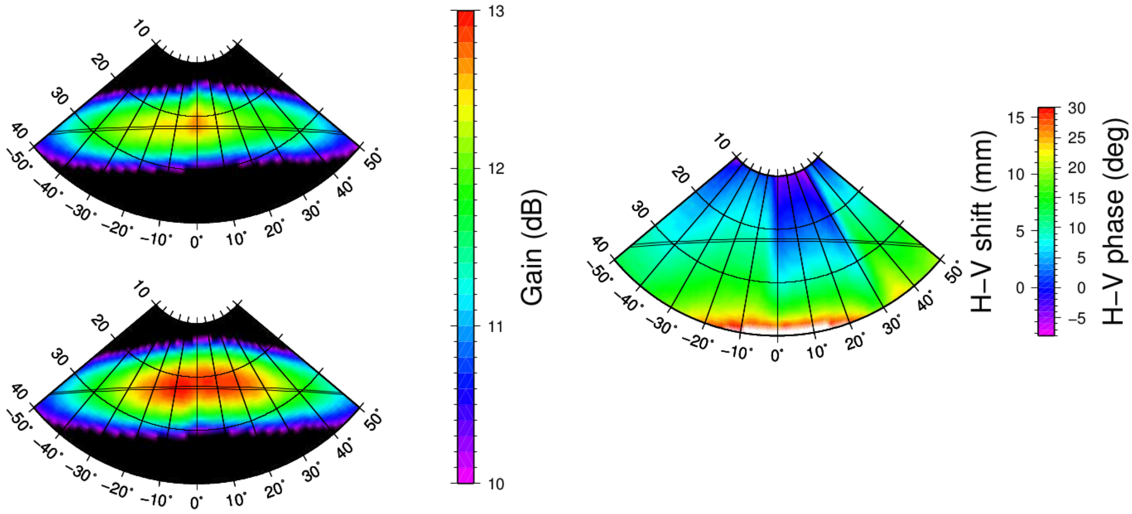

Figure 2.4: (Left): Gain antenna patter for H-port (top) and V-port (bottom). (Right): Differential phase pattern. The double curved line crossing 0-azimuth at $\simeq$ -22 deg. elevation corresponds to the approximate 20 bottom kilometres of the Earth atmosphere. Figure from Cardellach et al. [2014], Fig. 5.

PAZ satellite	
Mass	1400 kg
Section	hexagonal
Width	2.4 m
Length	5 m
Expected life	7 years (goal 10 yr)
Mean orbit semi-major axis	6883.495 km
Mean orbit eccentricity	0.00107759
Mean inclination	97.4219 deg
Mean orbit altitude (MSL)	514 km

Table 2.1: Summary of PAZ satellite and orbit characteristics.

Even though GNSS signals should experience very little attenuation even under cloud and precipitation conditions, it is necessary to examine the expected value of the phase precision under all possible scenarios. Such analysis has been done using real COSMIC data collocated with TRMM products, in order to derive a relationship between the SNR, and therefore the phase precision, and the rain conditions. For this study, two different set of collocations have been used. First, the two dimensional 3-h batch TRMM 3B42 product has been used to perform two dimensional collocations with the COSMIC ROs. This has resulted in about 420.000 cases, occurred in 2007, where the RO has crossed an area scanned by TRMM. The second set of collocations is obtained from collocating the COSMIC ROs with the three dimensional orbital 2A21 TRMM products. Here the whole COSMIC mission is used, resulting in about $17,000$ collocations. The details of the collocation exercise, for both the 2D and the 3D datasets, is explained in Section 4.2.

The first set, called hereafter the *2D collocations*, are used to obtain a rough estimate of the intensity of rain that a RO has crossed. Given the huge number of collocations, these results are considered statistically significant. On the other hand, the second set, called hereafter the *3D collocations*, provide an almost simultaneous (15 minutes of maximum difference between measurements) and collocated information, which allows a realistic characterization of the RO crossing a rainy scenario. However, these collocations are less likely to occur and, for instance, from the $17,000$ cases only around 600 show heavy rain.

Given the integral nature of the intended measurement, the rain intensity and the rain extension crossed by the GNSS link are equally important for the final observable. Hence, the information used to perform the statistics are the mean rain rate along the ray-path, $\langle R \rangle$, and the length of the ray portion that has crossed rain, L. Then, for each of the analysed rays, the height of its tangent point and the measured SNR are used to obtain the phase precision as a function of tangent point's altitude.

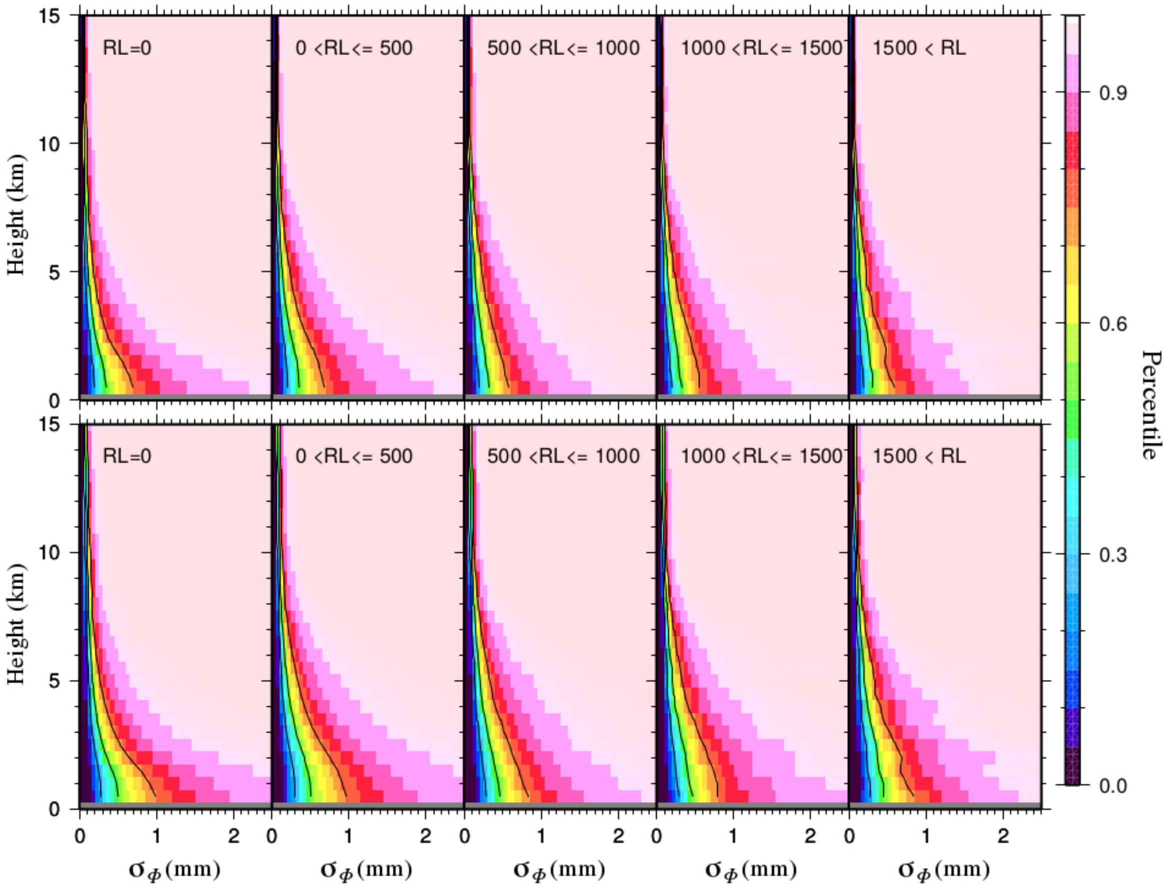

Figure 2.5: (Top row) Percentile fraction of the precision of COSMIC's phase-delay measurements, σ_ϕ, as computed from real COSMIC 1-s SNR observations, collocated with 2D TRMM products. These are classified, from left to right, according to the product of the rain rate and the rain path length, $\langle R \rangle \cdot L$. (Bottom row) Same as top row, but here the performance of the antenna is assumed to be 3dB worse. The thin black lines represent the 25th, 50th and 75th percentile, respectively. Figure from Cardellach et al. [2014], Fig. 6.

In addition, the same exercise is performed assuming that the performance of each of the PAZ's linear polarization ports could be 3dB worse than the COSMIC ones. The SNR measurements used for this study are obtained at 1 second rate.

The results are classified under different rain scenarios, characterized by the product of $\langle R \rangle$ and L. The results for the *2D collocations* are shown in Figure 2.5, where the top row correspond to the actual COSMIC measurements and in the bottom row a -3dB performance has been applied on these measurements. The same results for the *3D collocations* are shown in Figure 2.6. From the *2D collocations* one can infer that the precision is not significantly affected by precipitation, but there exist a noticeable degradation of the precision using the -3dB measurements.

The case of *3D collocations* is affected by the fact that less events are considered, but the results are perfectly consistent with those of the *2D collocations*. In Figure 2.7

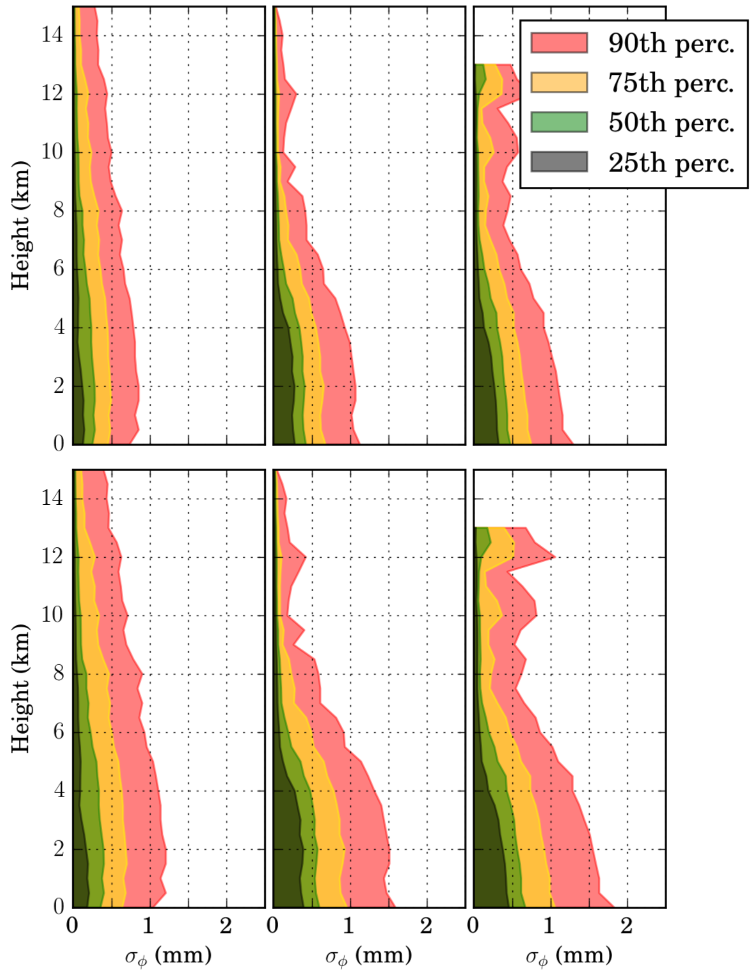

Figure 2.6: Same as in Figure 2.5, but here the collocations between COSMIC and the 3D TRMM products are used. Due to less number of collocations than in Figure 2.5, here only three $\langle R \rangle \cdot L$ ranges are used: from left to right, $\langle R \rangle \cdot L = 0$; $\langle R \rangle \cdot L < 500$; $\langle R \rangle \cdot L > 500$. Top and bottom row show the results using the actual COSMIC 1-s measurements and those where the performance is 3dB worse, respectively.

---

there are shown the number of cases as a function of $\langle R \rangle$ and L. Even though there are many more RO events in the *2D collocations* (left panel), the counts are also high for the *3D collocations* (right panel) because here all the rays of the RO events are used. This implies approximately between 1500 and 2000 rays per RO.

In Figure 2.7 can be observed a consequence of the use of the 3D TRMM products. That is, due to the limited swath length of the TRMM radar, the collocated RO tend to exhibit shorter distances through rain than those derived using the 2D products, which do not have a spatial limitation. This can happen when the RO is not aligned with the TRMM travel direction, but with a high perpendicular component. Then, the TRMM radar do not see the rain outside its swath, and the collocated RO could be missing precipitation information that is actually crossing. This is clear in the

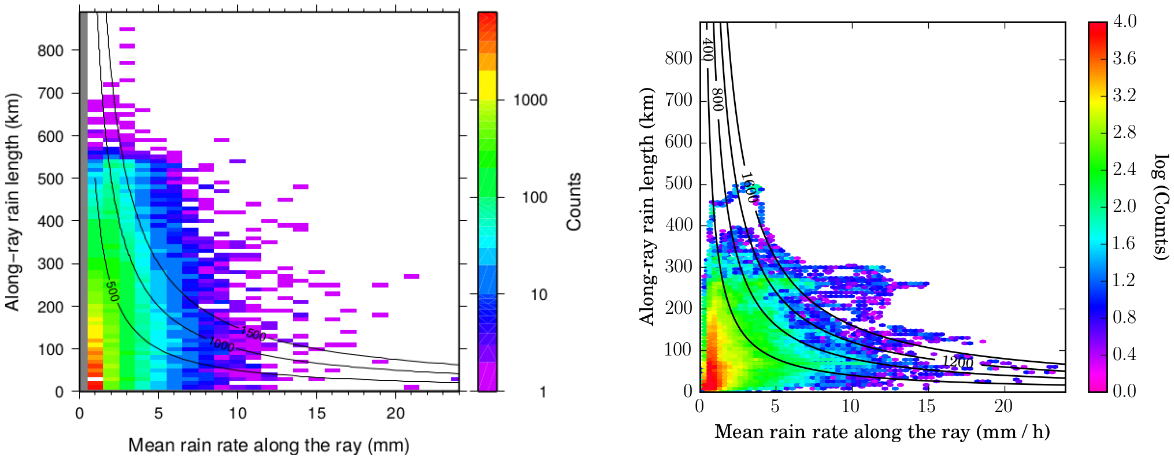

Figure 2.7: (Left): Two-dimensional histogram of the COSMIC events collocated with the 2D TRMM products, according to both main rain rate and total rain length along the radio link. (Right) Same as in the left panel, but for the collocations between COSMIC and the 3D TRMM products. The black line represent the $\langle R \rangle \cdot L$ contours for different arbitrary thresholds. Left figure is from Cardellach et al. [2014], Fig. 7.

right panel of Figure 2.7, where it can be seen how the counts for large L in the *3D collocations* drop much faster than in the *2D collocations*.

The results for the 75th percentiles of the phase precision as a function of height are summarized in Table 2.2. The phase difference precision is derived from Equation 2.5 accounting for the fact that the observable is a difference between the measurement in two ports, and therefore the error at each port has to be propagated. In this case, the σ_ϕ obtained from the COSMIC measurement (only one port), is multiplied by $\sqrt{2}$ to account for the two ports (assumed to have uncorrelated noise). The PAZ's antennas are expected to perform better than the COSMIC ones. However, being linearly polarized antennas, they might suffer from polarimetric mismatch. Therefore, the expected phase difference precision for PAZ will lay somewhere in between the precision derived using COSMIC -3dB and the actual measurement, when propagated to two ports (lower rows in Table 2.2). As a conservative threshold, the PAZ's observable precision is set to 1.4 mm at the surface level, improving with altitude. Thus, any precipitation event inducing a differential phase shift larger than 1.4 mm will be detected, and it will be masked by the noise otherwise. A sensitivity analysis for the expected performance of the technique is presented in Section 5.1, based on these thresholds.

	COSMIC (mm)	COSMIC -3dB (mm)	H (km)
σ_ϕ (1-port)	0.1	0.15	>10
	0.3	0.35	5 - 10
	0.6	0.8	2 - 5
	0.7	1	<2
$\sigma_{\Delta\phi}$ (2-ports) ($\sigma_\phi \cdot \sqrt{2}$)	0.1	0.2	>10
	0.4	0.5	5 - 10
	0.9	1.1	2 - 5
	1	1.4	<2

Table 2.2: Expected precision for PAZ's phase delay observables, based on the 75th percentile of Figure 2.5. The four top rows correspond to the phase precision measured at 1 port, for the actual COSMIC measurements (left) and the -3 dB degradation of the antenna performance (right), for different height ranges. The four bottom rows correspond to the same results but propagated to the two ports differentiation observable.

Part II

MODELS AND SIMULATIONS

3 THEORETICAL BACKGROUND

This chapter provides most of the theoretical background and expressions that are going to be used in the following chapters. It aims to describe the relevant theory with enough detail to understand the processes that electromagnetic waves undergo. First, a basic description of the electromagnetic wave propagation theory is provided, with special focus in the expressions needed for the hydrometeor scattering problem within the framework of GPS signals.

Then, the part of microphysics of precipitation that have a direct incidence in the problem treated here is introduced: the particle size distribution. A brief description and the derived quantities that are important for the simulations are provided.

Finally, the expected systematic errors derived from instrumentation and the ionosphere incidence into the polarimetric observables are discussed.

3.1 ELECTROMAGNETIC PROPAGATION

3.1.1 *Wave equation*

The mathematical description of all classical electromagnetic phenomena is based on Maxwell equations. Their extensive formulation, derivation and the exact methods to obtain solutions are beyond the scope of this work. Hence, the reader is referred to the literature, for example, to Jackson [1998] for exhaustive derivations of Maxwell equations and further discussion. A fundamental feature of the Maxwell equations is that they allow for a simple travelling plane wave solution, which represents the transport of electromagnetic energy from one point to another. The basic solution of a plane wave propagating in a homogeneous medium without sources is given by:

$$\mathbf{E}(\mathbf{r},t) = \mathbf{E}_0 e^{(i\omega t - i\mathbf{k}\cdot\mathbf{r} + i\phi)}; \qquad \mathbf{H}(\mathbf{r},t) = \mathbf{H}_0 e^{(i\omega t - i\mathbf{k}\cdot\mathbf{r} + i\phi)} \tag{3.1}$$

where $\mathbf{E}$ is the electric field, $\mathbf{H}$ is the magnetic field, $\omega = 2\pi f$, f is the frequency; $\mathbf{E}_0$ and $\mathbf{H}_0$ are constant vectors, ϕ is an arbitrary vector phase, and the wave vector $\mathbf{k}$ is constant and it may be complex:

$$k = k_{\mathrm{Re}} + ik_{\mathrm{Im}} \tag{3.2}$$

where k_{Re} and k_{Im} are real vectors. Its absolute value relates to the wavelength so that $|\mathbf{k}| = 2\pi/\lambda$. Then Equation 3.1 can be written as:

$$\mathbf{E}(\mathbf{r}, t) = \mathbf{E}_0 e^{(\mathbf{k}_{\mathrm{Im}} \cdot \mathbf{r})} e^{(iwt - i\mathbf{k}_{\mathrm{Re}} \cdot \mathbf{r} + i\phi)} \tag{3.3a}$$

$$\mathbf{H}(\mathbf{r}, t) = \mathbf{H}_0 e^{(\mathbf{k}_{\mathrm{Im}} \cdot \mathbf{r})} e^{(iwt - i\mathbf{k}_{\mathrm{Re}} \cdot \mathbf{r} + i\phi)} \tag{3.3b}$$

where $\mathbf{E}_0 e^{(\mathbf{k}_{\mathrm{Im}} \cdot \mathbf{r})}$ and $\mathbf{H}_0 e^{(\mathbf{k}_{\mathrm{Im}} \cdot \mathbf{r})}$ are the amplitudes of the electric and magnetic waves, and $wt - \mathbf{k}_{\mathrm{Re}} \cdot \mathbf{r} + \phi$ is their phase.

The Maxwell equations demand that $\mathbf{k} \cdot \mathbf{E}_0 = 0$ and $\mathbf{k} \cdot \mathbf{H}_0 = 0$, indicating that the electromagnetic wave is transverse, i. e. , both $\mathbf{E}_0$ and $\mathbf{H}_0$ are perpendicular to $\mathbf{k}$. Moreover, Equation 3.1 can be expressed as

$$\mathbf{H}(\mathbf{r}, t) = (\omega\mu)^{-1} \mathbf{k} \times \mathbf{E}(\mathbf{r}, t),$$

thus, the plane electromagnetic wave can be expressed only in terms of the electric or the magnetic field. Hereafter, only the electric field will be used to express the electromagnetic wave equations.

Assuming homogeneous waves (i. e. , k_{Re} and k_{Im} are parallel):

$$k = k_{\mathrm{Re}} + ik_{\mathrm{Im}} = \omega\sqrt{\epsilon\mu} = \frac{\omega n}{c}, \tag{3.4}$$

where

$$n = n_{\mathrm{Re}} + in_{\mathrm{Im}} = \sqrt{\frac{\epsilon\mu}{\epsilon_0\mu_0}} = c\sqrt{\epsilon\mu} \tag{3.5}$$

is the complex refractive index. Therefore, substituting k by n into Equation 3.3, it can be seen how the imaginary part of the refractive index determines the decay of the amplitude of the wave as it propagates, while the real part of n determines the phase velocity of the wave. The phase velocity is the velocity at which the planes of constant phase move along the direction of propagation, and is defined as

$$v_{ph} = \frac{c}{n_{\mathrm{Re}}}. \tag{3.6}$$

3.1.2 *Polarization of electromagnetic waves*

Polarization describes the time dependent direction of the oscillating electromagnetic field $\mathbf{E}(\mathbf{r}, t)$, at a point $\mathbf{r}$ in space. In an isotropic medium, $\mathbf{k}$ and $\mathbf{E}_0$ are perpendicular, thus there are two dimensions where vector $\mathbf{E}_0$ is confined. Let's consider now a system of coordinates defined by a unitary vector in the direction of the propagation vector, $\hat{k}$, a unitary vector perpendicular to the gravity vector in addition to $\hat{k}$, defined as $\hat{h}$, and the corresponding orthogonal vector, defined as $\hat{v}$. These three vectors define a reference system. Locally, $(\hat{h}, \hat{v}, \hat{k})$ can be identified as the Cartesian coordinates $(\hat{x}, \hat{y}, \hat{z})$. Therefore, $\hat{h}$ and $\hat{v}$ identify the horizontal and the vertical components of the electromagnetic field, respectively. When $\hat{k}$ is parallel to the Earth's surface, $\hat{v}$ is parallel to the gravity vector.

Since $\mathbf{k}$ and $\mathbf{E}_0$ are perpendicular, the electromagnetic field can be expressed by the superposition of two orthogonal components oriented in the plane formed by $\hat{h}$ and $\hat{v}$:

$$\mathbf{E}(\mathbf{r}, t) = a_{\mathrm{h}} e^{i\phi_{\mathrm{h}}} e^{i(wt - \mathbf{kr})} \hat{h} + a_{\mathrm{v}} e^{i\phi_{\mathrm{v}}} e^{i(wt - \mathbf{kr})} \hat{v}. \tag{3.7}$$

Here, only plane waves are considered, and only the real part of the field is physically relevant. Thus, the electromagnetic field can be expressed as:

$$\mathbf{E}(\mathbf{r}, t) = a_{\mathrm{h}} \cos(wt - \mathbf{kr} + \phi_{\mathrm{h}}) \hat{h} + a_{\mathrm{v}} \cos(wt - \mathbf{kr} + \phi_{\mathrm{v}}) \hat{v}. \tag{3.8}$$

The two orthogonal components of $\mathbf{E}$ are:

$$\begin{aligned} E_{\mathrm{h}} &= a_{\mathrm{h}} \cos(\tau + \phi_{\mathrm{h}}) \\ E_{\mathrm{v}} &= a_{\mathrm{v}} \cos(\tau + \phi_{\mathrm{v}}) \end{aligned} \tag{3.9}$$

where $\tau = wt - \mathbf{kr}$. These can be thought as the coordinates of the points of the curve that describes the end point of the electromagnetic vector at a typical plane in space. The relationship between them describes the polarization of the wave. One of the simplest cases would be $a_{\mathrm{v}} = 0$, which would imply a linearly horizontal polarized wave. Rearranging the terms in Equation 3.9 one obtains:

$$\begin{aligned} \frac{E_{\mathrm{h}}}{a_{\mathrm{h}}} &= \cos(\tau)\cos(\phi_{\mathrm{h}}) - \sin(\tau)\sin(\phi_{\mathrm{h}}) \\ \frac{E_{\mathrm{v}}}{a_{\mathrm{v}}} &= \cos(\tau)\cos(\phi_{\mathrm{v}}) - \sin(\tau)\sin(\phi_{\mathrm{v}}) \end{aligned} \tag{3.10}$$

and after some mathematical manipulations,

$$\left(\frac{E_{\mathrm{h}}}{a_{\mathrm{h}}}\right)^2 + \left(\frac{E_{\mathrm{v}}}{a_{\mathrm{v}}}\right)^2 - 2\frac{E_{\mathrm{h}} E_{\mathrm{v}}}{a_{\mathrm{h}} a_{\mathrm{v}}} \cos(\delta) = \sin^2(\delta) \tag{3.11}$$

where $\delta = \phi_{\mathrm{v}} - \phi_{\mathrm{h}}$. This is a general expression for the elliptical polarization state, that would lead, for example, to circular polarization when $a_{\mathrm{h}} = a_{\mathrm{v}}$ and $\delta = \pi/2$. To know the complete representation of the elliptical polarization one needs to know the shape, size and orientation of the ellipse that the wave trace in the plane perpendicular to its propagation direction, i. e. in the $\hat{k} = 0$ plane. This trace can be seen in Figure 3.1.

The ellipticity angle γ determines the shape of the ellipse. The ellipticity can be defined through γ:

$$e = \frac{b}{a} = \tan(\gamma) \tag{3.12}$$

where the semi-major axis, a, can be identified with a_{h}, and the semi-minor axis b can be identified with a_{v}. Therefore, the ellipticity $e = a_{\mathrm{v}}/a_{\mathrm{h}}$. On the other hand,

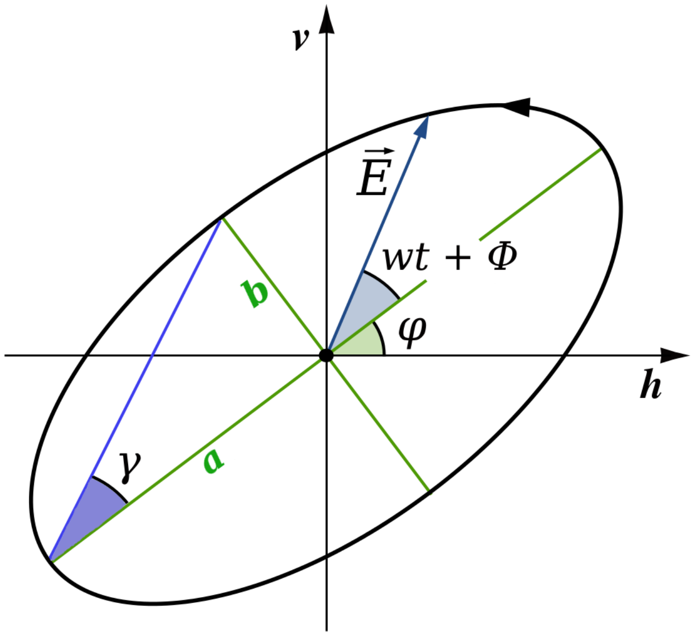

Figure 3.1: Elliptical trace in the plane perpendicular to the propagation direction.

the orientation angle φ determines the orientation of the ellipse with respect to the horizontal axis (in this case), and is related to the electromagnetic field as:

$$\tan(2\varphi) = \frac{2a_\mathrm{h}a_\mathrm{v}\cos(\delta)}{|a_\mathrm{h}|^2 - |a_\mathrm{v}|^2}. \tag{3.13}$$

These and more relationships between the electromagnetic field and the ellipsometric angles are derived in Humlíček [2004].

It is also necessary to introduce the Stokes parameters, useful for characterizing the polarization state of the electromagnetic waves. They are defined as follows:

$$I = |E_\mathrm{h}|^2 + |E_\mathrm{v}|^2 \tag{3.14a}$$

$$Q = |E_\mathrm{h}|^2 - |E_\mathrm{v}|^2 = I\cos(2\varphi)\cos(2\gamma) \tag{3.14b}$$

$$U = 2\Re\{E_\mathrm{h}^* E_\mathrm{v}\} = I\sin(2\varphi)\cos(2\gamma) \tag{3.14c}$$

$$V = 2\Im\{E_\mathrm{h}^* E_\mathrm{v}\} = I\sin(2\gamma) \tag{3.14d}$$

The first Stokes parameter corresponds to the total power of the electromagnetic wave and the other parameters define the polarization state. They are usually given as a vectorial form of the type: $q = [I, Q, U, V]$. For instance, a fully polarized wave, linearly polarized in the $\hat{h}$ direction has the Stokes vector $[1, 1, 0, 0]$, and a RHCP wave has $[1, 0, 0, 1]$.

3.1.3 *Jones representation for polarized waves*

The electromagnetic field can be expressed using phasors as well, in such a way that for example Equation 3.8 can be expressed as:

$$\mathbf{E} = \begin{bmatrix} E_{\mathrm{h}} \\ E_{\mathrm{v}} \end{bmatrix}, \tag{3.15}$$

called the Jones representation. This example uses the linear basis, but any arbitrary orthogonal basis can be used. For instance, a normalized wave linearly polarized in the $\hat{h}$ axis can be represented as

$$\mathbf{E} = \begin{bmatrix} 1 \\ 0 \end{bmatrix}_l \tag{3.16}$$

and now the subindex l explicitly indicates that linear basis $\{\hat{e}_h, \hat{e}_v\}$ is used. Similarly, a normalized wave purely right hand circularly polarized, can be represented as

$$\mathbf{E} = \begin{bmatrix} 1 \\ 0 \end{bmatrix}_c \tag{3.17}$$

where now the circular basis $\{\hat{e}_R, \hat{e}_L\}$ is used. Here, R and L stands for RHCP and Left Hand Circularly Polarized (LHCP).

Another useful relationship for this work is the complex polarization ratio [e. g. Deschamps, 1951], also called relative polarization and that is obtained as the ratio between the two components of the Jones vector representing an electromagnetic field, in any base:

$$\chi_{xy} = \frac{\mathbf{E}_y}{\mathbf{E}_x} = |\chi| e^{i\delta} \tag{3.18}$$

where $|\chi|$ is the ratio of magnitude between the two components of the field and δ is the phase difference between them, in the corresponding basis. Following Boerner [2007], it can be shown how a normalized electromagnetic field can be expressed as a function of the polarization ratio:

$$\mathbf{E}_{XY} = \frac{1}{\sqrt{1 + \chi_{xy}\chi_{xy}^*}} \begin{bmatrix} 1 \\ \chi_{xy}. \end{bmatrix}. \tag{3.19}$$

This relationship is useful to express the RHCP and LHCP in the linear basis: for circular polarization, the magnitude of the two components is the same, while the phase difference in the linear basis is $\pi/2$ (RHCP case). Then, $\chi_{\mathrm{hv}} = i$, and therefore:

$$\mathbf{E}_R = \frac{1}{\sqrt{2}} \begin{bmatrix} 1 \\ i \end{bmatrix}_l \tag{3.20a}$$

$$\mathbf{E}_L = \frac{1}{\sqrt{2}} \begin{bmatrix} 1 \\ -i \end{bmatrix}_l . \tag{3.20b}$$

Since GPS emit circularly polarized waves, and the receiving antenna for Pol-RO will be linearly polarized, these are important relationships.

3.1.3.1 *The GPS signal*

The GPS satellites emit, in principle, RHCP electromagnetic waves. However, the RHCP may not be perfect, and a certain LHCP component may be present. The presence of a LHCP component can be accounted as follows:

$$\mathbf{E}^c = E_0^c \begin{bmatrix} 1 \\ m e^{i\Delta} \end{bmatrix} \tag{3.21}$$

where m is called the tolerance term, and Δ is the phase that might be introduced along with the LHCP component. According to Navstar GPS [2013a], the L1 ellipticity shall be no worse than 1.2 dB for BlockII/IIA and no worse than 1.8 dB for Block IIR/IIR-M/IIF/GPS III space vehicles. This means that m should range between 0 (for perfect RHCP) and 0.2 for the worst case scenario. The L2 ellipticity shall be no worse than 3.2 dB for Block II/IIA and no worse than 2.2 dB for Block IIR/IIR-M/IIF and GPS III. The value Δ can be any value between 0 and 2π and no publicly available documents inform about its actual or expected values.

3.1.4 *Scattering by single particles*

Let's now consider the case where a particle is placed in the homogeneous medium where the electromagnetic wave is propagating through, so that the incident field $\mathbf{E}^{\mathbf{i}}$ is perturbed. In its integral form, the perturbed field (so called the scattered field) outside the perturbing particle is:

$$\mathbf{E}^s(r) = \nabla \times \nabla \times \frac{1}{4\pi} \int_v (\epsilon_{\mathrm{r}} - 1) \mathbf{E}_T^{\mathrm{in}}(r') \frac{e^{-ik_0 R}}{R} \mathrm{d}v \tag{3.22}$$

where ϵ_{r} is the relative permittivity, $R = |\vec{r} - \vec{r}'|$ is the distance between the particle and the place where the field is evaluated, v is the particle volume over which the integral is performed, and $\mathbf{E}_T^{\mathrm{in}}$ is the total electromagnetic field inside the particle, which depends on the incident field and the polarization ($\vec{P}$) of the dielectric particle [Bringi and Chandrasekar, 2001]. When the field is evaluated far enough, the far-field approximation applies and after several mathematical manipulations, one ends up with:

$$\mathbf{E}^s(\vec{r}) = \frac{k_0^2}{4\pi}(\epsilon_\mathrm{r} - 1)\frac{e^{-ik_0 r}}{r}\int_v \left[\mathbf{E}_T^{\mathrm{in}}(r') - \hat{r}(\hat{r}\mathbf{E}_T^{\mathrm{in}})\right] e^{ik_0 \vec{r}\hat{r}} dv. \tag{3.23}$$

It can also be expressed as:

$$\mathbf{E}^s(\vec{r}) = \vec{f}\ \frac{e^{-ik_0 r}}{r} \tag{3.24}$$

where $\vec{f}$ is the far-field vector scattering amplitude:

$$\vec{f} = \frac{k_0^2}{4\pi}(\epsilon_\mathrm{r} - 1)\int_v \left[\mathbf{E}_T^{\mathrm{in}}(r') - \hat{r}(\hat{r}\mathbf{E}_T^{\mathrm{in}})\right] e^{ik_0 \vec{r}\hat{r}} dv \tag{3.25}$$

A more detailed derivation of these expressions can be found in, for example, Bringi and Chandrasekar [2001]. Therefore, the main unknown here is the internal field, which is directly related with the incident field. How $\vec{f}$ depends on E^i can be obtained through approximations or through numerical computations. For example, when the dielectric particle is small compared to the wavelength (Rayleigh regime), the internal field can be obtained through the electrostatic solution, and the far-field scattering vector is expressed as:

$$\vec{f} = \frac{k_0^2}{4\pi}\frac{(\epsilon_\mathrm{r} - 1)}{(\epsilon_\mathrm{r} + 2)}3V\left[\mathbf{E}^\mathrm{i} - \hat{r}(\hat{r}\cdot\mathbf{E}^\mathrm{i})\right] \tag{3.26}$$

where V is the particle volume. Since the scattering depends on the incidence field direction, $\hat{\imath}$, and where it is evaluated (scattering direction), $\hat{s}$, the far-field scattering vector can be written as $\vec{f}(\hat{s},\hat{\imath})$. Using this convention, the far field scattering vector for the forward scattering configuration is expressed as $\vec{f}(\hat{\imath},\hat{\imath})$, and the backscattering one is expressed as $\vec{f}(-\hat{\imath},\hat{\imath})$.

Now consider an incident wave described in the linear basis with the Jones representation (e. g. Equation 3.15). Assuming that the scattering reference system is aligned with the propagation reference frame defined previously, the scattered field can be written as a function of the incident field as:

$$\begin{bmatrix}\mathbf{E}_\mathrm{h}^\mathrm{s}\\ \mathbf{E}_\mathrm{v}^\mathrm{s}\end{bmatrix} = \frac{e^{-ik_0 r}}{r}\mathbf{S}\begin{bmatrix}\mathbf{E}_\mathrm{h}^\mathrm{i}\\ \mathbf{E}_\mathrm{v}^\mathrm{i}\end{bmatrix}, \tag{3.27}$$

where $\mathbf{S}$ is the amplitude scattering matrix:

$$\mathbf{S} = \begin{bmatrix}S_\mathrm{hh} & S_\mathrm{hv}\\ S_\mathrm{vh} & S_\mathrm{vv}\end{bmatrix}. \tag{3.28}$$

The elements of $\mathbf{S}$ have units of length. $\mathbf{S}$ describes the transformation of the transverse components of the incident wave into the transverse components of the scattered wave in the far-field region. Therefore, $\mathbf{S}$ depends on the particle responsible for the scattering. It depends on its composition, shape, size and orientation, and in Chapter 4 it is shown how it is computed and used.

Alternatively, it is also possible to work on the Stokes vectors. Then, instead of the incident and scattered fields, the phase matrix (a normalized Mueller 4x4 matrix) relates the incident power with the scattered one. Therefore, it relates the incident with the scattered Stokes vectors:

$$\begin{bmatrix} I^{\mathrm{s}} \\ Q^{\mathrm{s}} \\ U^{\mathrm{s}} \\ V^{\mathrm{s}} \end{bmatrix} = \frac{1}{r^2}\,\mathbf{Z}\begin{bmatrix} I^{\mathrm{i}} \\ Q^{\mathrm{i}} \\ U^{\mathrm{i}} \\ V^{\mathrm{i}} \end{bmatrix} = \frac{1}{r^2}\begin{bmatrix} Z_{11} & Z_{12} & Z_{13} & Z_{14} \\ Z_{21} & Z_{22} & Z_{23} & Z_{24} \\ Z_{31} & Z_{32} & Z_{33} & Z_{34} \\ Z_{41} & Z_{42} & Z_{43} & Z_{44} \end{bmatrix}\begin{bmatrix} I^{\mathrm{i}} \\ Q^{\mathrm{i}} \\ U^{\mathrm{i}} \\ V^{\mathrm{i}} \end{bmatrix} \tag{3.29}$$

where the elements of $\mathbf{Z}$ are combinations of the elements of $\mathbf{S}$:

$$\begin{aligned}
Z_{11} &= \frac{1}{2}(|S_{\mathrm{hh}}|^2 + |S_{\mathrm{vv}}|^2 + |S_{\mathrm{hv}}|^2 + |S_{\mathrm{vh}}|^2) \\
Z_{12} &= \frac{1}{2}(|S_{\mathrm{hh}}|^2 - |S_{\mathrm{vv}}|^2 - |S_{\mathrm{hv}}|^2 + |S_{\mathrm{vh}}|^2) \\
Z_{13} &= \Re(S_{\mathrm{hh}}S^*_{\mathrm{hv}} + S_{\mathrm{hv}}S^*_{\mathrm{vv}}) \\
Z_{14} &= \Im(S_{\mathrm{hh}}S^*_{\mathrm{hv}} + S_{\mathrm{hv}}S^*_{\mathrm{vv}}) \\
Z_{21} &= \frac{1}{2}(|S_{\mathrm{hh}}|^2 - |S_{\mathrm{vv}}|^2 + |S_{\mathrm{hv}}|^2 - |S_{\mathrm{vh}}|^2) \\
Z_{22} &= \frac{1}{2}(|S_{\mathrm{hh}}|^2 + |S_{\mathrm{vv}}|^2 - |S_{\mathrm{hv}}|^2 - |S_{\mathrm{vh}}|^2) \\
Z_{23} &= \Re(S_{\mathrm{hh}}S^*_{\mathrm{hv}} - S_{\mathrm{hv}}S^*_{\mathrm{vv}}) \\
Z_{24} &= \Im(S_{\mathrm{hh}}S^*_{\mathrm{hv}} - S_{\mathrm{hv}}S^*_{\mathrm{vv}}) \\
Z_{31} &= \Re(S_{\mathrm{hh}}S^*_{\mathrm{vh}} + S_{\mathrm{vh}}S^*_{\mathrm{vv}}) \\
Z_{32} &= \Re(S_{\mathrm{hh}}S^*_{\mathrm{vh}} - S_{\mathrm{vh}}S^*_{\mathrm{vv}}) \\
Z_{33} &= \Re(S_{\mathrm{hh}}S^*_{\mathrm{vv}} + S_{\mathrm{hv}}S^*_{\mathrm{vh}}) \\
Z_{34} &= \Im(S_{\mathrm{hh}}S^*_{\mathrm{vv}} - S_{\mathrm{hv}}S^*_{\mathrm{vh}}) \\
Z_{41} &= -\Im(S_{\mathrm{hh}}S^*_{\mathrm{vh}} + S_{\mathrm{hv}}S^*_{\mathrm{vv}}) \\
Z_{42} &= -\Im(S_{\mathrm{hh}}S^*_{\mathrm{vh}} - S_{\mathrm{hv}}S^*_{\mathrm{vv}}) \\
Z_{43} &= -\Im(S_{\mathrm{hh}}S^*_{\mathrm{vv}} + S_{\mathrm{hv}}S^*_{\mathrm{vh}}) \\
Z_{44} &= \Re(S_{\mathrm{hh}}S^*_{\mathrm{vh}} - S_{\mathrm{vh}}S^*_{\mathrm{vv}})
\end{aligned} \tag{3.30}$$

S and **Z** formulations are equivalent, and they are going to be important in order to derive quantities related to the propagation of the electromagnetic waves through hydrometeors.

3.1.5 *Propagation through hydrometeors*

This subsection follows a similar reasoning as in Oguchi [1983] and Bringi and Chandrasekar [2001]. The propagation of electromagnetic waves through media filled by hydreometeors can be described as if the wave were travelling through a media with an effective propagation constant, k_{eff}, that depends on the one particle forward scattering vector, $\vec{f}$ (Equation 3.25):

$$k_{\text{eff}} = k_0 + \frac{2\pi n_{\text{p}}}{k_0}\,\hat{k}\,\vec{f}(\hat{\imath},\hat{\imath}) \tag{3.31}$$

where k_0 is the propagation constant in the vacuum and n_p is the number of particles in the region, and the forward scattering configuration is used. This implies that the real part of k_{eff} will induce an additional shift in the phase of the wave, and its imaginary part will induce attenuation. A plane wave propagating along z can be expressed as:

$$\mathbf{E}(z) = \hat{k}E_0\,e^{\Im\{k_{\text{eff}}\}z}\,e^{-i\Re\{k_{\text{eff}}\}z} \tag{3.32}$$

In the matrix form, with the incident wave defined in the linear basis, and using a transmission matrix $\mathbf{T}$, the propagation is expressed as:

$$\begin{bmatrix} E_{\text{h}}(z) \\ E_{\text{v}}(z) \end{bmatrix} = \mathbf{T}(z)\begin{bmatrix} E_{\text{h}}(0) \\ E_{\text{v}}(0) \end{bmatrix} = \begin{bmatrix} e^{\lambda_1 z} & 0 \\ 0 & e^{\lambda_2 z} \end{bmatrix}\begin{bmatrix} E_{\text{h}}(0) \\ E_{\text{v}}(0) \end{bmatrix} \tag{3.33}$$

where $\lambda_1 = -ik^h_{\text{eff}}$ and $\lambda_2 = -ik^v_{\text{eff}}$ are the eigenvalues of the medium, and there is assumed that particles have its symmetry axis horizontally oriented (so no crosspolarization terms are induced). Given the context, one can drop the k_0 term from Equation 3.31 to only account for the differences with respect to the free space propagation. For each polarimetric component p, the medium induces an specific phase shift (K_p) and an specific attenuation (A_p) that can be defined as:

$$K_p = -\Im\{\lambda_p\} = \frac{2\pi n_{\text{p}}}{k_0}\,\Re\{\hat{p}\cdot\vec{f}\} \tag{3.34}$$

in rad km^{-1} and

$$A_p = 20\log_{10}\left(\frac{|\mathbf{E}(z)|}{|\mathbf{E}(0)|}\right)\frac{1}{z} = -(8.686)\,\Re\{\lambda_p\} = -(8.686)\frac{2\pi n_{\text{p}}}{k_0}\,\Im\{\hat{p}\cdot\vec{f}\} \tag{3.35}$$

in dB km^{-1}, where $\hat{p}$ is the polarization unit vector ($\hat{h}$ or $\hat{v}$ for the linear basis case). Accounting for the size dependence of n_{p} and $\vec{f}$, and using the matrix component notation introduced in Equation 3.27, these expressions can be written as:

$$K_p = \frac{2\pi}{k_0}\int \Re\{S_{pp}\}N(D)\mathrm{d}D \tag{3.36}$$

$$A_p = -8.686\,\frac{2\pi}{k_0}\int \Im\{S_{pp}\}N(D)\mathrm{d}D \tag{3.37}$$

where $N(D)$ is the drop size distribution, in mm^{-1} m^{-3}, and D is the equivolumetric diameter of the particle, i.e. the volume it would have if it was an sphere.

At this point, a few important observables can be defined. Let's consider a circularly polarized incident wave, defined in the linear basis. This is the general conditions of a GPS emitted electromagnetic wave that travels through precipitation media and reaches a linearly polarized antenna (i. e. Pol-ROs). The observables that are worth to be defined are the differential phase shift between the two components, the so called specific differential phase shift (K_{dp}), and the differential attenuation (A_{dp}). Equations (3.35) to (3.36) lead to:

$$K_{\mathrm{dp}} = -\Im\{\lambda_1 - \lambda_2\} = K_{\mathrm{h}} - K_{\mathrm{v}} = \frac{2\pi}{k_0} \int \Re\left\{S_{\mathrm{hh}} - S_{\mathrm{vv}}\right\} N(D) \mathrm{d}D \tag{3.38}$$

and:

$$A_{\mathrm{dp}} = \Re\{\lambda_1 - \lambda_2\} = A_{\mathrm{h}} - A_{\mathrm{v}} = -8.686 \frac{2\pi}{k_0} \int \Im\left\{S_{\mathrm{hh}} - S_{\mathrm{vv}}\right\} N(D) \mathrm{d}D. \tag{3.39}$$

The cumulated effect along the ray-path (L) of these quantities are called the tropospheric differential phase delay ($\Delta\Phi^{\mathrm{trop}}$) and the tropospheric differential attenuation (ΔA^{trop}) expressed as:

$$\Delta\Phi^{\mathrm{trop}} = \int_L K_{\mathrm{dp}}(z) \mathrm{d}z \tag{3.40}$$

and

$$\Delta A^{\mathrm{trop}} = \int_L A_{\mathrm{dp}}(z) \mathrm{d}z. \tag{3.41}$$

In the case of standard RO, the interest recalls only in the excess phase or total attenuation that hydrometeors induce to the incident circularly polarized wave with respect to what would have had in the free space, but not to the differential quantities. In this case, a mean effective propagation constant is defined

$$k_{\mathrm{eff}}^{\mathrm{mean}} = \frac{k_{\mathrm{eff}}^{h} + k_{\mathrm{eff}}^{v}}{2}, \tag{3.42}$$

so that the specific excess phase delay that is induced in the RHCP wave is

$$K_{\mathrm{exc}} = \frac{2\pi}{k_0} \int_D \langle \Re\{S_{ij}\} \rangle N(D) \mathrm{d}D = \frac{2\pi}{k_0} \int_D \frac{\Re\{S_{\mathrm{hh}} + S_{\mathrm{vv}}\}}{2} N(D) \mathrm{d}D, \tag{3.43}$$

and the specific attenuation is

$$\begin{aligned} A_{\mathrm{exc}} &= -8.686 \frac{2\pi}{k_0} \int_D \langle \Im\{S_{ij}\} \rangle N(D) \mathrm{d}D \\ &= -8.686 \frac{2\pi}{k_0} \int_D \frac{\Im\{S_{\mathrm{hh}} + S_{\mathrm{vv}}\}}{2} N(D) \mathrm{d}D. \end{aligned} \tag{3.44}$$

Their cumulated effects along L are defined as:

$$\Phi_{\mathrm{exc}}^{\mathrm{trop}} = \int_L K_{\mathrm{exc}}(z) \mathrm{d}z \tag{3.45}$$

and

$$A_{\mathrm{exc}}^{\mathrm{trop}} = \int_L A_{\mathrm{exc}}(z) \mathrm{d}z. \tag{3.46}$$

3.1.6 *Propagation through the ionosphere*

The ionosphere is the region of Earth's atmosphere that extends from 80 km of altitude to more than 800 km (up to the magnetosphere), and contains free electrons. In this region, the solar irradiation is high enough to ionize some atmospheric molecules. The density of the free electrons varies with height, having a maximum peak around 250 - 400 km. It also depends on the solar activity, time of the day and geographic location, and the Earth's magnetic field.

Electromagnetic waves travelling through the magnetized plasma filling the ionosphere undergo changes in their polarization, due to the plasma birefringence and optical activity. These changes can be described as how they affect the three Stoke's parameters that characterize the polarization state of an electromagnetic wave [Segre, 1999]. The change of the polarization state can be split into the contribution from the parallel component of the magnetic field (with respect to the direction of propagation of the electromagnetic wave), $B_{\parallel}$, and the contribution from the perpendicular component, $B_{\perp}$. These are the Faraday rotation and the Cotton-Mouton effect, respectively. In differential form, these effects are defined as [Zhang et al., 2010]:

$$d\Omega_{\mathrm{F}} = -\frac{\omega_{\mathrm{p}}^2 \omega_{\mathrm{c}}}{2c\omega^2}\frac{B_{\parallel}}{B}\mathrm{d}z \tag{3.47}$$

and

$$d\Omega_{\mathrm{CM}} = \frac{\omega_{\mathrm{p}}^2 \omega_{\mathrm{c}}^2}{2c\omega^3}\left(\frac{B_{\perp}}{B}\right)^2 \mathrm{d}z \tag{3.48}$$

where ω_{p} is the plasma frequency, and ω_{c} is the cyclotron frequency, defined as:

$$w_{\mathrm{p}}^2 = \frac{n_{\mathrm{e}} q^2}{m_{\mathrm{e}} \epsilon_0} \qquad w_{\mathrm{c}} = \frac{|q| B}{m_{\mathrm{e}}},$$

where q and m_{e} are the charge and the mass of the electron, and n_{e} is the electron density of the region. The Faraday rotation would introduce a rotation on a linearly polarized incident wave, while the Cotton-Mouton effect would induce a phase shift between the orthogonal components of the wave. However, the factor w_{c}/w present in Equation 3.48 makes the Cotton-Mouton effect about 3 orders of magnitude smaller than the Faraday effect, at the GNSS frequencies (considering their maximum possible value in the magnetic field projection term). Therefore, the Cotton-Mouton effect can be neglected in the vast majority of cases, since the results for the Faraday effect are already small, of about few degrees as it will be shown in Section 4.3.

Using the definitions of ω_{p} and ω_{c}, a more general relationship for Ω_{F} can be obtained, relating Ω_{F} with the electron density and the wave frequency:

$$d\Omega_{\mathrm{F}} = \frac{2.36 \cdot 10^4}{f^2} n_{\mathrm{e}}(\vec{l})\, \vec{B}(\vec{l}) \cdot \hat{l}\, \mathrm{d}l. \tag{3.49}$$

The Faraday rotation induces a standard rotation in linear basis:

$$T_\Omega = \begin{bmatrix} \cos(\Omega) & \sin(\Omega) \\ -\sin(\Omega) & \cos(\Omega) \end{bmatrix}. \tag{3.50}$$

When the incident electromagnetic wave is circularly polarized, it can be shown that the Faraday rotation has no practical effect into the relative polarization of the wave. The Faraday rotation rotates the linearly polarized waves, and since a circularly polarized wave can be expressed as a combination of two equal linearly polarized waves, the effect would be the same to each of them, and therefore the rotation would not be noticeable. This can be shown using the complex depolarization ratio:

$$E(0) = \frac{1}{\sqrt{2}} \begin{bmatrix} 1 \\ i \end{bmatrix} \qquad \Rightarrow \qquad \chi = i$$

$$E(z) = \frac{1}{\sqrt{2}} T_\Omega \begin{bmatrix} 1 \\ i \end{bmatrix} = \frac{1}{\sqrt{2}} \begin{bmatrix} \cos(\Omega) + i\sin(\Omega) \\ i\cos(\Omega) - \sin(\Omega) \end{bmatrix} \qquad \Rightarrow \qquad \chi = \frac{ie^{i\Omega}}{e^{i\Omega}} = i$$

However, as mentioned in Section 3.1.3.1, the GPS emitted waves might not be perfectly circularly polarized, and therefore the Faraday rotation affects the relative polarization, inducing a rotation of the ellipse orientation, φ, and a phase shift. Similarly, even though the emitted signal was perfectly circularly polarized, it can become elliptical after crossing an hydrometeor layer. This implies that when rain is present, the ionosphere will induce a polarimetric phase shift into the signals at the ionosphere after crossing the troposphere, on its way to the receiver.

The fact that the ionosphere is affecting the polarization state of the wave has an important implication. The measurements of the phase difference will include a ionospheric term in addition to the hydrometeors' contribution. Thus, to infer precipitation and clouds information, one has to correct for the ionospheric effects first. This will be further developed in Section 4.3.

3.2 MICROPHYSICS OF PRECIPITATION

The study of the physics ruling the processes involved in clouds formation, growth and evolution, and precipitation are essential for the modelling and the understanding of the observations. The microphysics is usually referred to as the physics underlying most of the processes that particles forming the clouds undergo, while the macrophysics is more related to the dynamics of the formation and evolution of cloud systems.

For this dissertation, the main focus will be put in the parameters describing the state of the cloud or precipitation at a given moment, and less efforts will be dedicated in the description of the evolution of the state of the clouds. Hence, knowing the current state of a cloud implies to know how many, of which type and how big are the particles forming the cloud. This is something that can be described using the Particle Size Distribution (PSD), or Drop Size Distribution (DSD) when referring specifically to raindrops. Through the PSD most of the remote sensing observables can be associated to a physical quantity. Therefore, most of this section will be dedicated to describe and understand the PSD of hydrometeors.

3.2.1 *The Hydrometeor's Particle Size Distribution*

Different particle size distributions have been proposed for the study of microphysical parametrizations. Distributions like the gamma distribution function, the exponential or the log-normal have been used to describe observations of precipitation phenomena [e. g. Straka, 2009]. The PSD that is going to be used in this study is the gamma shaped probability function. It quantifies the number of particles of a certain size, in a integrable function of the form:

$$N(D) = N_0 D^{\mu} e^{-\Lambda D} \tag{3.51}$$

where $N(D)$ is the particle concentration representing the number of particles per diameter interval per unit volume, in mm^{-1} m^{-3}; D is the equivolumetric particle diameter in mm; N_0 is the scale parameter, in mm$^{-1-\mu}$ m^{-3}; Λ is the slope parameter, in mm^{-1}; and μ is the shape parameter, which is unitless [Ulbrich, 1983]. One particular case of the gamma particle size distribution is the exponential one. The Marshall-Palmer is a widely used model that uses an exponential distribution, and is used here for comparison purposes [Marshall and Palmer, 1948]. The parameters of these distributions are all mathematical parameters, and they do not represent physical quantities. For this reason, a "normalized" particle size distribution was introduced [e. g. Testud et al., 2000, 2001], so that:

$$N(D) = N_0^* F_{\mu}(D/D_m) \tag{3.52}$$

where:

$$F_{\mu} = \frac{\Gamma(4)}{3.67^4} \frac{(3.67+\mu)^{4+\mu}}{\Gamma(4+\mu)} \left(\frac{D}{D_\mathrm{m}}\right)^{\mu} e^{-(3.67+\mu)\left(\frac{D}{D_\mathrm{m}}\right)}. \tag{3.53}$$

Now, the PSD depends on D_m (in mm), which is the diameter of the mean volume particle, and on N_0^* (in mm^{-1} m^{-3}), that represents the intercept parameter of an exponential distribution with the same Water Content (WC) and D_m. Furthermore, N_0^* is proportional to WC and D_m as:

$$N_0^* = \frac{4^4}{\pi\rho} \frac{WC}{D_\mathrm{m}^4}. \tag{3.54}$$

This approach is useful for rain studies, but is also valid for ice [Delanoë et al., 2005, 2014]. In the case of ice, the D variable, defined as the equivolumetric diameter of the particles, has to be defined as the equivalent melted diameter (D_eq), i. e. the diameter of an ice particle melted into water, with spherical shape:

$$D_\mathrm{eq} = \left(\frac{6\,M(D_\mathrm{max})}{\pi\rho}\right)^{\frac{1}{3}}, \tag{3.55}$$

where $M(D_{\text{max}})$ is the mass as a function of the maximum size of the particle. Relationships for $M(D)$ for different ice crystals have been derived, for example, in Pruppacher and Klett [1997].

3.2.1.1 *Moments of the DSD: derived quantities*

Through the moments of the particle size distribution many physical quantities and observables can be derived, and therefore, related among them. The general expression for the nth moment of the PSD distribution is:

$$M_n = \int N(D) D^n \mathrm{d}D \tag{3.56}$$

which, for a general gamma sized size distribution can be expressed as [Testud et al., 2001]:

$$M_n = N_0 \frac{\Gamma(n+\mu+1)}{\Lambda^{n+\mu+1}}. \tag{3.57}$$

The different moments can be used to derive different quantities. As an example, D_{m}, in mm, is defined as the forth moment divided by the third:

$$D_{\text{m}} = \frac{M_4}{M_3} = \frac{4+\mu}{\Lambda}. \tag{3.58}$$

The effective diameter, D_{eff}, in mm, is defined as the third moment divided by the second:

$$D_{\text{eff}} = \frac{M_3}{M_2} = \frac{3+\mu}{\Lambda}. \tag{3.59}$$

The third moment can also be used to obtain the water content. Both for ice and water, depending on the density in use, the expression, in g m^{-3}, is as follows:

$$WC = \frac{\rho\pi}{6} \int N(D)\, D^3\, \mathrm{d}D. \tag{3.60}$$

Similarly, the rain rate in mm h^{-1} is defined as:

$$R = 0.6\,\pi\, 10^{-3} \int v(D)\, N(D)\, D^3\, \mathrm{d}D \tag{3.61}$$

where $v(D)$ is the terminal fall velocity of the particles, in m·s^{-1}. It is a function of the diameter, and it goes as a power law of the form $v = aD^b$ [e. g. Straka, 2009].

The radar reflectivity factor (Z) is a measure of the particle's cross section weighted over a volume, and it is related to the sixth moment of the PSD:

$$Z = \int N(D)\, D^6\, \mathrm{d}D \tag{3.62}$$

in $\mathrm{mm}^6\ \mathrm{m}^{-3}$ under the Rayleigh regime. When Rayleigh conditions do not apply, Z is represented as a function of the back scattering cross section, σ_{bk}, and it is called the equivalent radar reflectivity factor, Z_e:

$$Z_\mathrm{e} = \frac{\lambda^4}{\pi^5 |K_\mathrm{w}|^2} \int \sigma_{\mathrm{bk}}(D) N(D) \mathrm{d}D \tag{3.63}$$

where $K_\mathrm{w} = (n_\mathrm{w}^2 - 1)/(n_\mathrm{w}^2 + 2)$, and n_w is the complex refractivity index of water. Here, n_w and σ_{bk} depend on the radar frequency.

Therefore, the PSD is what relates the observed quantities with the physical values, such as Z to R or to WC. Relating them in practice is not straightforward. Many studies tried to find a $Z - R$ relationship (see a review of several of them in Rosenfeld and Ulbrich [2003]). Mathematically, it can be shown that Z and R are related through a power law of the form

$$Z = AR^b \tag{3.64}$$

where the parameters A and b depend on the parameters of the PSD that is used [Steiner et al., 2004]. Thus, the relationship changes with different PSD, which implies that a global and unique $Z - R$ relationship does not exist. The PSD changes depending on the type of rain, even from storm to storm. It is even possible that it changes within the same event. Similar features are encountered in trying to relate Z to WC, both for ice and rain (e. g. Hagen and Yuter [2003]; Hong et al. [2008]). Similarly, R can be estimated from the K_{dp} measurements, also with a relationship between them of the form of a power law [e. g. Chandrasekar et al., 1990; Ryzhkov and Zrnić, 1996; Junyent and Chandrasekar, 2016]. However, the $R - K_{\mathrm{dp}}$ relationship is highly frequency dependent.

3.2.2 *Generation of simulated observables*

When only measurements of reflectivity are available, one has to choose one of the relationships mentioned above to derive the physically meaningful variables. Alternatively, one can obtain all the possible relationships, by constructing all the mathematically possible PSDs and discarding those physically meaningless. Hence, a set of mathematically valid $(N_0, \Lambda, \mu)^i$ triplets can be used in order to obtain the PSDs. Each triplet has an associated physical magnitude:

$$(N_0, \Lambda, \mu)^i \rightarrow N(D)^i \rightarrow (N_\mathrm{w}^i, D_\mathrm{m}^i, K_{\mathrm{dp}}^i, Z_\mathrm{e}^i, \mathrm{LWC}^i, D_{\mathrm{eff}}^i, R^i, \ldots).$$

Depending on the hydrometeor being modelled, not all $N(D)$ parameters will be physically consistent, that is, fall in ranges that have been observed amongst various ground validation data [Williams et al., 2014].

For example, in Figure 3.2 it can be seen a set of 70,000 different DSDs, from which the N_w and D_m is derived, and the Liquid Water Content (LWC) is computed. Here, values of R larger than 300 mm h^{-1}, D_m larger than 5 mm, and N_w larger

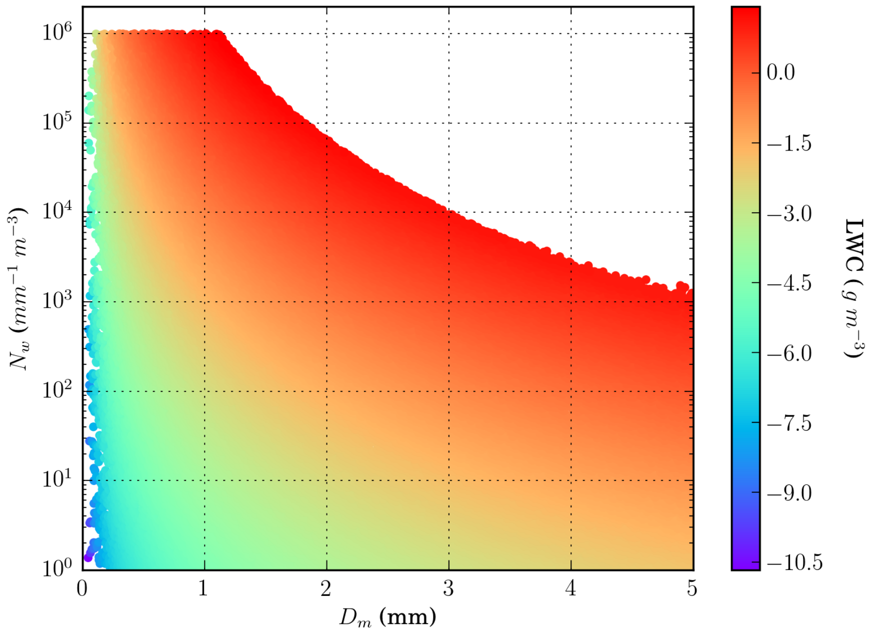

Figure 3.2: N_w as a function of D_m for all the generated DSDs. Colorbar represents the LWC.

than 10^6 mm^{-1} m^{-3} are discarded. Figure 3.3 shows the relationship between Z and R for the same set of DSDs (in the Rayleigh regime). In addition, several $Z - R$ relationships from Rosenfeld and Ulbrich [2003] are shown, for comparison. It can be seen how, being these relationships empirically measured under different rain scenarios, the drop size distribution changes a lot from place to place.

Remote sensing measurements, like those by radars, only obtain the Z and therefore some assumptions on the PSD have to be done. In Chapter 4, the PSDs are going to be needed in order to compute the desired observables. What is going to be done, when possible, will be to rely on the assumptions made by weather radar community, inferring the PSD from the given observables. Most of the data that is going to be used contains the measurements of Z and some derived quantities, such as LWC, Ice Water Content (IWC), or R. Using a plot like Figure 3.3 one can derive, well enough, which is the approximate PSD that has been used, from a measurement of Z and a measurement of R, for example.

3.3 THEORETICAL SYSTEMATIC ERRORS

After the description of all the processes involved in the propagation of the signal through the atmosphere that are relevant to the polarimetric observables, the systematic effects that are a priori expected can be investigated. If the systematic errors are well characterized, its effect can be mitigated through calibration during the spaceborne mission.

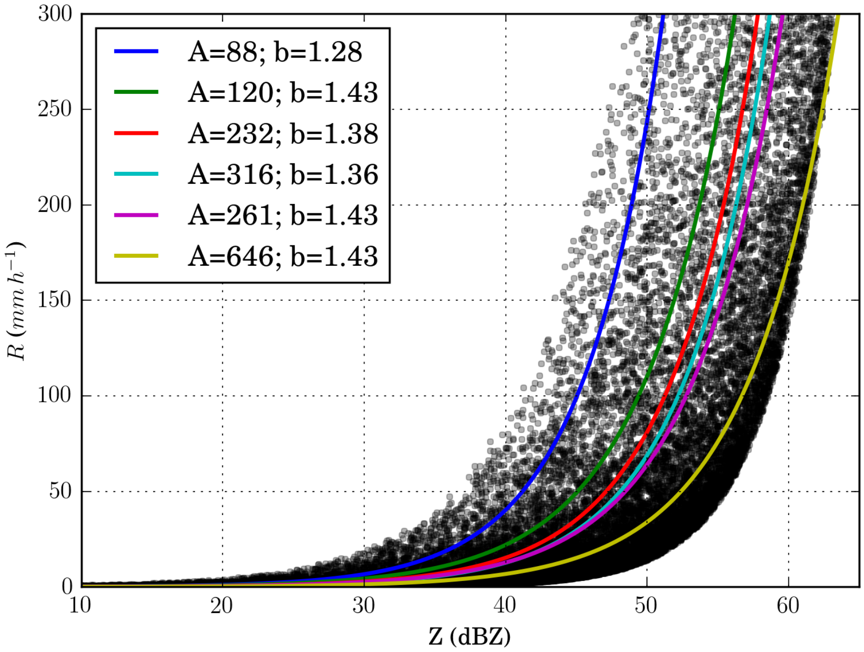

Figure 3.3: The black dots show $Z-R$ relationship for all possible DSDs in Figure 3.2. Overplotted in solid colored lines, different relationships from Rosenfeld and Ulbrich [2003] are shown, labeled with the A and b parameters of Equation 3.64.

3.3.1 *Receiving system*

The receiving system is understood here as the LEO Pol-RO antennas and the receiver. The antennas introduce a differential phase shift and a gain variation that depends on the angle at which the incoming wave reaches the antenna, thus on the relative positions of the LEO and the GPS. For the ROHP-PAZ experiment, the differential phase that is introduced follows a pattern that was measured in an anechoic chamber and it is therefore known, as well as the gain patterns (shown in Figure 2.4).

In addition, the receiver will introduce an arbitrary differential phase between the two polarization ports. The reason is that both ports measure the received phase independently, hence, they are both initialized with an arbitrary phase that is different in the two ports. This implies that an absolute measurement will be impossible to achieve (explained in Section 1.1.1). However, what is needed is the relative difference between the measurements in the region where there is no rain and the ones in the region where rain is expected. The phase difference induced by the receiver is constant during the whole continuous observation (called arch), hence the relative difference will cancel its contribution. Equivalently, the calibration of the receiver offset will be possible when the continuous arch of data starts above the precipitation zone.

3.3.2 *Ionosphere*

The emitted signal from the GPS can be expressed, in the circular basis (see Section 3.1.3.1), as:

$$\mathbf{E}^c = E_0^c \begin{bmatrix} 1 \\ me^{i\Delta} \end{bmatrix}$$

The Δ and the m quantify the deviation of the signal polarization from the RHCP case. It is generally expected that GPS do not emit perfectly circularly polarized waves (i. e. Δ and m are not 0), so those waves can experience a polarimetric phase shift due to the Faraday rotation. The values that Faraday rotation can have are statistically discussed in Section 4.3. Consequently, the measured polarimetric phase shift will have a contribution that comes from the ionospheric effect, and it will depend on the polarimetric purity of the emitting satellite, the ionosphere state, and the alignment between the RO geometry and the Earth magnetic field (as shown in Section 3.1.6).

3.3.3 *Calibration*

To fully characterize the signal and to perform a proper calibration, full knowledge of the antenna pattern, the amplitude and phase of the wave, and the characterization of the wave at the emitter (i. e. Δ and m) would be needed. It is very unlikely that all these parameters can be fully described. However, there is no need of an absolute value to achieve the kind of observable that is aimed here. In this sense, what is required is the difference that the observable has between the region where rain is expected and above it.

Being the receiving system derived errors either known or constant, these are not the most problematic ones. On the other hand, the differential phase shift induced by the ionosphere depends on the polarization state of the wave. Therefore, even though the behaviour of the ionospheric effect can be considered constant (or linear) when the ray scans the lower tropospheric layers, the depolarization by hydrometeors change the effect that the ionosphere has into the wave afterwards. The impact of this effect into the polarimetric observable depends basically on the ionospheric state.

A full dedicated study on proposed calibration algorithms and the separability of the different contributions on the polarimetric observables will be described in [Tomás et al., 2017], and is left out of the scope of this dissertation. In brief, these algorithms will use the amplitude and the phase of both GPS L1 and L2 polarimetric signals to estimate the effect that ionosphere induces to the polarimetric observable. A separation of its contribution is then attempted, so that what remains is the hydrometeor effect. This approach has been shown to be feasible in the performed simulations, which are based on the results presented in Chapter 4.

4 SIMULATIONS

The simulations are one of the most important topics of this thesis. Since precipitation-induced depolarization features of GNSS-RO signals have not been studied before, it is the first time that forward scattering simulations of this kind are performed. The scattering properties of the different hydrometeors that are found in the atmosphere are computed, examined and related to radar observables, with the purpose of validation and anticipation of realistic scenarios for further analysis.

The simulations are performed for four different frequency bands: L1 band, corresponding to GNSS signals; K_u band, corresponding to the TRMM radar and one of the two frequencies used by the GPM radar; K_a band, corresponding to the remaining GPM radar frequency; and W band, corresponding to the CloudSat radar. The computed quantities are used to derive the polarimetric GNSS observables, the radar observables and other values that will be useful for the analysis presented in the following chapters. Afterwards, the collocations between the COSMIC mission and the aforementioned satellites are introduced, and their observables are combined in order to obtain realistic and yet simulated polarimetric measurements.

The effects of the ionosphere into the polarimetric GNSS-RO observables is simulated too. Data from models coincident with the observations is used. The results are stored in a database, which facilitates their analysis in the form of end-to-end simulations. The structure, how it is built and the use of the database is explained at the end of this chapter. The importance of the database recalls in the fact that it can be used as an anticipation of the data that will be provided by the actual satellite, where the identification of systematic errors, building of inverse algorithms, and identification of other issues can be tested.

4.1 FORWARD SCATTERING SIMULATIONS

The computation of the scattering properties related to the different hydrometeors can be done using analytic and computational methods. In this section the suitability of these methods according to each hydrometeor type and to different scenarios is reviewed. The parameters of final interest are all related in a way or another to the real and imaginary parts of the **S** components (defined in Equation 3.28). For example, K_{dp} depends directly on the real part of the copolar components of **S** (see

Equation 3.38), while the signal attenuation is related to the imaginary part of **S** (see Equation 3.39):

$$K_{\mathrm{dp}} = \frac{2\pi}{k_0} \int \Re\{S_{\mathrm{hh}} - S_{\mathrm{vv}}\} N(D) \mathrm{d}D$$

$$A_{\mathrm{dp}} = -8.686 \frac{2\pi}{k_0} \int \Im\{S_{\mathrm{hh}} - S_{\mathrm{vv}}\} N(D) \mathrm{d}D.$$

On the other hand, Z_{e} is proportional to σ_{bk} (see Equation 3.63), that depends on the phase matrix, **Z** (which in turn depends on **S**, see Equation 3.30):

$$\begin{aligned} \sigma^{\mathrm{V}}_{\mathrm{bk}} &= 2\pi \langle \mathbf{Z}_{11} + \mathbf{Z}_{12} + \mathbf{Z}_{21} + \mathbf{Z}_{22} \rangle \\ \sigma^{\mathrm{H}}_{\mathrm{bk}} &= 2\pi \langle \mathbf{Z}_{11} - \mathbf{Z}_{12} - \mathbf{Z}_{21} + \mathbf{Z}_{22} \rangle \end{aligned} \tag{4.1}$$

The methods discussed in this chapter are approximations to solve the electromagnetic scattering equations to obtain **S**. They strongly depend on the particle shape and size with respect to the electromagnetic wavelength, thus the model is also frequency-dependent. In this work, the used frequencies correspond to L, C, K, and W bands. In the case of L band (corresponding to GNSS signals) the interest recall in the horizontal and the vertical co-polar components of **S**. For C, K and W bands, which correspond to the bands used by the precipitation satellites and weather radars, the focus should be on the backscattering cross section, σ_{bk}. For this reason, the computations are performed in a different geometric configuration depending on the situation: for GNSS-RO signals, **S** is computed using forward scattering and horizontal incidence; when thinking about weather radars, the computations are performed using back scattering and horizontal incidence as well, but for satellite radars, the incidence is taken as vertical. This has direct implications in the way the computations are performed, either by changing reference system of the particle or by changing the inputs in the different scattering codes.

4.1.1 *Simulation methods*

4.1.1.1 *Rayleigh scattering*

When the scatterer particles are much smaller than the wavelength, the scattering properties can be described by the Rayleigh approximation [Rayleigh, 1871]. The requirement that a particle equivalent size parameter (χ) has to fulfil to be considered under the Rayleigh regime is

$$\chi = \frac{2\pi a_{\mathrm{eff}}}{\lambda} < 0.1, \tag{4.2}$$

where a_{eff} is the effective radius. Thus, this method is adequate for particles much smaller than the wavelength that are nearly spheric. Considering a raindrop of about 6 mm of effective diameter, interacting with a en electromagnetic wave of wavelength of about 190 mm, corresponds to a $\chi \simeq 0.1$. This is in the limit of the applicability of the Rayleigh approximation, and therefore one has to be cautious.

However, if the particle is suspended in a medium with similar optical properties (so called *soft* particles), the Rayleigh-Gans approximation can be applied [Bohren and Huffman, 1983]. This approximation simplifies the scattering problem and allows the computation of **S** of arbitrary shaped particles, bigger than those allowed by the Rayleigh regime, but that have to fulfil the following requirements:

$$\begin{aligned} |n-1| &\ll 1 \\ kD|n-1| &\ll 1. \end{aligned} \tag{4.3}$$

where n is the refractive index, and k is the wave number $(2\pi/\lambda)$. Being the refractive index of water and ice much larger than 1, is not clear if Rayleigh-Gans approximation should be used in this study. Still, ice particles can be modelled as oblate spheroids with an effective refractive index that is a mixture of ice and air, so it is smaller than that of pure ice and under certain scenarios the simplification can be used. The modelling of ice particles is treated in Section 4.1.2.

The Rayleigh-Gans approximation is based on an extension of the Rayleigh scattering (e. g. Equation 3.26) by introducing a form factor F, that is integrated over the particle volume and accounts for the deviation from the Rayleigh solution [e. g. Bringi and Chandrasekar, 2001]:

$$\begin{aligned} S_{\text{hh}} &= \frac{3k^2}{4\pi} KVF(\theta_s, \theta_i) \\ S_{\text{vv}} &= \frac{3k^2}{4\pi} KVF(\theta_s, \theta_i) \cos(\theta_s) \end{aligned} \tag{4.4}$$

$$F(\theta_s, \theta_i) = \frac{1}{V} \int exp(i\delta(r)) dv, \qquad exp(i\delta(r)) = r \cdot (k^i - k^s) \tag{4.5}$$

where $K = (n^2-1)/(n^2+2)$, r is the position vector of the volume elements and $k^{i,s}$ are the wave vectors for the incident and the scattered fields, respectively. The angles θ_s and θ_i indicate the scattering angle and the incidence angle, respectively. For the specific case of spheroids we obtain:

$$S_{\text{hh,vv}} = \frac{\pi D^3}{6\lambda^2} \frac{1}{L_{\text{hh,vv}} + \dfrac{1}{\epsilon - 1}} \tag{4.6}$$

being ϵ the dielectric constant of the particle and $L_{\text{hh,vv}}$ the depolarization parameters, defined as:

$$L_{\text{vv}} = \frac{1 - L_{\text{hh}}}{2} \tag{4.7}$$

$$L_{\text{hh}} = \frac{1+f^2}{f^2} \left(1 - \frac{\arctan(f)}{f}\right); \qquad f = \sqrt{\frac{b^2}{a^2} - 1} \tag{4.8}$$

for oblate spheroids ($a < b$) and

$$L_{\mathrm{hh}} = \frac{1-e^2}{e^2}\left[\frac{1}{2e}\ln\left(\frac{1-e}{1+e}\right) - 1\right]; \qquad e = \sqrt{1-\frac{b^2}{a^2}} \tag{4.9}$$

for prolate spheroids ($b < a$), where a is the rotation axis and b the axis aligned with the horizon. Further relationships among these quantities and radar observables can be found, for example, in Bringi and Chandrasekar [2001]; Ryzhkov et al. [2011].

The different scenarios and different hydrometeor types will determine the method one should use to compute such quantities. For example, simple approximations like the ones introduced in this subsection may suit when trying to obtain the forward/back scattering cross sections, while they fail to reproduce the polarimetric observations related to the copolar components of the scattering amplitude matrix [e. g. Tyynelä et al., 2013].

4.1.1.2 *Mie scattering*

The Mie scattering provides an analytic solution of the scattering properties of a solid and homogeneous spherical particle. The incident electromagnetic waves are considered to be plane-parallel, and the scattered and internal electromagnetic fields are expressed as spherical wave functions. As well as the Rayleigh approximation, this method fails to reproduce the properties of highly asymmetric particles, i.e. ice crystals, and specially when obtaining the polarimetric quantities. Mie scattering is mainly used when particles can be considered spheric and their size is similar to the wavelength of the incident electromagnetic field. The studies in this dissertation do not include analysis under Mie scattering model.

4.1.1.3 *T-matrix*

The T-matrix method was formulated by Waterman [1965] as a general scattering formulation for non-spherical particles. The most used computational implementation was developed in Mishchenko et al. [1996]. The concept is based on relating the incident and the scattered fields through the **S** matrix, that is determined from surface integrals that depend on the shape of the particles. With the Mishchenko implementation, it is possible to perform scattering calculations for spheroidal, cylindrical and Chebyshev particles. It uses a right handed spherical coordinate system with its origin fixed inside the particle. In the far field region, the electromagnetic wave is given by:

$$\begin{bmatrix} E^{\mathrm{s}}_{\mathrm{h}} \\ E^{\mathrm{s}}_{\mathrm{v}} \end{bmatrix} = \frac{\exp(ikr)}{r}\mathbf{S}(\hat{s},\hat{\imath})\begin{bmatrix} E^{\mathrm{i}}_{\mathrm{h}} \\ E^{\mathrm{i}}_{\mathrm{v}} \end{bmatrix}. \tag{4.10}$$

Here there is introduced the dependence of the **S** on the scattering and incidence directions, and the same convention as in Equation 3.27 is followed. This method is useful and convenient to obtain the amplitude scattering matrix for raindrops, at all the frequencies of interest in this work. However, T-matrix is not suitable for calculations involving ice crystals, since they are arbitrary shaped and highly asymmetric.

All the calculations performed in this thesis using the T-matrix code have been obtained using the *Python* adapted package *pyTmatrix* described in Leinonen [2014], based on Mishchenko implementation and oriented to obtain the most used variables in the weather radar community. This makes the scattering amplitude matrix easy to be obtained.

4.1.1.4 *The Discrete Dipole Approximation*

The Discrete Dipole Approximation (DDA) is a finite representation of a continuous target, by means of discrete dipoles. These dipoles interact with the other dipoles through their electric fields, and are often considered coupled dipoles. On the contrary of the previously mentioned method, which depends on the particle surface, DDA is volume dependent, so it can properly work with arbitrary shaped particles. Its main drawback is the computing time, which can be too high depending on the relationship between the particle size, the number of dipoles used to represent the particle and the wavelength.

Among the DDA implementation codes, two of them are used for this work. These are the DDScat [Draine and Flatau, 2013] and the ADDA [Yurkin and Hoekstra, 2011]. For convenience purposes, the DDScat is used to compute scattering properties for single ice crystals and ADDA is used to perform computations for aggregates of ice particles. The DDScat and ADDA codes use the notation of Bohren and Huffman [1983], so in the far field, the wave is described as:

$$\begin{bmatrix} E_{\mathrm{h}}^{\mathrm{s}} \\ E_{\mathrm{v}}^{\mathrm{s}} \end{bmatrix} = \frac{\exp(ikr)}{-ikr} \begin{bmatrix} S_2 & S_3 \\ S_4 & S_1 \end{bmatrix} \begin{bmatrix} E_{\mathrm{h}}^{\mathrm{i}} \\ E_{\mathrm{v}}^{\mathrm{i}} \end{bmatrix}. \tag{4.11}$$

DDScat does not compute the $\mathbf{S}$ matrix directly, but it provides a matrix called f_{ml} [Draine, 1988] that is related to $\mathbf{S}$ through:

$$f_{11} = iS_2; \qquad f_{12} = -iS_3; \qquad f_{21} = -iS_4; \qquad f_{22} = iS_1 \tag{4.12}$$

In addition, DDScat provides the phase lag factor (Q_{pha}), defined as the change suffered by the phase of the wave propagated through a certain medium with respect to the phase it would have had if propagated in vacuum [Draine, 1988]. This quantity, computed for the vertical and the horizontal components, can be used also to derive the differential phase delay.

As it has been seen, to compare the results among different methods is not straightforward. One important thing to be taken into account is the formalism that is in use, i. e. in which notation (Mishchenko or Bohren) are they based (see Equation 4.10 and Equation 4.11). Thus, some manipulations are needed before any direct comparison of the results provided by the two methods.

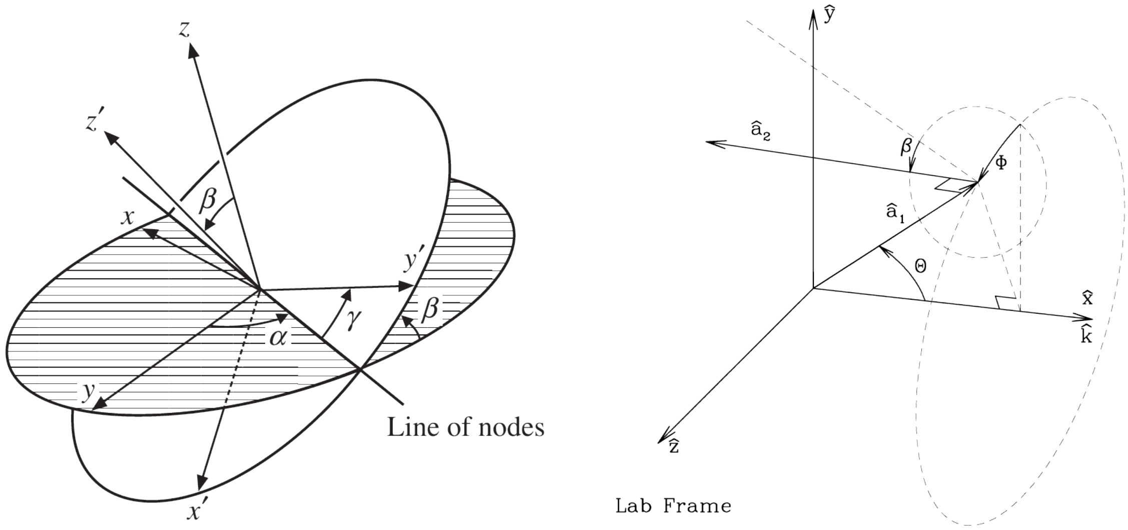

(a) T-matrix (b) DDA

Figure 4.1: Reference frames and rotation angles used by (a) T-matrix code and (b) DDA code. Images adapted from Mishchenko et al. [2002] and Draine and Flatau [2013].

4.1.1.5 *Reference frames*

The reference frames used in the T-matrix code and in the DDA code are different, but are equivalent. The T-matrix works in the Particle frame of reference, and the DDA works in the Lab frame of reference. They are shown in Figure 4.1. For the simulations done in this work, we define two angles that correspond to the particle system of reference: the canting angle and the rotation angle. The canting angle (γ_c) is defined as the tilt angle from the vertical axis of rotation of the particle, which for most of the particles, is the axis of symmetry. Once the particle is tilted a certain canting angle, then the rotation angle (θ_r) is defined as the angle that the particle is rotated around the local vertical axis. Combining this two angles one can obtain all the possible positions of the particle with respect to the incident electromagnetic field.

To obtain such rotations in the reference frames shown in Figure 4.1, a combination of (α, γ, β) for the T-matrix and a combination of (Θ, Φ, β) for the DDA has to be related to each (γ_c, θ_r) pair. In the case of T-matrix, this is easy and it is already implemented in the most used codes. For DDA is a bit more complicated. First, the particle has to be placed taking into account that the wave incidence direction is $\hat{x}$, the horizontal polarization has to lay on the $\hat{x} - \hat{z}$ plane, and the vertical polarization lays on the $\hat{x} - \hat{y}$ plane. Then, the angle Θ can be identified as the canting angle γ_c and the vectors describing the particle orientation can be build using the instructions from the user guide of DDScat [Draine and Flatau, 2013, Eqs. (29) to

(31)]. Once γ_c is fixed, a rotation around $\hat{y}$ has to be applied ($\mathbf{R}(\theta_r)$) to sample all θ_r.

4.1.2 *Particle modelling*

Along with the scattering codes, the particle modelling is fundamental to reproduce the observations. Lots of efforts have been made in order to perform such modelling, from exact representations of the particles to simple representations of the hydrometeors as oblate / prolate spheroids. Here it is extensively reviewed the case of rain drops and ice crystals. Event though they are not so widely used in this work, melting particles (accounting for melting hail and graupel) are also mentioned and a few ideas about their modelling are also given.

4.1.2.1 *Raindrops*

Raindrops have been modelled since rain is remote sensed. The different scattering properties depend on the shape, size, and composition of the particle. Therefore, the expected radar reflectivity due to rain, for example, requires a proper modelling of the raindrops. The raindrop shape is usually modelled as pure liquid water spheroid with a shape that depends on its size. It is expressed as a relationship between the two symmetry axis: the axis ratio. Even though there were attempts to find a shape model for raindrops since back in the 50ths, the first good approximation of the actual raindrop shape appears in Pruppacher and Beard [1970], that used a wind tunnel to study water drops suspended in an air stream. Later, Beard and Chuang [1987] proposed an equilibrium model based on numerical computations of the hydrostatic balance between the external aerodynamic pressure and the internal pressure. Their model can be expressed, in terms of the axis ratio, as follows:

$$\begin{aligned}\frac{b}{a} =& 1.0048 + 5.7\times10^{-4}D - 2.628\times10^{-2}D^2 + 3.682\times10^{-3}D^3 \\ &-1.677\times10^{-4}D^4.\end{aligned} \tag{4.13}$$

being a the semi major axis, b the semi minor axis, and D is the equivolumetric diameter. This is the most widely used model for raindrop shapes, in agreement with most of the newest evaluations of the raindrop axis ratio [Beard et al., 2010]. In Figure 4.2 the equilibrium drop shape model of Beard-Chuang is shown (left), and comparisons with more recent measurements, like wind-tunnel experiments and 2 Dimensional Video Disdrometer (2DVD) measurements [Thurai et al., 2009] are shown in the right panel.

Rain drops tend to align parallel to the horizon when they fall. Nevertheless, when wind shear is present, the drops could be tilted. This effect is called canting and is quantified by γ_c (see Section 4.1.1.5). Field measurements have set the γ_c

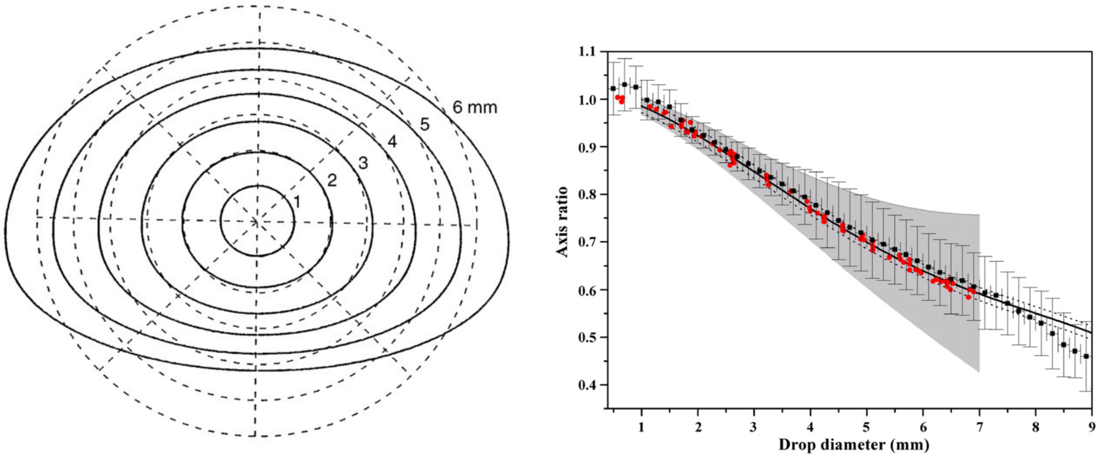

Figure 4.2: (Left) Equilibrium drop shape from Beard and Chuang [1987]. (Right) Mean axis ratio as a function of drop diameter from wind tunnel experiment (red dots) and the 2DVD measurements (black dots) from Thurai et al. [2009]. The shaded area represents the drop oscillations from the wind-tunnel data, and the vertical bars ($pm1\sigma$) represent the standard deviation of the 2DVD axis ratio distributions. The small horizontal bars represent the bin width of the 2DVD interval. The solid line is the Beard-Chuang model axis ratio and the dotted lines are the upper and lower bounds. Image adapted from Thurai et al. [2009].

to be within $\pm 2.25°$, supported by the 82% of the observations [Wang, 2013]. As convention, the γ_c distribution is assumed to have a Gaussian form, with mean $0°$ and a standard deviation around $\sim 7°$ [Beard et al., 2010]. Another effect that raindrops can undergo is oscillation, but it is not taken into account in this study. This effect could have implications in varying the axis ratio as a function of diameter, but only in less than a 10% of the cases a noticeable deviation is observed [Thurai et al., 2014]. In addition, its effect into the polarimetric observables might not be so relevant, since their expressions are at the end depending on the mean axis ratio versus diameter function, and are independent of the variance of the axis ratio distribution [Bringi and Chandrasekar, 2001].

The mentioned characteristics are driving the interaction between electromagnetic waves and raindrops. One last property important in this interaction is the complex water permittivity. For this study, the Liebe et al. [1991] model is used for water particles.

4.1.2.2 *Ice crystals*

Modelling of atmospheric ice particles has become a challenge for the last decades. The single-pure ice crystals are very thin, with a high axis ratio, and therefore computations using the T-matrix code are not possible. This leads to two solutions: (1) to compute the scattering properties approximating the ice particles as oblate spheroids composed of a mixture of ice and air, using the Rayleigh-Gans method; or (2) to compute the exact scattering problem using the DDA method and realistic ice crystal models. The main inconvenient for the former is that it is only possible to do so for a range of sizes and frequencies, and that the density, axis ratio and dielectric properties have to be carefully estimated. On the other hand, the second solution involves huge computing times and the need of having exact particle shapes.

A good approach on the approximation of ice particle as spheroids and computations of radar observables can be found in Ryzhkov et al. [2011]. However, their study only contains particles of an axis ratio larger than 0.6 (as they can compare the approximations with T-matrix computations). Here, the DDA method and realistic particle shapes have been used in order to derive the scattering properties of ice.

Ice crystals shapes

As it is been said, to perform the computations with the DDA method, exact particle shapes are needed. The particles have to be described by discrete dipoles, distributed into a grid. The dipole sizes, the dielectric constant and the wavelength have to fulfil the following requirement to ensure the convergence of the method:

$$|n|kd < 1.0 \tag{4.14}$$

where n is the refractive index, k is the wavenumber and d is the diameter of the dipoles [Draine and Flatau, 1994]. In this study, two groups of particles have been used. On one hand there are the single crystals: needles, bullet rosettes, hexagonal plates, and dendrites; on the other hand, there are the aggregated particles. To model the first group, the scripts provided by Dr. Liu and R. Honeyager, detailed in Liu [2008], have been used. Some of the used particles are sketched in Figure 4.3. The choice of these particles is based on the literature, where the results of several experimental campaigns of in-situ collection of ice particles can be found [e. g. Iwai, 1989; Heymsfield et al., 2002a; Bailey and Hallett, 2009; Cotton et al., 2013]. Also, they are relatively easy to model.

As for the aggregates, they have been constructed using a code provided by Y. Leinonen, in the way described in Leinonen [2013]; Leinonen and Moisseev [2015]. The dendritic aggregates have been chosen as representatives of the most common aggregate particles [Leinonen and Szyrmer, 2015], and are the ones used in the present scattering computations. Some aggregates are sketched in Figure 4.4. In the growth process of the aggregates, an orientation of the primitive particles is assumed. They are assumed to fall with its longest axis oriented horizontally (parallel to the horizon), and they encounter other particles to form the aggregate. The number of primitive particles in each aggregate determines the maximum dimension of the final aggregate. A binned range of dimensions has been populated with a large number of aggregates, to have enough statistics to avoid the rotation averaging. Since the growth of the aggregates includes a certain degree of randomness,

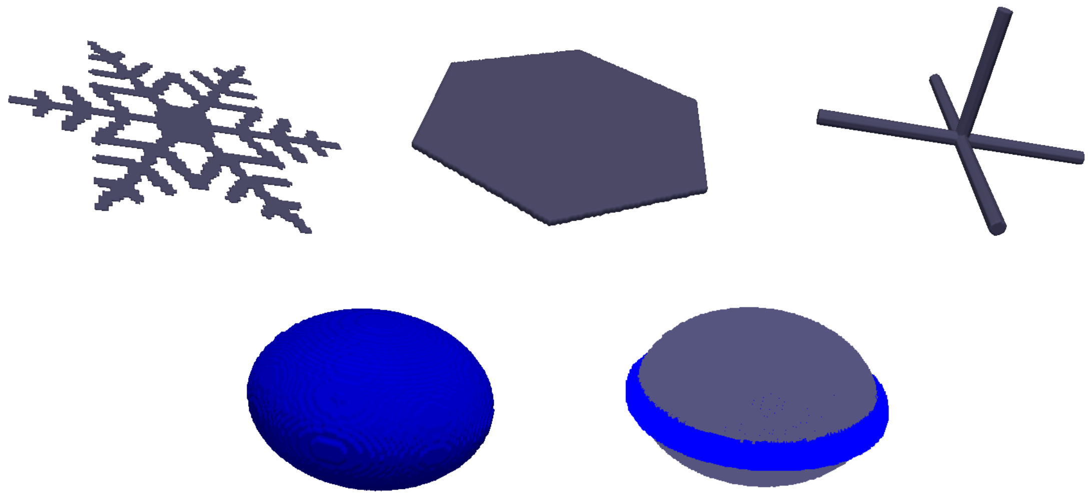

Figure 4.3: Images of the particle shapes used for the scattering simulations with DDA. Top row: dendrite, hexagonal plate and bullet rosette; bottom row: raindrop represented as a water ellipsoid, and a melting hail particle. The blue color indicates liquid water phase, and gray corresponds to pristine ice. Images not to scale.

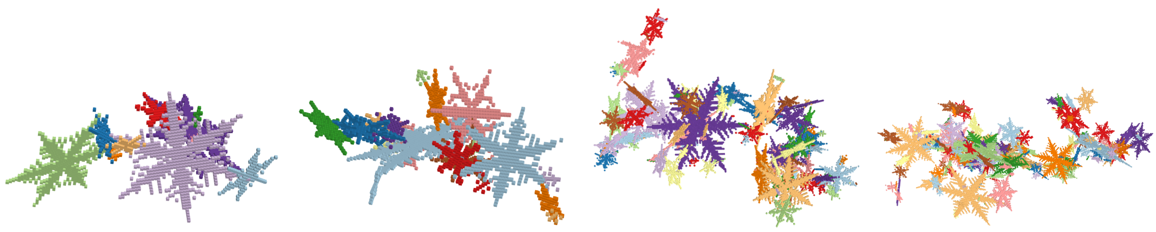

Figure 4.4: Images of the dendritic aggregates used in the scattering simulations with DDA. From left to right, aggregates formed by 10, 25, 130 and 200 single dendrites, respectively. Images not to scale.

it is considered that when the fixed range of diameters is fully populated, their averaged scattering properties represent good enough the population.

Distribution of shapes as a function of temperature

In order to reproduce the satellite / radar measurements of ice reflectivity and the related quantities, the distribution of the particle shapes must be taken into account. Different particles have different radiative outputs. The distribution, although not solely, depends on the temperature. Smaller particles are considered to be dominant in very low temperatures, while bigger are dominant near freezing level, with a peak of maximum sizes of plate-like particles between $-15°C$ and $-20°C$ [Libbrecht, 2005]. Most of the studies stating or using relationships between

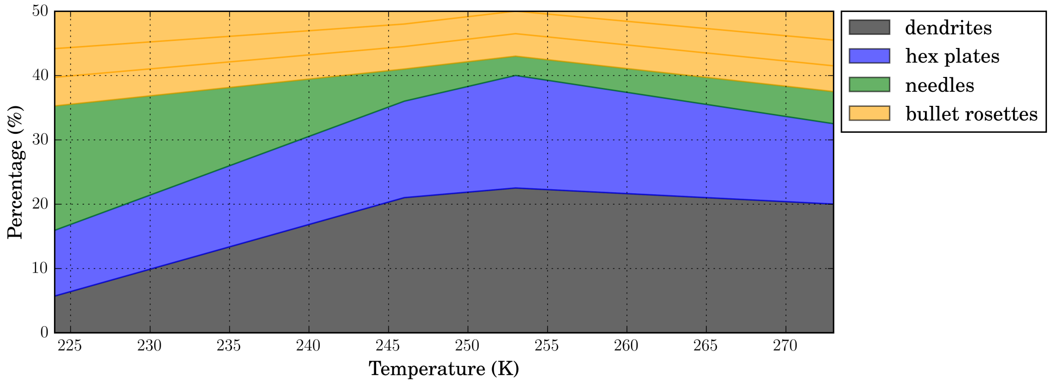

Figure 4.5: Diagram of the distribution of ice habits considered at each temperature. As the temperature decreases, the needle shaped particles and bullet rosettes become dominant. Between 250 and 260 K there is the region where plate-like particles dominate.

temperature and particles shapes and sizes are qualitative rather than quantitative. See for example the habit diagrams in Bailey and Hallett [2009] or the observations of Noel et al. [2006] and Kennedy and Rutledge [2011]. A more quantitative study of this kind can be found in Yoshida et al. [2010]. Following the results in the aforementioned references, an arbitrary relationship between the ice habits and temperature has been constructed. It is shown in Figure 4.5. In addition to the crystal habits shown in Figure 4.5, there is assumed that the 50% of the crystals at all temperatures are in the form of aggregates. The ice particles shape and size are only considered here to depend on the temperature, and dependence on other parameters like humidity or water vapour saturation is not taken into account.

Orientation of the particles

Infer whether ice particles are horizontally or randomly oriented is a complete field of study by itself. Horizontally oriented crystals have implications on the radiative processes in clouds. For example, differences of the order of 40% are reported in the cloud albedo (i.e. the total reflected radiation) between regions with horizontally oriented crystals and regions where ice crystals are randomly oriented [Hirakata et al., 2014]. There is no consensus in the amount of ice that is horizontally oriented with respect to that with no preferable orientation. However, it seems clear that in warm clouds ($-30°C < T < -10°C$) these preferential orientation occurs, and the fractions reported vary from 30% to almost 90% of the total ice, depending also on the latitude [Bréon and Dubrulle, 2004; Noel and Chepfer, 2010; Zhou et al., 2013]. Is therefore common to assume that ice particles are horizontally oriented, even in convective storms in the presence of turbulence (Hubbert et al. [2014] and references therein).

In this study, the orientation of the particles has a critical implication: if the particles are not horizontally oriented, no positive polarimetric phase shift is expected. The effect into the K_{dp} of a region of randomly oriented ice crystals would cancel out, showing no significant phase shift. There exist also the case where the particles can induce a negative K_{dp}: in the presence of very strong electric fields. Negative small K_{dp} regions have been reported either in a time varying scenario [e. g. Caylor and Chandrasekar, 1996], or in the middle of a larger positive K_{dp} region [e. g. Hubbert et al., 2014]. However, vertical alignment happens only in smaller particles in most of the cases, and therefore in a mixture of large horizontal oriented particles and smaller vertical oriented particles, its effect is easily masked [Carey et al., 2009]. The effect of vertical aligned ice crystals is not going to be taken into account in the simulations (where mainly horizontal orientation is assumed), but is something that has to be taken into account when analysing real measurements.

4.1.2.3 *Melting particles*

While hail and graupel are usually assumed to produce a low signature in K_{dp}, due to their nearly spheric and irregular shape, the case may be different when these particles undergo a melting process [Straka et al., 2000; Dolan et al., 2013]. During the melting, a water torus shaped shell can appear around the frozen particle, modifying the dielectric properties of the particle and decreasing its axis ratio. This model, first stated in Rasmussen and Heymsfield [1987], has been used for simple calculations of the melting hail polarimetric signatures [e. g. Ryzhkov et al., 2013; Dolan et al., 2013; Thurai et al., 2015], and could imply an enhancement of the K_{dp} under certain scenarios. Also observations from polarimetric radar support this theory [e. g. May et al., 2001].

In this study, melting particles are modelled using two concentric ellipsoids, the inner one composed entirely by ice, and the outer one by water, trying to emulate the torus shaped form of Rasmussen and Heymsfield [1987]. The axis ratio is ranged from 0.4 to 0.8, and their size from 1 to 10 mm. An example of a melting particle is shown in Figure 4.3, in the bottom - right side. However, melting particles are not used in the large scale simulations, and are only included when examining singular cases like in the case of the field campaign data. This is due to the difficulty of assigning these kind of particles to a scenario defined only by single polarization reflectivity measurements, which will be the case when using data from satellite-based radars.

4.1.3 *Simulation results*

4.1.3.1 *Validation of the different methods*

In order to compare the performance of some of the different codes mentioned above, a simple exercise has been performed. The backscattering cross section and

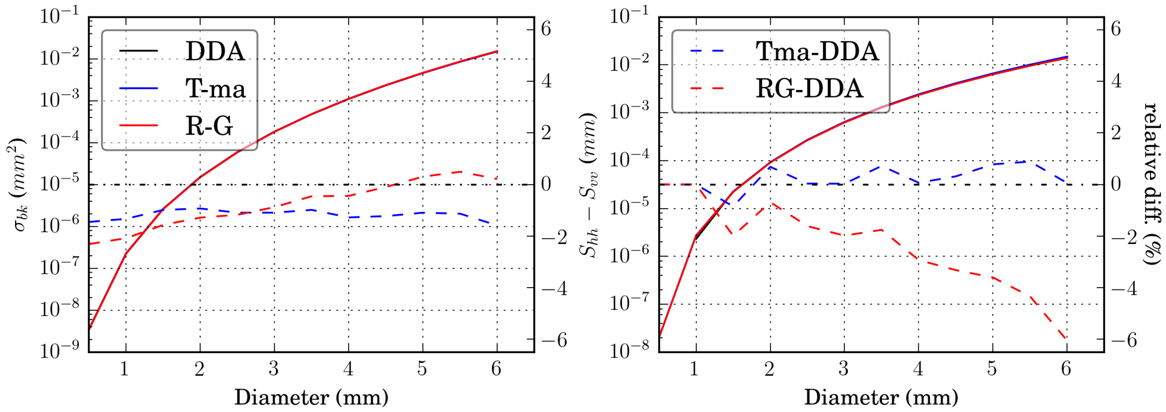

Figure 4.6: Results of the comparison among different scattering methods using L band frequency for a water drop. (Left) The backscattering cross section as a function of the equivalent diameter. The dashed lines correspond to the relative difference between the T-matrix and the DDA (blue) and the Rayleigh-Gans and the DDA (red). (Right) The same as left panel, but for the real part of the horizontal minus the vertical component of the scattering amplitude matrix.

the horizontal and vertical components of the scattering amplitude matrix for a water drop have been computed using the T-matrix code, the DDScat code and the Rayleigh-Gans approximation. The frequency used in this exercise is L1 band. Results are shown in Figure 4.6. It can be seen that for the σ_{bk}, the results obtained through the different methods are very close to each other (relative differences smaller than a 2%) for all particle diameters. On the other hand, for the $S_{\mathrm{hh}} - S_{\mathrm{vv}}$ it can be seen how the results for the Rayleigh-Gans approximation are worse as the diameter of the particle increases. This is something expected seeing Equation 4.2 and Equation 4.3, and it is the reason to use the T-matrix code instead of the Rayleigh-Gans approximation. Since the results of the T-matrix and DDA are so similar, and being the DDA method more computer resource consuming, the T-matrix is the method that is finally used for water drops simulations.

4.1.3.2 *Results for single particles*

The **S** for individual particles is simulated. The results are then used, together with the DSD, to obtain the desired observables (e. g. Equation 3.38, Equation 3.39 and Equation 3.63). The results for the single scattering simulations are shown in this subsection. They are performed using all the possible orientations, i.e. (γ_c, θ_r) ranging from 0 to 90 degrees and taking advantage of the symmetry properties to save computing time. Once **S** is computed for all orientations, there is assumed that the particles can have a certain canting angle, but they are randomly distributed along the rotation angle. Therefore, results are averaged for all θ_r for each γ_c. This procedure can be seen in Figure 4.7, for the case of a dendritic shaped particle.

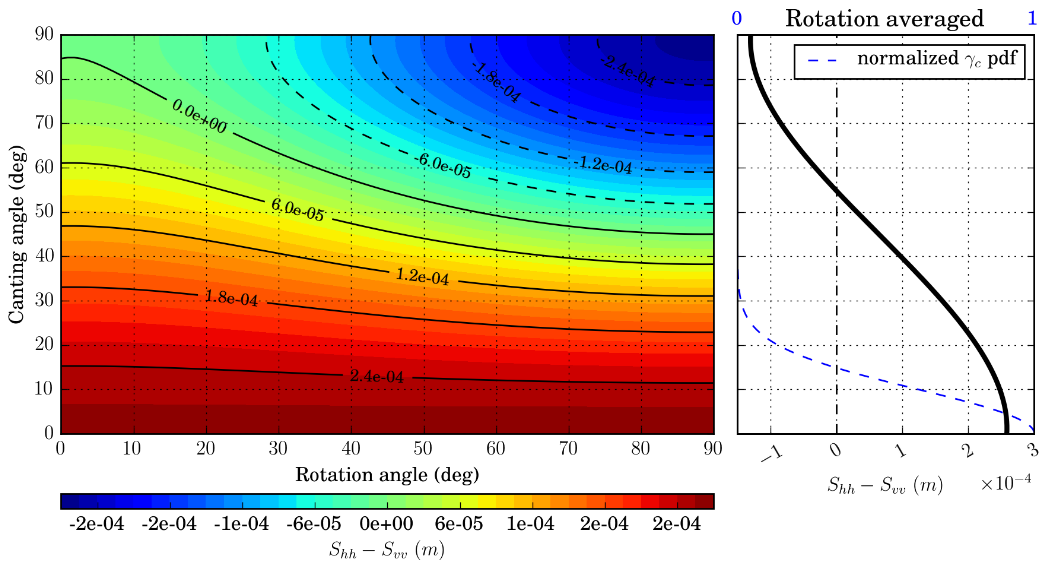

Figure 4.7: Results for the scattering computations over a dendrite shaped ice particle of 838.29 μm of effective radi. (Left) Results for $S_{\text{hh}} - S_{\text{vv}}$ (colorscale) as a function of rotation angle and canting angle. (Right) The rotation averaged $S_{\text{hh}} - S_{\text{vv}}$ as a function of canting angle (bottom axis) and the normalized gaussian γ_c distribution ($\langle\gamma_c\rangle = 0$; $\sigma_{\gamma_c} = 10$) used for weighting the $S_{\text{hh}} - S_{\text{vv}}$ results (blue, top axis).

Even though **S** is computed for all possible orientations, in this work there is assumed that particles tend to fall horizontally oriented, i. e. with its long axis parallel to the horizon. So, computations are performed for a mean canting angle of 0° with a standard deviation of 10°, which is lightly over-conservative with respect to that mentioned in Section 4.1.2.1. For computations involving quantities that will be needed for the GNSS observables, the propagation will be in forward scattering configuration and the incidence will be horizontal. Therefore the results of $S_{\text{hh}} - S_{\text{vv}}$ for L1 band are obtained using this configuration. On the other hand, the values needed for the radar observables will be obtained using a back-scattering propagation and a vertical incidence, since the results in this section are for satellite based radars that obtain their measurements through a nadir-looking radar. This latter configuration is used for the σ_{bk} results shown along this subsection.

Results for this configuration for water droplets are shown in Figure 4.8. In the left panel, the results for the $S_{\text{hh}} - S_{\text{vv}}$ (L1; horizontal; forward-scattering configuration) are presented. It can be seen how for small effective diameters, the contribution to $S_{\text{hh}} - S_{\text{vv}}$ is very low, because small droplets are nearly spherical (see Equation 4.13). As the diameter increases, $S_{\text{hh}} - S_{\text{vv}}$ increases as well. In the right panel there is shown the results for the σ_{bk} for three different frequency bands (K_u, K_a and W; vertical; back-scattering configuration).

Similar computations are performed for ice particles. In figure Figure 4.9 there are shown the results for $S_{\text{hh}} - S_{\text{vv}}$ (top row) and for σ_{bk} (bottom row), using the

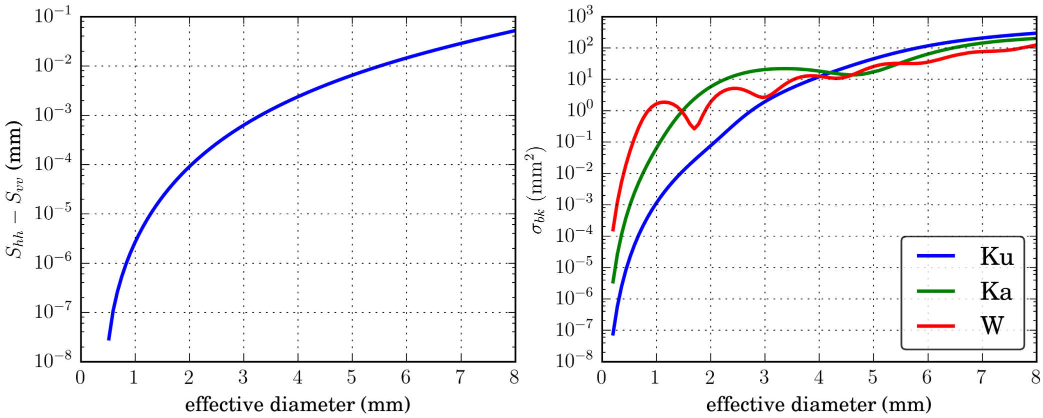

Figure 4.8: Results for (left) $S_{\mathrm{hh}} - S_{\mathrm{vv}}$ and (right) σ_{bk} for a water drop, as a function of the effective diameter. For the left panel, results are obtained using L1 band frequency and a forward scattering and horizontal propagation. For the results in the right panel, K_u, K_a and W frequency bands are used, in a back-scattering and vertical propagation.

same configuration criteria as above. The $S_{\mathrm{hh}} - S_{\mathrm{vv}}$ results show how the particles that contribute the most are the plate-like shaped particles (dendrites and hexagonal plates). The reason is that these kind of particles are very asymmetric. On the other hand, aggregates contribute less than the plate-like particles, since they are rather irregular in shape, while their contribution is larger for nadir radar configurations as the effective area from nadir is rather large. Aggregates are also less dense because the aggregation process leaves empty space between the particles that form the aggregate. Needle shaped particles are the ones that contribute the less, since they are very small. The results for σ_{bk} are frequency and shape dependent, as it can be seen in the results for the different frequency bands (bottom row).

4.1.3.3 *From single scattering to radar observables*

The scattering results shown in the previous subsection account for individual particles. The results depend on the shape and the size of the particle used in the computations. However, in a precipitation event there are many particles, and they are distributed by shape according to the particle distribution and by size according to the particle size distribution. Through the particle size distribution is how the scattering properties are related to the observables. This is specified in Equation 3.38 and Equation 3.63 for the cases of K_{dp} and Z_{e}, which are two of the main observables of interest in this work. A perfect scenario for these assessment and simulation studies would be to relate the Z_{e} measurements of the clouds and precipitation radars to the K_{dp} that would finally produce the $\Delta\Phi$ that a GNSS polarimetric receiver would measure. As it can be seen in Section 1.3.3.1, this is not straightforward.

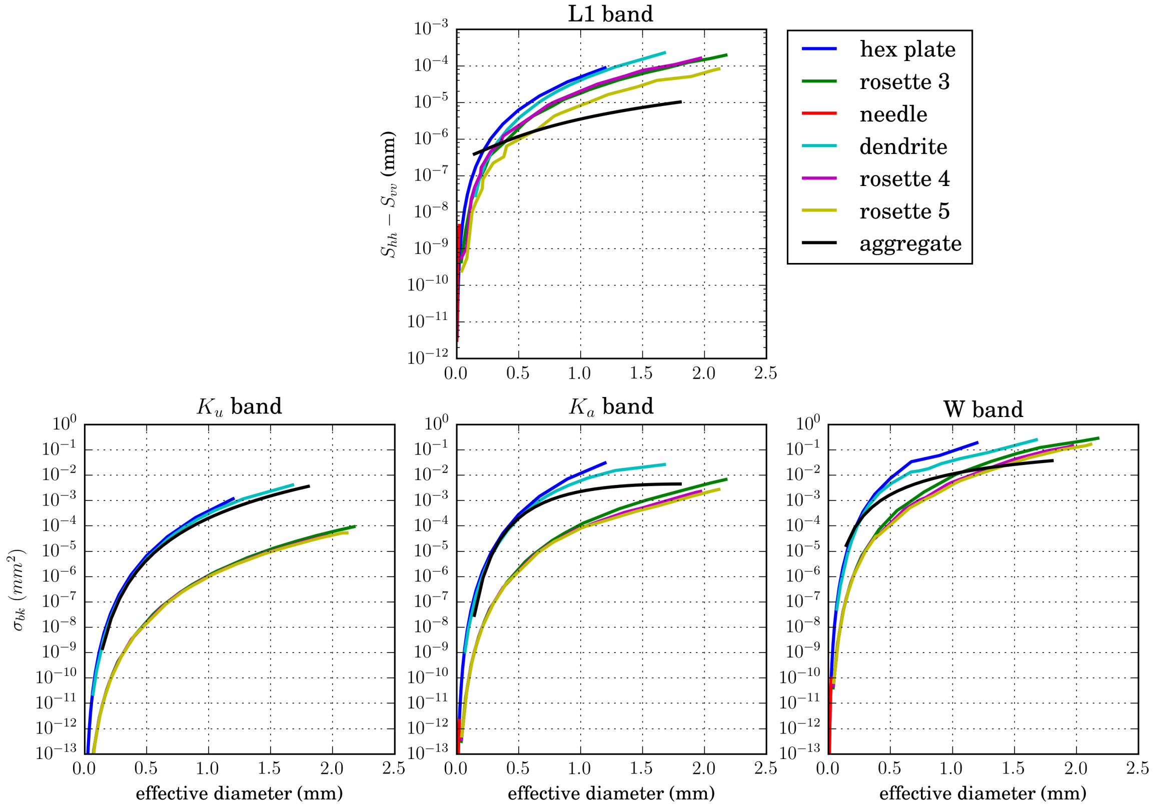

Figure 4.9: Results for (top) $S_{\mathrm{hh}} - S_{\mathrm{vv}}$ and (bottom) σ_{bk} for several ice particles, as a function of the effective diameter. For the top row, results are obtained using L1 band frequency and a forward scattering and horizontal propagation. For the results in the bottom row, from left to right, K_u, K_a and W frequency bands are used, in a back-scattering and vertical propagation.

Since a unique particle size distribution does not exist, a set of random mathematically possible PSDs are built (see Section 3.2.2). Using these distributions one can obtain the $Z_{\mathrm{e}} - K_{\mathrm{dp}}$ relationships under very different scenarios. The results for rain drops are shown in Figure 4.10 and the results for all the ice particles are shown in Figure 4.11. These results are obtained for the three different frequency bands that are recurrently being used in this work. It can be seen in these figures the variability introduced by the different distributions, so that for each value of Z_{e} one can find a wide range of K_{dp} values.

4.1.3.4 *Derived quantities*

Water content can be derived from the particle size distribution, and it is more physically meaningful than the Z_{e}. Therefore, a relationship between WC and K_{dp} would be ideal for this work. But like the $Z_{\mathrm{e}} - K_{\mathrm{dp}}$ relationship, this one is not easy to be obtained. Using the same method as in the previous subsection, a set of particle size distributions is built, and the LWC and the IWC for rain and ice

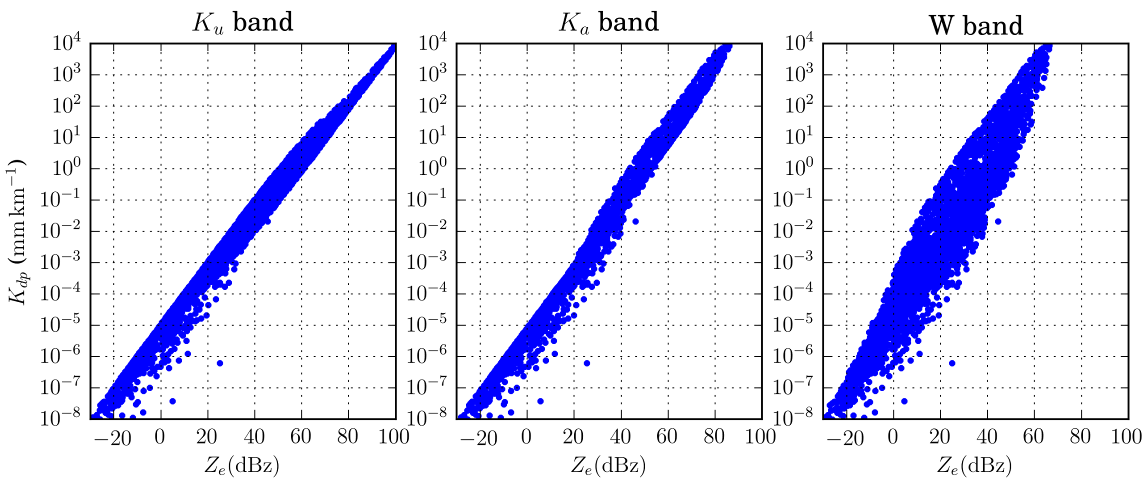

Figure 4.10: Relationship between the backscattering Z_e for K_u, K_a and W frequency bands and the forward scattering K_{dp} for L1 band and for water drops. Results obtained using several random mathematically possible drop size distributions.

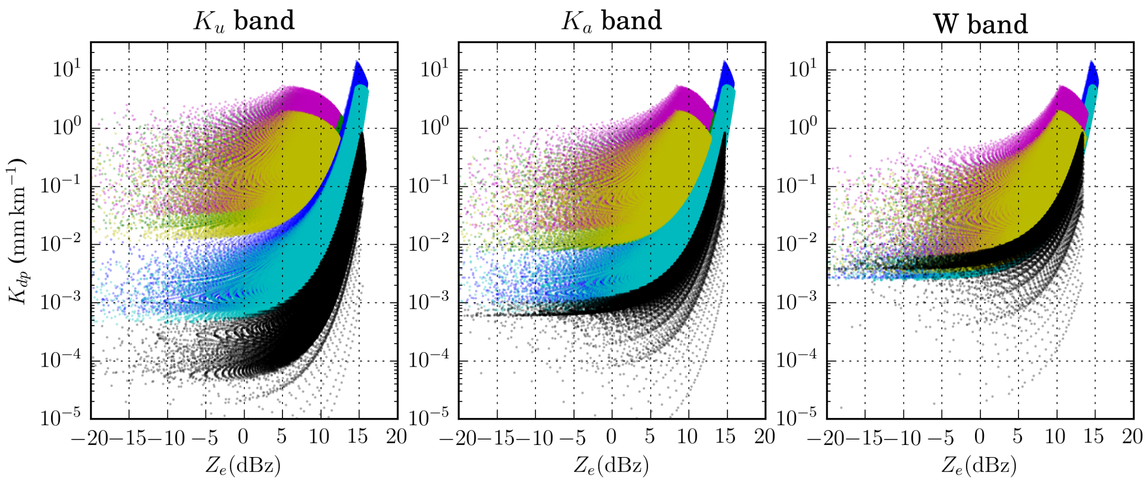

Figure 4.11: Relationship between the backscattering Z_e for K_u, K_a and W frequency bands and the forward scattering K_{dp} for L1 band and for the different ice particles. Results obtained using several random mathematically possible particle size distributions. Same colorscale as in Figure 4.9.

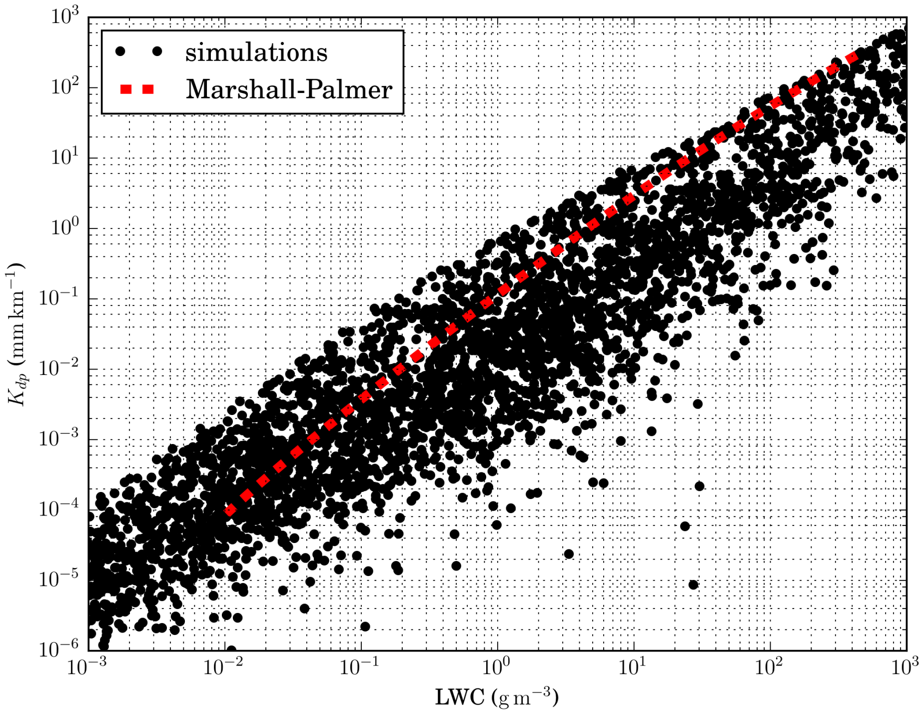

Figure 4.12: Relationship between the LWC and the K_{dp} for water drops, using the same drop size distributions as in Figure 4.10. In addition to the simulated data, the relationship using the Marshall-Palmer drop size distribution is plotted for comparison.

particles are derived. Results of the resulting relationship between LWC / IWC and K_{dp} are shown in Figure 4.12 and Figure 4.13. The $LWC - K_{\mathrm{dp}}$ relationship shows a large variability depending on the chosen drop size distribution, where K_{dp} can range two orders of magnitude for a fixed LWC. For comparison purposes, the relationship that would be obtained using the Marshall-Palmer DSD is overplotted in red.

For ice particles, the $IWC - K_{\mathrm{dp}}$ relationship is shown in Figure 4.13. There is shown in orange the results obtained using an ensemble of different particles distributed according to the chart shown in Figure 4.5, for a temperature that has been randomly chosen within the range shown in Figure 4.5 for each of the simulated points. In addition, in green there are the results if only dendrites were present. As explained in Figure 4.9, plate-like are the ones that contribute the most to the K_{dp}. In addition, as a proxy of the performed simulations, the theoretical relationship derived in Bringi and Chandrasekar [2001], and used, for example, in Kennedy and Rutledge [2011] is overplotted, for particles with an axis ratio of 0.1 and for 0.9. This theoretical relationship works for plate-like particles, horizontally oriented and under the Rayleigh regime, which is the case for L1 frequency band. The simulations performed here using realistic particle shapes agree quite well with the theoretical

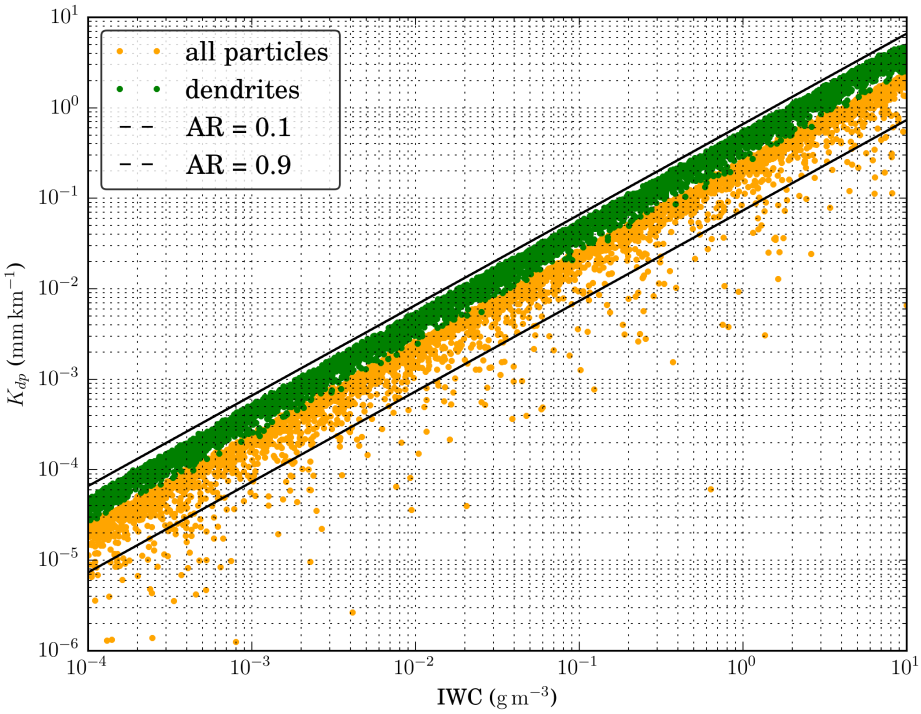

Figure 4.13: Relationship between the IWC and the K_{dp} for ice particles. In orange, results using all the mentioned ice particles, in green the results using only dendrites. Temperature is randomly chosen for each of the simulated points, and then the different shapes are distributed accoring to Figure 4.5. The black lines are the top and bottom limits, corresponding to axis ratios of 0.1 and 0.9, respectively, of the results obtained using the IWC - K_{dp} relationship for plate-like ice particles from Bringi and Chandrasekar [2001]; Kennedy and Rutledge [2011].

relationship. However, different axis ratios can induce a difference in the K_{dp} of about one order of magnitude.

It is also necessary to explore the effect of clouds and precipitation into other observables, such as the excess phase and the attenuation that hydrometeors are inducing to the RHCP signals. The excess phase is defined in Equation 3.43 and the signal attenuation is defined in Equation 3.44. Results of signal attenuation as a function of the water content, both for rain and for ice particles is shown in Figure 4.14 (black and red dots, respectively). These results show that the attenuation due to rain and ice particles is small, and can be neglected under most of the scenarios. It is also shown in Figure 4.14 the differential attenuation between the horizontal and the vertical polarization (defined in Equation 3.39), which is very small as well. With the given sensitivity of the antennas and receivers, would not be possible to detect such small differential effects, and therefore attenuation is not taken into account in following analysis.

The excess phase due to hydrometeors is defined as the extra delay that is induced into the RHCP GNSS signal, solely caused by the hydrometeors. In Fig-

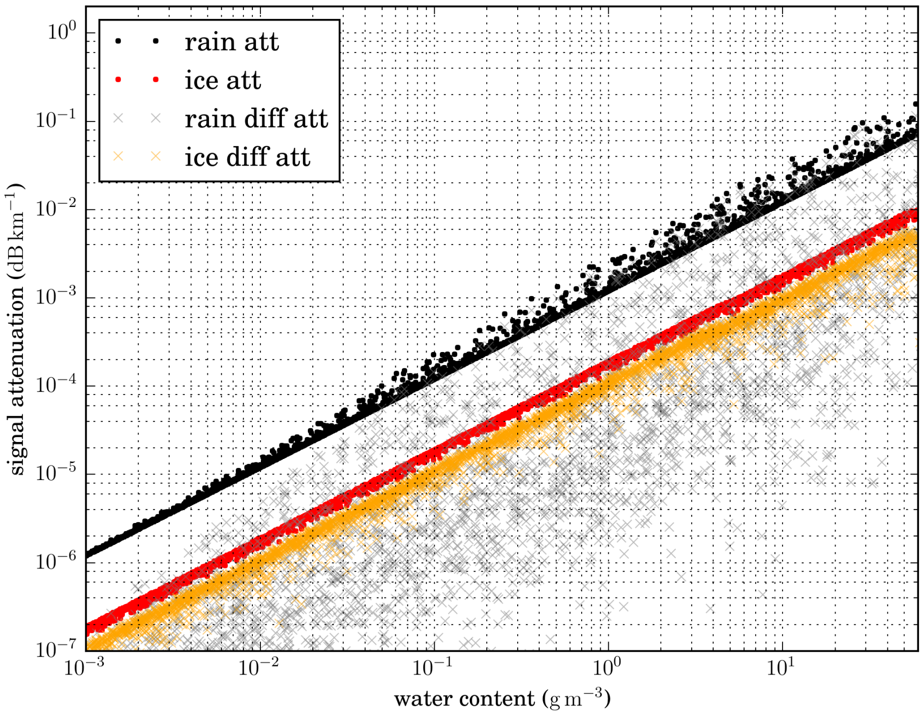

Figure 4.14: Relationship between the WC and the L1 RHCP signal attenuation for rain drops (black dots) and ice particles (red dots). It is also represented the differential attenuation for rain drops (gray crosses) and for ice particles (orange crosses). The observables are generated using the same procedure as in Figure 4.10 and Figure 4.13

ure 4.15 there is shown the relationship between the water content and the excess phase caused by the hydrometeors (rain drops in black and ice particles in blue) into the RHCP GNSS signals. If it is compared to Figure 4.12 it can be seen that the hydrometeor rain-induced phase excess can be up to one order of magnitude larger than the polarimetric differential one. One could then consider the total excess phase as the RO observable for precipitation, rather than the polarimetric shift. However, it is difficult to identify this quantity as a direct observable since it is not possible to distinguish it from the delay caused by the atmospheric density. Yet, it is important to quantify it because it is affecting the standard RO, and therefore can have an impact into the standard retrievals. How the excess phase caused by hydrometeors is affecting the standard RO retrievals and which is the impact that it has is examined in Section 6.1.

Looking at the results of this subsection, there is one conclusion that can be extracted. There exists a large variability when trying to relate the derived quantities, such as LWC, IWC, etc., with the polarimetric and non-polarimetric observables. This variability comes from the multiple particle size distributions that can be used, and is a problem that is not easy to solve. As seen in the introduction, there is a lot of dedicated studies trying to derive and parametrize the microphysics of clouds

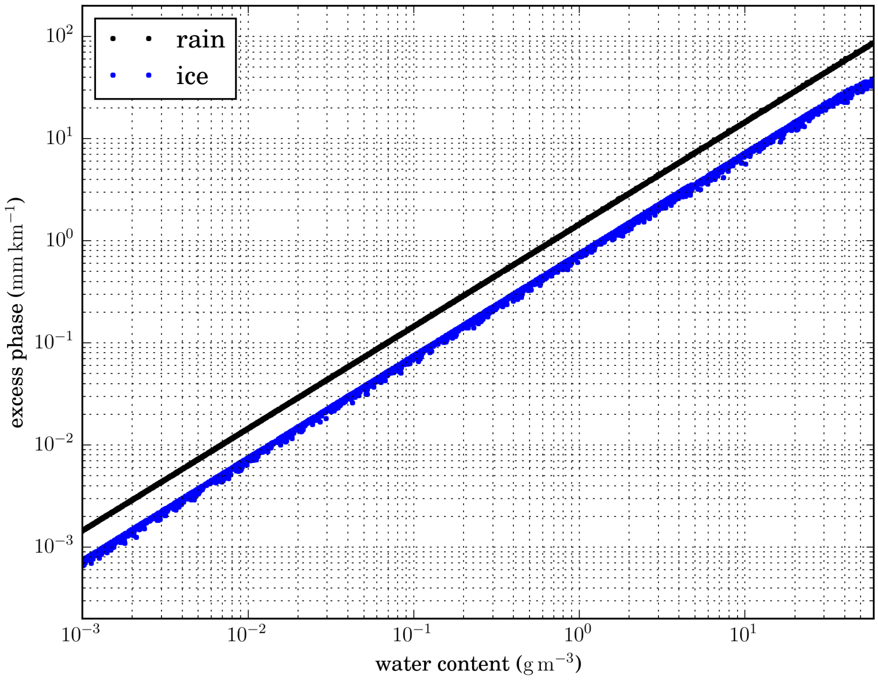

Figure 4.15: Relationship between the WC and the excess phase relationship for a RHCP signal at L1 frequency band, caused by rain (black) and ice particles (blue). The observables are generated using the same procedure as in Figure 4.10 and Figure 4.13

and precipitation, and one key step is to obtain the parameters of the particle size distribution. It is therefore outside the scope of this work to deal with issues that can arise from a certain choice of the particle size distribution. In the cases where satellite data is used, the PSD provided by the mission retrievals is going to be used, with the procedure explained in Section 4.2.1. When this information is not available, a certain variability due to different choices of the PSD has to be assumed.

Besides the choice of the particle size distribution, the percentage of horizontally oriented particles with respect that those that are not is also critical, mainly for the ice particles. The results shown here assume that all particles are horizontally oriented, which could not be the case for many scenarios. Then, a scaling factor should be included (accounting for the percentage of horizontally oriented particles), and the results for the K_{dp} have to be used as an upper bound of its maximum magnitude. The amount of horizontally oriented particles is usually not known, and for instance, is not provided by the CloudSat satellite. The K_{dp} is the observable that is most sensitive to the orientation of the particles, while the other observables (Z_e, phase delay, attenuation) are mainly sensitive to the total amount of particles. In Table 4.1 there is summarized the reliability of the simulations, taking into account how the simulations are performed and the assumptions that have been made.

	Rain	Ice particles
K_{dp}	Reliable	Upper bound
Z_e	Reliable	Reliable
Phase delay	Reliable	Reliable
Attenuation	Reliable	Reliable

Table 4.1: Observables and their reliability according the simulations and their assumptions.

4.1.3.5 *Multi-frequency comparison*

GNSS satellites operate at L2 and L5 frequency bands in addition to L1. The possibility of having extra measurements for these frequencies of the same events is in principle an advantage. However, since the scattering happens within the Rayleigh regime for all these three frequency bands, the scattering results are linearly dependent on the frequency, and therefore is difficult to extract information about the particle size distribution or other precipitation quantities using combinations among the frequency bands. In Figure 4.16 it can be seen the ratio between the K_{dp} obtained at L1 and L2, and the ratio between the K_{dp} obtained at L1 and L5, as a function of the liquid water content. For comparison, in the top panel there are plotted also other combinations using higher frequency bands.

These results show how for lower and closer frequencies, the deviations from the ratio between wavelengths (red dashed lines in Figure 4.16) is smaller, and when the frequency is increased, more dispersion is observed. This is an expected behaviour when the scattering of one of the frequency bands is happening outside the Rayleigh regime. When observing the results for the K_{dp} ratio between L1 and L2, and L1 and L5, it can be seen how the ratio starts to differ from the wavelength ratio when the LWC is high. This is a due to the large drops that start to dominate in the high liquid water content. However, differences are small enough to be considered in the Rayleigh regime (less than a 2%).

4.2 COLLOCATIONS

With the aim of performing realistic end to end simulations, a collocation exercise between the COSMIC mission and TRMM, GPM and CloudSat missions has been performed. From the COSMIC standard RO retrievals one can obtain actual measured values, such excess phase, signal to noise ratio, accurate satellite positions for ray-tracing purposes, etc. These products, together with the precipitation and clouds observations, can be used to simulate the polarimetric observables that PAZ satellite will obtain, with the added value of having real precipitation measurements. The reason to use COSMIC is the huge amount of occultations that has obtained, providing high quality standard RO retrievals during a large period of

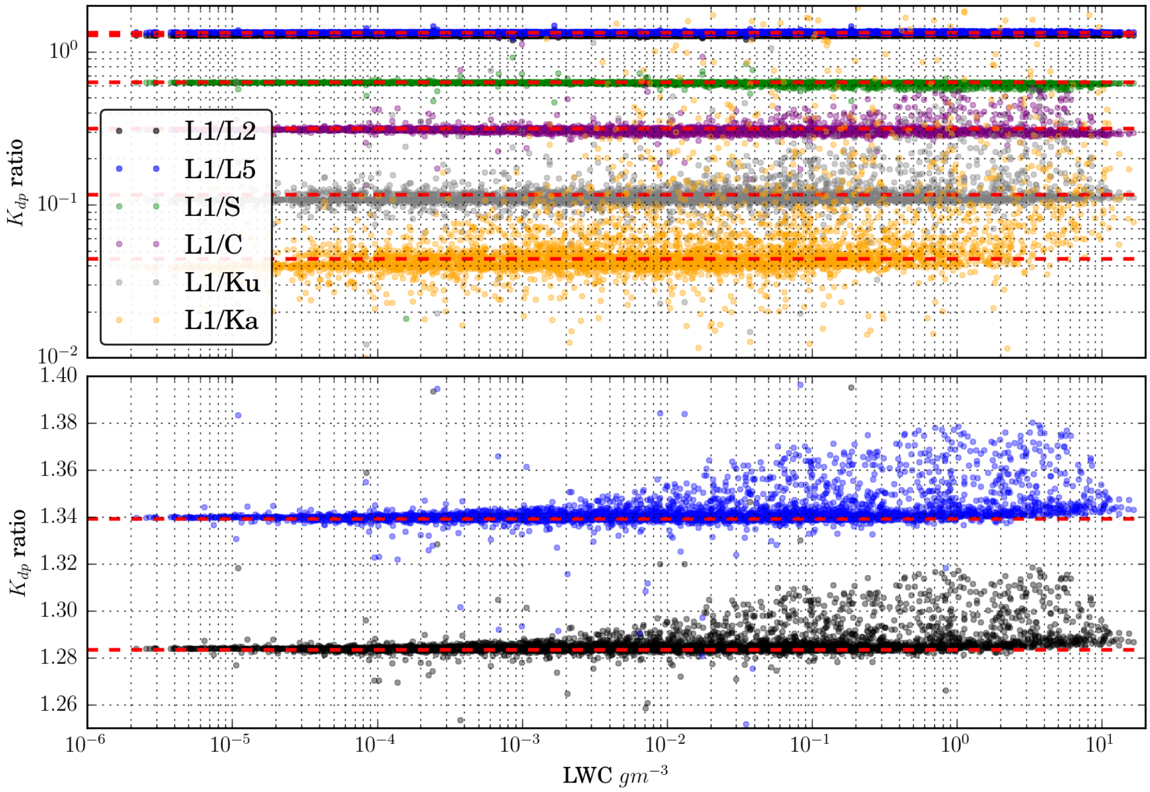

Figure 4.16: (Top) Comparison among several linear K_{dp} ratios between L1 band and L2, L5, S, C, and K bands, for raindrops. The observables have been obtained throuhg the same procedure as in the previous figures. (Bottom) A more detailed look into the ratios between L1 and L2 bands, and L1 and L5 bands. Red dashed lines indicate the ratios between the different wavelengths.

time (since 2006 and still providing). This allows to look for collocations with other satellites during a long span of time.

The whole COSMIC mission has been checked against TRMM, GPM and CloudSat, looking for coincidences between the orbits of the satellites and RO locations. Among all the found coincidences, one is accepted if the occultation location is within the swath area of the satellite radar (in the case of CloudSat, a ± 50 km margin is given), and the measurements by the radar are less than 15 minutes away from the RO event. With these constraints, one ends up with 16,881 collocations between COSMIC and TRMM, 4,370 collocations between COSMIC and GPM, and 5,125 collocations between COSMIC and CloudSat. A summary of these collocation criteria are shown in Table 4.2.

These collocations are initially classified for a general analysis. Information from the satellite radars is extracted and stored in some fields, that are the following:

- Number of radar vertical profiles that fall within 100 km from the RO coordinates;

satellite	Geo	time	number of coll.
TRMM	RO within swath	< 15 min	16, 881
GPM	RO within swath	< 15 min	4, 370
CloudSat	RO within ±50 of track	< 15 min	5, 125

Table 4.2: Some of the criteria and statistics of the collocations between COSMIC mission and TRMM, GPM and CloudSat.

- Number of radar bins with Z_e in the range of [20,30] dBZ for TRMM and GPM, and [−10,0] dBZ for CloudSat, within 100 km from the RO coordinates;
- Number of radar bins with Z_e in the range of [30,40] dBZ for TRMM and GPM, and [0,10] dBZ for CloudSat, within 100 km from the RO coordinates;
- Number of radar bins with Z_e in the range of [40,50] dBZ for TRMM and GPM, and [10,20] dBZ for CloudSat, within 100 km from the RO coordinates;
- Number of radar bins with Z_e larger than 50 dBZ for TRMM and GPM, and larger than 20 dBZ for CloudSat, within 100 km from the RO coordinates;
- Number of radar vertical profiles with surface rain rate larger than 0.1 mm h^{-1}, within 100 km from the RO coordinates;
- Average rain rate of all those profiles with positive rain rate (mm h^{-1});
- Maximum surface rain rate encountered in all the profiles (mm h^{-1}).

All the collocations are shown in Figure 4.17, where the locations of all of them are plotted on the map. The color scale represent the number of bins with $30 < Z_e < 40$ dBZ ($0 < Z_e < 10$ dBZ for CloudSat), which hereafter will be the Z_e range used to identify rain in the profile, i. e. if there are pixels in this Z_e range, the profile is identified as rainy, while if there are no pixels in this Z_e, the profiles are assumed not to contain rain. In the case of CloudSat profiles, instead of rain, reflectivity indicates clouds and ice particles. An histogram of the events that show rain (or clouds) versus those that does not show any are plotted next to the map (right on Figure 4.17), showing the distribution of precipitation and cloud events as a function of latitude.

These collocations allow two kinds of analysis: (1) to know if the RO happened in a rainy environment or not, which allow for a classification of events very valuable in terms of analysing the thermodynamics of precipitation. This kind of analysis has been performed and will be detailed in Chapter 6. The other analysis that can be done is (2) to perform exact three dimensional interpolations between the RO ray trajectories and the rain (cloud) profiles, and infer which would have been the polarimetric differential phase shift that rain (clouds) would have induced into the GNSS signals, and use this information as a realistic simulation of the polarimetric

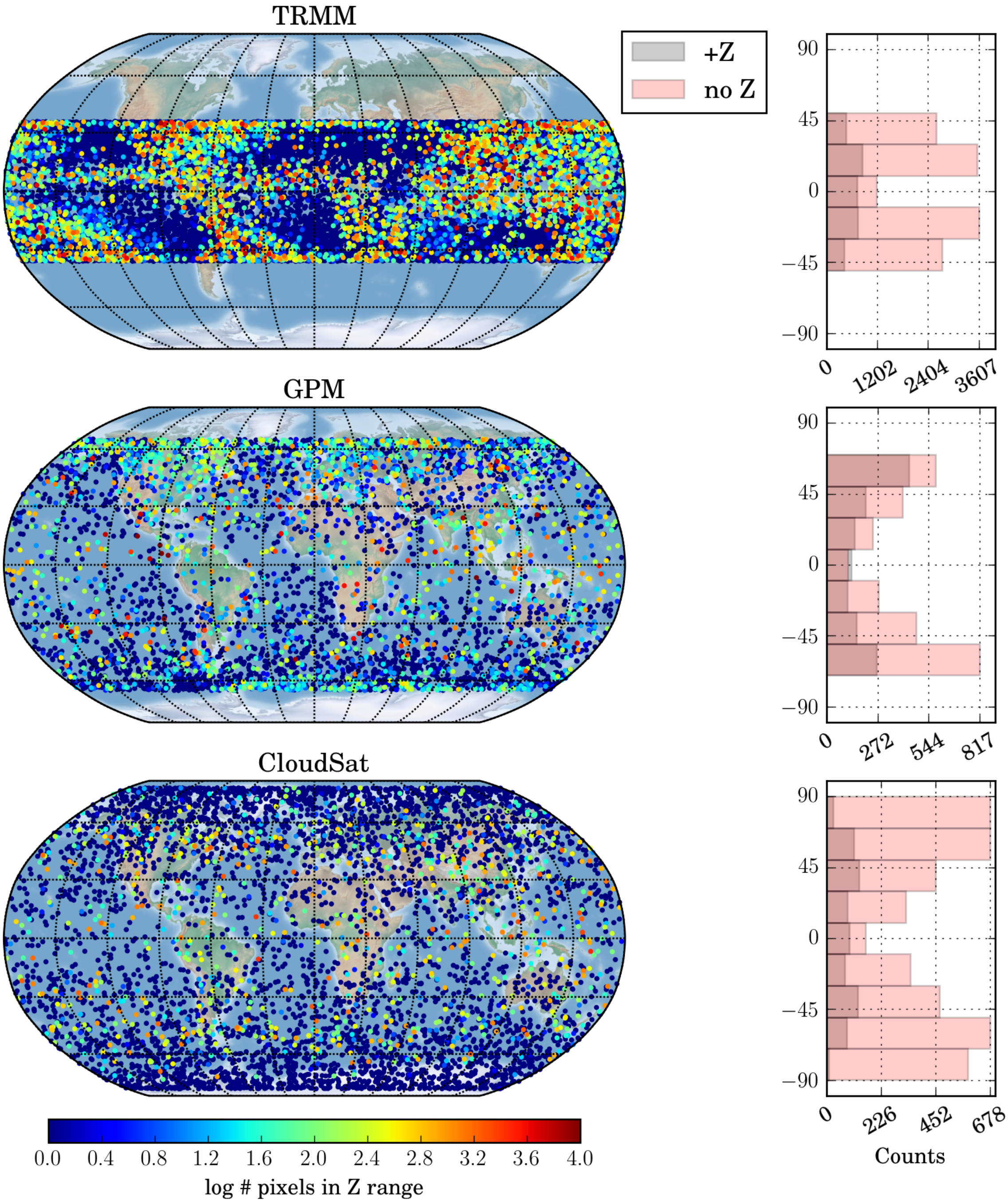

Figure 4.17: (Left) collocations between COSMIC RO and TRMM (top), GPM (middle) and CloudSat (bottom) locations. Colorscale represents the number of pixels in the [30,40] Z_e range ([0,10] for CloudSat). (Right) The correspondent histograms for the number of events as a function of latitude, with a positive number of pixels in the second Z_e range (black) and without any of them (red).

experiment. Several steps are needed for this analysis, and these are detailed in the following sections.

As a first step, the collocation list is examined, and for each event the corresponding data file is located and obtained. On the Radio Occultation side, the used files are the *atmPhs*, *ionPhs* and the *atmPrf*, obtained from the UCAR COSMIC Data Analysis and Archive Center (CDAAC) database. For the radar products, the needed files are different depending on the satellite. For TRMM, the used data products are the *2A21* and the *2A25*, called orbital products that provide three dimensional radar observations and derived products. For GPM, the used files are the ones called *DPRGMI*, which contain a three dimensional combination of the radar and radiometer observations, and provide the derived products as well. For CloudSat, the needed files are the *GEOPROF* and the *CWC-RO*, which also provide the measurements of the radar and the derived quantities.

4.2.1 *Observable mapping*

Fist of all, the radar observables have to be linked to the observable that one wants to simulate (e. g. K_{dp}, attenuation, excess phase, etc.), using the information obtained in Section 4.1.3.4. As it has been shown, there is not a unique relationship between radar observables and K_{dp} due to the variability of the PSD. Therefore, a choice has to be made. The safest option is to use the PSD that has been provided by the mission in use (TRMM, GPM, or CLoudSat). To do so, one can look for the parameters of the PSD in the radar data products. If they are not provided, then the PSD can be inferred using the radar reflectivity and the derived products such as the water content, and identify which relationship is applied between them. In Figure 4.18 and Figure 4.19 there is shown an example of this procedure, for TRMM and GPM, and for CloudSat, respectively. In grey there is plotted the simulations of LWC (or IWC) as a function of Z_{e} for each satellite radar frequency band, where the variability is clearly observed. Overplotted there are the measurements of the radar for a certain event, and the derived quantity provided. Each Z_{e} measurement is identified with a water content product, which are related by a chosen PSD. This PSD is then identified and used to compute the desired observables.

In Figure 4.18, the points are coloured as a function of the air temperature in the measurement region. This temperature is obtained from a model and provided along the water content products. Although the plot can be misleading (the points with cooler temperature are plotted above those with higher temperature), only a few percentage (< 10%) of the points have temperatures below 260 K. It is interesting to recall that for the same Z_{e} value, the largest water contents tend to correspond to the cooler regions.

In the case of rain (Figure 4.18), the simulations space agree perfectly with the observations space, so the identification of the DSD can be performed with no further assumptions. In the case of ice particles (Figure 4.19), the simulation space also agrees quite well with the observations, but there are two regions of the observed

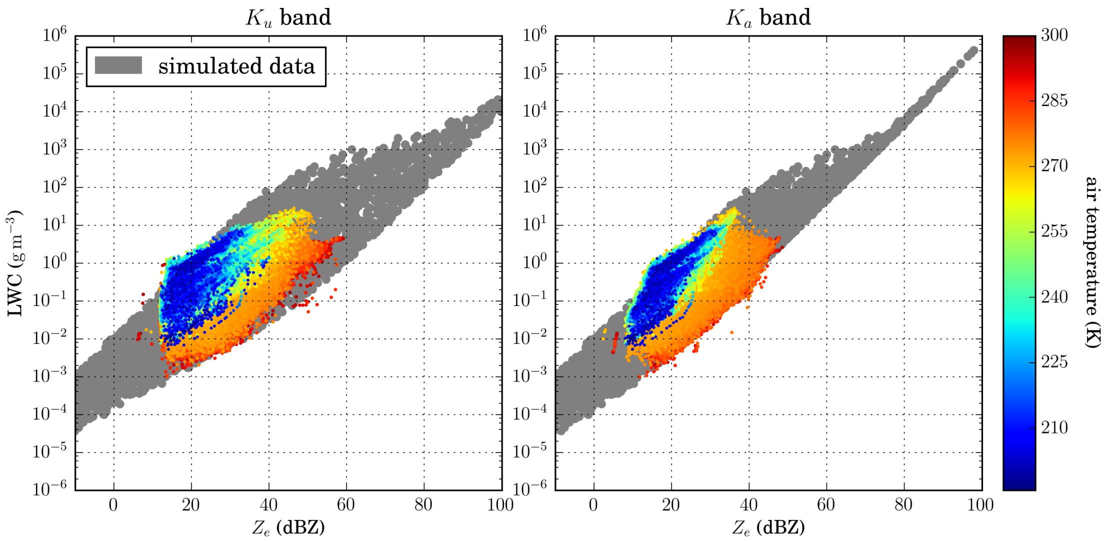

Figure 4.18: $Z_e - IWC$ relationship as seen from GPM (colored dots) and using simulated data (gray), for K_u band (left) and for K_a band (right). Color scale represent the air temperature in the measured region. This plot shows good agreement within observations and simulations.

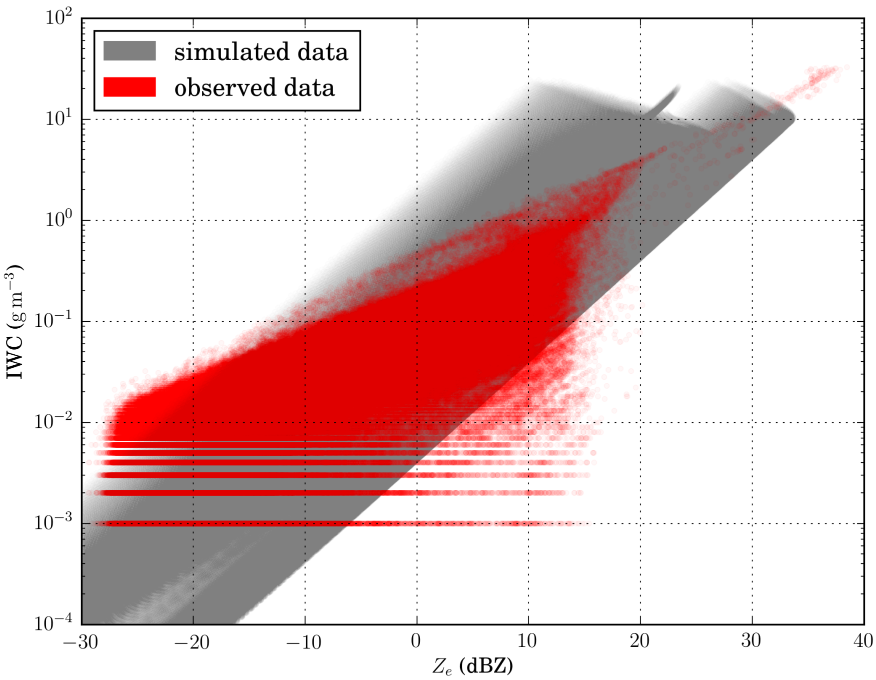

Figure 4.19: $Z_e - IWC$ relationship as seen from CloudSat (red) and using simulated data (gray), for W band. This plot shows good agreement within observations and simulations, with the exception of a small region with low Z_e and relatively high IWC, and a few points with high Z_e and low IWC.

measurements that fall outside the simulations range. These are the region with low reflectivity and high ice water content, and the region with large reflectivity with low ice water content. Nonetheless, most of the observations are well characterized by the simulations. For those points outside the simulated range, only the IWC information is used, and it is related to the observables to simulate using mean values of the relationships shown in Figure 4.13, Figure 4.14, and Figure 4.15.

4.2.2 *Ray-Tracer*

Before it is possible to simulate the $\Delta\Phi$, it is necessary to know whether the RO event has actually crossed rain or ice, or not. For this is necessary to reproduce the ray trajectories that the GNSS signals followed from the GPS to the LEO. Atmospheric ray tracers are the tools required for such analysis. They solve the path integrals taking into account the positions of the GPS and the LEO at every time, and the vertical refractivity profile. See for example Aparicio and Rius [2004]. For this work there have been used two different ray tracers, one of them coded by Dr. J.M. Aparicio, called Occultation Analysis Tools (OAT), and the other one by Dr. Chi Ao (JPL). Most of the results were obtained using the latter.

Ray tracers are able to simulate the ray trajectories, and provide an estimation of the excess phase and the coordinates of the ray points. In this case, the inputs are the CDAAC *atmPhs* and *ionPhs* files for the GPS and LEO locations, and the *atmPrf* for the refractivity profile. Like most of the atmospheric ray tracers, an atmosphere with spheric symmetry is assumed, and therefore no horizontal gradients of refractivity are taken into account. The use of both *atmPhs* and *ionPhs* files are needed in order to probe all the atmosphere, since *atmPhs* only include the lower layer of the atmosphere, and *ionPhs* the upper ones.

What is used here are the ray trajectory points; each ray corresponds to each step of the input files. The *atmPhs* files provide the GPS and LEO locations every 20 ms, while *ionPhs* provide their locations every 1 s. For each of these times (GPS and LEO locations) the ray tracer computes 30 points of the ray trajectory. When the tangent point of the ray is above 20 km, the ray trajectory is interpolated at 300 points equally spaced below the height of the LEO. Otherwise, the ray is interpolated to 100 points above 20 km and 200 points below, providing a higher sampling rate in the region where clouds and precipitation occurs.

The lower layers of the atmosphere represent a challenge for these ray tracers, and in most of the cases they experience problems of convergence, stopping the simulation several dozens of seconds before the actual occultation. This implies that the bottom of the RO is not simulated by the ray tracer. To solve this issue, basic extrapolation techniques have been applied. The extrapolation is performed using the fact that the origin and end of the rays that have not been simulated are known, and the minimum height that the RO event has reached is also known. Then, several assumptions are made: (1) the tangent point of the last ray is the minimum height that the RO reaches; (2) every ray reaches a height that is lower

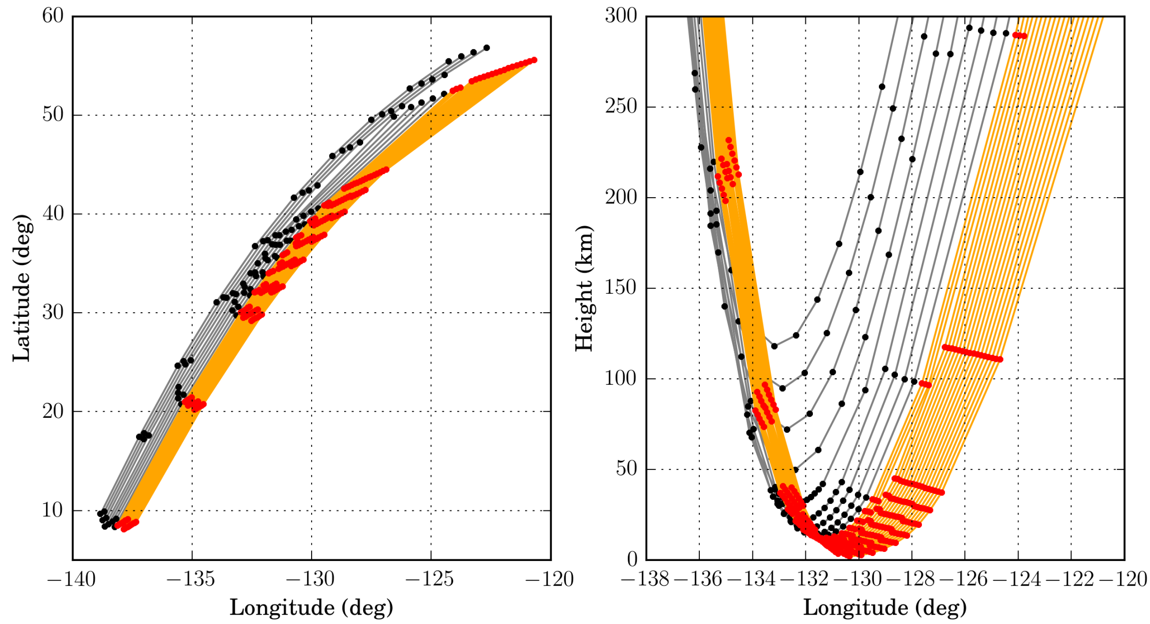

Figure 4.20: Example of the ray trajectories for a RO event. (Left) projection of the original 30 points of the ray trajectories obtained with the ray tracer, on the longitude - latitude plane. The last points towards the GPS direction are not shown (in this example, GPS would be located in the upper right part of the plane). (Right) Projection of the ray trajectories on the longitude - height plane, truncated at 300 km of altitude for illustration purposes. The trajectories on gray are those simulated by the ray-tracer, and those in orange are the ones obtained by the extrapolation technique. Only few rays are shown for illustrative purposes.

than the previous ray. Then, similar geometric features of the last simulated rays are used to simulate the remaining rays. This assumptions and technique could be smoothing the ray trajectories in the bottom layers of the atmosphere, but they can be considered realistic enough for the purposes of identifying if the RO has crossed rain, and have a realistic approximation of which areas and which length have the rays crossed. An example of the result after the ray-tracer simulation and the extrapolated ray trajectories can be seen in Figure 4.20.

4.2.3 *Interpolation and integration*

At this point, the scenario is fully described: a large variety of particles present in the atmosphere under precipitating and cloudy scenarios are simulated in terms of their scattering properties; these scattering properties are used to derive the observables that satellite radars are providing; these observables and their derived quantities are used to compute the differential polarimetric quantities. On the other hand, the ray trajectories for the RO events are simulated as well. Therefore, the interpolation of the differential quantities into the simulated GNSS ray trajectories would fully describe how GNSS signals are affected by rain and clouds at each point along its ray trajectory, and will allow to simulate the final polarimetric observables that a polarimetric-capable RO mission would measure

The interpolation is performed using a fast algorithm that for each of the ray trajectory points, it looks for the 8 closest points of the radar - derived quantities, and performs a weighted mean. This gives the information of Z_e and water content provided by the radars at each of the RO ray points. Then, the quantities K_{dp}, A_{dp}, K_{exc} and A_{exc} are obtained using the observable mapping techniques.

There are two things that are important to highlight: the first one is that the angle of incidence at each point of the trajectory has to be taken into account when performing the simulations, and the depolarizing effect could be slightly reduced (this reduction is very small, and the incident angles are never larger than 2.5°); and the second thing is that the RO ray trajectories scan the atmosphere in a slant direction rather than vertical. This implies that the rain and cloud structures are not vertically sensed. This effect can be seen in the left panel of Figure 4.20, where the displacement of the rays over the longitude - latitude plan is evident.

Once the interpolations are performed, the last step is to compute the integration of the differential quantities along each ray trajectory, obtaining in this way the integral measurements of $\Delta\Phi^{trop}$, ΔA^{trop}, Φ^{trop}_{exc} and A^{trop}_{exc} (Equation 3.40, Equation 3.41, Equation 3.45, and Equation 3.46, respectively). These observables are given as a function of the height of the tangent point of the ray (or time of the RO observation). Examples of the interpolation and the integration are shown in Figure 4.21 and Figure 4.22.

4.2.4 *Additional collocation exercises*

4.2.4.1 *2D collocations*

Even though the 3D collocations described above are the most realistic simulations of Pol-RO events, the number of available cases is low, and therefore the statistical analysis is limited. This is why a 2D collocation exercise has also been performed, allowing the analysis of a higher number of events. This exercise uses the TRMM 3B42 products, which provide the rain rate on a 2 dimensional grid of 0.25×0.25 degrees, in 3 hour batches. The main drawbacks are the lack of a vertical structure and the resolution, both in space and time, which is rather low. On the other hand, these products allow for a massive collocation study, which enhances the statistical significance of the results.

The collocation has been performed using actual COSMIC measurements between June 1, 2006 and December 31, 2007. Each of the events has been linked to a 3-h batch TRMM 3B42 product. Then, for each RO event, one ray is inspected. It can be the one corresponding to the lowest tangent point or the one corresponding to a given altitude of the tangent point. The choice is random, choosing among $h =$ 0, 1, 2 or 4 km altitude. The selected height is used to compute the straight line (i. e.

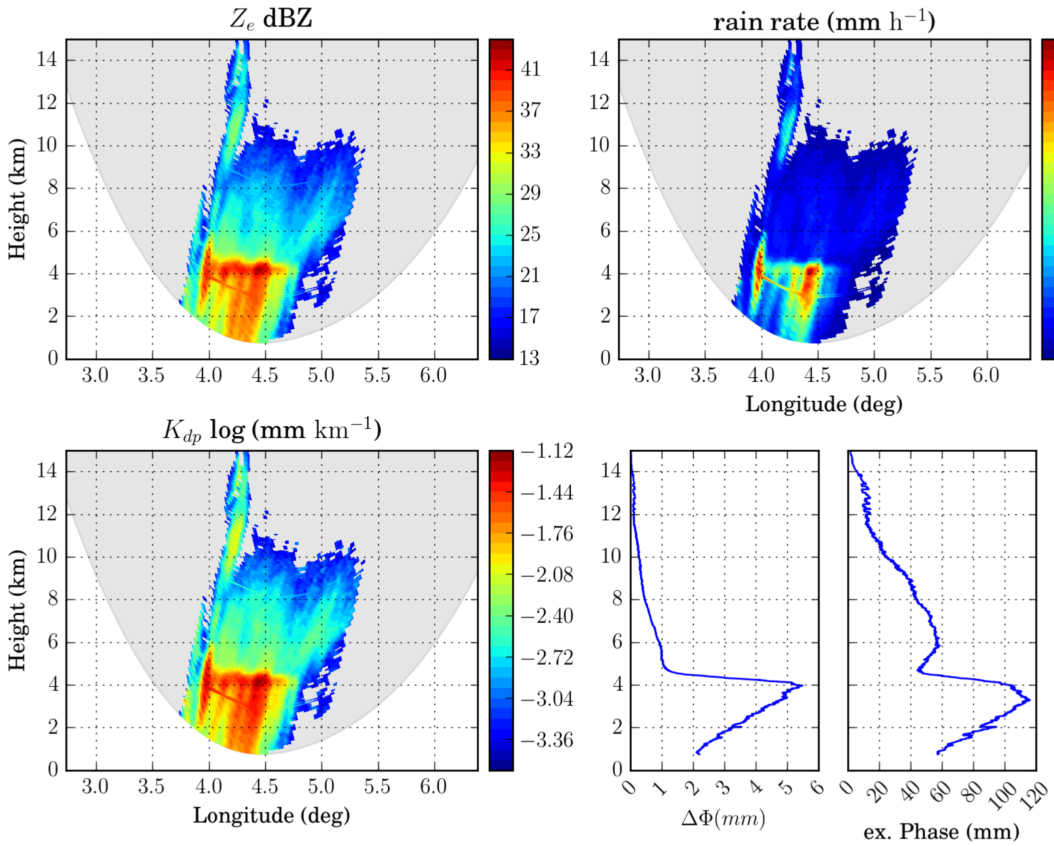

Figure 4.21: Example of a RO events collocated with TRMM, interpolated and integrated. The top-left panel shows the radar reflectivity measured by TRMM (top case) as a function of longitude and height; The top-right panel shows the rain rate measured by TRMM; The bottom-left panel shows the K_{dp} simulated from the satellite measurements; and the bottom right panel correspond to the integrated L1 differential phase shift and the total L1 RHCP excess phase due to the hydrometeors, as a function of the tangent point height. The gray region represents all the RO ray trajectories.

no bending taken into account) with the same orientation as the actual COSMIC RO link. The segment of this line that remains below the $H_{\mathrm{rain}}^{\mathrm{top}}$ is projected into the TRMM 3B42 surface product. $H_{\mathrm{rain}}^{\mathrm{top}}$ is taken to be 6 km in the Tropics, and 3 km in the mid-latitudes.

The R information from the TRMM 3B42 product is used to derive the K_{dp}, using the Marshall-Palmer DSD. With the K_{dp} and the length of the segment, the $\Delta\Phi^{\mathrm{trop}}$ can be computed. A sketch of this approach is shown in Figure 4.23. For each event, $\Delta\Phi^{\mathrm{trop}}$ is stored. In addition, the mean rain rate along the ray path, $\langle R \rangle$, is computed as $\langle R \rangle = \sum_{R_i>0}(R_i \cdot l_i)/L$. L is the length of the ray-path within the rain, and is defined as $L = \sum_{R_i>0} l_i$. Note that l_i is the projected length of the segment into each of the TRMM 3B42 grid cells. Both $\langle R \rangle$ and L are stored for all the events, for classification purposes.

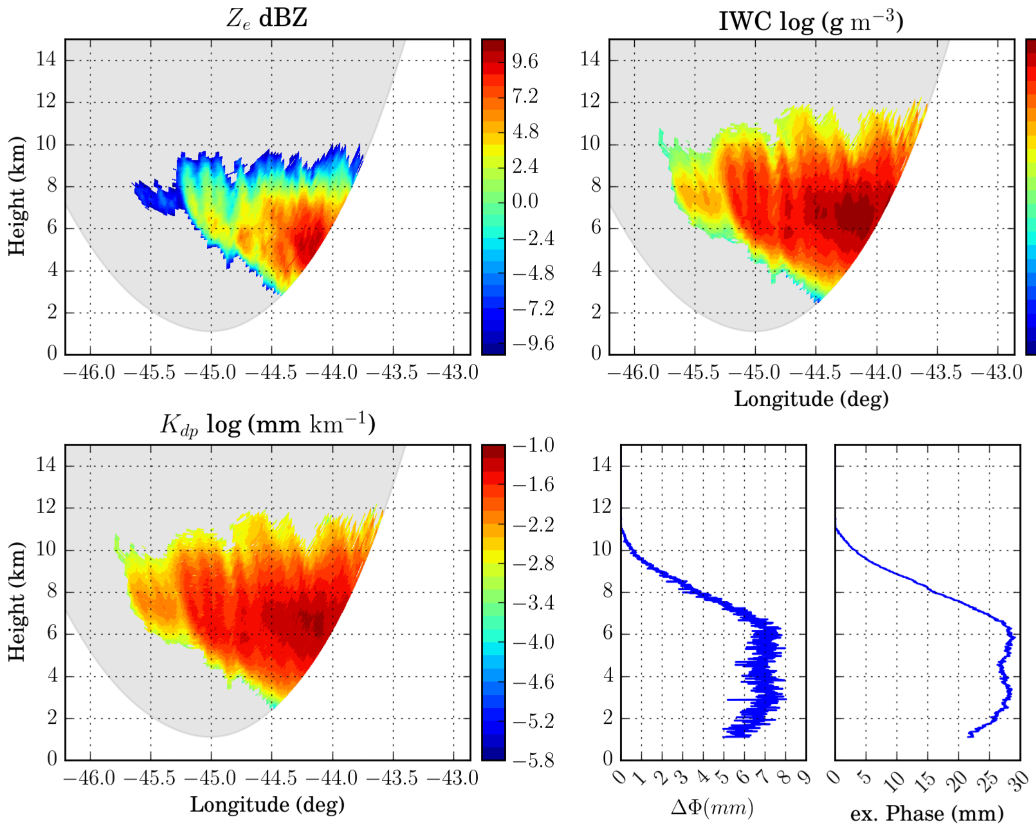

Figure 4.22: Same as Figure 4.21, but here the collocation is with CloudSat. In the top-right panel, instead of rain rate here there is represented the IWC (in logarithmic scale).

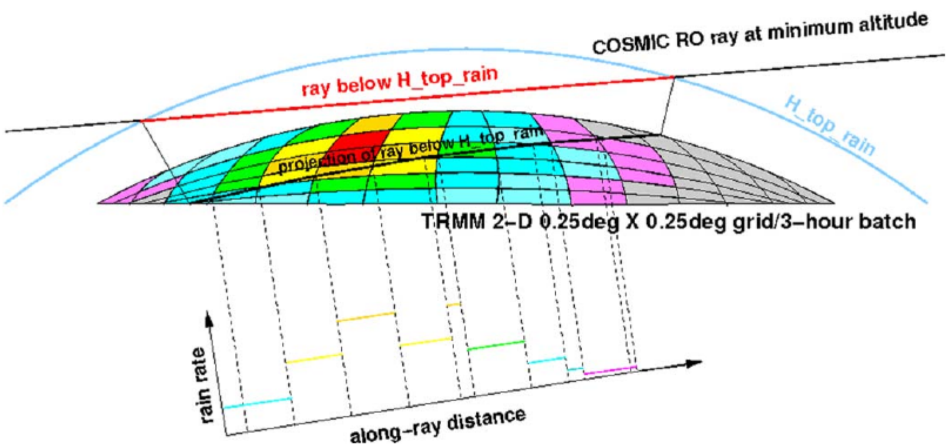

Figure 4.23: Sketch of the 2D collocation approach, using the COSMIC RO events and the TRMM 3B42 3-h products. Image from Cardellach et al. [2014], Fig. 11.

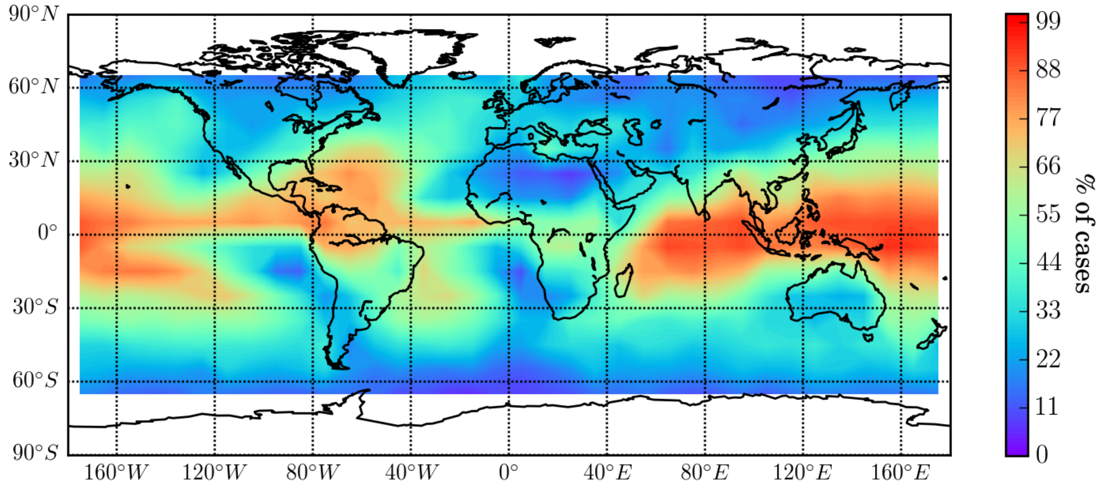

Figure 4.24: Global map of the percentage of GPM collocations that have rain in the profile.

4.2.4.2 *fake 3D collocations*

The orbital *2B.GPM.DPRGMI* products are used to generate a large amount of Pol-RO observables, $\Delta\Phi^{\text{trop}}$. Differently from the collocation exercises described above, the actual COSMIC RO data are not used here. To perform this exercise, several actual RO ray trajectories have been collocated artificially (i. e. the coincidence in space and time is forced) along each GPM satellite orbit, aligned with the satellite travel direction. Then, each of them is interpolated with the GPM orbit slice, obtaining a three dimensional profile of the radar observations mapped onto the *fake* RO plane. Even though here the actual products from a RO are not available, the polarimetric observables can still be simulated as it is done in the actual 3D collocations.

The artificial collocations will represent the real proportion of rain events versus all the observations, in the range comprising -60 to 60 degrees of latitude. Thus, it can be used as a realistic example of the polarimetric mission. The data used here contains all the GPM observations from its launch to the time of writing. Approximately $250,000$ Pol-ROs are simulated, with the correspondent realistic $\Delta\Phi^{\text{trop}}(h_{tp})$, as a function of the tangent point's height. In addition, the $\langle R \rangle$ and the L for each of the RO rays are also computed. A global map of the percentage of GPM collocations that have rain in the profile is shown in Figure 4.24.

4.3 IONOSPHERE

A similar procedure as the explained above can be used to perform simulations on the ionospheric state, and which would have been its effect into the polarimetric signals. To evaluate the effect, Equation 3.47, Equation 3.48, and Equation 3.49 have to be computed, and therefore the magnetic field and the electron density at each

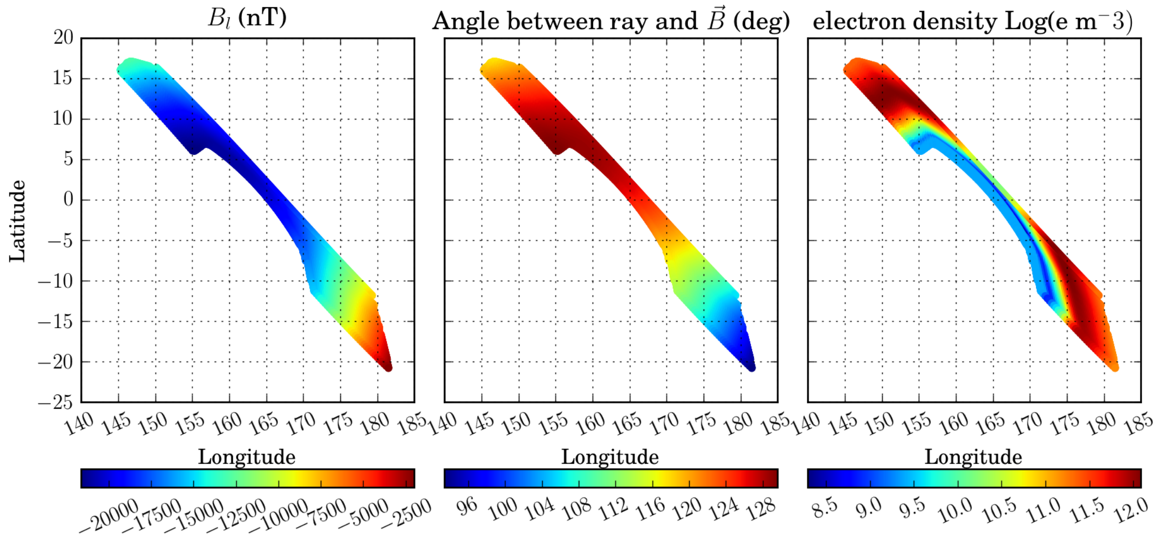

Figure 4.25: Collocation and interpolation results of the ionosphere information into the RO rays, represented here as their projection into the longitude - latitude plane. From left to right, the along-ray component of the magnetic field, the angle between the magnetic field vector and the ray propagation direction, and the electron density. Clarification: the ray's tangent points correspond to those points closer to the center of the longitude - latitude plane, while the points placed in the upper left corner correspond to those closer to the GPS and higher altitude, and those in the lower right corner correspont to the LEO position and lower altitude.

of the RO ray-points are needed. The magnetic field in the RO region is obtained from the International Geomagnetic Reference Field (IGRF) model [e.g. Thébault et al., 2015], and the electron density is obtained from the International Reference Ionosphere (IRI) model [e.g. Bilitza et al., 2011]. These models provide the modelled magnetic field vector and the modelled electron density for a given region and time, among other quantities. In addition to the magnitudes of the magnetic field and the electron density, a very important quantity to be obtained is the angle between the magnetic field vector and the RO ray propagation direction, which is not intuitively easy to figure out.

For each of the RO events, the ray points of each of the trajectories are collocated and interpolated with the model outputs, and the corresponding computations are performed. An example of the along-ray component of the magnetic field, the angle between the magnetic field vector and the ray propagation direction, and the electron density at each point of a RO event is shown in Figure 4.25. From these quantities, differential (at each point) and integrated (for each ray) values are derived. The integrated quantities, which are used for further analysis, are separated so that they are contributed by two regions, called ionosphere 1 and ionosphere 2. Ionosphere 1 is defined as the region of the ionosphere that the ray first finds on its way from the GPS to the tangent point. The ionosphere 2 is defined as the

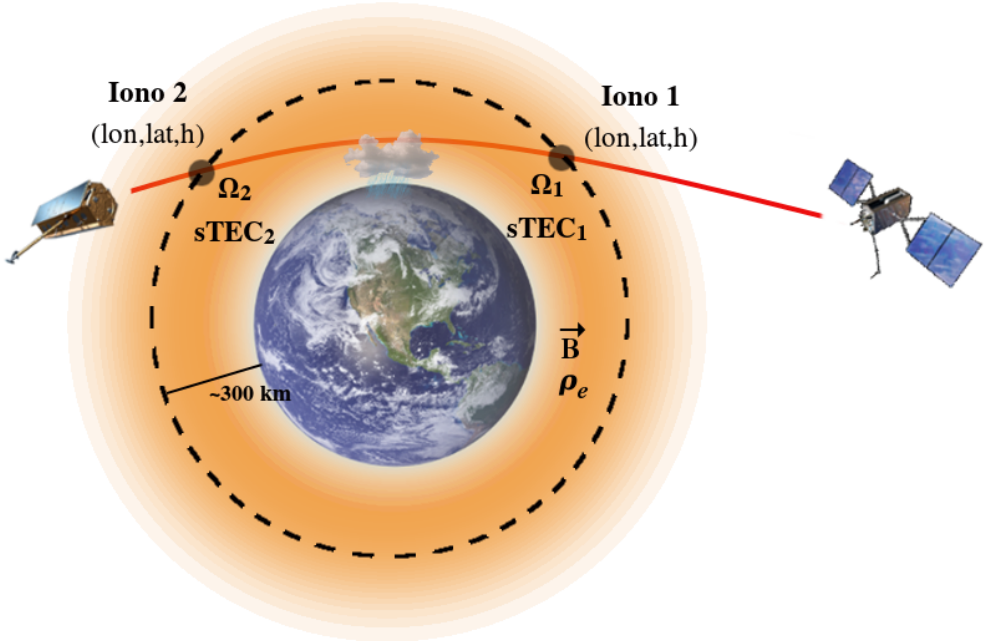

Figure 4.26: Schematic representation of the GNSS-RO signal crossing the ionosphere. The dashed line represents the height where the information of the ionosphere is represented. The part 1 represents the frist part the ray encounters on its way to the tangent point, and the part 2 is the exiting part. These differetiation make sense when the ray's tangent point is low, and cross an hydrometeor layer in between ionosphere 1 and 2.

---

last part of the ionosphere that the ray encounters after the tangent point on its way to the LEO. While for the rays crossing the ionosphere through its top layers this separation may not make sense, because the ray is only going through one effective ionosphere layer, the bottom rays are travelling through two very different regions of the ionosphere when entering and exiting the troposphere, that can be separated by thousands of kilometres. In addition, and due to the fact that the ionosphere is defined here only above 100 km, the ray can find a precipitation layer between the two separate ionosphere layers, which are then affecting the ray as three different independent layers. This situation can be seen in Figure 4.26. The ionospheric-related integrated values of each ray are collapsed and represented in a representative point of each region, taken to be approximately at a height of 300 km.

As it has been argued in Section 3.1.6, only the Faraday rotation is relevant for this study:

$$d\Omega_{\mathrm{F}} = \frac{2.36 \cdot 10^4}{f^2} n_e(\vec{l})\, \vec{B}(\vec{l}) \cdot \hat{l}\; dl.$$

This effect has been computed for the collocated cases described in the Section 4.2. The results for Ω_{F} for each of the rays of each of the collocated RO are divided into the different years, and the histograms of the results are shown in Figure 4.27 and

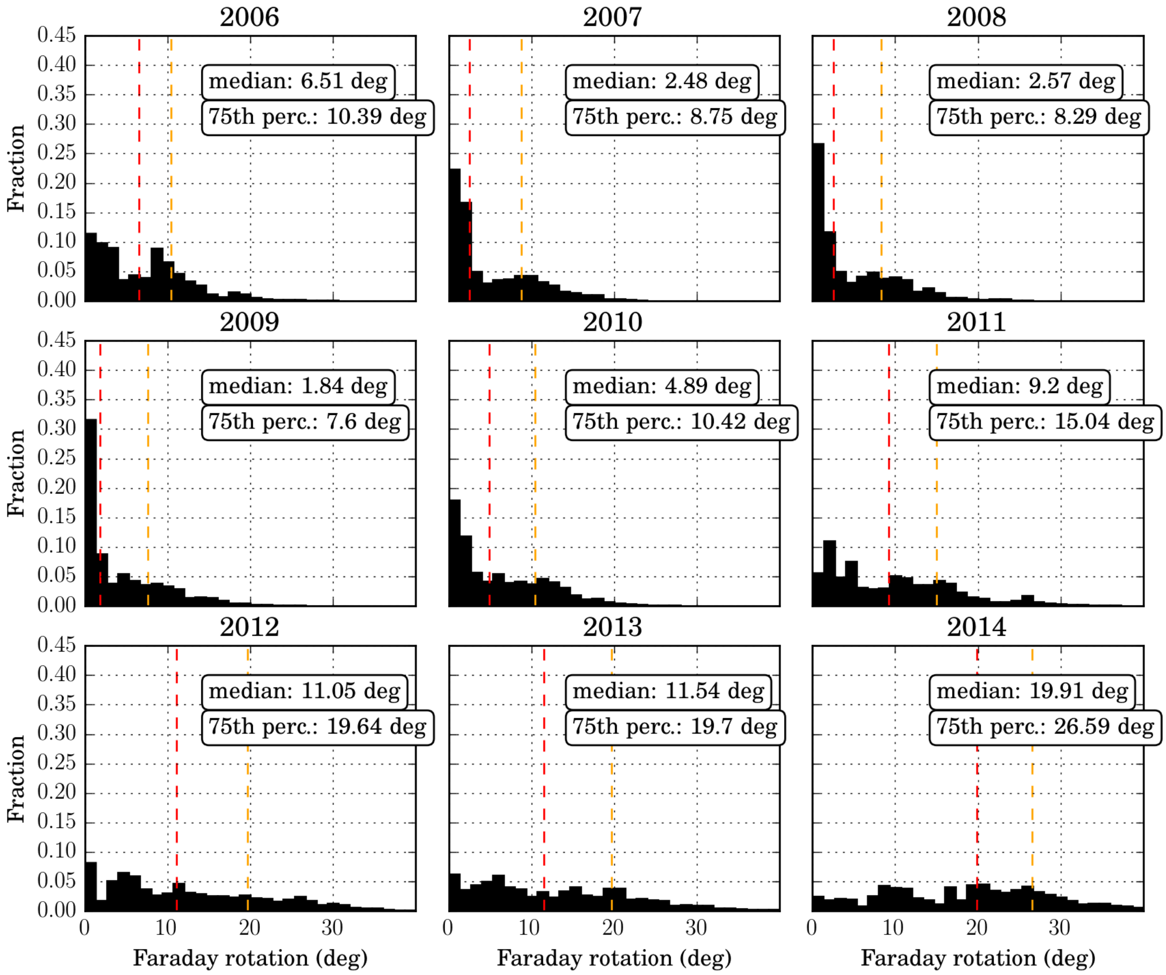

Figure 4.27: Histograms for the Ω_F for the collocated RO, divided by years. The red vertical dashed line indicates the median, and the yellow one indicates the 75th percentile.

Figure 4.28. The absolute value of the total Faraday rotation, and the absolute value of the Faraday rotation only due to the second part of the ionosphere are shown. Two major conclusions can be extracted from these results. First, that the value of the Faraday rotation is generally small, i. e. the 75% of the simulated data lay below 20 deg for most of the cases; and second, that this effect is strongly dependent on the solar activity. The shape of the histograms changes depending on whether there is an epoch of minimum activity in the solar cycle (i. e. 2008, 2009), when the Faraday effect is close to 0 deg., or there is maximum activity (i. e. 2013, 2014), when it takes values that are sparse between 0 and $\sim$ 30 deg.

The effect of the Faraday rotation is important because it changes the polarimetric phase shift between the H and V components of an elliptically polarized wave, if the wave differs from the exact circular polarization case. In the context of this thesis, this happen when the emitted wave from the GPS is not purely RHCP (see Section 3.1.3.1), and when the signal has already crossed an hydrometeor depolar-

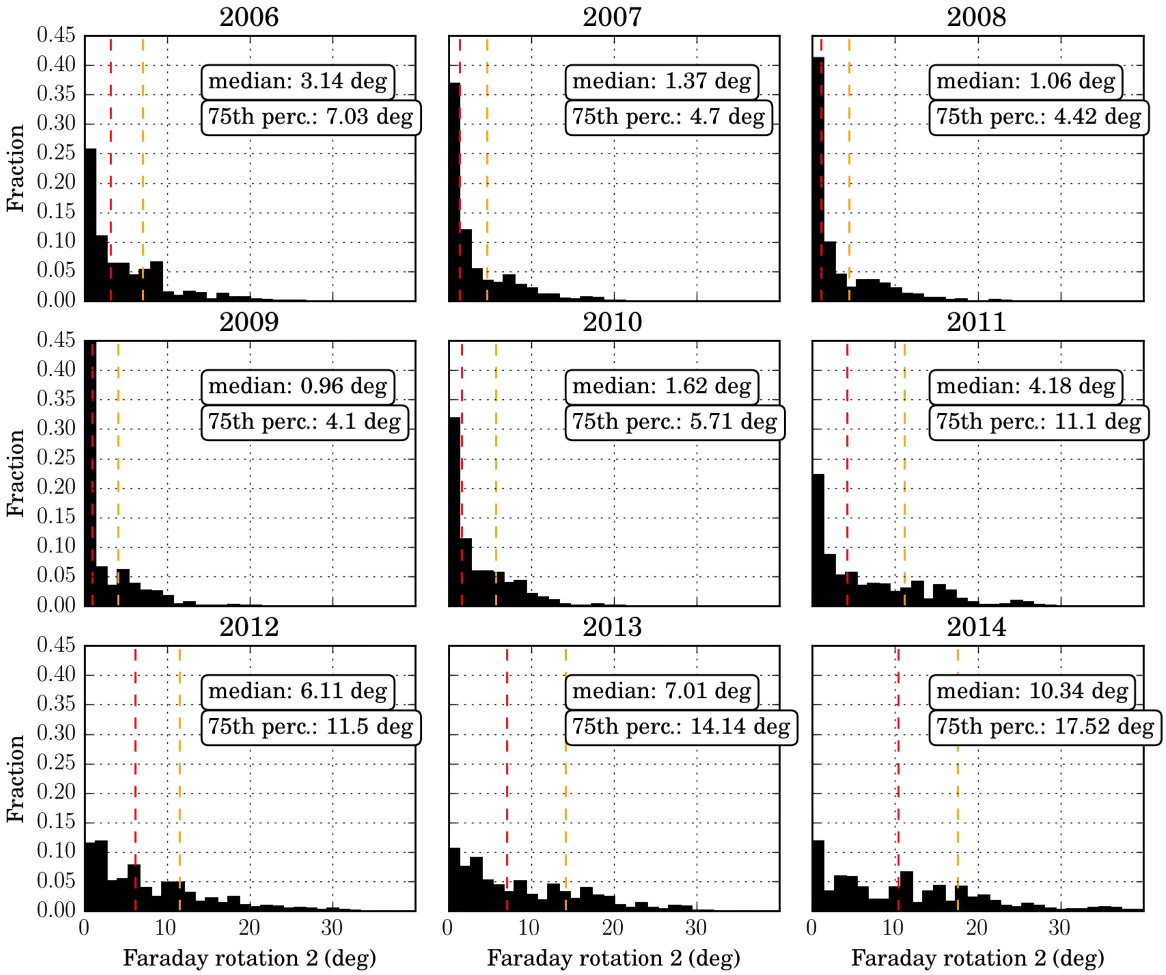

Figure 4.28: Histograms for the Ω_2, i. e. the effect only due to the second part of the ionosphere, for the collocated RO, divided by years. The red vertical dashed line indicates the median, and the yellow one indicates the 75th percentile.

ization layer. This implies that the ionospheric effect must be taken into account as a systematic effect when analysing the Pol-RO data from a LEO. The algorithms to correct for this effect will be detailed in Tomás et al. [2017] and are left out of the scope of this dissertation.

4.4 DATABASE

The processed collocated RO are stored in a database for further analysis. The whole process is shown in a flow diagram in Figure 4.29. After the collocation, interpolation, and integration process, one has a huge amount of information, that can be classified in three tables. The first one is called *radio occultation*, and it contains information corresponding to each RO as a whole, information that is useful for classification and identification of each event. It has fields such as the CDAAC

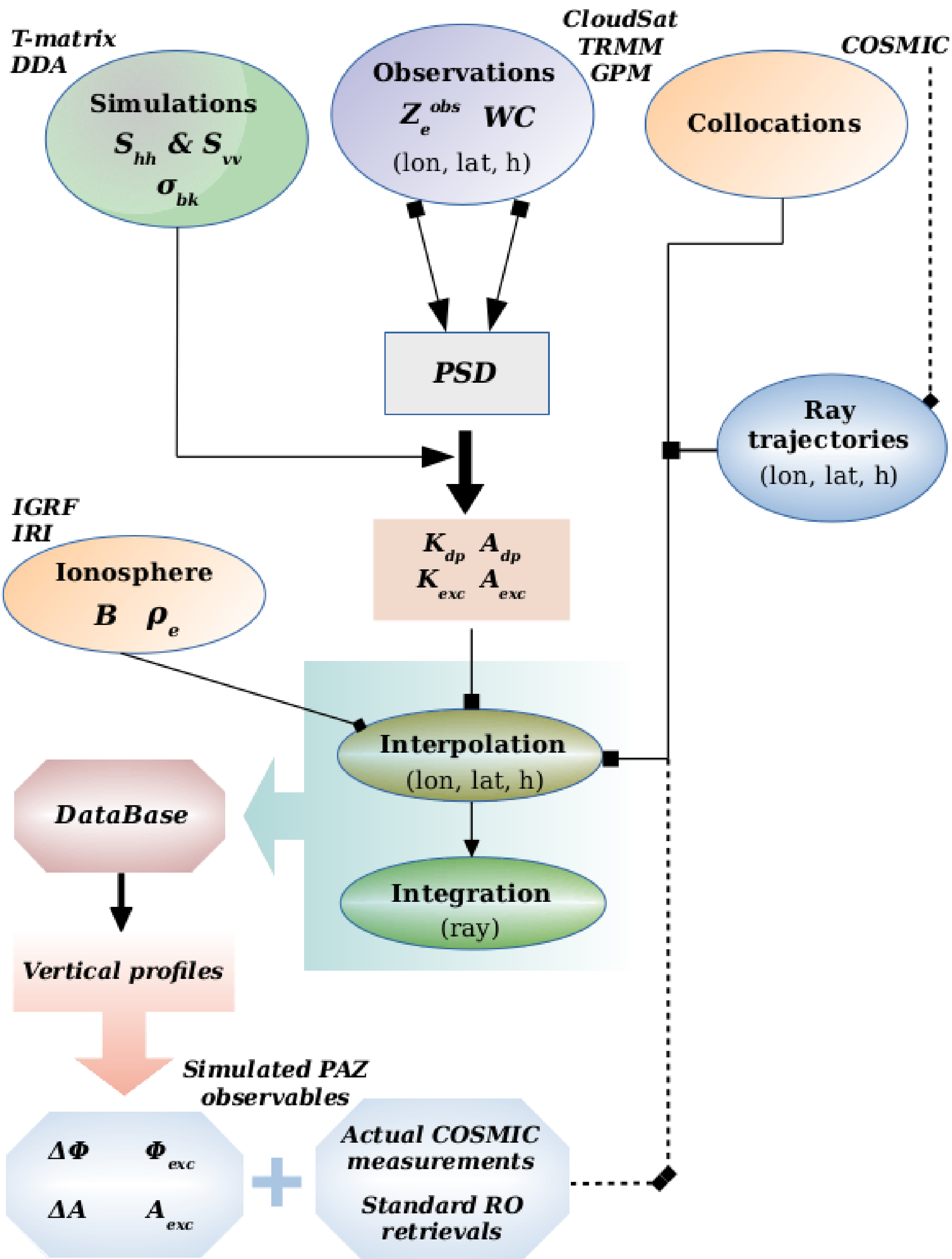

Figure 4.29: Flow diagram that summarizes all the steps followed to obtain the final integrated measurements and the vertical profiles.

Field	Description
occ_id	CDAAC RO ID
date	Date of the RO
time_utc	UTC time of the RO
lon_ro	Longitude coordinate of the RO
lat_ro	Latitude coordinate of the RO
azim_occ	Azimuth of the RO
start_time_gps	Start time of the RO in gps time units
sat_coll	Satellite that provide the radar information
dt_coll	Δ time between RO and satellite radar overpass
check_iono	Flag to indicate if ionosphere has been processed
check_hyd	Flag to indicate if hydrometeors have been processed
truncate_ion	Flag to indicate if *ionPhs* file was available
max_delay	Maximum polarimetric phase shift found in the whole RO

Table 4.3: Database structure for the *radio occultation* table.

ID for each RO, the maximum polarimetric phase shift induced by hydrometeors, the time and coordinates of the RO, which satellite has provided the radar products, etc. The second table is called *rays* and it contains along ray integrated quantities, so there is one entry per every ray in the RO event (which correspond to 1 ray per each time of observation). This table has, for example, the actual SNR and excess phase provided by the COSMIC mission, the height of the tangent point of each ray, the polarimetric phase shift derived for each ray, etc. The last table is called *ray_points*, and it contains information regarding each of the ray points. So, there are 300 entries per ray. It has the interpolated Z_e at each of the ray points, the derived LWC or IWC for each of the points, the K_{dp}, etc. Thus, the size of each table of the database grows exponentially. A brief description of the fields and tables of the database are shown in Table 4.3, Table 4.4, and Table 4.5.

All these data represents a synthetic simulation of the polarimetric mission. Combining both the simulated polarimetric parameters and the actual COSMIC measurements, realistic observations in terms of noise, spatial distribution and phase measurement precision can be achieved. It can be used as a testing bench for all the algorithms that are being designed for the mission, as well as to test the applications that the Pol-RO data will have for actual scenarios.

An example of all the contributions to the final observable is shown in Figure 4.30. Here it can be seen how the ionosphere is contributing to $\Delta\Phi$. In this case, $m \neq 0$ (in Equation 3.21), therefore a $\Delta\Phi$ appears even in the upper layers of the atmosphere, where precipitation is not present.

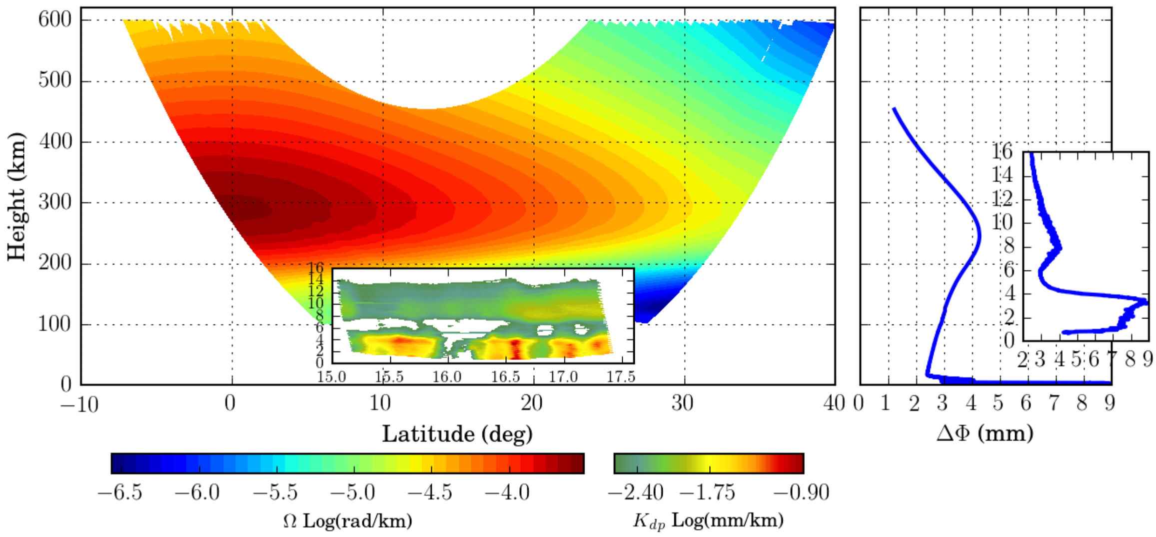

Figure 4.30: RO event collocated and interpolated with ionospheric and precipitation information. Left panel shows the specific Ω interpolated into the RO rays. The inset left panel shows the zoom of the lowest part of the troposphere, where precipitation is present. Note that in the lowest 100 km the ionosphere is not taken into account. The right panel shows the total L1 ΔΦ as a function of each tangent point's height. The inset panel is a zoom of the lowest rays.

Field	Description
id	Auto increment ID (database primary key)
occ_id	CDAAC RO ID
time	Time in s of the ray emission with respect to the *atmPhs* time
h_tp	Height of the tangent point of the ray
lon_ro	Longitude coordinate of the tangent point of the ray
lat_ro	Latitude coordinate of the tangent point of the ray
omega_1	Faraday rotation Ω induced by ionosphere between GPS and TP
omega_2	Faraday rotation Ω induced by ionosphere between TP and LEO
h_i1	Height representing ionosphere between GPS and TP
lon_i1	Longitude representing ionosphere between GPS and TP
lat_i1	Latitude representing ionosphere between GPS and TP
h_i2	Height representing ionosphere between TP and LEO
lon_i2	Longitude representing ionosphere between TP and LEO
lat_i2	Latitude representing ionosphere between TP and LEO
stec_i1	Integrated TEC along ray in the ionosphere between GPS and TP
stec_i2	Integrated TEC along ray in the ionosphere between TP and LEO
snr_occ	Measured Signal to Noise ratio from *atmPhs* file
dph_occ	Measured Excess phase for L1 from the *atmPhs* file
dph_sim	Simulated Excess phase for L1 using the ray tracer
at_*p*_*hyd*	Integrated attenuation for *p* polarization induced by *hyd* (rain/ice)
phi_*p*_*hyd*	Integrated phase delay for *p* polarization induced by *hyd* (rain/ice)

Table 4.4: Database structure for the *rays* table.

Field	Description
`id`	Auto increment ID (database primary key)
`ray_id`	Ray ID, for relating *ray_points* and *rays* tables
`h`	Height of the ray point
`lon`	Longitude coordinate for the ray point
`lat`	Latitude coordinate for the ray point
`d`	Distance between ray points
`alpha_v`	angle between the direction vector and the horizontal at the ray point
`z_ka`	Measured Z_e by GPM DPR at K_a frequency band at each ray point
`z_ku`	Measured Z_e by GPM DPR at K_u frequency band at each ray point
`z_trmm`	Measured Z_e by TRMM at K_u frequency band at each ray point
`z_csat`	Measured Z_e by TRMM at K_u frequency band at each ray point
`temp`	Temperature from the *atmPrf* interpolated at each ray point
`iwc`	Satellite derived IWC
`lwc`	Satellite derived LWC
`rr`	Satellite derived rain rate
`theta`	Angle between the Earth magnetic field and the ray direction
`p_e`	Electron density
`b_l`	Longitudinal component of the Earth magnetic field
`b_t`	Transversal component of the Earth magnetic field
`d_omega`	differential Faraday rotation $d\Omega$ at each ray point
`d_deltacm`	differential phase shift induced by Cotton-Mouton effect
`a_`*`p_hyd`*	Differential attenuation for p polarization induced by *hyd* (rain/ice)
`k_`*`p_hyd`*	Differential phase delay for p polarization induced by *hyd* (rain/ice)

Table 4.5: Database structure for the *ray_points* table.

Part III

RESULTS

5

POLARIMETRIC RADIO OCCULTATION SIMULATED RESULTS

The new polarimetric RO concept and its context has been explained in Part I. Furthermore, the noise level assessment has set a minimum threshold of what PAZ is going to be able to detect. In Part II the theoretical background has provided the tools to perform the simulations, which have been deeply discussed. Combining what has been provided in Part I and Part II, in this chapter there are presented the main results of the simulations applied to the polarimetric experiment. These are the anticipated retrievals that PAZ will provide. In addition, a first approach on how the polarimetric observables can be related to geophysical information is explained.

A brief investigation on how weather forecast model outputs can be used to perform polarimetric simulations is shown. Finally, the ability to disentangle the contribution from the intensity and the contribution from the extension of the precipitation is assessed in the last section of the chapter.

5.1 ANTICIPATED PRODUCTS OF POL-RO OBSERVATIONS

Polarimetric Radio Occultations (Pol-ROs) will scan the atmosphere as standard ROs do, providing vertical profiles of several thermodynamic quantities. In addition, Pol-ROs will also give information about precipitation and frozen hydrometeors in the form of differential polarimetric phase shift, an integrated quantity along the ray path from the GPS to the LEO. The contribution from the hydrometeors will come from the part of the ray crossing the lower troposphere.

The polarimetric phase shift due to the hydrometeors is defined in Section 3.1.5 as:

$$\Delta\Phi^{\mathrm{trop}} = \int_L K_{\mathrm{dp}}(z)\mathrm{d}z,$$

and it is the main observable of any Pol-RO experiment. However, it does not provide explicitly any geophysical information. It will be the aim of this section to link the $\Delta\Phi^{\mathrm{trop}}$ to the rain intensity that the ray has crossed, something that has to be done in a probabilistic way.

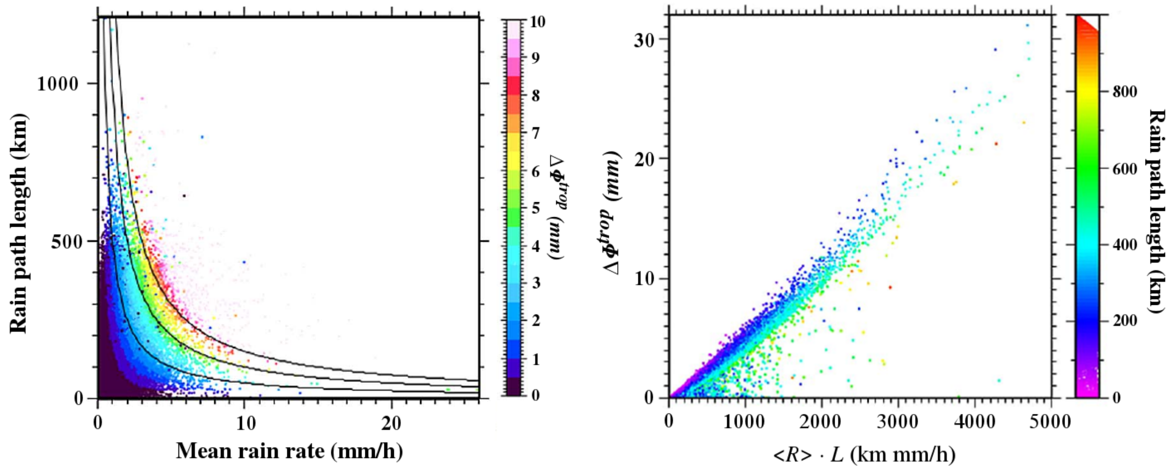

Figure 5.1: Results for the 2D collocated cases that reach the surface level. (Left) The rain path lenght, L, as a function of the mean rain rate long the ray, $\langle R \rangle$, with the colorscale representing the $\Delta\Phi^{\text{trop}}$. The solid lines indicate constant values of $\langle R \rangle \cdot L$. (Right) $\Delta\Phi^{\text{trop}}$ as a function of $\langle R \rangle \cdot L$, with the colorscale representing the L. Figure from Cardellach et al. [2014], Fig 12.

Nevertheless, a sensitivity analysis for the PAZ satellite is presented first. The objective is to assess the magnitude of the rain induced polarimetric features and the percentage of detected cases that are expected, as a function of the rain intensity.

5.1.1 *Sensitivity analysis*

From the $\Delta\Phi^{\text{trop}}$ expression is easy to see how both the rain intensity (effect included in the K_{dp}) and the rain extension (or length) play an important role in the magnitude of the final observable. In fact, it is very difficult to distinguish between both contributions solely analysing $\Delta\Phi^{\text{trop}}$. This is clearly seen using the results of $\Delta\Phi^{\text{trop}}$ for the 2D-collocated cases explained in Section 4.2.4.1. $\Delta\Phi^{\text{trop}}$ is plotted as a function of the rain path length (L) and the mean rain rate along the ray path, $\langle R \rangle$, in Figure 5.1-left panel. $\Delta\Phi^{\text{trop}}$ is plotted as a function of ($\langle R \rangle \cdot L$) in the right panel. Only those RO events that reach the surface level are plotted. It can be seen how different combinations of $\langle R \rangle$ and L can lead to similar values of $\Delta\Phi^{\text{trop}}$.

From the values of $\Delta\Phi^{\text{trop}}$ in Figure 5.1 it is possible to infer how many of them would have been detectable. Using the information from Table 2.2 and given that the cases plotted in Figure 5.1 correspond to events that reach the surface, it is possible to state that those points with $\Delta\Phi^{\text{trop}} < 1.4$ mm would not be detectable (the points in the darkest blue region in the left panel of Figure 5.1). Hence, the % of events that are going to be detectable if they exceed a certain $\langle R \rangle$ is quantifiable, and it is shown in the middle column of Table 5.1.

The same kind of exercise can be performed with the 3D collocated RO events with the TRMM satellite, from the database introduced in Section 4.4. In this case,

Precipitation intensity $\langle R \rangle$	% detectable cases (2D)	% detectable cases (3D)
> 0.5 mm/h	24 %	31 %
> 1 mm/h	41 %	44 %
> 2 mm/h	72 %	62 %
> 3 mm/h	83 %	72 %
> 4 mm/h	88 %	79 %
> 5 mm/h	90 %	84 %
> 10 mm/h	95 %	93 %

Table 5.1: Percentage of collocated cases where rain induce a polarimetric phase shift above the detectability level, for both the 2D collocation exercise and the 3D collocation exercise.

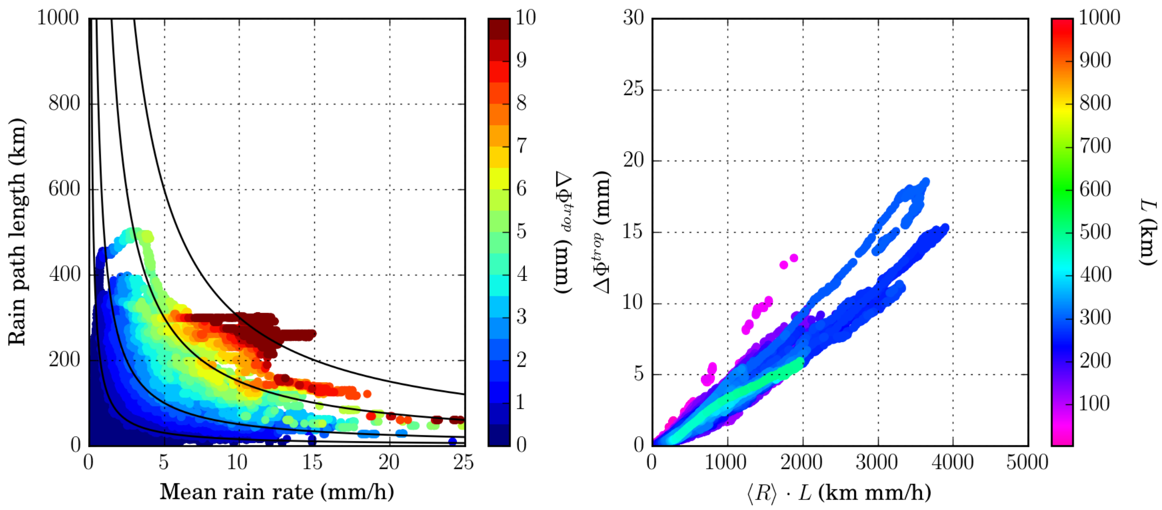

Figure 5.2: The same as in Figure 5.1, but for the 3D collocated cases.

it is possible to work ray by ray, since all the information is available for each of them. The same results as in Figure 5.1 are shown in Figure 5.2 for the 3D collocation case. In addition to a less number of RO events, the 3D collocations can have the L reduced due to the fact that the TRMM radar swath is limited, and ROs oriented perpendicular to the travel direction of the radar can be truncated. The results for the % of detectable cases for the 3D collocated events that exceed a certain $\langle R \rangle$ are shown in Table 5.1, right column. Both the results from the 2D and the 3D collocations show a reasonable agreement, taking into account the different approaches. From both can be stated that the detectability increases with $\langle R \rangle$, and that most of the moderate to heavy precipitation events will be detectable with PAZ.

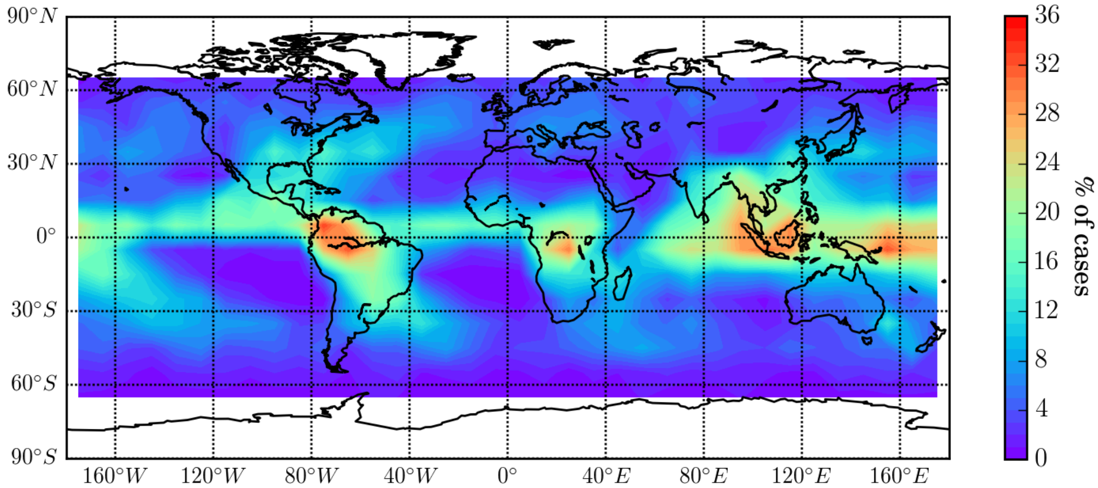

Figure 5.3: Global map of the percentage of detectable cases for all the GPM fake collocations.

5.1.1.1 *Geographical and seasonal patterns*

Using the *fake* 3D collocations described in Section 4.2.4.2 and the results already obtained from the sensibility analysis using the 2D and the 3D collocations, the geographical and seasonal patterns can be investigated. For this exercise the detectability threshold from Table 2.2 is used for all the observations, as a function of the tangent point's height. Then, a Pol-RO event is identified as detectable if any of its $\Delta\Phi^{\mathrm{trop}}(h_{\mathrm{tp}})$ measurements exceed this detectability threshold. A global map with the percentage of detectable cases out of all the GPM fake collocations is shown in Figure 5.3. Comparing Figure 5.3 with Figure 4.24 it can be seen how certain regions tend to have rain that will be more detectable than other regions. For example, rain events in central Africa will be more detectable than those in the Indian ocean, which are more frequent.

The same kind of analysis can be performed separating the events by season. The percentage of detectable cases depending on the season is shown in Figure 5.4. Here it can be seen how the detectable cases increase in the corresponding summer in each region. Therefore, there are more detectable cases in the northern hemisphere during the July-August-September season. On the other hand, there are more detectable cases in the southern hemisphere during the January-February-March season. Near the equator, the percentage of detectable cases remains more or less constant for all seasons. The spring and autumn seasons show similar patterns.

Finally, the percentage of detectable cases depending on the rain intensity is shown in Figure 5.5. The patterns for the lightest rain threshold ($\langle R\rangle > 0.1$ mm/h) show the same features as Figure 5.3, as it is expected. When rain intensity increases, the detectability also increases with similar patterns as shown in Figure 4.24, and

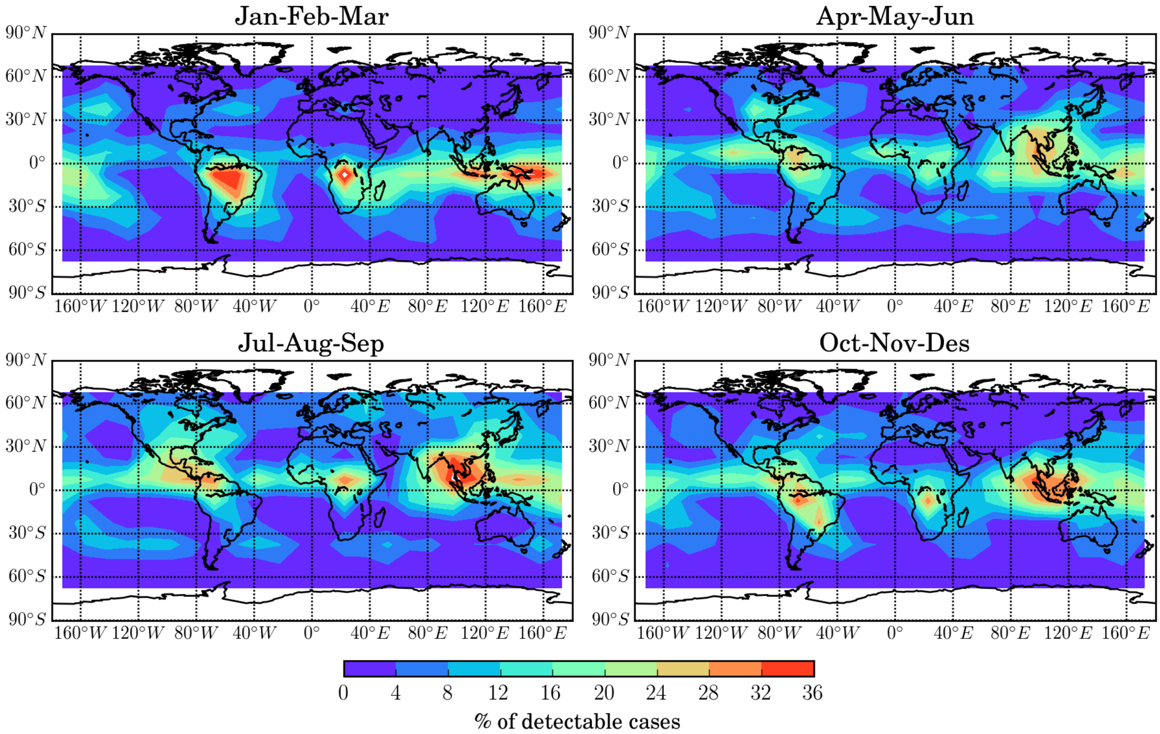

Figure 5.4: Seasonal distribution of the % of detectable cases.

with percentages in agreement with Table 5.1. When the $\langle R \rangle$ is high enough, most of the events are detectable regardless of the region. Hence, this exercises enhance the consistency among all the exercises that have been performed in the previous sections.

5.1.2 *Probability of precipitation exceedance*

In the previous section, the probability for an event exceeding a certain $\langle R \rangle$ to be detectable has been estimated. Here, the inverse approach is addressed:

> what $\langle R \rangle$ has been exceeded by an observation with a certain $\Delta\Phi^{\text{trop}}$?

Solving this question establish a relationship between a geophysical quantity, the $\langle R \rangle$, and the $\Delta\Phi^{\text{trop}}$ observation, although it remains probabilistic. To perform such calculations, a Look Up Table (LUT) that relates each $\Delta\Phi^{\text{trop}}$ with a $\langle R \rangle$ has to be build with a huge number of cases. Ideally, these cases have to be well distributed in time and space to capture seasonal and geographic patterns. To do so, the set of artificial Pol-RO observables generated and explained in Section 4.2.4.2 is used.

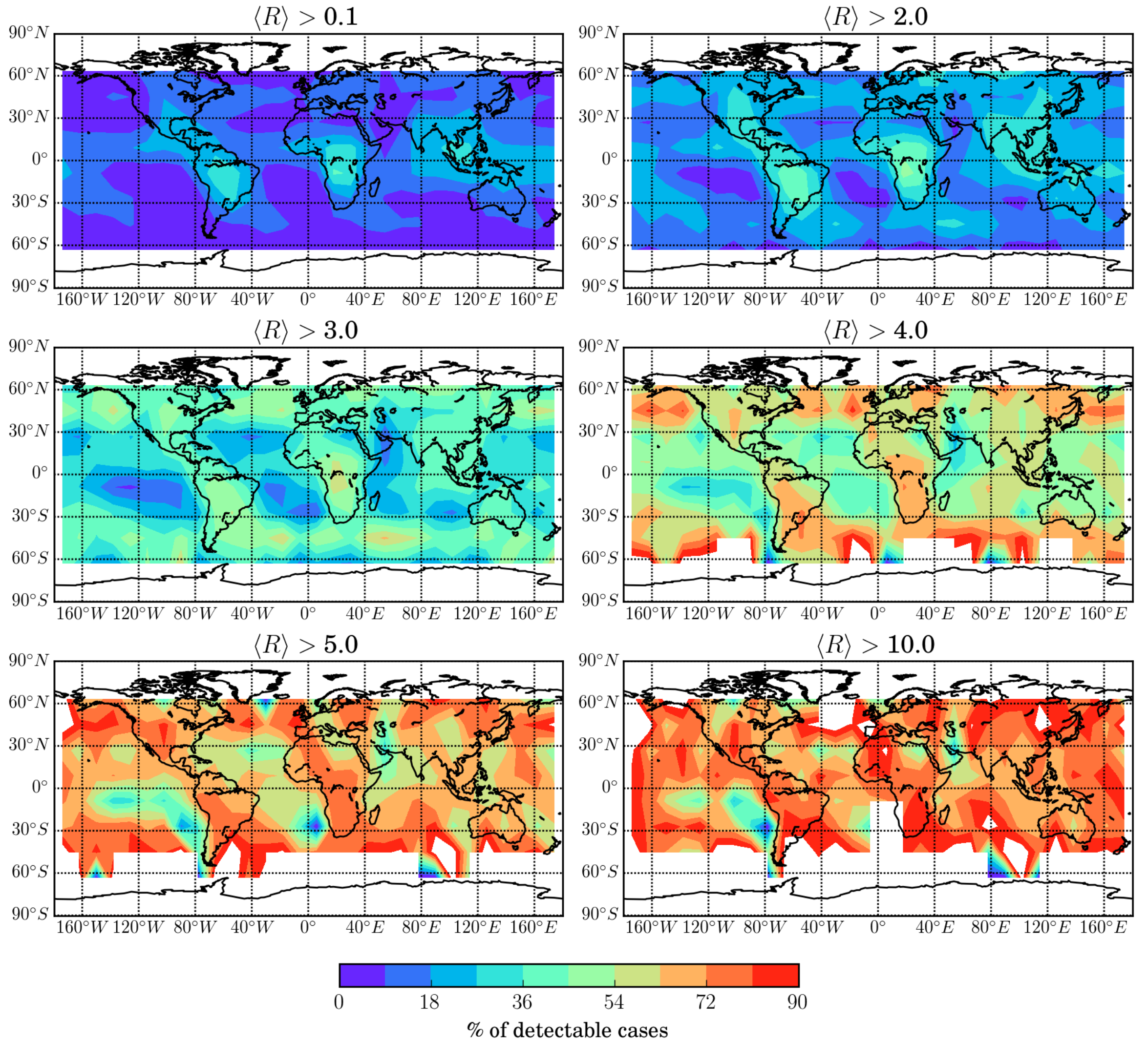

Figure 5.5: Geographical distribution of the % of detectable cases, for different $\langle R \rangle$, indicated on top of each panel.

5.1.2.1 *Look-Up Tables*

With all the simulated Pol-RO observables, a LUT is built. The observations can then be then checked against this LUT to relate the observed quantity to a geophysical one, in a probabilistic way. In this case, one needs to relate the $\Delta\Phi^{\text{trop}}(h_{\text{tp}})$ with the $\langle R \rangle(h_{\text{tp}})$. The LUT is built following the procedure below:

- All the observations are classified as a function of its $\Delta\Phi$ magnitude and as a function of its h_{tp}, in a two dimensional grid. Each bin is defined so that it has a width of 0.5 mm-delay and a height of 0.25 km, and must have at least 4 events in it to contribute to the LUT. The observations that have not crossed rain are excluded.

- Each $\Delta\Phi^{\text{trop}}(h_{\text{tp}})$ value has a $\langle R \rangle$ that corresponds to that same observation. Hence, the $\langle R \rangle$ values are implicitly classified according to $\Delta\Phi^{\text{trop}}(h_{\text{tp}})$.
- The 25th percentile of the $\langle R \rangle$ values of each bin is determined, i. e. a value is defined so that the 75% of the $\langle R \rangle$ data in the bin is larger than it.
- Therefore, a $\langle R \rangle^{25\text{th}}$ is defined for all the $\Delta\Phi^{\text{trop}}(h_{\text{tp}})$ grid, so that it is possible to state that the 75% of the times that an observation has a certain value $\Delta\Phi^{\text{trop}}(h_{\text{tp}})$, it will correspond to a $\langle R \rangle$ larger than the corresponding $\langle R \rangle^{25\text{th}}$.

The LUT built for all the data is shown in Figure 5.6. The LUT establish the mean precipitation intensity $\langle R \rangle$ that an observation is likely to be exceeding. Several other LUTs are afterwards constructed. First, two LUTs that account for the 5th and the 50th percentile of $\langle R \rangle$. The former indicates the $\langle R \rangle$ that will be exceeded the 95% of the time that an observation has a given $\Delta\Phi^{\text{trop}}(h_{\text{tp}})$. The later states the $\langle R \rangle$ that is equally likely to be exceeded or not, given a $\Delta\Phi^{\text{trop}}(h_{\text{tp}})$. The combination of these three LUTs give a complete probabilistic view of the scenario, with three representative thresholds: 5th, 25th and 50th percentiles. The same exercise is performed using the maximum R crossed along the ray path, R_{max}, instead of $\langle R \rangle$. All these LUTs for the whole set of data are shown in Figure 5.7. The lower the percentile, the more conservative the relationship between the observable and the geophysics quantity, in terms of intensity. Moreover, with a more conservative threshold the confidence in the relationship is larger.

The best possible scenario would be to have LUTs like the described ones for every region and every season. However, having this depend on the amount of data that is available. While for low values of $\Delta\Phi$ and low altitudes a decent number of cases is relatively easy to be obtained, to build a complete LUT requires large statistics. Let's define four parameters to estimate the completeness of LUTs, i. e. how populated the defined grid is: the maximum $\Delta\Phi$ (14 mm in the case of Figure 5.6); maximum height (11 km in the case of Figure 5.6); % of populated bins (70 % in the case of Figure 5.6); and the bin size (0.5 mm $\times$ 0.25 km in the case of Figure 5.6). The construction of a regional LUT has been attempted, using regions of 20 $\times$ 20 degrees, equally distributed around the globe in the -60,60 latitude range. The grid size used is 0.75 mm-delay $\times$ 0.5 km, and the results for the parameters that account for the completeness of the LUTs are shown in Figure 5.8. All the generated LUTs are shown in Figure 5.9.

One obvious conclusion from the regional LUTs is that in the regions where the rain is less frequent, more observations are needed in order to populate the LUTs. These results also show the different characteristics of the rain in different regions. For example, there are regions where with less observations, a larger portion of the grid is populated. This means that even though rain might be less frequent, the kind of rain is more likely to induce large $\Delta\Phi^{\text{trop}}(h_{\text{tp}})$. Hence, it make sense to apply different LUTs for observables in different regions. In this direction, all the LUT for the different regions can be compared looking at Figure 5.9. It can be seen how the LUTs, in addition to be differently populated, show different rain

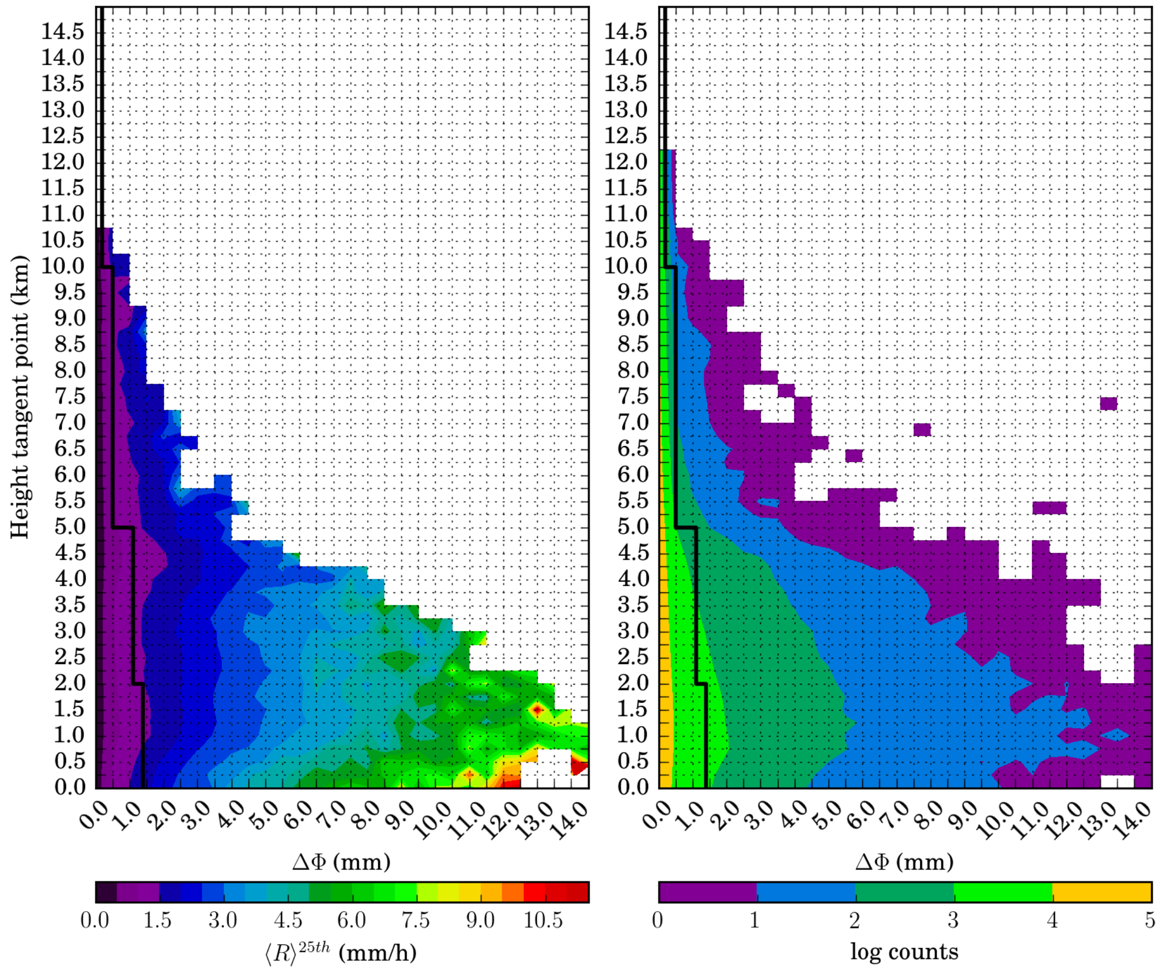

Figure 5.6: Look Up Table to relate a $\langle R \rangle$ to a $\Delta\Phi^{\mathrm{trop}}(h_{\mathrm{tp}})$ observation. (Left) The values of the 25th percentile of $\langle R \rangle$ as a function of $\Delta\Phi^{\mathrm{trop}}$ and the height of the tangent point. (Right) The number of observations that lay in each of the bins of the defined grid. The solid black line indicates the detectability threshold, according to Table 2.2.

characteristics. For example, the $\langle R \rangle^{25\mathrm{th}}$ associated to a certain $\Delta\Phi^{\mathrm{trop}}(h_{\mathrm{tp}})$ varies from region to region.

The differences in $\langle R \rangle^{25\mathrm{th}}$ among different regional LUTs are further investigated in Figure 5.10. Each LUT is compared with all the rest in the following way. First, the Earth globe is split into 20×20 deg bins, which are represented like in Figure 5.9. Here, instead of filling the bins with the corresponding LUTs, they are filled with the same 20×20 deg grid. Then, for a given location i, all the LUTs corresponding to another location j are subtracted from the LUT at that location i, element-wise. That is, all the $\langle R \rangle^{25\mathrm{th}}$ of the LUT i, corresponding to each $\Delta\Phi^{\mathrm{trop}}(h_{\mathrm{tp}})$, are compared to the $\langle R \rangle^{25\mathrm{th}}$ of the other LUT j corresponding to the same $\Delta\Phi^{\mathrm{trop}}(h_{\mathrm{tp}})$. Then, the mean value of the resulting grid is taken and represented in the j location of the i

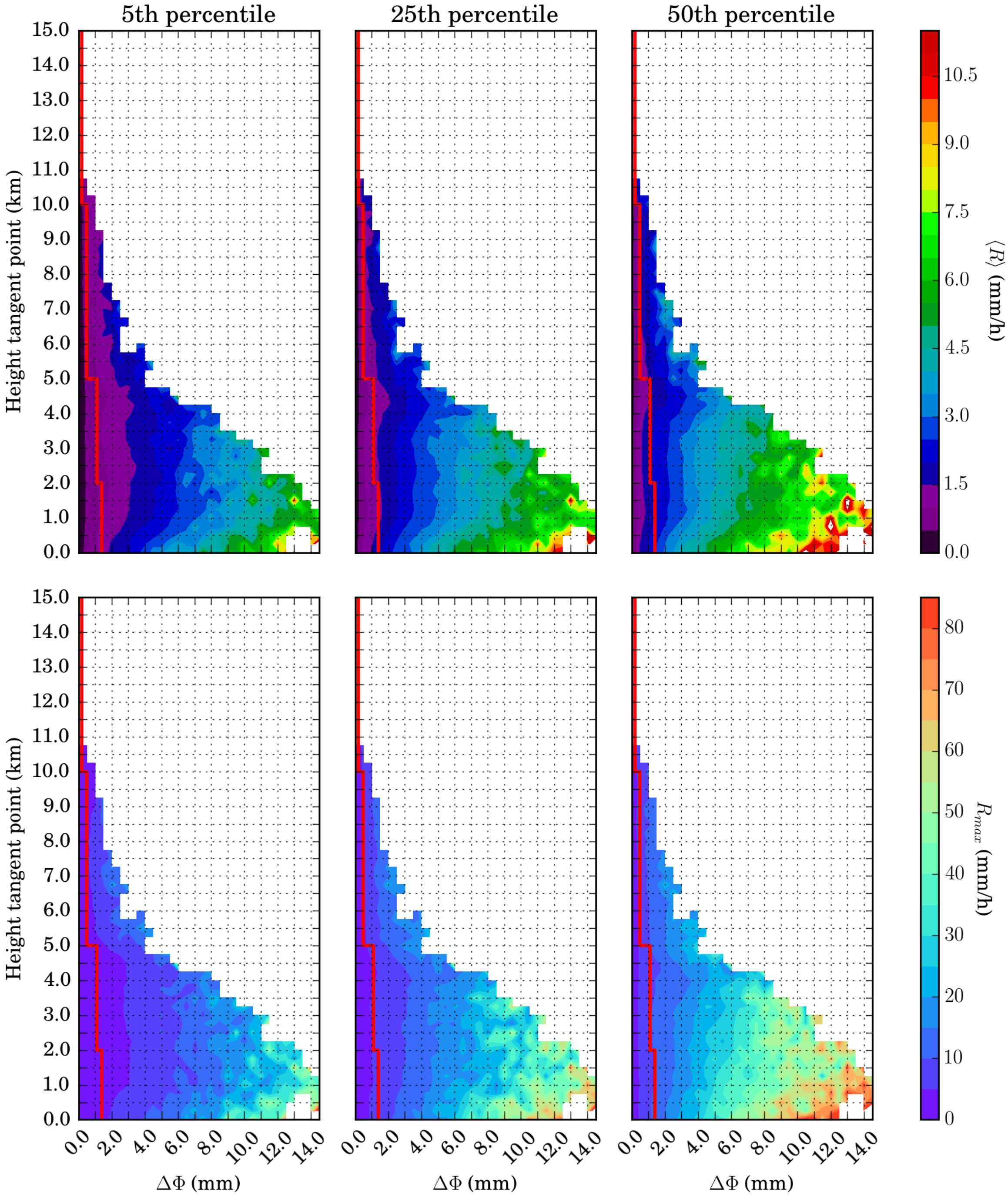

Figure 5.7: The three representative LUTs for $\langle R \rangle$ and R_{max}. From left to right, the values for the 5th, 25th and 50th percentiles, respectively. The top row shows the values of $\langle R \rangle$ and the bottom row the values for R_{max}. The solid red line indicates the detectability threshold.

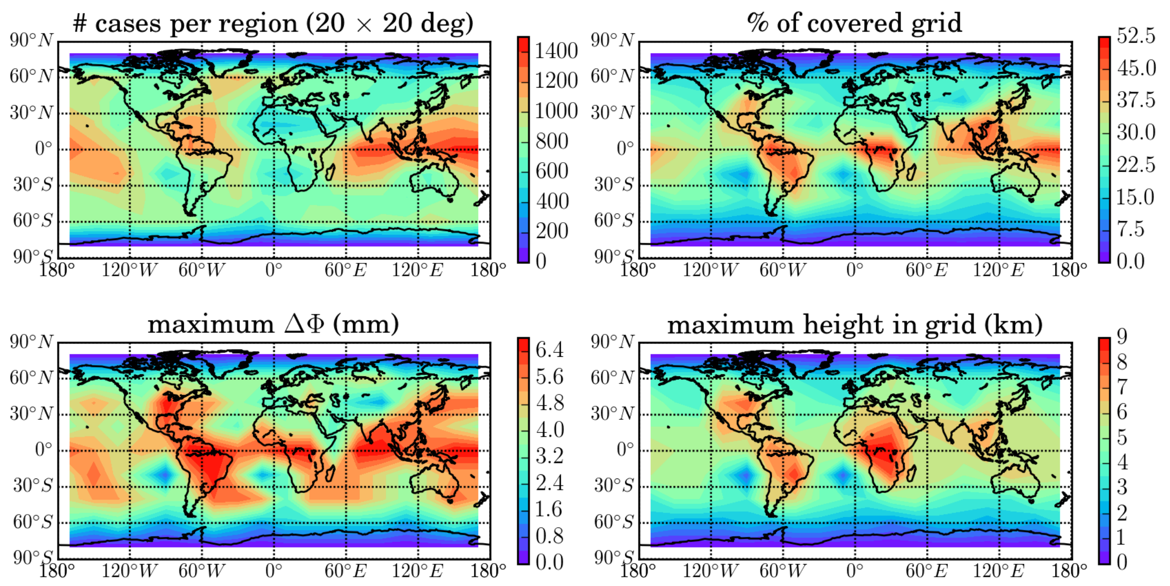

Figure 5.8: Statistics for the regional LUTs. (Top left) Number of Pol-RO events that are populating the corresponding regional LUT with at least one of its observations, i. e. one of the rays of this Pol-RO crossed rain; (Top right) % of the grid that is covered. In Figure 5.6 and Figure 5.7, using all data, the grid up to 14 mm and 11 km was covered in its 70%; (Bottom left) Maximum $\Delta\Phi$ with a populated bin; (Bottom right) Maximum height with a populated bin.

grid. Therefore, at each location i, there is a grid with all the locations j containing the mean value of the LUTs differences:

$$\left[(\Delta\widehat{LUT})^j\right]_i = \frac{1}{N_{\text{bins}}}\sum_n \left((\langle R\rangle^{25\text{th}})^i_n - (\langle R\rangle^{25\text{th}})^j_n \right)$$

where n represents each of the grid bins of a given LUT, hence going from 0 to N_{bins}; and i and j indicate the location, hence the (lon,lat) pair that identifies each LUT. There are 9 divisions in latitude and 18 divisions in longitude, which imply that there are a total of 162 location (lon,lat) pairs. Therefore, i and j range from 0 to 162.

While each of the bins in Figure 5.9 represent a LUT, with $\Delta\Phi$ in the x axis and h_{tp} in the y axis, in Figure 5.10 each of the bins represent the whole globe, being longitude in the x axis and latitude in the y axis. Therefore it is easy to identify visually the main differences among the different regional LUTs. The most obvious difference is between the tropics and mid-latitudes. The values for $\langle R\rangle^{25\text{th}}$ are larger in the tropics than outside for the same observed $\Delta\Phi^{\text{trop}}(h_{\text{tp}})$. There are also differences among LUTs in the same latitudes, although these are more subtle. This exercise explicitly show the need of comparing the observations to the corresponding regional LUT, which represents better the characteristics of that region's precipitation. In addition to Figure 5.9 and Figure 5.10, the corresponding figures for the 5th and 50th percentiles, and for the R_{max} instead of $\langle R\rangle$ are also

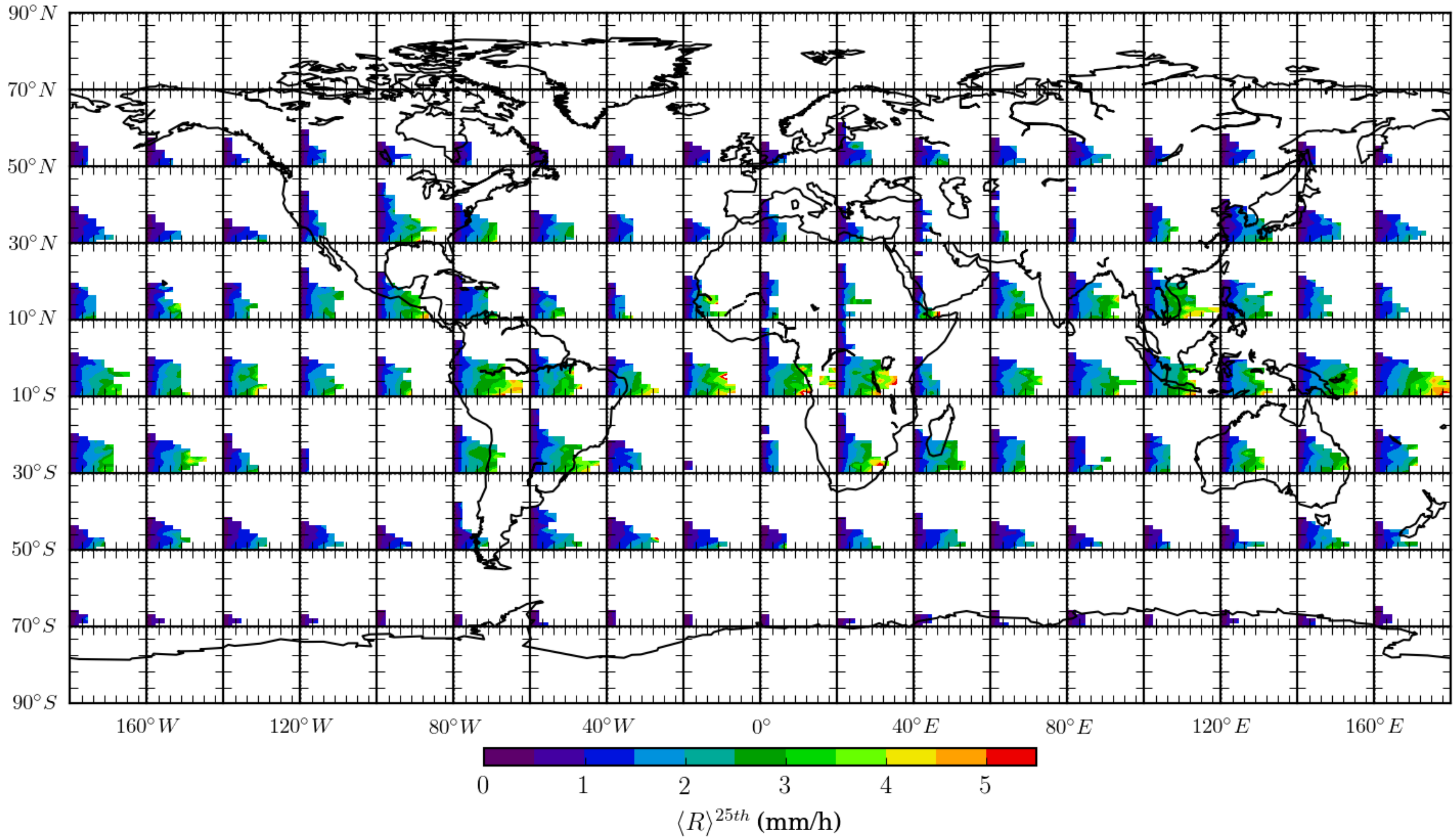

Figure 5.9: Regional LUTs. The limits of each of the bins are $0 < \Delta\Phi^{\mathrm{trop}} < 7.5$ for the x axis and $0 < h_{\mathrm{tp}} < 10$ for the y axis.

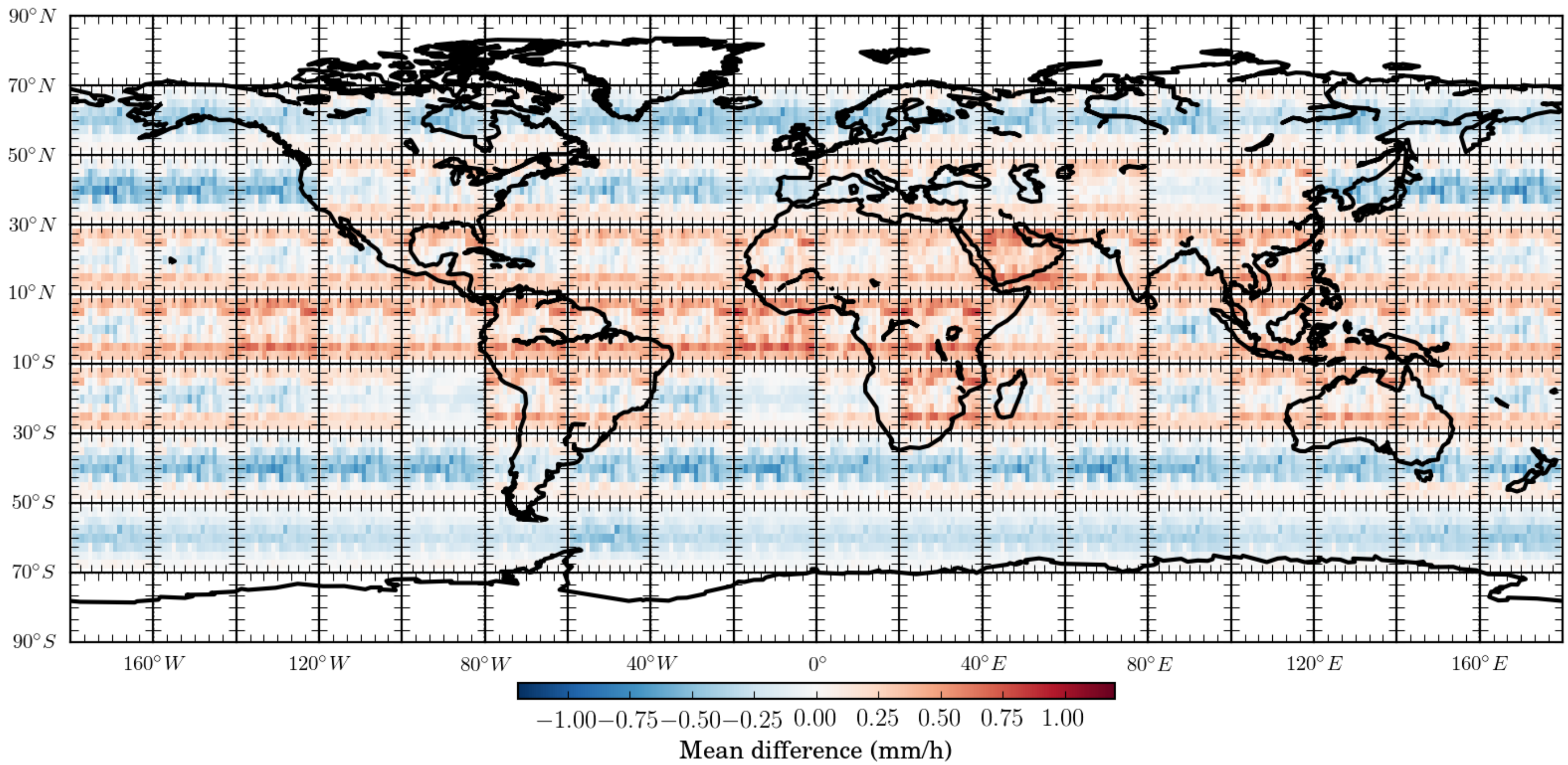

Figure 5.10: Regional mean R differences among all LUTs. Each of the bins represents the difference between the LUT corresponding to that (lon,lat) minus all the remaining LUTs, so that each bin has all the longitud and latitude represented.

build, and can be found in Appendix A. Also, there have been built the same figures for the maximum differences, instead of mean values:

$$\left[(\Delta LUT)^j\right]_i^{\max} = \max\Big\{ \left((\langle R\rangle^{pth})_1^i - (\langle R\rangle^{pth})_1^j\right), \left((\langle R\rangle^{pth})_2^i - (\langle R\rangle^{pth})_2^j\right), \dots, \left((\langle R\rangle^{pth})_{N_{\text{bins}}}^i - (\langle R\rangle^{pth})_{N_{\text{bins}}}^j\right) \Big\}$$

where pth is the percentile, which can be the 5th, the 25th and the 50th.

New observations are obtained every day, therefore the LUTs can be improved daily. These LUTs have to be populated as much as possible so they become statistically significant. In addition to the regional LUTs shown above, seasonal classifications would improve even more the applicability of these LUTs, since rain patterns change with season (as is been shown in Figure 5.4). However, not enough observations are yet available to perform such classification. However, this exercise shown the methodology that will be followed once enough observations are obtained. A dedicated study on the performance and applicability of the generated LUTs is published in [Cardellach et al., 2017, *submitted*].

5.2 SIMULATIONS USING WRF MODEL: APPLICATIONS TO AIRBORNE RO

In the context of an RO airborne campaign conducted by Scripps Institution of Oceanography (SIO), a few simulations exploring the feasibility of detecting significant Pol-RO signatures were performed using Weather Research and Forecasting (WRF) model outputs. The two moment microphysics scheme implemented in the WRF model provides information of the mass mixing ratios and number concentration for several hydrometeor species, and can be used to obtain their PSD [e. g. Morrison et al., 2009]. Therefore, the WRF model outputs are well suited to be used as inputs to perform the polarimetric simulations.

The case in study was an atmospheric river [Neiman et al., 2008] hitting the west coast of the United States around February 6th 2015. Several flights were performed collecting airborne ROs. The aim of this study was to identify in which of the flight tracks the link between the airplane and the GPS was crossing rain, and whether significant rain inducing noticeable $\Delta\Phi^{\text{trop}}$ would be present or not. The experiment was performed by Dr. J. Haase and her group at SIO, and the data from the model and the plane trajectories were provided by Dr. M. Murphy (SIO).

The WRF model predicts the total number concentration, N, the mixing ratio q and the specified μ for all hydrometeor species, and they can be used to obtain the gamma PSD parameters (e. g. Equation 3.51) as follows [Morrison et al., 2009]:

$$\lambda = \left[\frac{cN\Gamma(\mu+d+1)}{q\Gamma(\mu+1)}\right]^{\frac{1}{d}} \tag{5.1}$$

$$N_0 = \frac{N\lambda^{\mu+1}}{\Gamma(\mu+1)} \tag{5.2}$$

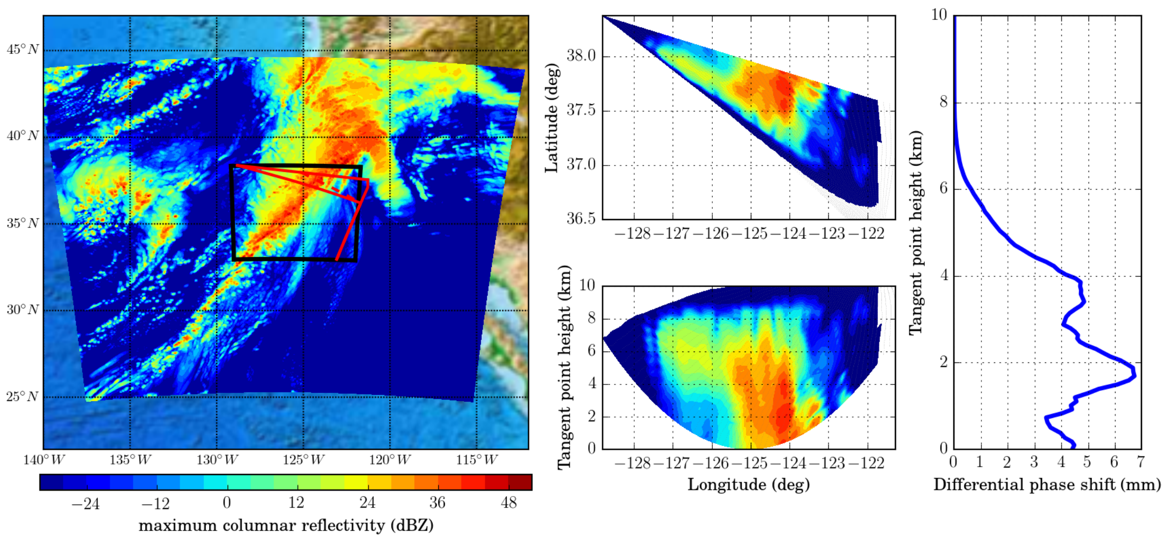

Figure 5.11: (Left) In red, the contour that delimitates the RO links between the GPS and the airplane across the atmospheric river, characterized by the maximum reflectivity in each vertical column. The black rectangle indicates the portion of data used for the simulations. (Center) The radar reflectivity derived from the WRF model outputs interpolated into the RO ray trajectories, projected in the longitude-latitude plane (top) and projected into the longitude - height plane (bottom). (Right) The simulted $\Delta\Phi^{trop}$ as a function of the tangent point's height.

where Γ is the Euler gamma function, and c and d are the parameters of the power law mass-diameter ($m - D$) relationship of the hydrometeors, where $m = cD^d$. These parameters can be found, for example in Straka [2009]. Once the PSD is obtained, it is straightforward to derive the $\Delta\Phi^{\text{trop}}$ using the simulation results shown in Chapter 4, and Equation 3.38 and Equation 3.40. The ray-tracer mentioned in Section 4.2.2 is used to obtain the RO ray trajectories, using the airplane trajectory, the GPS position, and the vertical refractivity profile predicted by the model.

5.2.1 *Case examples*

Besides $\Delta\Phi^{\text{trop}}$, deriving the radar reflectivity that is obtained from the computed PSD is useful in terms of comparison with previous exercises. In the Rayleigh regime it can be computed using Equation 3.62. The derived Z and the simulated $\Delta\Phi^{\text{trop}}$ for the strongest of the studied cases is shown in Figure 5.11. The figure shows the flight track, the radar reflectivity interpolated into the RO links, and the simulated $\Delta\Phi^{\text{trop}}$ that results from the interpolation.

The case in Figure 5.11 shows an scenario that, according to the WRF model predicted outputs, the Pol-RO would have measured detectable phase shifts. Therefore, airborne Pol-ROs must be taken into account in the future as a possibility as well.

5.3 TOMOGRAPHIC APPROACH

The main observable of the Pol-RO technique is the polarimetric phase shift. The fact that it is an integrated measurement that is contributed all along the ray path induces an ambiguity between the contribution of the intensity and the extension of the observed phenomena that is very difficult to disentangle. In an attempt to disentangle the two contributions, a two dimensional tomographic approach has been proposed. This section is based on Padullés et al. [2016b].

Tomographic techniques are based on a reconstruction of a cross-sectional imaged object by solving a set of line integrals, obtained from scanning the object from different directions [Herman, 2009]. In this case, the 2 dimensional object that has to be reconstructed is the rain intensity mapped into the RO plane, i.e. the vertical surface where the radio-links are contained. The RO plane is divided into a set of two dimensional voxels. Each voxel is crossed by several consecutive rays with slightly different directions. Therefore, the length of each voxel that is crossed by each ray is different. This allow to construct a linear set of equations, and the inversion of the rain intensity at each voxel is attempted by solving it. Due to the geometry of the problem, the variety of directions at which voxels are crossed is more restricted than in standard tomographic techniques. For this reason, additional constraints are needed to obtain robust solutions.

5.3.1 *Technique*

The aim here is to untangle the along-ray integrated rain information provided by $\Delta\Phi^{\text{trop}}(h_{\text{tp}})$ using tomographic techniques. In order to apply the tomographic approach, the problem needs to be discretized, and a grid of voxels is created. Each voxel has the same area and the aim is to retrieve the mean rain intensity within its boundaries. The choice of the voxel's size defines the resolution of the tomographic solution. In Figure 5.12 there is a visual representation of the voxels and the ray's geometry.

Each ray i of the RO has a $\Delta\Phi$ measurement associated. Hence, each $\Delta\Phi_i$ can be modelled as the sum of the contribution of the K_{dp}^j corresponding to each voxel j times the length that the ray has crossed that voxel, L_i^j:

$$\Delta\Phi_i = \sum_j L_i^j K_{\text{dp}}^j \tag{5.3}$$

where i indicates the number of rays and j the number of voxels. This configuration leads to a linear problem of the form $\mathbf{d} = \mathbf{Gm}$, where $\mathbf{d}$ is an array of observed $\Delta\Phi_i$, typically of dimension 1300 (approximate number of rays of RO observations performed normally at 50 Hz in the lower troposphere), $\mathbf{G}$ is the contribution matrix of elements L_i^j (i.e. the data kernel), and $\mathbf{m}$ is the array of K_{dp}^j, the unknown to be inverted. The defined grid for $\mathbf{G}$ has a resolution of approximately 9.5 km in the horizontal and approximately 250 m in the vertical. The resolution is determined

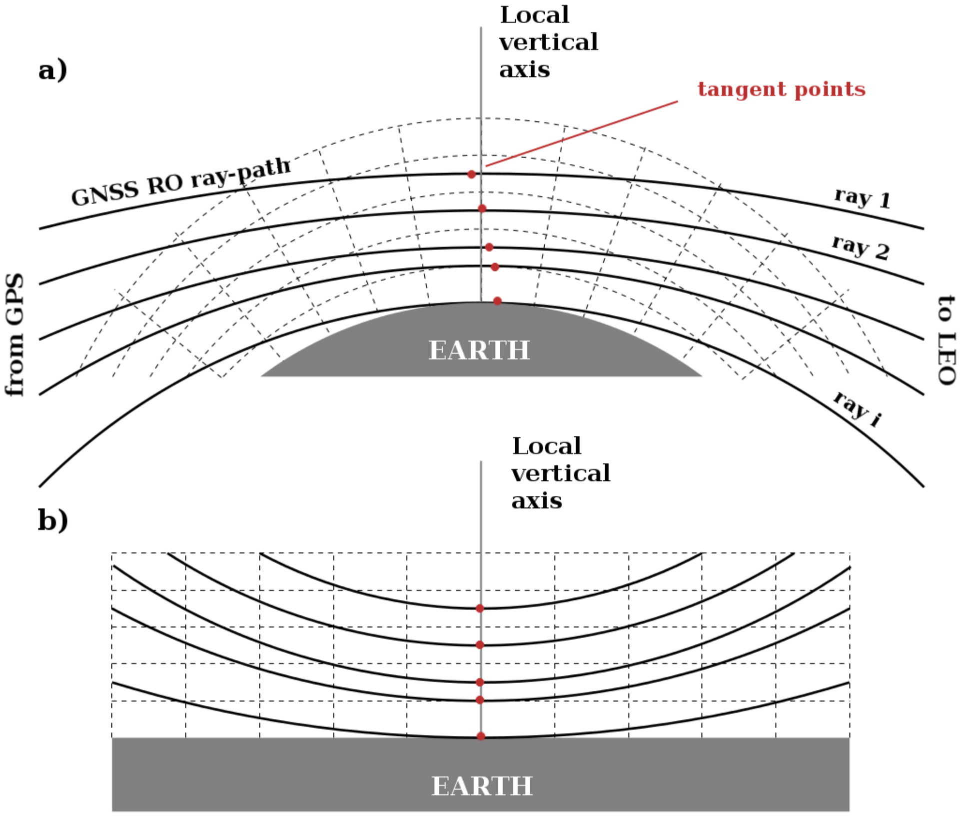

Figure 5.12: Sketch of the tomographic approach across the propagation plane. Only a few rays are displayed for clarity purposes. (a) Representation of the geometry of the rays and the voxels; (b) Same as in the (a) panel, but represented as a function of the local altitude and along-ray angular distance to the tangent point. Figure from Padullés et al. [2016b], Fig.1.

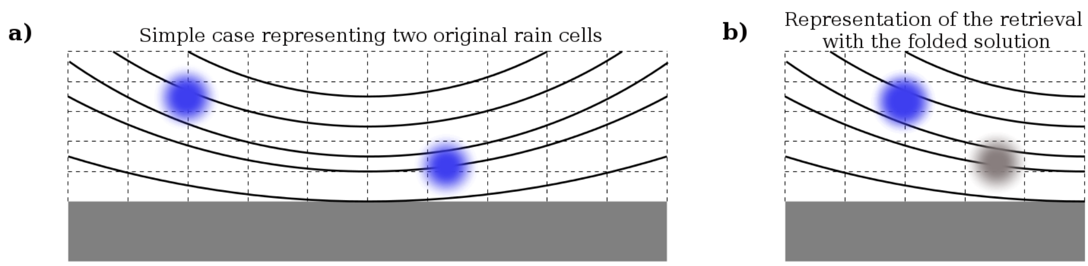

Figure 5.13: (a) Theoretical representation of two rain structures superimposed in the RO plane; (b) the retrieval that would be obtained with the tomographic technique. It is shown how, due to the folded solution, the two rain structures shown in (a) are obtained in the left half of the RO plane. In blue, the rain structure that is retrieved in its original position, and in grey the rain structure retrieved in a symmetrical position but in the opposite half of the RO plane (mirror ambiguity). Figure from Padullés et al. [2016b], Fig.1.

by the precipitation data that is used in the simulations, i. e. the TRMM and GPM products, since the simulated results are going to be checked against these data. Then, the linear problem defined in Equation 5.3 is solved using the least squares criterion [e. g. Tarantola, 2005]:

$$m = (G^T G)^{-1} G^T d \tag{5.4}$$

In order to ensure that Equation 5.4 has a solution, and that is as close as possible to the true one, some simplifications and constraints have to be applied to the system. The simplifications relate to the RO plane and are the following:

- To align all the rays in order to have the tangent point at the same position on the horizontal axis. This simplification can be seen in Figure 5.12, with red dots.
- To invert only half of the RO plane, i. e. the part of the rays from the GPS (or the LEO) to the tangent point. Figure 5.13 shows this simplification.

The RO plane it is not a vertical plane, but it is a surface defined by the positions of the GPS and the LEO at each time. Therefore, it implies a slant scanning of the rain, rather than vertical. Forcing each ray to have the tangent point aligned in the horizontal dimension restricts the movement of the tangent point to one dimension, although the true movement is in two dimensions (latitude and longitude). The error that the first simplification is adding to the retrieval depends on the movement of the tangent point. In the cases used in this work, the projection of the movement into one dimension is smaller than the resolution of the technique. However, depending on the RO geometry there can be cases where the tangent point movement is large [Foelsche et al., 2011] and the first simplification could be adding errors.

The second simplification is a critic one. The reason why it has to be applied is the geometrical symmetry between the **G** elements on either side of the tangent point. Due to the spherically symmetric atmosphere assumption (see Section 4.2.2), the rays are identical at both sides of its tangent point, and this geometrical feature would lead to a non-invertible system. What is suggested is to solve the system assuming that only one half of the RO plane exists. Since the observable ($\Delta\Phi(h_{\mathrm{tp}})$) is anyway scanning the whole ray, the solution will include the rain information from both plane halves in the retrieved half-plane (folded solution). That is, the size and intensity of the precipitation cells is solved but the solution has mirror-ambiguity with respect to the tangent point. Thus, at a first approximation, the solution will only tell the distance at which the rain cells are from the tangent point (beside size of the cells and intensity). This is sketched in Figure 5.13: in panel *a* there is a representation of two rain structures, and in panel *b* the retrieved structures affected by the mirror-ambiguity.

The main constraint that we apply to help the invertibility of the system is the clustering of the rain voxels:

- Each voxel intensity is assumed to be a linear combination of its surrounding voxels intensities

This condition forces a smooth behaviour of the rain cells with respect of the surroundings. This constraint reduces the degrees of freedom of the system and yields more robust solutions.

Note that both the simplifications and the constraints could benefit from external information, such as meteorological models. This would require a dedicated study not covered in this section, which is focused on a first attempt to apply 2-D tomographic techniques for individual RO events. If the technique is shown to have a good performance with stand-alone information, taking into account the aforementioned limitations, further analysis could be made using forecast models information. This could help on distinguishing among contributions coming from different areas mapped into the single RO plane half, according to the probability of precipitation, for example.

After applying the simplifications and the constraint, the system is inverted using a two-step procedure. First, a regularization method called Truncated Single Value Decomposition (TSVD) [Hansen, 1987] is used. This method increases the stability of the solution with respect to the standard one by removing the smallest eigenvalues. Otherwise, tiny modifications of the input could induce big changes in the output, leading to unrealistic solutions. At this point, two more constraints are defined:

- The rain intensity solution obtained with the TSVD method is used to define a mask: those voxels with an intensity above a certain threshold are candidates to hold rain, while the rest are assumed not to contain any rain in it;

- Those voxels placed in the lowest and closest to the tangent point areas in the RO plane are neglected, if their retrieved rain intensity is much higher than those placed right above them. The reason is that the lowest rays of the RO tend to introduce an overestimation of the rain intensity in the area closest to the tangent point. This happens when the RO is less dense in the lowest part, in terms of number of rays. Thus, the remaining voxels are added to the previously defined mask.

The first step has constrained the rain to certain voxels, so the K_{dp} space is significantly reduced. It is now possible to proceed with the second step by solving directly Equation 5.4 (no further constraints) within this reduced space of unknowns.

5.3.2 *Simple case simulation example*

The performance of the technique on idealized simulated scenarios is assessed here. To do so, only one half of the RO plane is used to simulate both the source of the observable and the retrieval. Three different sources are simulated. The three of them represent rain, as given by the K_{dp}. The distribution of the K_{dp} is simulated

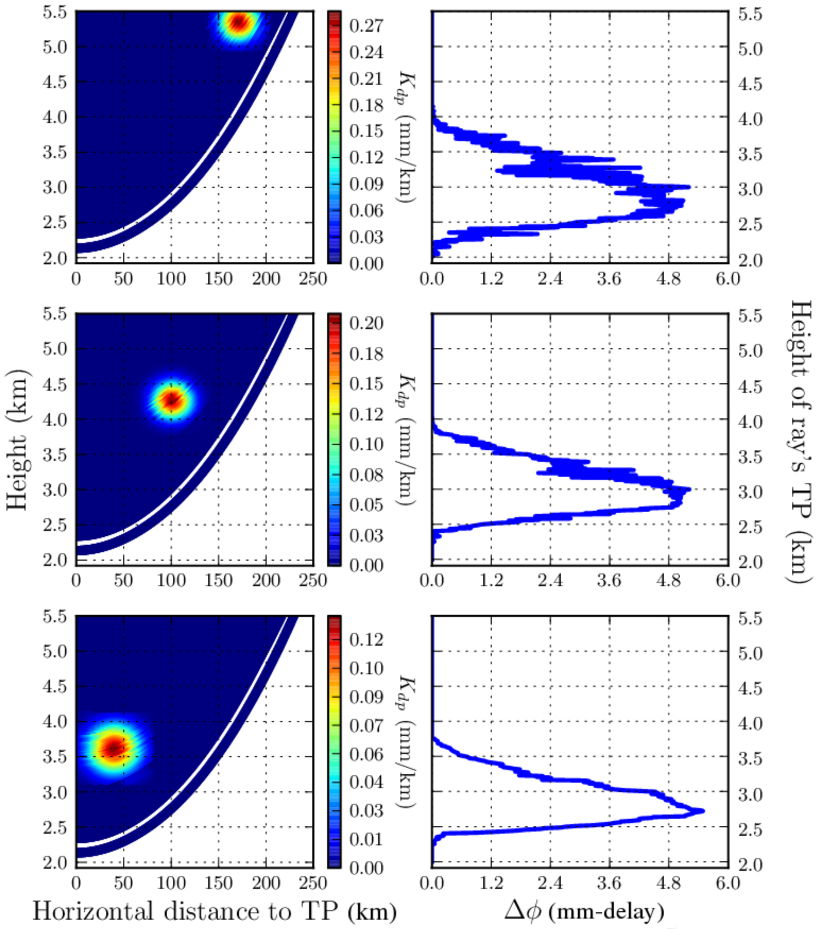

Figure 5.14: Simulated precipitation clouds with similar rain structures placed in different heights and locations across the tomographic plane. (Left) The traced RO rays and the interpolated K_{dp} at each ray-point are shown. The density of rays corresponds to an actual RO observation, which typically scans the lower troposphere with more than 1300 rays. (Right) The corresponding observables, $\Delta\Phi(h_{\text{tp}})$, as a function of each ray's tangent point altitude. Figure from Padullés et al. [2016b], Fig. 2.

as a two dimensional Gaussian, that is mapped into the simulated GNSS signals. For each case, the magnitude of the K_{dp}, its size and its position is different. The integral measurement along the rays is the observable $\Delta\Phi(h_{\text{tp}})$. The three cases are shown in Figure 5.14, left column, and their respective observables are shown in the right column.

The three different cases are thought to have one thing in common: they all produce an observable that has a maximum around the same tangent's point height and the same approximate magnitude. Thus, despite they are placed at three different locations, one observer could not distinguish which one is closer to the tangent point, or which one is placed at a higher altitude, by only looking at the $\Delta\Phi(h_{tp})$

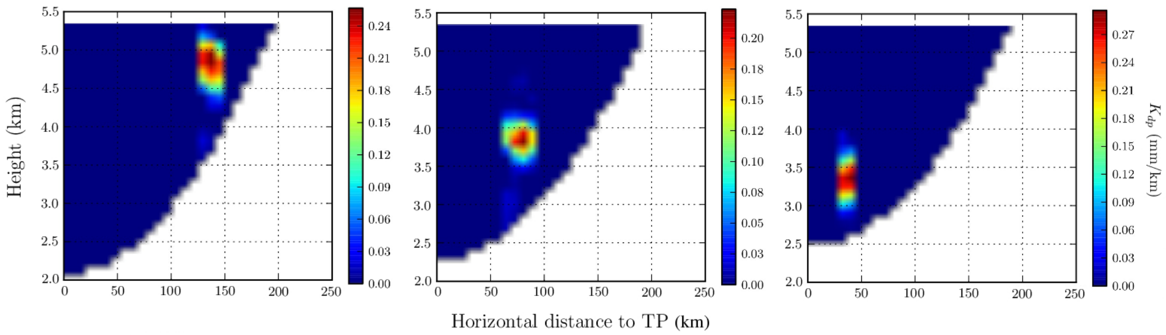

Figure 5.15: The recovered rain structures from the simulated observations in Figure 5.14 using the tomographic approach. Figure from Padullés et al. [2016b], Fig. 3.

profile. The same way, one cannot tell either if the contribution to the observable peak comes from a concentrated intense point or a sparse distribution of light rain.

In Figure 5.15 there is shown the result of applying the tomographic approach, following the method explained in previous section, to the observables in the right panel of Figure 5.14. The conclusions one can obtain from the results in Figure 5.15 are the following:

Qualitatively, the results of the tomographic approach provide more information and of greater value than the $\Delta\Phi(h_{\text{tp}})$ alone. The retrieval of the three different cases associate the observable to a concentrated region of rain, and in addition the sources are placed correctly, i.e. the first one is at a higher altitude than the rest, and the second one is placed at a higher altitude than the last one. Similarly, with the horizontal distance to the tangent point.

Quantitatively, the error of the retrieved height of the source is smaller than 1 km, while it ranges from 10 to 50 km in the horizontal dimension. Regarding the magnitude of the K_{dp}, the relative difference between the simulated and the retrieved one is less than a 10% in the first two cases, while in the third case the retrieved magnitude is two times the simulated one. Differences in the retrieved magnitude are directly related with differences in the retrieved size: when the source is overestimated in size, the intensity is underestimated, and vice versa, as expected from Equation 5.3.

The technique definitely shows an improvement of the $\Delta\Phi(h_{\text{tp}})$-alone observable providing approximate positions and structure of the sources, for the simple simulated cases shown here. It also shows potential for the fully characterization of the rain for certain simple cases. In the next section the same method is applied to real rain scenarios, in order to check the performance in realistic cases.

5.3.3 *Realistic rain scenarios simulation*

In order to test the technique in real rain conditions, real rain products from TRMM for different days, seasons and geolocations are used. The used TRMM products are

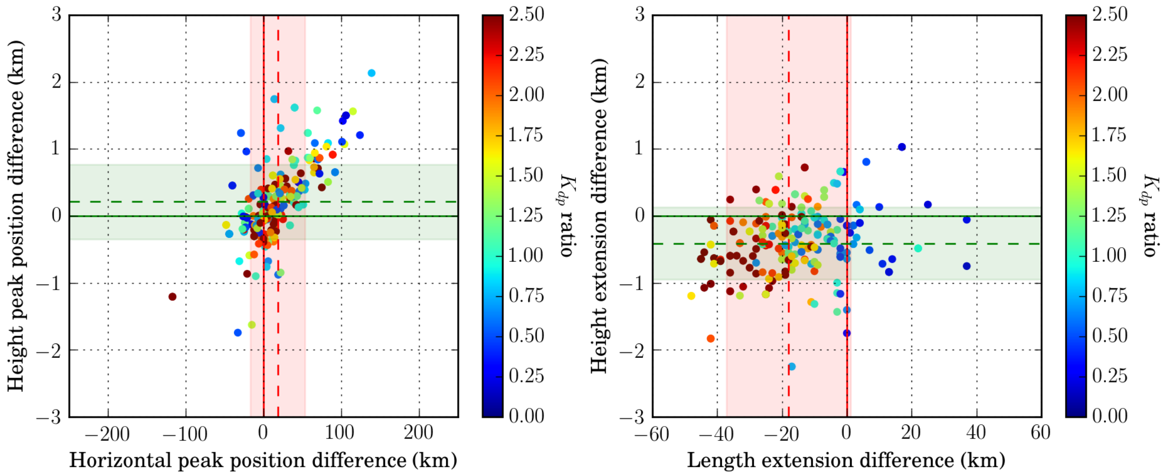

Figure 5.16: Statistical results for the simulated collocation between RO and real TRMM rain profiles: (left) The results for the rain cell peak position difference between the original and the retrieved one ($X_{\text{TRMM}} - X_{\text{tomo}}$). The solid red and green lines show the zero lines, while the dashed lines show the mean in the horizontal and vertical axis respectively. The shadowed green / red areas show the standard deviation of the means. The color scale shows the K_{dp} ratio between the original and the retrieved rain cell peak. (Right) The same as in the left panel but for the rain cell extension. Figure from Padullés et al. [2016b], Fig. 4.

the 3 dimensional combined rainfall profiles 2B31. Several TRMM orbits have been searched for heavy rain events, and these cases have been artificially collocated with a set of radio occultation rays, similarly as in Section 4.2.4.2. The total number of analysed events is 259. Again, only half of the RO plane has been used for this analysis.

After the collocation exercise, the $\Delta\Phi(h_{\text{tp}})$ is available for each of the 259 cases along with the K_{dp} at each ray point. Then, the tomographic approach is applied. Quantitatively, three aspects of the rain can be efficiently characterized: the position of the peak, the extension of the rain cell, and its intensity. The position of the peak is defined as the location of the point with the highest K_{dp} in the RO plane, i. e. its horizontal distance to the tangent point and its height. The extension of the rain cell is defined as the horizontal and vertical size of the region containing values of K_{dp} larger than the 60% of the maximum. And the intensity is taken as the maximum value of the K_{dp} for each case. These quantities are obtained for both the actual TRMM rain measurements mapped into the RO half-plane and for the retrieval, and are then compared. The results for the position, extension and intensity differences are shown in Figure 5.16.

The mean difference in horizontal positions of the cell peak is:

$$X_{\text{TRMM}} - X_{\text{tomo}} = 18.2 \pm 35.1\text{km}$$

and the mean difference in altitude of the cell location is:

$$Y_{\text{TRMM}} - Y_{\text{tomo}} = 0.22 \pm 0.56\text{km}.$$

For the extension of the rain cells, the mean difference in the horizontal is:

$$Lx_{\text{TRMM}} - Lx_{\text{tomo}} = -17.94 \pm 19.19\text{km}$$

and in height extension it is:

$$Ly_{\text{TRMM}} - Ly_{\text{tomo}} = -0.41 \pm 0.54\text{km}.$$

The retrieval tends to place the rain closer to the tangent point than it actually is, and tends to yield a larger rain structure than the original one, especially in the horizontal direction. There are two explanations for this trend. In the first place, the horizontal resolution is large (~ 9.5 km), thus the extension of the small rain cells is easily overestimated. The second reason is the clustering constraint, which mixes and blurs the voxels' solutions. This effect is particularly strong when the original rain is not close together but it has several columnar sub-structures. Then it is more difficult for the technique to resolve the columns individually, and tends to result in a joint and fainter rain cell. Moreover, the errors in the extension determination of the rain cells induce an error in the intensity retrieval as mentioned in the previous section. However, multi-columnar structures have also been correctly solved in certain cases as is shown in Figure 5.17.

In Figure 5.17 there is shown the original and the retrieved rain for 8 cases. For the first four panels (*a* to *d*), the retrieval has captured well enough the structure of the rain. Cases *e* and *f* show how the retrieval algorithm can blur multi-columnar rain structures and how the rain tends to be retrieved as a fainter and more homogeneous structure than it actually is. The last two cases, *g* and *h*, show two examples where the retrieval is not working well, failing to capture the structure and the position of the rain. The proportion of cases in Figure 5 aims to be a fair representation of the 259 cases, evaluated in terms of how the structure of the rain is captured by the tomographic technique.

In terms of analysing the practical application of this technique into the ROHP-PAZ experiment, it has to be taken into account that the RO provided refractivity profiles are mainly contributed by the region within ± 100 km around the tangent point [Kursinski et al., 2000]. Therefore, if one wants to relate the measured thermodynamic state to precipitation, the first step is to know if the main part of the detected precipitation is within the influence range. In Figure 5.18 there are two histograms showing the retrieved peak distances to the tangent point, for the cases where the original rain cell is within a distance of 100 km from the tangent point and for the cases where the original rain cell is further than 100 km from the tangent point. It can be seen how more than 80% of the cases are well placed within this region when the original one is inside. Only less than 10% are placed closer than 100 km from the tangent point when the original peak is not.

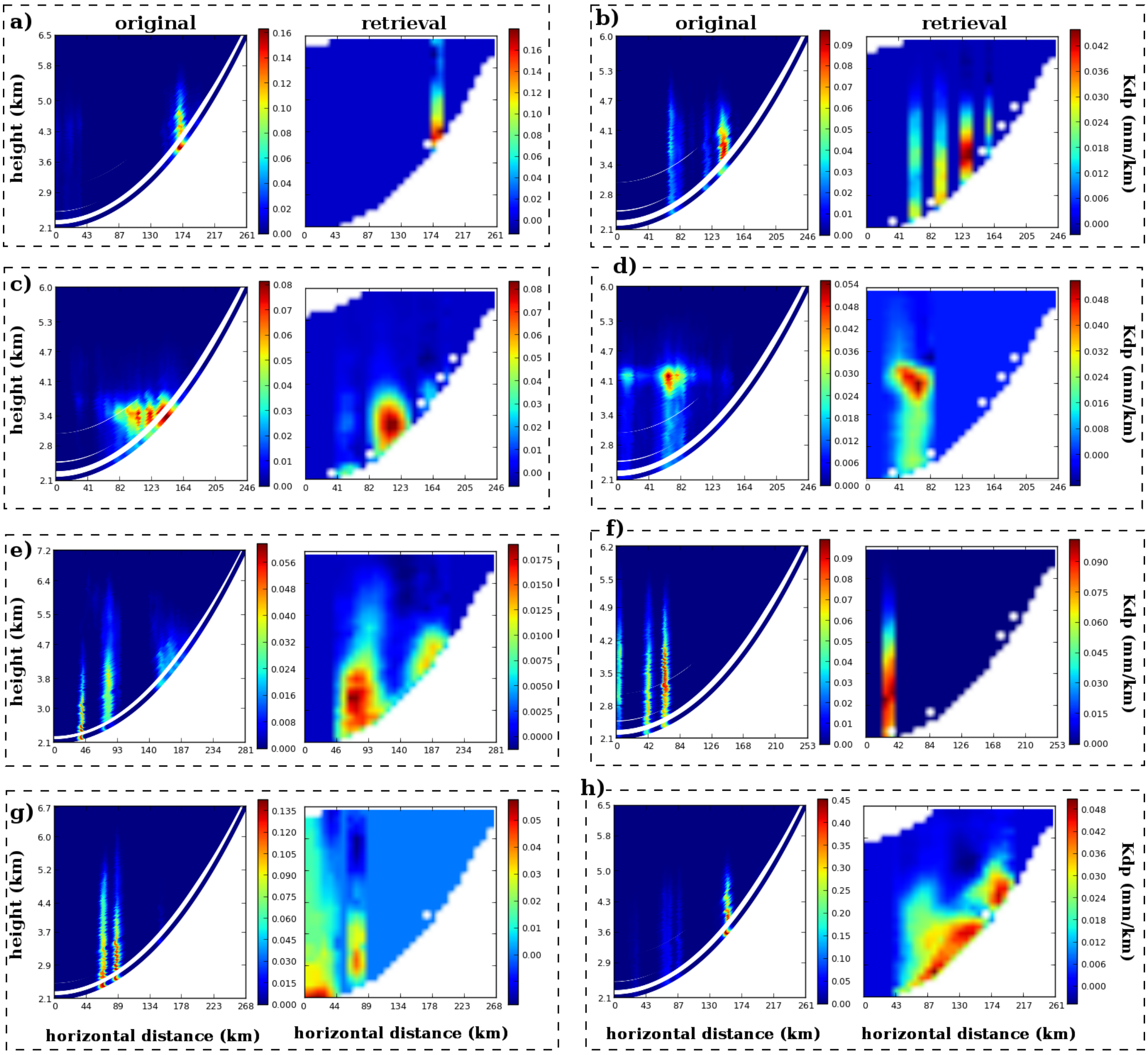

Figure 5.17: Examples of the retrievals for different rain cases. Each block represents the original TRMM rain cells (left), and the retrieved solution with the tomographic approach (right). The 8 different cases aim to be a fair representation of the 259 studied cases, in terms of how the structure of the rain is reconstructed with respect the original one. Figure from Padullés et al. [2016b], Fig. 5.

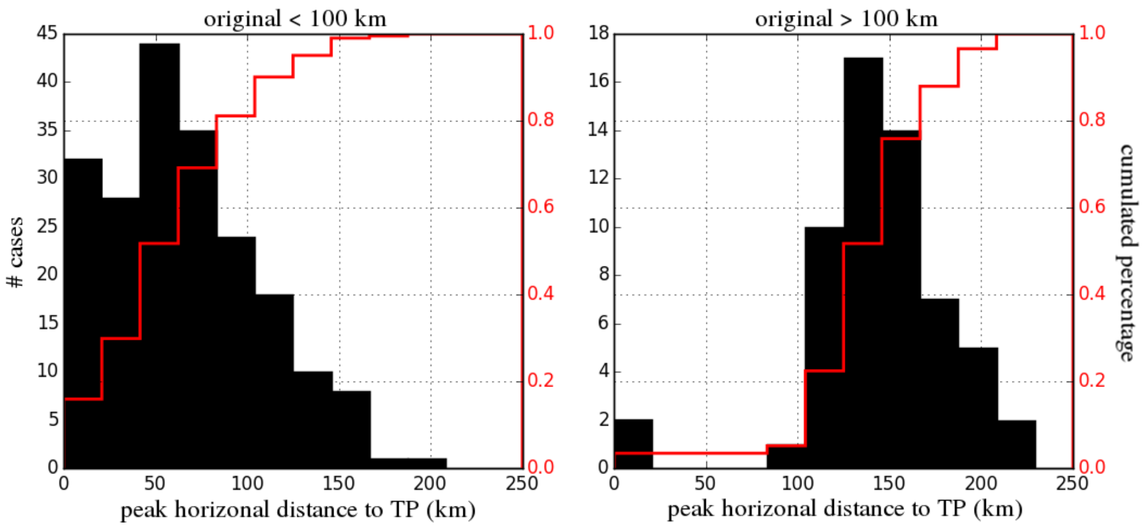

Figure 5.18: (Left) Histogram for the horizontal distance to the tangent point for the cases where the original peak is actually located within 100 km from the tangent point. (Right) The same histogram, but for the cases where the original peak is placed further than 100 km from the tangentpoint. The red line is the cumulated percentage of cases, ruled by the right axis. Figure from Padullés et al. [2016b], Fig. 6.

6 STANDARD RADIO OCCULTATION RESULTS

This chapter aims to show a few preliminary results and to launch some ideas on the impact of collocated thermodynamic products and rain information could have in the RO products. To do so, the profiles from the collocated RO with the precipitation missions (Section 4.2) are used. Two different analysis are performed: first, the thermodynamic products of those RO that may have crossed rain are compared to those that have not according to the collocated radar information. Then, the RO profiles are checked against model outputs. The performance of the models and the quality of the RO thermodynamic retrievals is assessed in the presence of precipitation.

The other exercise consists in identifying precipitation features using the RO refractivity alone, without the need of temperature, pressure of water vapour. A graphical technique is introduced, and few preliminary results are obtained using the collocated RO events.

6.1 REFRACTIVITY BIAS DUE TO HEAVY RAIN

The RO technique provides the refractivity vertical profiles. From refractivity, other thermodynamic profiles like temperature, pressure or water vapour can be derived. As it has been seen in Section 1.2.3, the use of model products are needed to go from refractivity to the set of three thermodynamic products (not needed if water vapour is neglected). In the neutral atmosphere, the refractivity is usually expressed as Equation 1.15:

$$N = a_1\frac{P}{T} + a_2\frac{e}{T^2}.$$

Here, the terms W_w and W_i (from Equation 1.14), which account for the contribution of the liquid and ice water contents, are neglected.

It is usual in the community to compare the profiles provided by the RO technique with those computed using model outputs [e. g. Schmidt et al., 2008; Von Engeln et al., 2009; Schreiner et al., 2011]. This provides an idea on how the model performs, or if there are evident errors in the RO product retrievals. One thing that has to be taken into account when doing these kind of analysis is that data from the model and from RO products are not completely independent, since RO products rely on first guesses from the models, and the models assimilate the RO profiles to obtain their products.

For purposes of comparison, CDAAC collocates, interpolates and provides the profiles from the ECMWF's ERA-40 reanalysis [e. g. Uppala et al., 2005], the NCEP's Global Forecast System (GFS) model [e. g. NOAA/NCEP, 2003] and the ECMWF's TOGA 2.5 degree Global Upper Air Analysis [e. g. ECMWF, 1990] along with the RO profiles. For each of the *atmPrf* and *wetPrf* profiles, which contain the dry and wet COSMIC RO retrievals, respectively, there are the corresponding *eraPrf*, *gfsPrf*, and *ecmPrf* profiles with the collocated values obtained from the respective models.

6.1.1 *Rain versus no rain profiles*

In this section, comparison between the RO retrievals and the model outputs are performed, with the aim of finding heavy rain features in such comparisons. The profiles that are compared are those introduced in Section 4.2, that have been collocated with the TRMM precipitation mission. Hence, two groups of profiles can be defined: those for which the radar information do not show any nearby pixel with positive Z, and those for which the radar shows at least 400 pixels with Z>30 dBZ in the neighbourhood of the occultation point. The latter are associated with moderate to heavy rain events.

These two groups of occultation events (rain and no-rain) are compared separately to the model outputs. The results of the comparison of the refractivity profiles are shown in Figure 6.1. The comparison show how, under rain conditions, there exist a positive refractivity bias with a peak around 4-5 km of height that do not exist in the no-rain profiles. This is more obvious in the comparison of the RO profiles with the ECMWF TOGA analysis and ERA-40 reanalysis, although it is also observed in the comparison with the GFS model outputs. In addition, an obvious negative bias can be seen below 2-3 km. This is further commented in the next subsection.

The refractivity of the models that is used in the comparisons is derived from their temperature, pressure and water vapour pressure profiles. Hence, the bias could arise from the fact that the water content terms are not taken into account when reconstructing refractivity from model outputs. The same way, if the water content terms are not taken into account when retrieving temperature, pressure and water vapour from the RO measured refractivity, some biases could be appearing too in the RO thermodynamic products under heavy rain conditions. The absolute differences in the temperature and pressure retrievals, between the RO products and the model outputs are shown in Figure 6.2. The features shown in this figure are expected from the biases in refractivity. Thus, systematically, the RO profiles have a larger refractivity, colder temperature and larger pressure profiles than models outputs, when heavy rain is present.

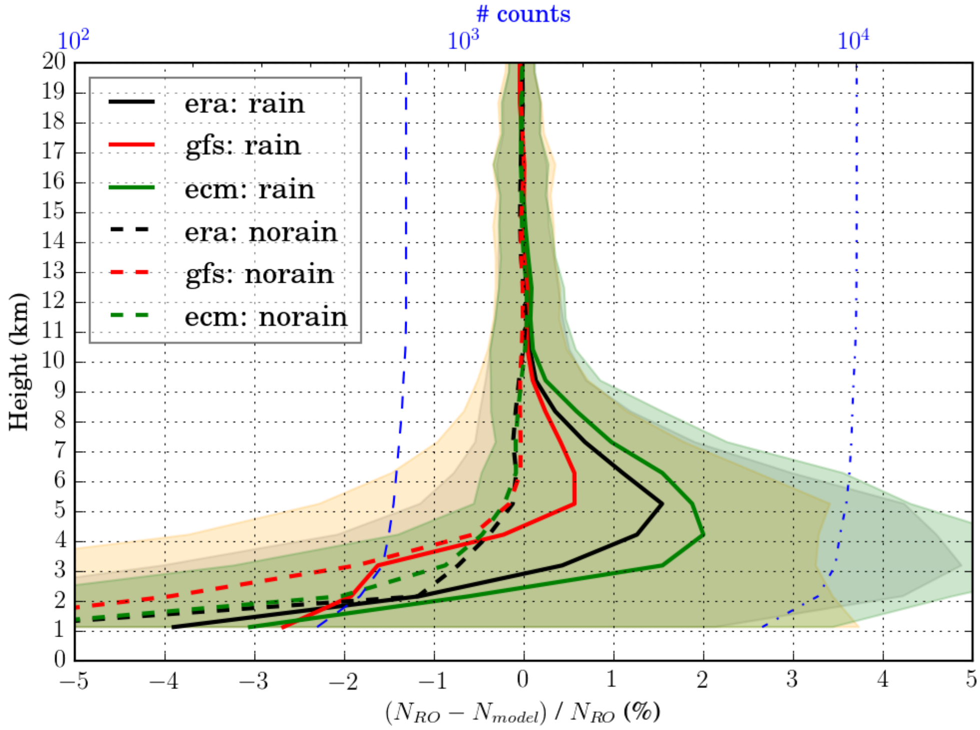

Figure 6.1: Refractivity profiles comparison between the UCAR *wetPrf* retrieval and the ERA40-Interim reanalysis products (black),the GFS model products (red) and the ECMWF TOGA analysis (green). The solid lines correspond to the comparsion between those profiles that have crossed rain, and the dashed lines correspond to those prifles that haven't. The shaded areas correspond to the standard deviation of the rain-profiles comparison, beign the gray the ERA-interim one,the orange the GFS's and the green the TOGA's. The blue axis indicates the number of profiles used for the non-rain analysis (dotted-dashed blue line) and for the rain analysis (dashed blue line).

6.1.2 *Bias sources*

The other major feature that can be seen in Figure 6.1, besides the positive bias around 4-5 km, is the negative bias appearing below 2-3 km. This bias is consistently appearing both in the rain and no-rain profiles. It and has been investigated before, for example, in Ao et al. [2003], Sokolovskiy [2003] and Xie et al. [2006] with data prior to the launch of COSMIC constellation, and in Xie et al. [2010] using COSMIC data. The bias is associated to Super Refraction (SR) layers, i.e. regions where the refractivity gradient is so large ($dN/dz < -157\,\mathrm{Nunits\,km^{-1}}$) that the rays are trapped inside the atmosphere, usually coincident with the ABL. When a SR occurs, an infinite continuum of refractivity profiles yields to the same bending angle profile (ill-defined problem), and the Abel transform fails to reconstruct correctly the refractivity below this layer, choosing the minimum refractivity solution as a truth. Thus, a negative bias in the comparison between the retrieved refractivity

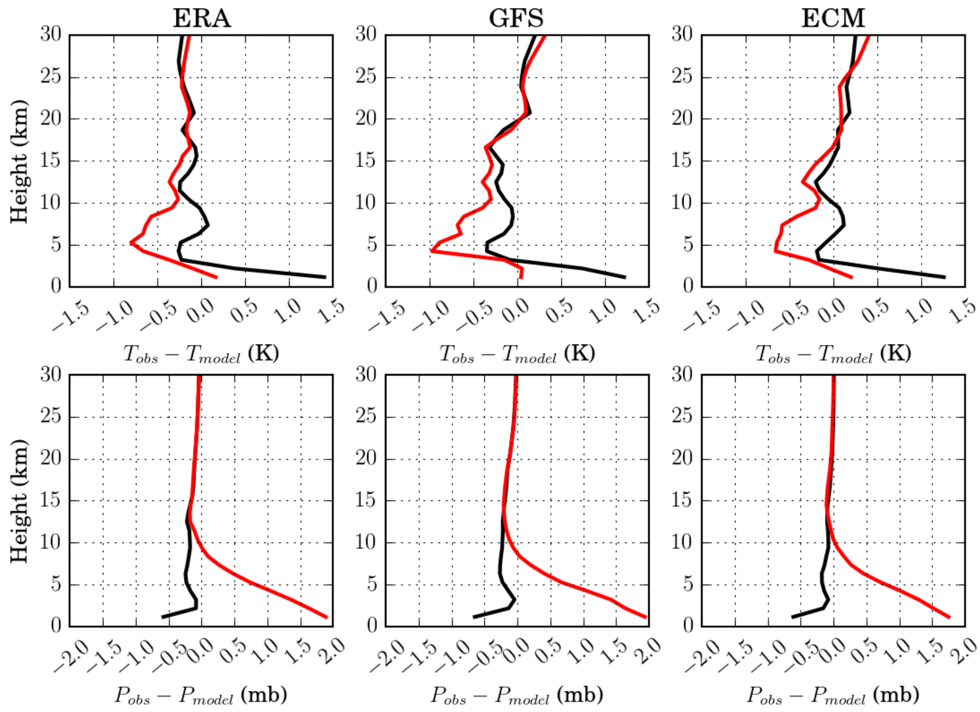

Figure 6.2: Temperature (top row) and pressure (bottom row) difference between the UCAR *wetPrf* and the ERA40-interim products (left column), the GFS model products (middle column) and the ECMWF TOGA analysis products (right column). The comparison is separated between the no-rain profiles (black) and the rain profiles (red).

and the models appear. This effect is specially significant in the tropics, and since the TRMM data used here covers mainly this region, the bias is significantly strong.

Other biases that have been studied are related to the azimuth of the radio occultation. The azimuth is defined as the angle with respect to the north of the projection of the RO on the longitude - latitude plane. Since COSMIC orbits have high inclination (larger than 70 degrees), this azimuth is closely related to the local azimuth, i. e. the angle between the velocity vector of the LEO and the LEO - GPS vector. Depending on the local azimuth, it has been shown how the movement of the tangent point can vary from less than 100 km to more than 500 km [Foelsche et al., 2011]. The azimuth depends solely on the positions and relative movements of the GPS and the LEO, and the larger the azimuth the more the tangent point moves. Large movements of the tangent point make the collocation of the RO retrievals and the model output profiles more difficult, so it can induce biases in the comparisons. To avoid this effect in the comparisons between the rain and no-rain profiles, the comparison has been done separating them into different azimuth ranges, and the results are shown in Figure 6.3. From this results, it can be seen how the comparison between the RO profiles and the model outputs is worse as the azimuth increases,

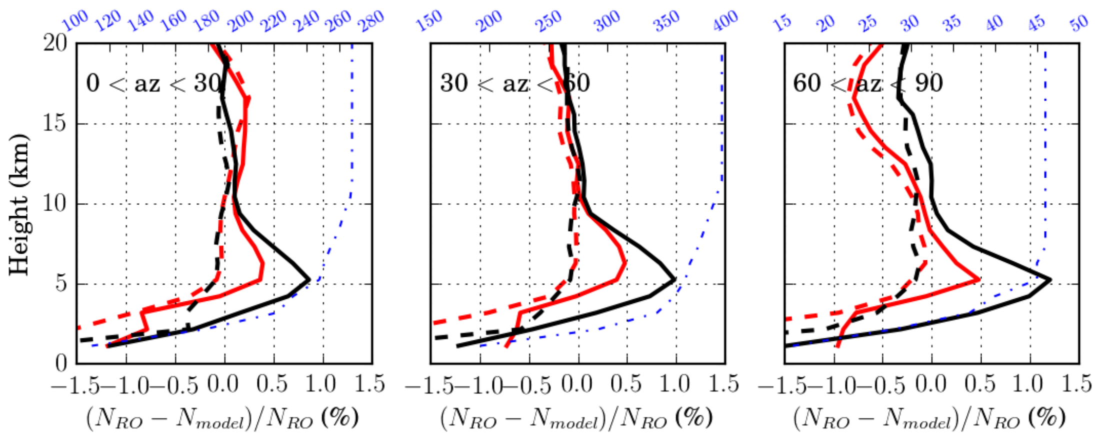

Figure 6.3: Same as in Figure 6.1 for the ERA40-interim (black) and GFS model (red) comparison with RO retrievals, but the profiles are here separated by their azimuth angle: 0 < az < 30 (left panel), 30 < az < 60 (middle panel) and az > 60 (right panel).

although it is only in the height where precipitation is expected that there exist a difference between the rain and the no-rain profiles.

Finally, the comparison is performed separating the profiles by regions, so that regional differences in the profile characteristics are also discarded. First, the comparison is performed by latitude intervals and it is shown in Figure 6.4. Then, the profiles are separated by regions, which are shown in Figure 6.5. It can be seen how similar biases appear between the rain and no-rain profiles, regardless the region, latitude, and RO azimuth angle, hence confirming that heavy rain can induce positive refractivity biases when comparing the measured RO refractivity and the model outputs.

6.1.3 *Impact of heavy rain into the RO excess phase*

In the previous section it has been shown that a positive refractivity bias appears under heavy rain scenarios, when comparing the RO measured refractivity with the model outputs. The origin of the bias is not clear, though.

The RO events collocated with TRMM have been used to build the database introduced in Section 4.4. Therefore, many of the profiles used in the comparisons of this section are in the database. For the events in the database, the phase excess due to hydrometeors, $\Phi_{\mathrm{exc}}^{\mathrm{trop}}$ (Equation 3.45), has been simulated. The actual COSMIC measurement for the excess phase is also stored in the database. Thus, the contribution of the precipitation into the measured excess phase is known. To determine if heavy rain is explicitly affecting the measured RO refractivity, the following exercise has been performed. Two profiles have been obtained from the database: the excess phase as a function of time for the actual COSMIC data, $\Phi_{\mathrm{exc}}(t)$, and the

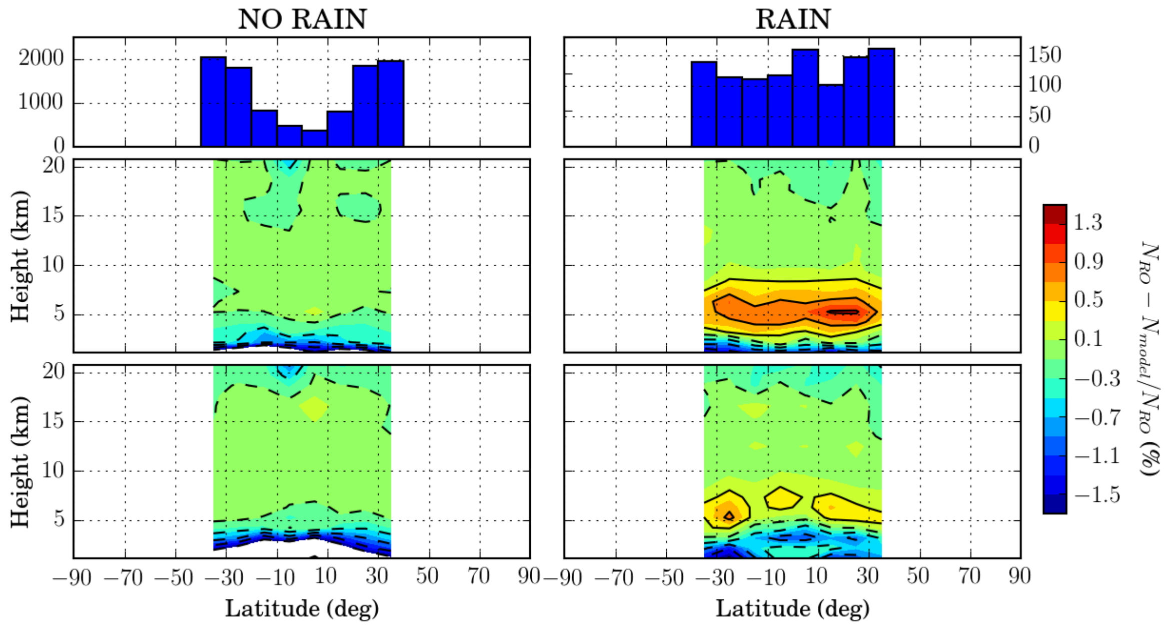

Figure 6.4: Fractional N difference between the RO retrievals and the ERA40-interim reanalysis (middle row) and the GFS model (bottom row) for the no-rain profiles (left column) and the rain profiles (right column) as a function of latitude and height. The top row indicates the number of profiles at each latitude interval.

excess phase with the Φ_{exc}^{trop} subtracted from it, $\Phi_{exc}^{NR}(t)$, hence the excess phase that would have been measured if the rays had not crossed any rain.

Then, both profiles, $\Phi_{exc}(t)$ and $\Phi_{exc}^{NR}(t)$, have been processed using the software Radio Occultation Processing Package (ROPP) [Culverwell et al., 2015] in order to obtain the RO retrievals. The profiles that have not been modified are also processed with the ROPP for consistency. The obtained refractivity profiles (N_{ROPP}^{R} for the cases where rain contribution is in the profile and N_{ROPP}^{NR} for the cases where the rain contribution has been removed) are then compared. No significant differences are found between the profiles as it can be seen in Figure 6.6. Hence, the contribution of rain to the phase excess does not have an impact into the retrieved refractivity.

Two ideas are worth mentioning. The first one is that if rain is inducing local variations in the refractivity, these are not well captured by the radio occultation retrievals based on Abel transform, which is designed to account for a spherical symmetric atmosphere [e. g. Ahmad and Tyler, 1999; Syndergaard et al., 2003]. This could explain why there are no differences between the retrievals that account for the rain contribution and those that are not. The second idea is that based on the differences in Figure 6.1 to Figure 6.5, models may be underestimating refractivity under heavy rain conditions, systematically providing lower values than those measured by ROs. This idea is reinforced by the fact that the performance among different models and reanalysis under heavy rain conditions is different, while its

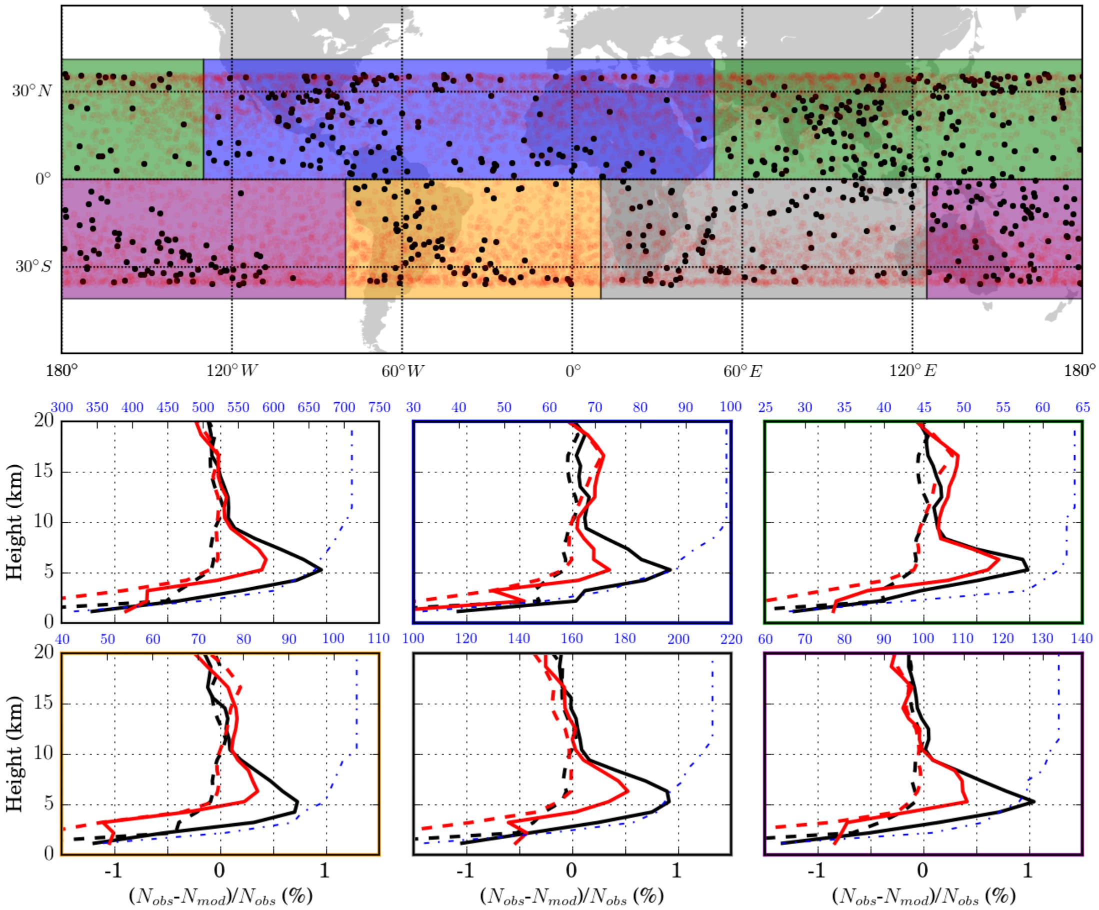

Figure 6.5: (Top) Scatterplot on the map that indicates heavy rain cases (black dots), and no-rain cases (red dots). Also, a regional differentiation is defined and shown here. (Bottom) Fractional differences between RO, and ERA40-interim (black) and GFS (red) models, as a function of height. Dashed lines indicate the no-rain cases, and the solid lines the rain cases. The blue dotted line indicates the number of counts. Each pannel corresponds to the same colored region in the top map, with the exception of the first pannel, which contains all the cases.

performance is equivalent when no rain is present. Finally, since the discrepancy between observations and models starts to be significant below 10 km for most of the analysed cases, it is likely that the impact of thick clouds and deep convective structures into the thermodynamic variables is not well modelled either. In consequence, further investigation is needed to solve this issue, and PAZ retrievals might be well suited dataset to do so, since it will incorporate the precipitation information along with the refractivity profiles.

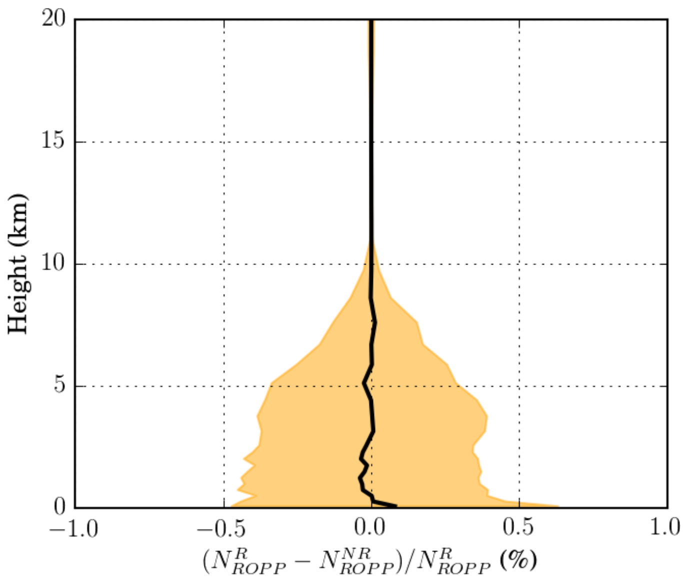

Figure 6.6: Fractional difference between the ROPP refractivity retrievals with (R) and without (NR) the rain contribution.

6.2 THERMODYNAMICS OF PRECIPITATING CLOUDS

Given the disagreement between the RO retrievals and the model outputs shown in Section 6.1, one might wonder how good are the RO thermodynamic profiles in the presence of precipitation, since they use model products to solve Equation 1.16 and Equation 1.17 when water vapour cannot be neglected. This is important because many studies use RO thermodynamic profiles to investigate clouds and precipitation processes [e. g. Biondi et al., 2012, 2013; Vergados et al., 2014].

Here a different approach is introduced. Instead of relying on RO temperature and moisture retrievals, precipitation processes are investigated using only RO refractivity and its derivative. RO refractivity is less model dependent than RO-retrieved temperature, pressure and water vapour (Section 1.2.3). With this purpose, several extra definitions are needed.

6.2.1 *Refractivity profiles for adiabatic and pseudoadiabatic processes*

In the first place, let refractivity be re-written as:

$$N(z) = \mathrm{k}_1 \frac{P(z)}{T(z)} \left[1 + \frac{\mathrm{k}_2 r(z)}{\epsilon + r(z)} \left(1 + \frac{\mathrm{k}_3}{T(z)} \right) \right] \tag{6.1}$$

where $\mathrm{k}_{1,2,3}$ are constants, r is the water vapour mixing ratio, and $\epsilon = R_d/R_v = 0.622$ is the ratio of the gas constant for dry versus moist air. The constants are usually taken to be $\mathrm{k}_1 = 77.6$, $\mathrm{k}_2 = -0.0927835$ and $\mathrm{k}_3 = -51930.56$. This equation is equivalent to Equation 1.14, but here the water vapour mixing ratio is explicitly shown.

Depending on the thermodynamic regime of the atmosphere, the refractivity changes differently as a function of height. For example, an air parcel undergoing an unsaturated adiabatic process, with well mixed water without sources or sinks of water vapour, will conserve the water vapour mixing ratio, i. e. $r(z) = r(z_0)$. Considering the process reversible, the moist potential temperature, Θ, is conserved (isentropic process) and temperature depends linearly on height: $T(z) = T(z_0) - \Gamma_\mathrm{d}(z - z_0)$ [Emanuel, 1994]. The Γ_d is the dry adiabatic lapse rate and is defined as:

$$\Gamma_\mathrm{d} = -\left(\frac{\mathrm{d}T}{\mathrm{d}z}\right) = \frac{g}{c_\mathrm{pd}} \frac{1+r}{1+r\left(\frac{c_\mathrm{pv}}{c_\mathrm{pd}}\right)} \tag{6.2}$$

where g is the gravitational acceleration and $c_\mathrm{pd,pv}$ are the heat capacities at constant pressure for dry and moist air, respectively.

Eventually, the air parcel becomes saturated, i. e. $r = r^*(T, P)$. Then, the temperature does not fall as rapidly as in an unsaturated expansion since it releases latent heat, and the (moist) adiabatic lapse rate is defined as [Emanuel, 1994]:

$$\Gamma_\mathrm{m} = -\left(\frac{\mathrm{d}T}{\mathrm{d}z}\right)_\mathrm{m} = \frac{g}{c_\mathrm{pd}} \frac{1+r}{1+r\left(\frac{c_\mathrm{pv}}{c_\mathrm{pd}}\right)} \left[\frac{1+\frac{L_\mathrm{v} r}{R_\mathrm{d} T}}{1+r_\mathrm{l}\frac{c_\mathrm{l}}{c_\mathrm{pd}+rc_\mathrm{pv}} + \frac{L_v^2 r(1+r/\epsilon)}{R_v T^2 (c_\mathrm{pv}+rc_\mathrm{pv})}}\right] \tag{6.3}$$

where L_v is the latent heat of vaporisation and r_l is the liquid water mixing ratio. When the atmosphere is very moist, the ratio $\Gamma_\mathrm{m}/\Gamma_\mathrm{d}$ is way smaller than unity.

It is convenient to define a pseudoadiabatic process where the r_l can be neglected, so that the entropy only depends on temperature and pressure [Emanuel, 1994]. Hence, pseudoadiabatic isentropic processes conserve the pseudoequivalent potential temperature, θ_ep, defined as:

$$\theta_\mathrm{ep} = T\left(\frac{1000}{P}\right)^{0.2854(1-0.28r)} \exp\left[r(1+0.81r)\left(\frac{3376}{T^*} - 2.54\right)\right] \tag{6.4}$$

where T^* is the virtual temperature and it is defined as:

$$T^* = \frac{1}{3.5\ln(T) - \ln(e) - 4.805} + 55. \tag{6.5}$$

Finally, the changes in temperature and pressure that keep the mixing ratio saturated can be expressed as:

$$\mathrm{d}r^* = \frac{r^*}{P-e}\left(P\frac{L_\mathrm{v}}{R_\mathrm{v} T^2}\mathrm{d}T - \mathrm{d}P\right). \tag{6.6}$$

All these equations are derived from basic principles in [Emanuel, 1994]. Using them, three different thermodynamic processes can be described: dry adiabatic,

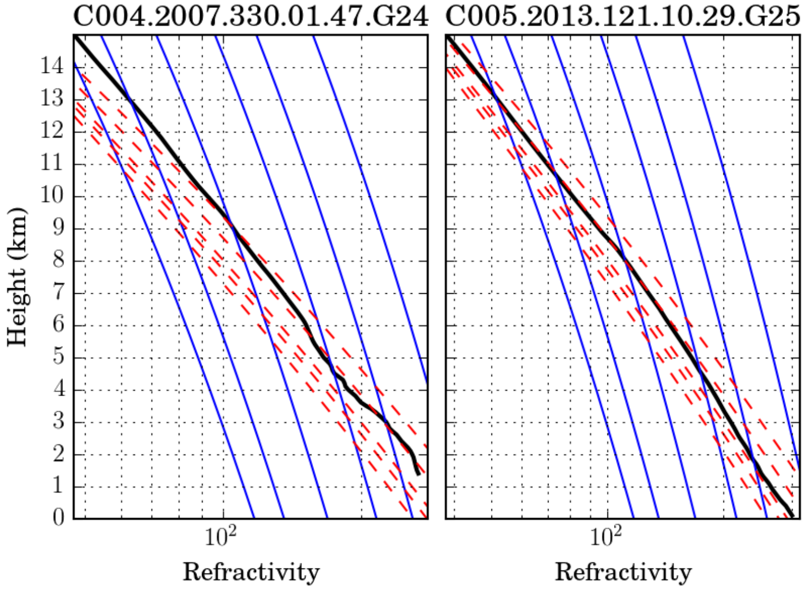

Figure 6.7: RO measured refractivity profiles (solid black line) along with the moist adiabatic family of theoretical refractivity curves (solid blue lines) and the saturated pseudoadiabatic family of theoretical refractivity curves (dashed red lines). Each panel is identified by the COSMIC id from which the refractivity is obtained.

moist unsaturated adiabatic, and saturated pseudoadiabatic. Refractivity can be obtained from T, P and e, and how they evolve in height depending on the thermodynamic regime depends on the relationships above. Using these relationships, and a set of initial conditions at a certain height, e. g. 20 km, it is possible to derive a family of refractivity curves as a function of height that follow each of the thermodynamic regimes. To do so, the initial values are propagated downwards following the lapse rates defined for each regime, in discrete height steps. At each height step, the lapse rate of T, P and e is updated with the new values.

This procedure has been followed in Figure 6.7, where for a set of $(T(z_0), P(z_0), e(z_0))$ at $z_0 = 20$ km, some of the families of moist adiabatic refractivity curves (constant mixing ratio) are plotted as solid blue lines and the saturated pseudoadiabatic ones as dashed red lines, along with the actual RO refractivity profile. What is physically relevant is to observe the behaviour of the RO measured refractivity (black solid line in Figure 6.7) with respect to the theoretical curves, specially the slope.

6.2.2 *Thermodynamic features in precipitating clouds*

This technique can be used to describe the behaviour of precipitating clouds without using model inputs, such as those needed to use the temperature or the water vapour retrieved by RO. One way to analyse precipitating clouds is to compare the refractivity gradient at each height with the one of the adiabatic and pseudoadiabatic theoretical refractivities at the same height. In Figure 6.7 it can be seen how

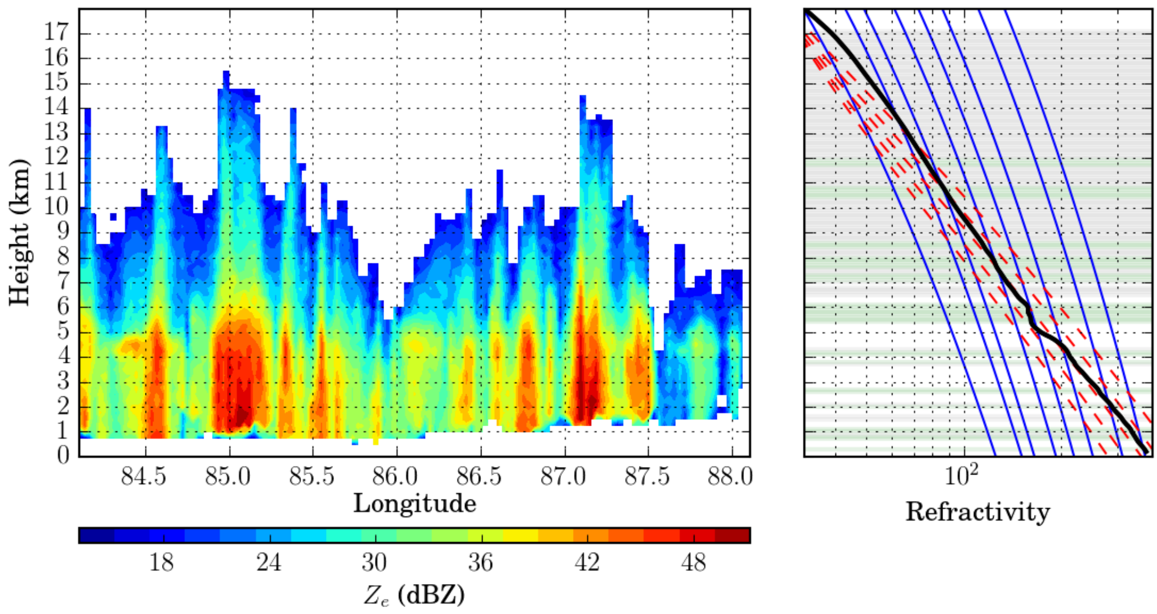

Figure 6.8: (Left) A vertical slice of a TRMM radar reflectivity profile, that has been collocated with the RO with id C005.2014.129.18.39.G29. (Right) The coincident RO refractivity measurement, along with the family of curves respresenting the moist adiabatic and saturated pseudoadiabatic theoretical refractivities, following line codes as in Figure 6.7. The horizontal color-bands represent the comparison of the measured refractivity gradient against the saturated pseudoadiabatic one: steeper than it (green), close to it (gray) and tilted up with respect to it (white)

the RO refractivity is some times following the slope of the saturated pseudoadiabatic lines (e. g. between 14 and 7 km of height in the right panel case), while eventually can change and follow a slope closer to that of the moist adiabatic one (e. g. between 6 and 4 km of height in the left panel case).

Using the collocated RO events, this features can be investigated in the presence of precipitating clouds. In figure Figure 6.8 there is shown a TRMM radar vertical slice, along with the coincident RO refractivity. In addition to the adiabatic and pseudoadiabatic family of theoretical refractivity curves, here there are plotted three different color-bands that represent the comparison of the RO refractivity gradient against the saturated pseudoadiabatic one: steeper than it (green), close to it (gray) and tilted up with respect to it (white). The comparison with the theoretical saturated pseudoadiabatic gradient is tricky, since it is not unique. For a measured refractivity, the combinations of T, P and e^* that reproduce the same refractivity at the same height are used to infer which is the gradient that refractivity would follow to stay in the same thermodynamic regime. Different combinations of T, P and e^* lead to different gradients. Therefore, the mean of the possible gradients is used for the comparison.

The kind of graphics like the ones in Figure 6.7 and Figure 6.8 intend to be a version of the commonly used thermodynamic diagrams, like the *skew-T* where pressure is plotted against temperature, or the *tephigram*, where potential temperature is plotted against temperature, among others [e. g. Bohren and Albrecht, 1998]. These graphics are useful to describe the state of the atmosphere, and to infer the stability of the measured air parcel with respect to the environment. The question for the graphics presented in this section is whether precipitation features can be inferred from them or not. Interesting features can be observed when analysing individual events. For example, different thermodynamic regimes can be identified in the RO measured refractivity from Figure 6.8, which can be associated to the TRMM measurements. The color bands indicate that the refractivity follows a slope which might be close to a saturated pseudoadiabatic one (gray), and suddenly changes to follow a moist adiabatic one (green), and finally refractivity increases with a faster pace than the pseudoadiabatic one (white). The fact that refractivity is close to one following a saturated regime may indicate the presence of clouds above precipitation, e. g. above 12 km.

A statistical analysis has been performed using the collocated RO profiles with TRMM and Cloudsat. Those profiles coincident with Cloudsat that do not show positive refractivity measurements are considered clear sky profiles, and those coincident with TRMM showing positive refractivity measurements are considered rain profiles. For all these profiles, the same comparison as in Figure 6.8 has been performed, and the results are shown in Figure 6.9. Hence, for each measured refractivity, its gradient is compared with the one that a saturated pseudoadiabatic profile would follow. The main observed feature is that rain refractivity profiles are, on average, closer to a saturated pseudoadiabatic regime than those profiles in clear sky scenarios, specially above 2-3 km (i. e. in the free troposphere). This agrees with the presence of clouds. The behaviour changes below, where precipitation phenomena is expected. A difference in the height of the transition can be seen between the tropics and mid-latitudes, which agrees with the fact that rain happens at higher altitudes in the tropics. Moreover, a smoother transition between the free and the lower troposphere is detected for precipitating scenarios. In addition, it has to be taken into account that the profiles might be affected by some of the biases mentioned in the previous section.

Therefore, this technique has potential for the analysis of the thermodynamics of precipitation due to its model-independent nature. Further investigation is also required to understand the features that precipitation might be inducing on refractivity gradients, and again, the PAZ dataset looks well suited for such analysis.

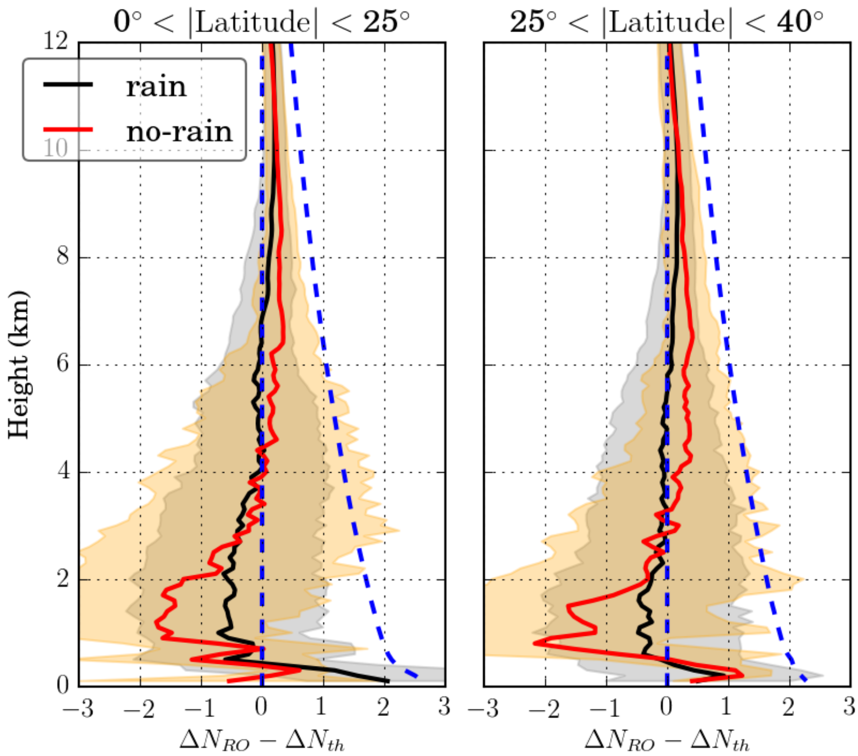

Figure 6.9: Comparison of the refractivity gradients against the saturated pseudoadiabatic theoretical gradient (zero line higligted by a blue-dashed line) and against the dry theoretical gradient (the zero is represented by the blue-dashed line in the right side, so that the differences stay always in the negative side). The black solid line represents the mean difference using the profiles that have crossed rain, while the red solid line represents the mean difference usign the profiles that have not crossed rain. The shaded areas are the standard deviations, grey and orange respectively. The left panel contains the profiles in tropical latitudes (|lat|< 25 deg.), and the right panel the profiles in extratropical latitudes (25 deg< |lat|< 40 deg).

7 ROHP-PAZ FIELD CAMPAIGN

Prior to the launch of the PAZ satellite, a field campaign was conducted in order to study, for the first time, GPS signals obtained at two polarizations in grazing angle geometry. The goal was to start identifying and understanding the factors that might affect the polarimetric signal. Positioned at the top of a mountain at 1670 m a.m.s.l., the experiment receiver was enclosed in a shelter with an engineering model of the PAZ's polarimetric antenna on a mast pointing at the horizon, and a commercial JAVAD receiver (provided by the German Research Center for Geosciences, GFZ). A zenith-looking geodetic GNSS antenna was also used for positioning. The RO antenna pointed south and to the horizon, and it tracked all the visible satellites in the east–west field of view from -5 to 40° of elevation and from 150 to 270° of azimuth (see Figure 7.1). Although all the satellites were tracked simultaneously, only those crossing the main beam of the antenna were used in the posterior analysis. For the time period analysed, the GNSS satellites with the highest number of samples are the ones identified by the PRN numbers G10, G14, G15, G22 and G31. The track of each GPS satellite on the sky repeats every day, with $\sim$ 4 minutes shift in time (sidereal day). Moreover, only the segments between 0° and 20° of elevation are used for the analysis, since the antenna performance reaches its optimal values within this range. Given the geometry of the experiment's field of view, in most of the cases only one of either the descending or ascending trajectories over the horizon provided data within the antenna field of view.

The main objective was to collect a large amount of data free of rain and to catch some heavy rain events in order to observe differences in the polarimetric observables between the two data sets. The area was chosen specifically for this purpose, given that the region is mainly dry and several intense local Mediterranean storms occur a few times per year [Lorente and Redaño, 1990; Casas et al., 2004; Ducrocq et al., 2014]. The experiment ran for 8 months, from 21 March to 10 October in 2014. During this period, it collected data for about 170 days. There were about 25 days of rain, of which 5 could be considered heavy rain. The results presented in this chapter are based on Padullés et al. [2016a].

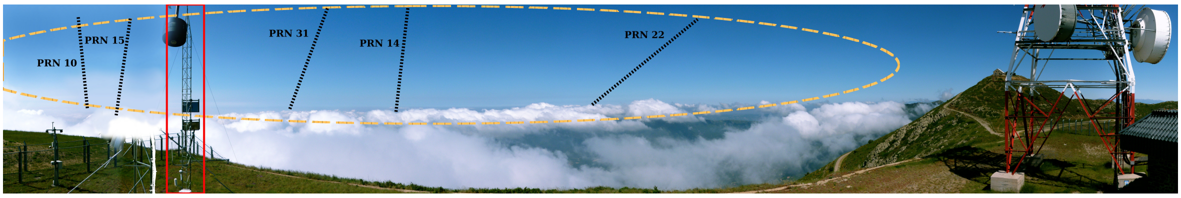

Figure 7.1: Panoramic view from the observation site. The field of view is the area comprising azimuths from $\sim 160°$ (left) to $\sim 270°$ (right), looking south. The yellow dashed line indicates the main lobe of the antenna (approximate). The black dashed lines represent the tracks of the GPS satellites followed, which repeat every sidereal day: from left to right, PRN 10, 15, 31, 14 and 22. Multiple metallic elements seen in the field of view, such as the meteorological station (inside the red outline), the fence, the telecommunications antenna, and others not pictured (metallic shelter, antenna supports, etc.), could affect the GNSS signal in the form of multipath interference. Figure from Padullés et al. [2016a], Fig. 1.

7.1 POLARIMETRIC GNSS DATA

7.1.1 *Observables*

GNSS signal observables are the carrier phase and the pseudo-range, described in Section 1.2.2, and are obtained here from the H and V ports of the polarimetric antenna. The geometry found in the experiment is not a common RO configuration though. Instead, the receiver is inside the atmosphere, i. e. on the ground, and therefore the tangent point–LEO trajectory is missing. The lack of symmetry and the non-existence of negative elevation observations mean that we cannot retrieve the standard thermodynamic profiles [Healy et al., 2002], which will be retrieved from the satellite in the future experiment. Moreover, the fact that the receiver is on the ground means that the radio link crosses all the atmosphere layers during all of the observation time. In this configuration, the sounding of the atmosphere is different from an RO one. This has an important implication for the observables.

The polarimetric GNSS observable $\Delta\Phi$ is the difference between the carrier phase delay measured in the H port and the one measured in the V port. The observations in the H and V ports of the polarimetric antenna are independent, and therefore the receiver treats them separately. The GNSS receivers keep track of the total phase relative to their initial measurement, but the value associated with the first measurement is arbitrary, as it has been explained in Section 1.1. In this case, both signals (H and V) suffer from this ambiguity (phase ambiguity, b) in their respective channel:

$$\Phi_p(t) = \rho(t) + \eta^p(t) + \eta_{\text{ion}}(t) + m^p(t) + \nu^p + C(t) + b^p, \tag{7.1}$$

where Φ is the measured carrier phase delay at the p port (H or V), ρ is the geometry range between the satellite and the receiver since the initial measurement (the same for H and V), η^i denotes the delay due to the neutral atmosphere, which contains the delays induced by the hydrometeors, hence it might be different in the two ports. η_{ion} denotes the ionospheric delay, that is considered equal for both ports in this situation. m represents the local multipath interference in each component, the term ν refers to the hardware effects of the receiver and the transmitter (such as noise, the effect of a possible difference in the cable's length, etc.), and C represents the clock drifts and errors. b is the arbitrary initial constant that does not depend on time. The only difference with respect Equation 1.4 is that here the multipath and the phase ambiguity terms are shown explicitly, and the clock errors are grouped. Most of these terms are common to both components; thus, the phase difference is

$$\Delta\Phi(t) = \eta_{\text{hyd}}^{H}(t) - \eta_{\text{hyd}}^{V}(t) + m + b + \nu, \tag{7.2}$$

where $m = m^{\text{H}} - m^{\text{V}}$, $b = b^{\text{H}} - b^{\text{V}}$ and $\nu = \nu^{\text{H}} - \nu^{\text{V}}$.

In this experiment there is not sufficiently precise pseudo-range measurements to solve the initial phase bias as is done in Blewitt [1989]. The expected phase difference due to hydrometeors, $\Delta\eta_{\text{hyd}}$, is in the range of millimetres, while the pseudo-range accuracies are of the order of centimetres. This term b changes in every arc of data (continuous tracking), and therefore the observation is not absolute but relative to the first measurement.

To avoid further problems, only the longest arcs of data is considered, and the rest, if any, are discarded. To enable comparison among different observations, each arc is forced to have a zero mean:

$$\Delta\Phi'(t) = \Delta\Phi(t) - \langle\Delta\Phi(t)\rangle\,. \tag{7.3}$$

This step homogenizes all the observations allowing the comparison among them. It removes the contribution from b and ν terms, but it also erases any constant signature of the polarimetric measurement. Thus, any rain contribution in which depolarization is present from the beginning and remains until the end of the observation will be missed. In a satellite-to-satellite geometry (PAZ scenario), even without knowing the arbitrary initial constants there is expected that the initial phase can be calibrated, since at the beginning of the occultation, the radio link between the GPS and the LEO does not cross the troposphere. A summary of the expected differences between the spaceborne mission and this ground experiment can be found in Table 7.1.

7.1.2 *Local multipath*

Local multipath is the result of the combination of the signal from the satellite and one or more signals from the same source that have followed different paths to reach the receiver, for example, by being reflected on the ground or on a metallic structure. It affects the phase differently in the H and in the V components, giving a pattern that depends on the surrounding geometry, environmental conditions and position of the transmitter. The antenna is placed over a shelter, which has several metallic pieces. Moreover, there is a meteorological station a few metres from the experiment. Thus, the data suffer from a severe local multipath interference. If the

Parameter	Ground-based experiment	ROHP-PAZ
Initial phase delay	unknown, need to subtract the mean value of each measured arc (Equation 7.3)	calibrated from the polarimetric phase difference at highest layers of the atmosphere
Local multipath	multiple reflectors and environmental dependency because of dry or wet changes in electrical permittivity of soil and structures	expected stable properties of local satellite structure; no expected dependency on the environment
Ionosphere	the signal only crosses the ionosphere once, before hydrometeor depolarization	double ionosphere crossing, one after hydrometeor depolarization. Calibration needed.
Thermodynamic profiles	refractivity, pressure, temperature and humidity cannot be extracted	refractivity, pressure, temperature and humidity can be derived

Table 7.1: Summary of the expected relevant differences between the ROHP-PAZ space-borne experiment and the conducted ground-based field campaign.

reflecting process affected both H and V equally, this effect would cancel in $\Delta\Phi$. However, metallic structures with longitudinal edges might affect the scattering in the two polarizations differently.

The GPS satellites have an orbit period of one sidereal day. This implies that, in ideal conditions, the local multipath pattern ought to repeat after a sidereal day since the satellite is again in the same position with respect the observation site (it follows the same azimuth – elevation curve every sidereal day). To characterize and, to a large extent, remove the local multipath pattern from the signal, the time series of observations $\Delta\Phi_{\text{day}}^{\text{PRN}}(t)$ are converted into elevation series $\Delta\Phi_{\text{day}}^{\text{PRN}}(\epsilon)$. Time can be mapped onto elevation using the GPS orbit information that provides a precise GPS position for each time. This conversion allows the direct comparison among the observations from different days, making the signal only dependent on the satellite position.

Once the direct comparison is possible, the local multipath pattern can be found by performing the average and the standard deviation of the $\Delta\Phi_{\text{day}}^{\text{PRN}}(\epsilon)$ for a given set of days. To account for all environmental conditions other than rain, the local multipath pattern is obtained using all the days identified as “no-rain” days. This identification is done taking into account information from two different sources: the ground weather station placed next to the observation site, and the radar reflectivity from the weather radar of the area. If the ground weather station indicates

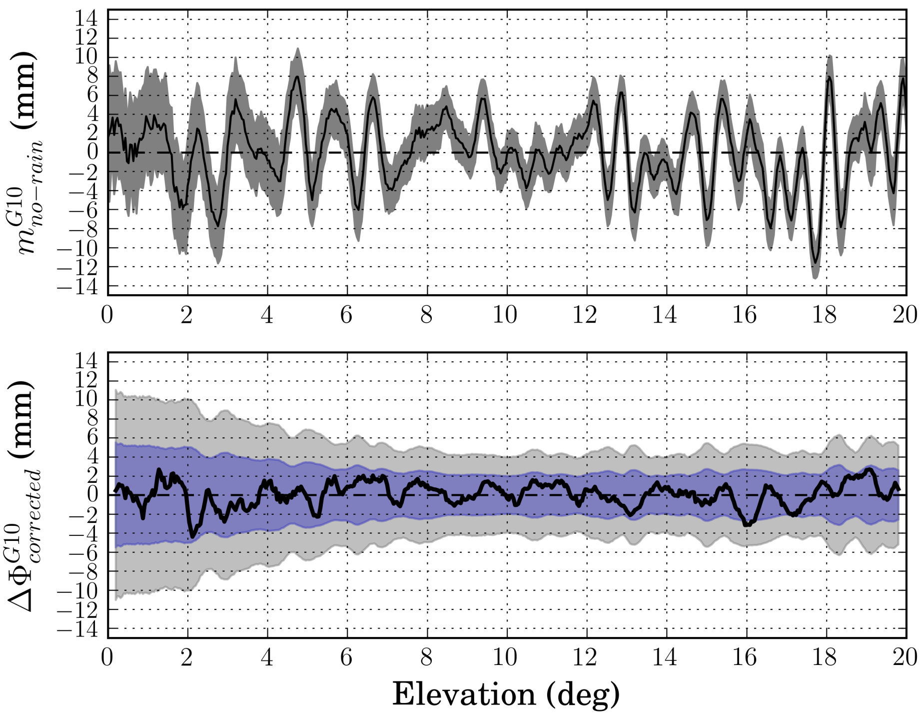

Figure 7.2: Examples of (top) local multipath pattern after applying Equation 7.3 for PRN 10 ($m^{\mathrm{G10}}_{\text{no-rain}}, \sigma^{\mathrm{G10}}_{\text{no-rain}}$), using a total of 132 days defined as no-rain days. Notice the large standard deviation at lower elevations and $\sigma^{\mathrm{G10}}_{\text{no-rain}}$ of about 2 mm at higher elevations. Bottom panel: corrected $\Delta\Phi^{\mathrm{PRN}}_{\text{day}}(\epsilon)$ for 16 April 2014 (black line) after applying Equation 7.4. The 1 and 2σ thresholds (local multipath standard deviation) are represented in blue and grey, respectively. Figure from Padullés et al. [2016a], Fig. 3.

that no rain was accumulated during the observation time and the weather radar indicates that no valid Z_e values were present between the antenna and the GPS, the day is labelled as no-rain. More details about the meteorological information used in the data analysis can be found in Section 7.2.

The average (m) and the standard deviation (σ) of the no-rain days ($m^{\mathrm{PRN}}_{\text{no-rain}}, \sigma^{\mathrm{PRN}}_{\text{no-rain}}$) represent the local multipath pattern for no-rain days and can be seen in Figure 7.2 (top). Note that the multipath pattern features vary between GPS transmitters because of different geometry; thus, interaction with the nearby structures. Usually, $\sigma^{\mathrm{PRN}}_{\text{no-rain}}$ is large at low elevations. It is well known from GNSS geodetic stations that signals received at low elevation angles present much larger multipath and variability [e. g. Larson et al., 2013]. To obtain the final measurement, i.e. the one that will be analysed, this local multipath pattern is removed from the measured signal $\Delta\Phi'(\epsilon)$:

$$\Delta\Phi^{\mathrm{PRN}}_{\text{day}}(\epsilon)\Big|_{\text{corrected}} = \Delta\Phi^{\mathrm{PRN}}_{\text{day}}(\epsilon)\Big|_{\text{observed}} - m^{\mathrm{PRN}}_{\text{no-rain}}(\epsilon)\,. \tag{7.4}$$

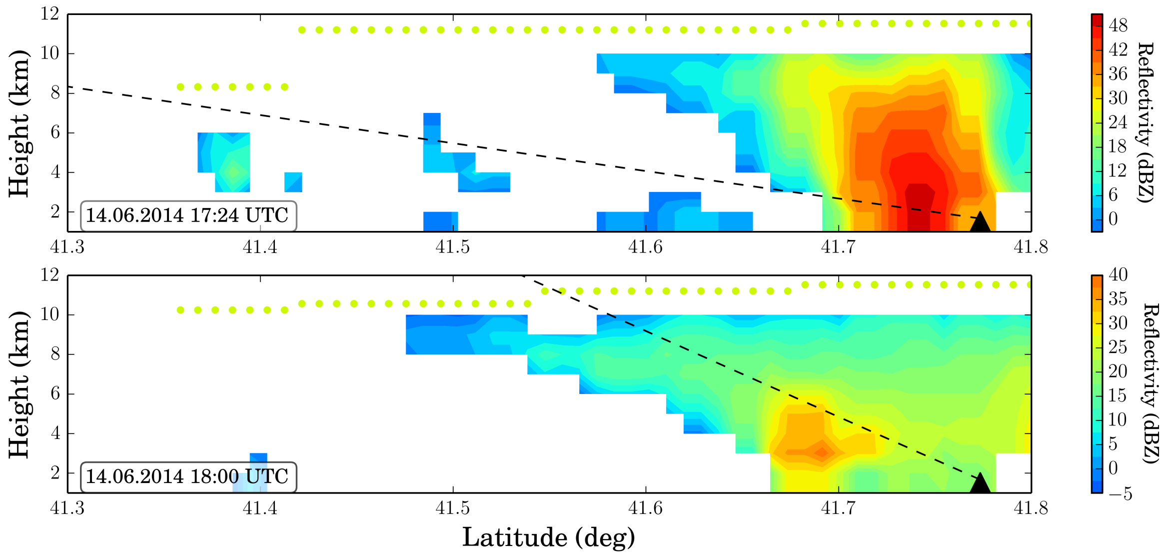

Figure 7.3: A vertical slice of radar reflectivity (shaded) at two epochs of a rising GNSS observation event. The dashed black line is the projection of the ray trajectory as simulated with OAT ray tracer on the described plane, and the dots correspond to the cloud top phase (CP) products. In this case, all the green dots indicate ice at the top of the clouds. Figure from Padullés et al. [2016a], Fig. 4.

The antenna pattern also affects the measurements differently in each component and induces a phase difference due to its different response to each polarization. Since the antenna is the PAZ's engineering model, its characteristics should be the same as those of the one mounted on the satellite, and its pattern is characterized in Figure 2.4. Its effect, though, is implicitly taken into account in the $m^{\mathrm{PRN}}_{\text{no-rain}}$ term (it is constant in time and only depends on the satellite position), and therefore it is implicitly corrected by applying Equation 7.4. Hereafter, the corrected measurement will be referred to as $\Delta\Phi^{\mathrm{PRN}}_{\mathrm{day}}(\epsilon)$. An example of corrected $\Delta\Phi^{\mathrm{PRN}}_{\mathrm{day}}$ is given in Figure 7.2 (bottom).

7.1.3 *Measurement precision*

Even though it would be possible to determine the carrier phase measurement precision as in Section 2.3, this would not be an actual value for the real precision of the polarimetric phase shift measurement in this experiment. Many factors, such as multipath interference, add dispersion to the observations and affect the actual precision of the measurement. These effects cannot be theoretically characterized and removed, but they have to be empirically determined.

Besides multipath interference, it has been explained in the previous sections of this dissertation that the ionosphere might induce a differential phase shift through the Faraday rotation effect, when the polarization of the wave is different from the RHCP case before crossing the ionosphere. In the geometry of this experiment, the signal is crossing the ionosphere only once, before crossing any hydrometeor depolarizing layer. In this case, the possible depolarization due to the ionosphere is only caused by the fact that the emitted signal might be different from the perfectly RHCP. Assuming that the deviation from the perfect RHCP case is constant in time for each GPS, it can be assumed that the possible depolarization due to the ionosphere along one arch is small and constant, hence it is implicitly corrected applying Equation 7.4. If this assumptions were wrong a trend would be observed in the data after the correction, which is not the case (see for example bottom panel in Figure 7.2, where no evident trend is observed).

Moreover, moist and temperature variations in the surroundings could lead to changes in the dielectric constant of the reflecting surfaces and therefore slightly modify the multipath pattern day after day. Among others, these effects add dispersion to the polarimetric phase shift measurement and cannot be disentangled from them. Therefore, they are ultimately included in the $\sigma^{\mathrm{PRN}}_{\text{no-rain}}$ term in Equation 7.4.

7.2 METEOROLOGICAL WEATHER DATA

The objective of the analysis is to understand the new polarimetric observations, which requires collocated meteorological information. The weather radar of the area, in situ radiosonde data and METEOSAT satellites measurements near the GNSS observational site are used in this study.

The Servei Meteorològic de Catalunya (METEOCAT) has a weather radar network covering the Catalan coastal area [Bech et al., 2004]. Data from one of the radars were provided, which has full coverage of the area under study. These radars are all Doppler systems, with one single polarization, operating at the C band (5.6 GHz). The provided data consist of the radar reflectivity (Z_e) in dBZ as a function of latitude, longitude and height. Its resolution is $1 \times 1 \times 1$ km in a grid of 300×300 km, per 10 km of height, and every 6 min. Since it is not a polarimetric radar, we cannot extract information such as K_{dp} or Z_{dr}, which would provide clues about the orientation of the particles. The minimum Z_{e} value that is considered valid is 0 dBZ; below this the signal is considered noise and it is removed.

METEOCAT also has a network of ground stations that provide the accumulated precipitation, temperature and relative humidity in 30 min batches. Within a radius of 30 km around the observation site, there are five ground weather stations, with one located a few metres from the GNSS antennas. Through them we can have an approximation of the surface rain rate during the rain events.

Besides the radar and ground stations data, Cloud Type (CTY), Cloud Top Phase (CP) and Cloud Top Height (CTH) data products from the nowcasting and very short-range forecasting (NWC-SAF) have been used. The data have been provided by the Agencia Estatal de Meteorología (AEMET) and the EUMETSAT. These data products are a combination of satellite observations and NWP model simulations. The satellite observations are obtained by the Meteosat Second Generation (MSG) stationary meteorological satellites. They measure brightness temperatures and radiances with a radiometer at 12 different wavelengths (4 ranging from 0.4 to 1.6 μm and 8 ranging from 3.9 to 13.4 μm). The horizontal resolution is $\sim$ 3 km and the products are available for the study area every 15 min [Aminou, 2002].

The collocated cloud observations from NWC-SAF (CTY, CP and CTH) are then interpolated on to the GNSS ray trajectories. Unfortunately, these sets of data do not provide information about the orientation of the ice particles. Only those with their major axis oriented horizontally would induce a positive polarimetric signature. These data are mainly used to identify the top of the clouds and to identify ice above the maximum height of the radar products.

To complement all the information, we use the measurements provided by METEOCAT's radiosondes. These radiosondes are launched twice a day (00:00 and 12:00 UTC) at a distance of approximately 50 km to the south-east of the antenna and provide temperature, pressure and humidity as a function of height. With the limited two-time daily soundings, the temperature and refractivity profiles can be interpolated into the GNSS observation time.

Once all the information is recompiled, exact collocations of the GNSS polarimetric observations with the weather data can be performed, using the same concept as in Section 4.2. An illustration of the performed collocation can be seen in Figure 7.3. Then, all the weather information for each of the points of the ray trajectory are interpolated. For this analysis, each ray consists of 500 points, meaning that each point is separated each from the next by $\sim$ 0.52 km. 501 rays are simulated between 0 and 20° of elevation.

7.3 STATISTICAL RESULTS: DOES RAIN INDUCE POLARIMETRIC FEATURES?

7.3.1 *Polarimetric signatures in $\Delta\Phi$ standard deviations*

Once the data have been preprocessed as described in Section 7.1, the analysis should determine whether the corrected $\Delta\Phi_{\text{day}}^{\text{PRN}}(\epsilon)$ is affected by rain or not. To do so, corrected $\Delta\Phi_{\text{day}}^{\text{PRN}}$ are grouped according to three different meteorological conditions. For each group, the standard deviation as a function of elevation $\sigma_{\text{met}}^{\text{PRN}}(\epsilon)$ is computed. The three meteorological conditions and the corresponding σ are as follows:

- dry days: days when the observation was made in a low relative humidity conditions (i.e. the relative humidity did not reach 100 %) according to the nearby ground weather station and without rain ($\sigma_{\text{dry}}^{\text{PRN}}(\epsilon)$). No-rain is labelled when the nearby ground weather stations do not accumulate any rain during the observation time and the interpolation of the weather radar data along the GNSS rays does not cross any area where valid Z_e values ($Z_\text{e} > 0$) are detected.

PRN	$\overline{\sigma_{\text{dry}}}$ (mm)	N_{dry}	$\overline{\sigma_{\text{wet}}}$ (mm)	N_{wet}	$\overline{\sigma_{\text{rain}}}$ (mm)	N_{rain}	P_F
G10	2.706	20	2.895	112	3.992	25	0.99
G15	1.808	20	2.263	108	2.597	29	0.89
G22	2.565	20	3.167	113	3.738	24	0.91
G14	3.386	20	3.698	114	4.108	23	0.79
G31	1.809	20	1.876	113	2.584	24	0.99

Table 7.2: Summary of the standard deviation analysis for the polarimetric phase differences under three different meteorological conditions (dry, wet and rain days). $\overline{\sigma_i}$ and N_i account for the mean standard deviation and the number of days used for each meteorological condition group i. P_F is the cumulative probability associated with the f statistic comparing the σ of the rain and the no-rain (wet and dry) days. The f statistic is the result of the F test, and P_F can be understood as the significance level at which we reject the null hypothesis that both samples come from the same population (rain vs. wet+dry).

- wet days: days with high relative humidity (i.e. the relative humidity reaches 100 %) during or before the observation according to the nearby ground weather station, with rain before or after the observation, or with both ($\sigma_{\text{wet}}^{\text{PRN}}(\epsilon)$).
- rain days: days when the GNSS rays crossed an area where valid Z_e values are detected by the weather radar ($\sigma_{\text{rain}}^{\text{PRN}}(\epsilon)$).

This classification has been done in order to compare different meteorological conditions. For example, high relative humidity conditions could have caused condensation, leading to a wet soil and different local multipath and antenna behaviour. The mean σ across all elevation observations for each GNSS satellite during the three different meteorological conditions is summarized in Table 7.2.

It can be seen that dry days always present a lower σ than the rest and that rain days exhibit the largest σ. The standard deviation for wet days is larger than for dry days, but the difference is less significant than for the rain days. There should not be any significant differences between wet and rain days, in terms of the immediate environment. For example, just after rain, the soil should be as wet as during the rain. Therefore, the larger σ on rain days compared with the wet days indicates that factors other than the enhanced local multipath interference due to the wet soil on the rain days have contributed to the enhanced polarimetric signature.

To check whether this difference is enough to result in different populations (i.e. whether the cause of the different standard deviations is that observations are under different scenarios and not due to the use of a different sampling), a statistical F test is performed [Walpole et al., 2012]. The f statistic is defined as the ratio of the variances (σ^2) of the samples that are being compared and P_F as the cumulative probability of f. Then, the *rain* days are compared with the *no-rain* days, where *no-rain* denotes all the *wet* and *dry* days. The results of P_F are shown in Table 7.2. It can be understood as the significance level that we are rejecting the null hypothesis, i.e. that the variances that we are comparing come from the same population. It can be seen that four out of the five analysed PRNs have a P_F large enough to state that there is a difference in the standard deviation that could be related to rain.

Hereafter and for the rest of the analysis, the correction of the $\Delta\Phi^{\mathrm{PRN}}_{\mathrm{day}}(\epsilon)$ is carried out as described in Equation 7.4 using $m^{\mathrm{PRN}}_{\text{no-rain}}$, which is computed as in Section 7.1.2, taking all the *dry* and *wet* days defined in this section into account together.

7.3.2 *Phase difference as a function of elevation*

Examining each event individually, more features can be observed. To carry out such an analysis, each observation $\Delta\Phi^{\mathrm{PRN}}_{\mathrm{day}}(\epsilon)$ is compared with the $\sigma^{\mathrm{PRN}}_{\text{no-rain}}(\epsilon)$. It is defined a $2\sigma^{\mathrm{PRN}}_{\text{no-rain}}$ threshold to detect polarimetric signatures in the signal: statistically speaking, $\sim 95\,\%$ of the data should be within $\pm 2\sigma^{\mathrm{PRN}}_{\text{no-rain}}$. Thus, only the remaining $5\,\%$ of the data points, or those rays affected by some polarimetric feature can lie beyond $\pm 2\sigma^{\mathrm{PRN}}_{\text{no-rain}}$.

Lacking an absolute reference for the phase difference and in order to identify points overpassing the $\pm 2\sigma^{\mathrm{PRN}}_{\text{no-rain}}(\epsilon)$ threshold, the idea is to find the elevation point where the difference between $\Delta\Phi^{\mathrm{PRN}}_{\mathrm{day}}(\epsilon)$ and $-2\sigma_{\text{no-rain}}(\epsilon)$ is minimal, which is identified as $\epsilon_{\min}$. Then, this difference is subtracted from the observation so that the observation is aligned in such a way that, for each event, its minimum lies on the line of the $-2\sigma_{\text{no-rain}}$ threshold:

$$\Delta\Phi_S(\epsilon) = \Delta\Phi(\epsilon) - \left(\Delta\Phi(\epsilon_{\min}) + 2\sigma_{\text{no-rain}}(\epsilon_{\min})\right). \tag{7.5}$$

Defining $2\sigma^{\mathrm{PRN}}_{\text{no-rain}}(\epsilon)$ as the no-rain noise level, $\Delta\Phi_{\mathrm{S}}$ can be understood as a bias-corrected settled phase difference. After this correction, the points outside the 2σ threshold can be easily detected. The region of $\Delta\Phi_{\mathrm{S}}(\epsilon)$ above the $+2\sigma_{\text{no-rain}}$ threshold is defined as follows:

$$\Delta\Phi_{+}(\epsilon) = \begin{cases} \Delta\Phi_{\mathrm{S}}(\epsilon) - 2\sigma(\epsilon) & \text{if} \quad \Delta\Phi_{\mathrm{S}}(\epsilon) > 2\sigma(\epsilon) \\ 0 & \text{if} \quad \Delta\Phi_{\mathrm{S}}(\epsilon) \leq 2\sigma(\epsilon). \end{cases} \tag{7.6}$$

$\Delta\Phi_{+}(\epsilon)$ would be the phase difference above the statistical no-rain noise level and its area is defined as A_Φ:

$$A_\Phi = \int \Delta\Phi_{+}(\epsilon)\mathrm{d}\epsilon. \tag{7.7}$$

An example of $\Delta\Phi_{\mathrm{S}}(\epsilon)$ and A_Φ is shown in the bottom plot in Figure 7.4. In this procedure, only the option of positive phase differences is considered, as it is expected for rain effects (see e. g. Chapter 2). 30 observations with $A_\Phi > 0$ are found, of which 28 correspond to rainy scenarios. This is the first direct observational evidence of the polarimetric signatures induced by precipitation conditions in the GNSS signals.

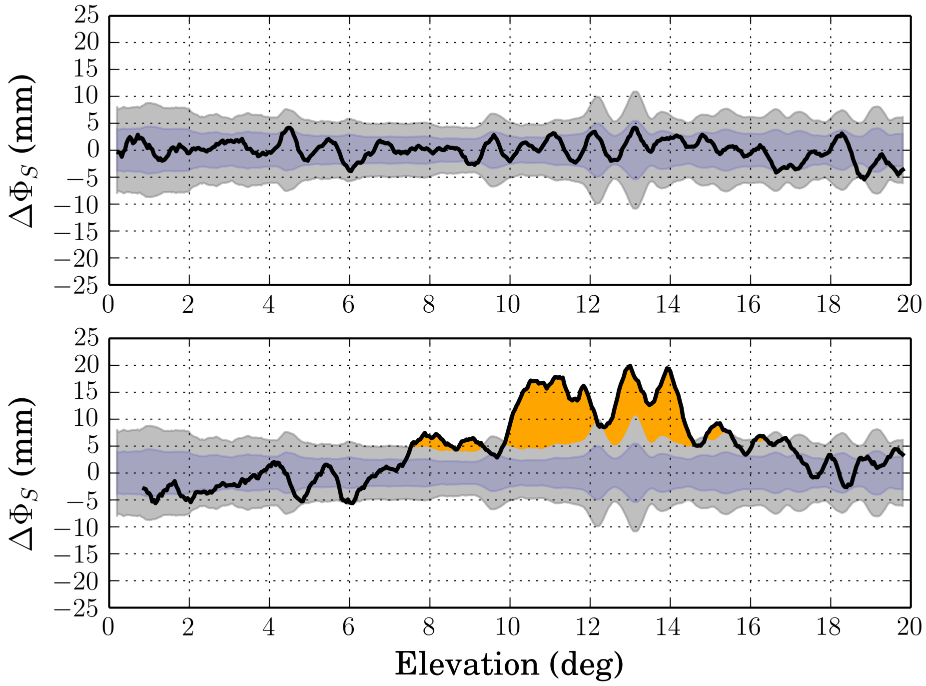

Figure 7.4: Examples of $\Delta\Phi_S(\epsilon)$ (black line), the $\pm\,\sigma_{\text{no-rain}}$ contour (blue) and the $\pm 2\sigma_{\text{no-rain}}$ contour (grey), for two observations of the PRN G22 on 26 May 2014 (top) and 14 June 2014 (bottom). The top $\Delta\Phi_S(\epsilon)$ measurement is well inside the 2σ contour, showing no polarimetric signatures. In the bottom panel, the case on 14 June 2014 (heavy rain event) shows large positive $\Delta\Phi_S(\epsilon)$. The value of $\Delta\Phi_S(\epsilon)$ above the $2\sigma_{\text{no-rain}}$ threshold will hereafter be called $\Delta\Phi_+$ and its area (orange zone) will be denoted by A_Φ. Figure from Padullés et al. [2016a], Fig. 5.

7.4 POLARIMETRIC OBSERVATIONS CONSISTENCY WITH MODELS

In order to explain the observations, the forward-scattering simulations from Chapter 4 are included. The aim is to simulate the effect of several kinds of hydrometeors, such as raindrops, pristine ice particles and melting ice particles, in order to cross-compare these effects with weather radar reflectivities, satellite observations and the measured phase differences.

For this experiment, the same exercise as in Section 4.1.3.3 has been performed, using the C band frequency that corresponds to the METEOCAT weather radar. Thus, K_{dp} is calculated for L-band frequency (GNSS observations) and Z_{e} for C-band frequency. This allows to relate the reflectivity from the weather radar in the C band with the GNSS observations in the L band. The simulations are performed using the same approach explained in Section 3.2.2, i. e. using all the mathematically valid particle size distributions and discarding those physically meaningless. Rain droplets, pristine ice crystals and melting particles are used as scattering sources. The results of the simulated K_{dp} and Z_{e} are shown in Figure 7.5.

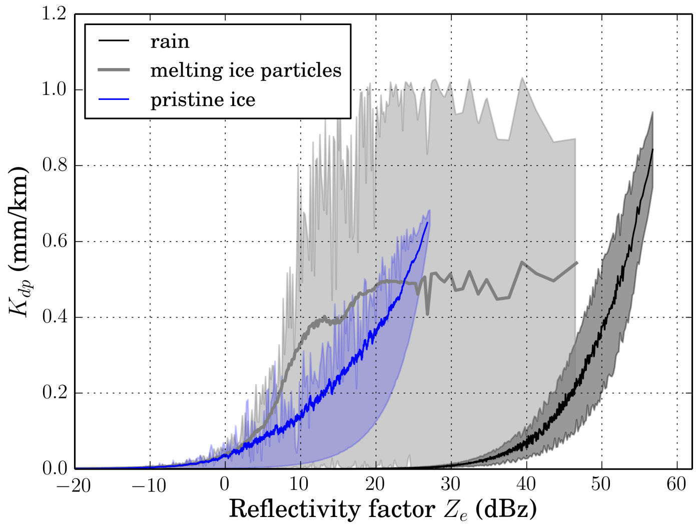

Figure 7.5: L-band forward scattering K_{dp} as a function of the C-band backscattering reflectivity factor Z_{e}, $K_{\mathrm{dp}}(Z_{\mathrm{e}})$, for all the possible physically valid $N(D)$ for each hydrometeor type: rain (black), melting ice particles (grey) and ice crystals (blue). Raindrops need high reflectivity to produce high K_{dp}, while ice crystals and melting ice particles can induce high values of K_{dp} at smaller values of Z_{e}. The thick lines overplotted represent the $Z_{\mathrm{e}} - K_{\mathrm{dp}}$ relation used in this analysis for each hydrometeor type. Figure from Padullés et al. [2016a], Fig. 7.

7.4.1 *Modelled A_Φ: rain effects*

At the beginning of the campaign, only rain was expected to affect the polarimetric signal. Some constraints have been applied to the (N_0, Λ, μ) triplets in order to use only those producing physically valid quantities: the R has been limited to be as high as $70\,\mathrm{mm\,h^{-1}}$ as suggested by the meteorological ground stations, and an upper limit of LWC was set to be $3\,\mathrm{g\,m^{-3}}$ according to the observational evidence of severe storms described in Black and Hallett [2012]. All the parameter triplets producing quantities out of these ranges are discarded.

To relate the observations from the weather radar and the measurements from the polarimetric antenna, the $Z_{\mathrm{e}} - K_{\mathrm{dp}}$ relation is needed. It can be seen in Figure 7.5 how a wide range of possible K_{dp} can be related to a given Z_{e}. For simplicity, the $Z_{\mathrm{e}} - K_{\mathrm{dp}}$ indicated by a thick line in Figure 7.5 is used. Hence, the expected A_Φ caused by rain for every GNSS measurement are simulated, using the radar Z_{e} values interpolated to GNSS ray trajectories and the chosen $Z_{\mathrm{e}} - K_{\mathrm{dp}}$ relationship. The results are shown as black dots in Figure 7.6. Despite the polarimetric signatures on rainy days, Figure 7.6 shows that raindrops alone do not induce the large polarimetric signals observed (black dots in Figure 7.6). Therefore, the effects of other hydrometeors must be taken into account.

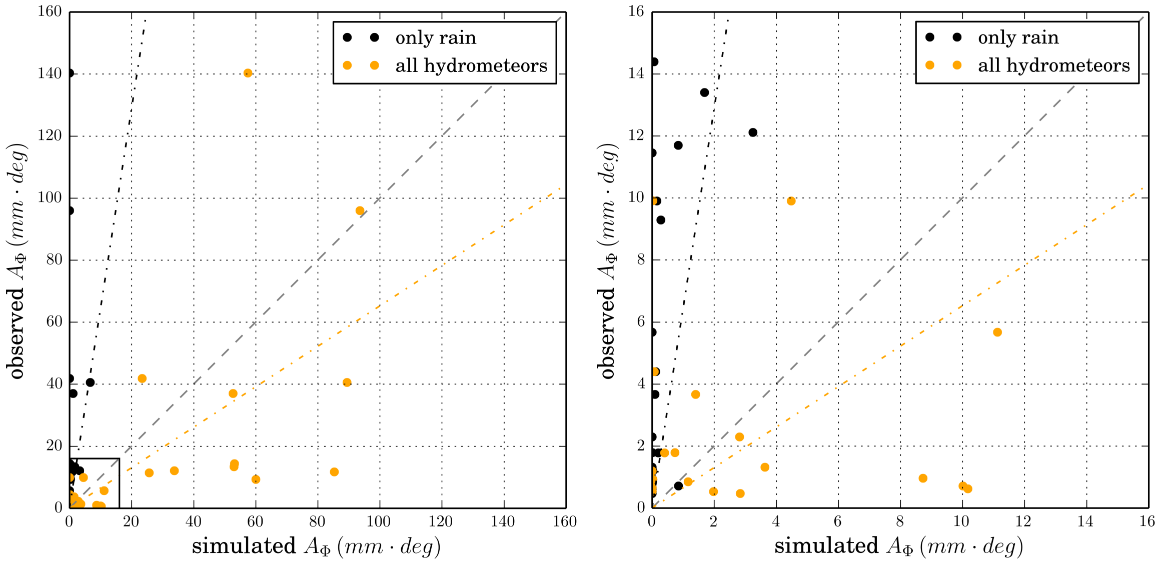

Figure 7.6: (Left) Observed versus simulated A_Φ. (Right) The area where $A_\Phi < 16$ mm deg in more detail. Black dots represent the simulated A_Φ using only raindrops, while orange dots represent the simulated A_Φ accounting for ice crystals and melting ice particles too. The dash–dot lines represent the best fitted line to the only rain A_Φ (black) and to the rain, ice and melting particles A_Φ (orange). Figure from Padullés et al. [2016a], Fig. 8.

7.4.2 *Could ice and melting particles explain the large polarimetric signatures?*

The aim here is to simulate the expected A_Φ induced by icy and melting particles. To do so the results from Section 4.1.3.3 for dendrites and melting particles are used. Their shapes can be seen in Figure 4.3, top left and bottom right, respectively.

A given ice-induced Z_e can be explained by a range of ice particle characterizations, such as different combinations of canting angle, IWC, percentage of horizontally oriented particles with respect to randomly oriented ones, or the predominant sizes of the particles. This diversity of ice conditions relate to a diversity of K_{dp}. This means that a given Z_e links to many possible K_{dp} values. In order to keep this modelling simplistic to understand the contributions and the order of magnitude of the polarimetric effect, and because of the lack of ancillary information to properly characterize the ice properties that actually occurred, only horizontally oriented dendrites are assumed in this experiment, with a maximum IWC of $1\,\mathrm{g\,m^{-3}}$. The maximum IWC is chosen according to the maximum values observed in Delanoë and Hogan [2010]. The chosen $Z_e - K_{dp}$ relation used for ice particles is highlighted with a thick blue line in Figure 7.5.

Melting ice particles have an even wider range of variability. As can be seen in Figure 7.5 (in grey), the possible Z_e and K_{dp} are widely spread. The $Z_e - K_{dp}$ relationship indicated by a grey thick line is used when accounting for melting ice particles. As for rain and pristine ice, this relation is rather arbitrary, as we do not have the required ancillary ground-truth information to properly characterize these particles, and the goal is to explain, to one order of magnitude, the measurements.

The contribution of rain, ice, and melting ice particles is separated according to the temperature. The temperatures are given by the METEOCAT's radiosondes, mentioned in Section 7.2. Noting that the radiosonde observation may differ in exact location and time, they are the closest to a true value of the temperature profiles. These radiosonde observations are in the GPS antenna field of view. For the cells above land (like the ones analysed here), METEOCAT profiles are less than 50 km away and temperatures above the boundary layer should be representative. The radar reflectivity measured at heights with temperatures above 1 °C is considered to come from rain. Particles between 1 and −5 °C are assumed to be melting ice particles. Below −5 °C they are assumed to be ice. Ice particles are assumed to be bigger between −5 and −20 °C because this region is considered to be the maximum dendritic growth zone [Kennedy and Rutledge, 2011]. Above the radar measurements, ice contributions are assumed when the simulated ray intersects with ice regions, according to the combination of the cloud top phase and cloud top height products from the NWC-SAF. In this case, the particles are assumed to be smaller. The thickness of the ice particle layer is assumed to be of about 2 km, in agreement with Noel and Chepfer [2010].

In addition, the contribution to A_Φ due to ice and melting particles is only simulated when the observed $\Delta\Phi_+(\epsilon)$ is positive. The reason is that if there were no measurement of $\Delta\Phi_+(\epsilon)$, there would not be oriented crystals in the ray path, nor a contribution to K_{dp}. The Cloud-Aerosol Lidar and Infrared Pathfinder Satellite Observation (CALIPSO) images [Winker et al., 2010] show how only some regions of the clouds contain oriented ice crystals. This is consistent with discontinuous positive observations of $\Delta\Phi$, as made here. In Figure 7.7 there is shown a CALIPSO image that corresponds to a overpass near the observation site. In the image different kind of hydrometeors can be identified, such as rain, ice and oriented ice. There are also some regions where the classification of the hydrometeor was not possible, which might correspond to mixed phase particles. Unfortunately, no collocations were found between CALIPSO and the experiment observations.

The results for the simulated A_Φ taking into account the different hydrometeors are shown by orange dots in Figure 7.6. For every black dot (only rain simulated) an orange dot is included. Since these dots are intended to reproduce the same observed A_Φ, there will be a black and an orange dot for every observed A_Φ. A block diagram is shown in Figure 7.8 to help the reader follow the steps that lead to the Figure 7.6 results. All the data, information and relations used from the data acquisition to the final results are summarized in it.

Comparing the corresponding black and orange dots for a given observed A_Φ, one may note how the simulated A_Φ increases significantly using all three hydrometeor types with respect to using only rain. Rain alone underestimates the actual values of A_Φ. However, in most of the cases the full hydrometeors simulated A_Φ is larger than the measured one (see the slope of the best fitted lines, dot–dashed in Figure 7.6). This means that A_Φ tends to be overestimated in the simulations with

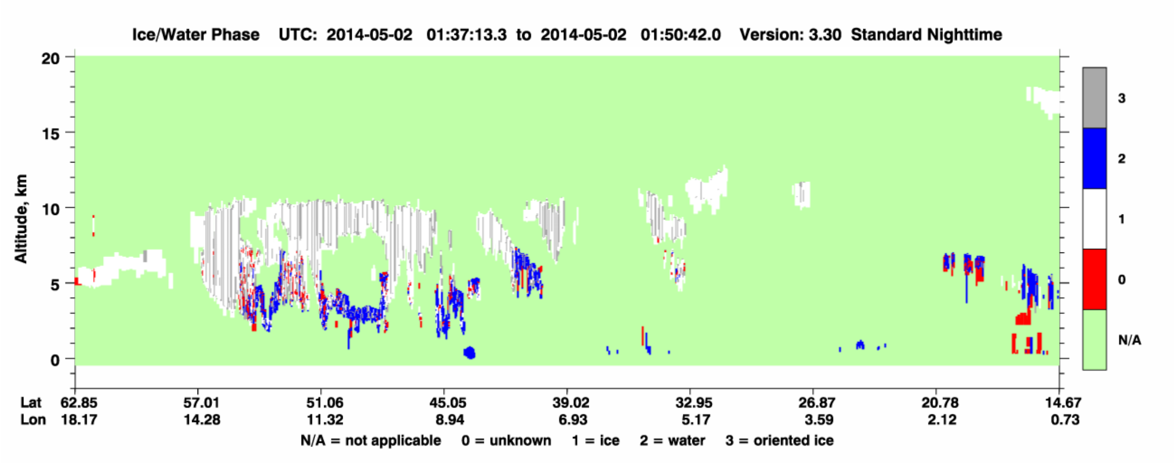

Figure 7.7: CALIPSO image example of an observation nearby the experiment site. In the image can be seen the different types of hydrometeors, like ice (identified as number 1), liquid water (identified as number 2), oriented ice particles (identified as number 3), and regions where a clear classification was not possible (mixed particles might be present in these regions). No collocations were found between the GNSS observations and a CALIPSO overpass.

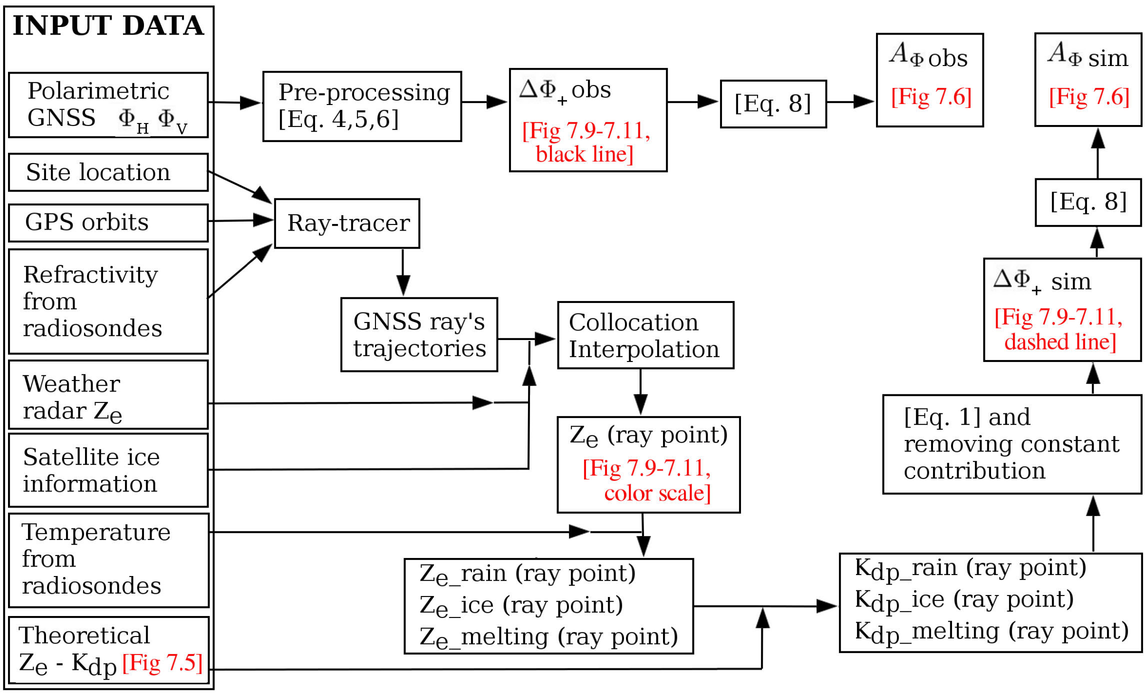

Figure 7.8: Block diagram showing all the data analysis and modelling process. All steps from the data acquisition to the final results are shown.

ice and melting particles (while underestimated with rain-only particles). Indeed, the particle characteristics that has been used in the simulations may increase the K_{dp}: the orientation of the particles is assumed to be horizontal (maximizing the polarimetric effect), and the type of particles is taken to be very asymmetric (when reality is more diverse).

Moreover, the model has been applied using the same $Z_{\mathrm{e}} - K_{\mathrm{dp}}$ relation for each hydrometeor type, in every analysed rainy event. Fine tuning of the parameters for each individual observation would be needed in order to reproduce the observations fairly, but this would not be possible to validate due to the lack of ancillary independent information, and it is thus beyond the scope of this work. Nevertheless, it can be seen how the inclusion of icy and melting particles besides rain can explain the order of magnitude of the observations.

7.4.3 *Illustration cases*

In order to further check the internal consistency of the measurements, a comparison among several observations for different PRNs is performed during the evolution of heavy rain episodes. In this section three such episodes are analysed: events on 14 June, 22 August and 26 May 2014. The analysis is performed by representing the weather radar data, the observed phase difference above the noise level ($\Delta\Phi_+$) and the simulated $\Delta\Phi_+$. An example can be seen in Figure 7.9. It corresponds to PRN 22 on 14 June 2014.

The figure shows each GNSS ray identified by its elevation angle. Every point along the ray is associated with its height (left y axis), and it is coloured according to the corresponding radar reflectivity Z_{e} (from the interpolation between the GNSS rays and the weather radar). In addition, every elevation angle is associated with a $\Delta\Phi_+$ measurement (an along-ray integral measurement), and it is plotted as a thick black line with the values indicated by the right y axis. The simulated $\Delta\Phi_+$ is plotted with dashed lines along with the measured $\Delta\Phi_+$, and its values are also given by the right y axis. Therefore, in these figures the measured and simulated phase differences are overlaid on the radar reflectivity. A temporal series of such plots for heavy rain episodes is shown in Figure 7.10 and Figure 7.11.

Figure 7.10 corresponds to events on 14 June, 22 August and 26 May 2014 (same day represented in the same column):

- In the case of 14 June 2014, according to the nearby meteorological ground stations, there was a maximum accumulation of rain of 14 mm in 30 min. This corresponds to peak rates of rain higher than 28 mm h^{-1}. Large positive $\Delta\Phi$ is present when large radar reflectivity is accumulated at high altitudes. This is in agreement with the fact that rain alone produces lower polarimetric signatures than the ones detected with the present configuration.

- On 22 August 2014, the nearby meteorological ground stations suggest peak rates of rain higher than 55 mm h^{-1} according to the accumulated precipita-

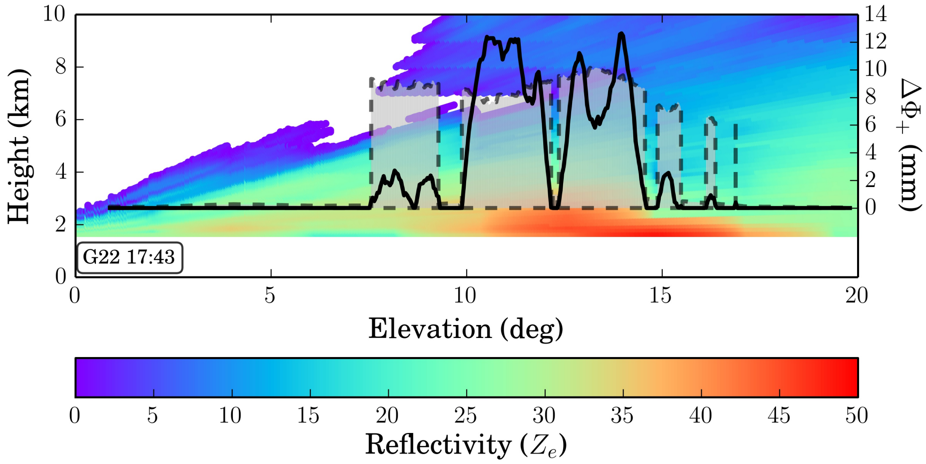

Figure 7.9: Each GNSS ray is identified by its elevation angle. Along a ray, each point can be identified by its height. The colour scale shows the weather radar reflectivity Z_e interpolated along the GNSS rays. The black line is the observed $\Delta\Phi_+$ (right y axis). Simulation results performed as described in Section 7.4 are represented by dashed lines. In the regions where actual data showed $\Delta\Phi_+ > 0$, all hydrometeors are taken into account in the simulations. Otherwise, only rain is simulated. Note also that fully oriented dendrite ice crystals have been considered in the simulation (it might not be necessary the case, information was not available). Figure from Padullés et al. [2016a], Fig. 10.

tion over 30 min. As in the previous case, positive $\Delta\Phi$ measurements are observed in the regions where significant Z_e reaches high altitudes and where the temperature is around or below 0 °C (ice and melting particles).

- For the last case, on 26 May 2014, there was no such high rain rate peak, but significant Z_e is also present at high altitudes, in agreement with the positive $\Delta\Phi$ observations.

Among all the studied cases (30), more than 93 % (28) can be explained by the combined hydrometeor modelling, i.e. the modelling can reproduce the order of magnitude of the observations. An example of one of the two cases in which the simulations failed to explain the observations can be seen in Figure 7.11: 9 July 2014. In this case, positive $\Delta\Phi$ measurements cannot be associated with any significant radar reflectivity nor with ice in the tops of the clouds crossed by the ray. Possible explanations could be some discrepancies due to missing observational data in the radar or errors in the temperature (which relies on the radiosonde interpolation) that might lead to a bad hydrometeor identification.

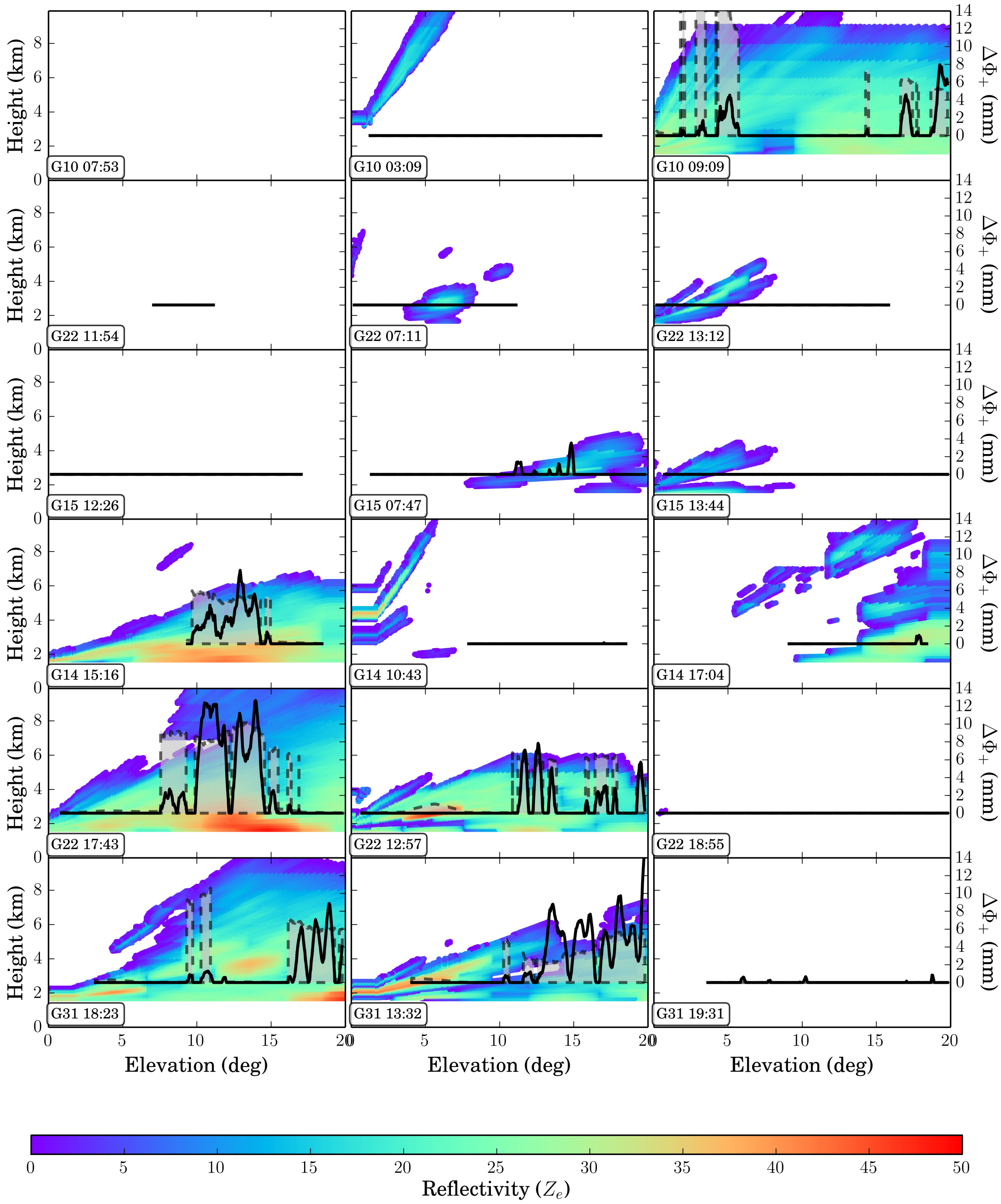

Figure 7.10: Rain episodes on 14 June 2014 (left), 22 August 2014 (middle) and 26 May 2014 (right). Each panel corresponds to a PRN, identified by the label in the lower left corner, along with the time when the satellite is at 10° of elevation. Note that the radio link with different PRNs corresponds to different times and also different azimuth. The rain episodes are sorted according to time, with the earliest at the top. Content of each panel is explained in the caption to Figure 7.9. Figure from Padullés et al. [2016a], Fig. 11.

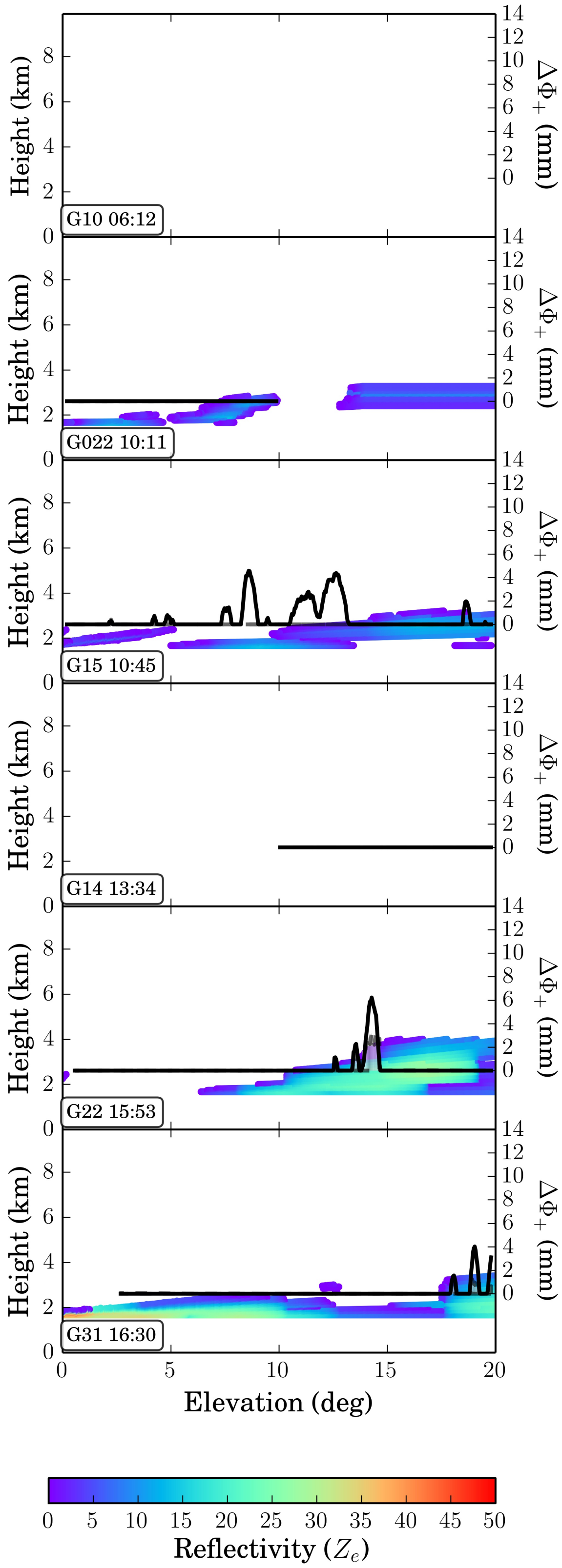

Figure 7.11: Same as Figure 7.10 but for 9 July 2014. The signal in PRN G15 could not be explained by the model simulation. Figure from Padullés et al. [2016a], Fig. 12.

8 DISCUSSION

This dissertation has covered the basic principles of the new Polarimetric Radio Occultation (Pol-RO) concept. The concept will be tested from space for the first time with the ROHP-PAZ mission. It is a proof of concept mission. Thus, the work prior to the launch has addressed three main general points: the description of the technique, its feasibility, and applications. The approaches that have been followed to address these points combine theoretical work, simulations and experimental data analysis. These methodologies have been performed simultaneously, so that the theoretical formulation has been improved with the feedback from the experimental data analysis, and then more realistic simulations have been obtained based on better modelling. This whole process yielded the results presented in this dissertation.

DESCRIPTION OF THE TECHNIQUE

The work performed for this dissertation has represented the first formulation of the polarimetric approach applied to radio occultations. The chosen observable has been the polarimetric phase shift $\Delta\Phi$, which is the integral along the ray path of the specific differential phase shift, K_{dp}. The derivation of these quantities has been treated in detail. Most of the content of the derivations is analogous to the theory used by the polarimetric weather radar community (but in forward scattering rather than backscattering), where the K_{dp} is a widely used quantity. The K_{dp} depends directly on the copolar components of the scattering amplitude matrix, **S**, which describes the properties of an incoming electromagnetic wave that is scattered by a hydrometeor. **S** depends basically on the composition, shape and orientation of the scattering particle, in such a way that completely symmetric particles produce no net effect on the K_{dp}, while asymmetric particles have enhanced contributions.

The development of the theory shows the strong dependence of the K_{dp} on precipitation microphysics, which is introduced by the particle size distribution. The most obvious consequence is that the higher the precipitation intensity, the larger K_{dp}. This means that K_{dp} is proportional to the rain rate and to the water content, quantities that are commonly used to describe the intensity of precipitation events. While, with rain, high intensity implies highly asymmetric particles, the case of ice particles is different. Ice particles can have rather arbitrary shapes, and the orientation can have a high degree of randomness as well. Then, their effect on the K_{dp} is more complex to model, and a high level of variability has to be expected when comparing simulated results with actual data.

In addition to the contribution from the K_{dp}, the extent to which K_{dp} is contributing is equally important to $\Delta\Phi$ due to its integral nature. The consequence of this is an ambiguity between the intensity and extension of the contributing phenomena, which in principle cannot be disentangled. This implies that no direct relationship can be inferred between the measured observable, $\Delta\Phi$, and the precipitation intensity.

The field campaign performed prior to the launch of the satellite had the aim of starting to identify and characterize the GNSS signal acquired using a two polarization antenna. The data analysis has revealed some limitations, especially technical ones, that arise from the polarimetric measurement. The different performance of the antenna depending on the followed satellite, the multipath effect from the surrounding elements, and the arbitrary initial phase introduced by the receiver have been the most important instrumental and technical systematic errors that have been found. While multipath is expected to be different, and hopefully less complex from space, the antenna pattern and the initial phase introduced by the receiver will be present in the upcoming spaceborne mission. Hence, these have been included and described in the theory section.

Besides the interaction with the hydrometeors, the antenna pattern and the receiver effects, something else is introducing a polarimetric phase shift: the ionosphere. The ionosphere depolarizes if the incoming signal is already depolarized, that is, it is not perfectly RHCP (or LHCP). This may occur because the emitting satellites induce a small LHCP component into the emitted signals, so they become elliptically polarized instead of circularly, or because of the depolarization induced by the hydrometeors before re-entering the ionosphere on the signal's way to the occulting receiver. This effect has been identified and described in this dissertation. Although it is usually small, this effect must be taken into account when analysing actual data, since a contribution to the $\Delta\Phi$ will come from the ionosphere.

FEASIBILITY

Once the technique has been described, the main question is whether it is possible to detect precipitation using Pol-RO or not. To answer this question, firstly, several simulation exercises have been performed. The objective has been to use actual data, both from the RO and the precipitation side and combine them to obtain as realistic a set of observables as possible. The actual RO data are the measurements performed by the COSMIC constellation, and the precipitation ones are those from the TRMM, GPM and CloudSat missions. These are all long term missions, hence their huge amounts of observations provide the opportunity to find enough coincident measurements in order to have RO measurements in a region sensed by a radar.

The first main finding that has been obtained using these data is the noise level that COSMIC shows when it is sounding a region where precipitation is present. The noise determines the precision at which the phase measurement can be achieved. Then, assuming that PAZ antennas will perform like COSMIC ones and accounting for the polarimetric mismatch, a detectable threshold of 1.4 mm phase delay can be set for the lower layers of the atmosphere. This is the precision that PAZ is expected to achieve in measuring the phase difference between its two ports, based on COSMIC measurements under precipitation conditions. Therefore, any precipitation event inducing a $\Delta\Phi$ larger than 1.4 mm will be detectable. This threshold improves with altitude.

To know how often a $\Delta\Phi > 1.4$ mm is induced by precipitation events, more complex simulations have been performed. Using the theoretical framework introduced in the first part of the dissertation, single particle simulations have been conducted using scattering codes like the *T-matrix* and the *DDA*. Simulations of the scattering of L band electromagnetic signals by different sized raindrops, different pristine ice particles, ice aggregates and partially melted particles have been computed. From these simulations, the scattering amplitude matrix is obtained, and is then weighted by the particle size distribution in order to obtain the K_{dp}. Drop size distributions are obtained using the precipitation mission's retrievals, which have been also simulated for the same set of particles as for the radar frequencies. The K_{dp}, which describes the precipitation in a region, is mapped onto the RO ray trajectories that are obtained through Ray-Tracing software. Therefore, after the integration of the K_{dp} contribution along the ray path, the $\Delta\Phi$ is obtained for each of the rays of the RO. Thus, it works as a forward operator that acquires radar observables to derive Pol-RO observables.

These simulations are used in three different approaches. In the first one, the simulations are applied only to one of the rays of the RO, using averaged precipitation measurements, hence obtaining fast results for a large quantity of events for a first statistical assessment. In this approach, the mean and the maximum rain rate along the ray path, the extension of the contributing area and the induced $\Delta\Phi$ are stored. The second simulation exercise has been to perform simulations of the $\Delta\Phi$ using real precipitation measurements on artificial RO events. In this case, the simulations provide vertical profiles of $\Delta\Phi$, and the corresponding mean and maximum rain rates of each of the rays are stored for further analysis. Finally, the third simulation exercise consists of simulating the $\Delta\Phi$ that COSMIC would have measured if it had had polarimetric capabilities, according to its actual measurements and the coincident precipitation information from the radar of the precipitation mission satellites.

From the first and second exercises, the percentage of detectable cases as a function of the rain's intensity can be obtained. From the simulations, it can be stated that around 40% of the rain events with a mean rain rate along the rain path larger than 1 mm/h will be detected with PAZ. This means that around 40% of these events induce a $\Delta\Phi$ above the detectability threshold for at least one of the rays. When the mean rain rate reaches 5 mm/h, the percentage of detectable cases is greater than 85%, and when it is larger than 10 mm/h, almost all of the cases are detectable ($\sim$ 95%). The distribution of detectable cases varies; it is more probable that a rain event will be detected in some regions than in others. Regions where it rains more tend to be the places where the precipitation is more *detectable*, although some exceptions exist. Seasonal variability is also observed.

The third simulation exercise is the most complex and the most complete. It provides, for each of the collocated events, the standard RO measurements from the COSMIC mission, and the simulated polarimetric observables based on the precipitation mission. This allows to use the actual phase, signal strength and ray trajectories to derive the realistic polarimetric observables together with real values of noise and precision, in addition to the thermodynamic retrievals obtained in the same scenario. These results, stored in a large database, can be used as a synthetic simulation of the polarimetric mission, and therefore data treatment and analysis can be tested on it. For example, the percentage of detectable cases previously obtained are confirmed using these realistic simulations, although a smaller number of cases can be used. The state of the ionosphere and the Earth's magnetic field are also included in this simulation exercise. Therefore, their impact on the polarimetric observables is taken into account. These data will be useful to test the calibration exercises that are needed to isolate the precipitation information from the rest of effects.

Field campaign

The field campaign, besides providing extremely valuable feedback for the end-to-end simulations, has provided the first experimental evidence that the effect of precipitation on the GNSS signals acquired by a two polarization antenna can be observed. These effects have been proven with a rigorous statistical analysis of about 170 days' worth of observations, where the local multipath represented the major challenge for the data analysis.

Once depolarizing effects during precipitation episodes had been statistically identified, individual events have been analysed in detail. The forward operator has been applied to this particular scenario using information from the weather radars, radiosondes and satellite imagery. Simulations for all kinds of hydrometeors have shown agreement to within an order of magnitude for most of the cases where polarimetric features have been observed in the data.

Being the first time that GNSS signals have been acquired in slant geometry with a polarimetric antenna, the campaign has been a success, both for the lessons that have been learned in terms of improving the simulations, the data analysis and the identification of systematic effects, and for the positive results in detecting polarimetric features in precipitation scenarios.

APPLICATIONS

The technique has been described, the simulations have been presented and the detection of precipitation has been proven feasible. Therefore, applications to exploit the technique have been designed and presented. In the first place, the database that has been built can be used as a test bench for any retrieval algorithm that needs to be tested. To test algorithms on such realistic data will make the identification of systematic errors easier when the actual data comes.

Using the forward operator, a relationship between the Pol-RO observable and geophysical information has been established, on a probabilistic basis. These are the mean and the maximum rain rate that the ray has crossed. To infer such relationship, a basic question has been formulated: what is the $\langle R \rangle$ (or the $R_{\max}$) that has been exceeded in the 75% of times that the $\Delta\Phi(h_{\text{tp}})$ has fell in a certain range? This question has been answered with the data generated by applying the forward operator with the whole actual GPM data, which has provided a whole set of look-up tables separated in 20×20 degrees areas all around the globe. This allows to treat each of the Pol-RO observations differently according to the region that is observed. For a complete view of the problem, the look-up tables have been constructed using not only the 75th percentile of the $\langle R \rangle$ and $R_{\max}$ data, but also the 50th and the 95th percentiles. These tables can be updated continuously with the new data that is provided by the precipitation missions.

Besides the probabilistic approach, a tomographic technique has been proposed in order to disentangle the ambiguity between the intensity and the extension of the precipitation of the Pol-RO observable. The technique has been tested theoretically and it has provided promising results. However, strong constraints are needed for it to be applicable to more realistic scenarios. Ancillary information (e. g. from models) could be introduced to improve the performance and reduce the constraints, hence further investigation with real data is needed. Nevertheless, it has been demonstrated that the technique performs well in discriminating rain events that are far from the tangent point, information that is useful when analysing the RO retrievals.

Using the collocated data, where for each RO event a coincident precipitation measurement has been identified, it has been possible to compare the RO thermodynamic profiles that are affected by rain with those that are not. An interesting finding has been to observe that the difference between the RO retrievals and the models and reanalysis outputs differs in the heights where precipitation is expected, in those profiles that have been obtained in regions where it was raining. The origin of this difference could not be readily identified, although some known biases affecting RO retrievals have been discarded. Further investigation will be needed in order to infer if this behaviour is due to intrinsic effects of the rain on the refractivity which are not well captured by ROs, or if it is a systematic underestimation of the precipitation in the refractivity provided by the models.

Similarly, refractivity profiles have been searched for specific features which could help to identify the presence of heavy rain without relying on other thermodynamic products that could be biased by model inputs. This has been addressed by means of comparing the refractivity gradient with the one it would have under certain atmospheric regimes, which can be associated with environments prone to developing precipitation. The regimes that have been checked are dry and moist adiabatic, and saturated pseudoadiabatic atmospheres. RO refractivity profiles obtained in regions where precipitation is present tend to follow more closely the saturated pseudoadiabatic reference gradient, which could be linked to the presence of clouds.

MAIN CONCLUSIONS

The main conclusions of this dissertation can be summarized in the following points:

- The technique has been described and a detectability threshold has been set, indicating that heavy precipitation events will be detectable with the ROHP-PAZ experiment.

- A forward operator, which uses weather radar measurements as inputs to provide the Pol-RO observables, has been defined and validated. Its performance is enhanced when additional information is provided, such as the standard RO retrievals. An end-to-end simulation has been performed using the forward operator and actual collocated measurements of ROs and precipitation, in order to simulate a polarimetric mission and to test the data analysis algorithms that will be needed for the mission.

- The first detection of effects from precipitation on GNSS polarimetric signals has been obtained during the field campaign. In addition, a-priori unexpected systematic effects have been detected, characterized and incorporated into the end-to-end simulation as a consequence of the field campaign data analysis.

- A probabilistic approach to identify the Pol-RO observable with geophysical information, such as the along-ray mean and maximum rain rate has been presented. This implies that vertical profiles of precipitation information can be effectively provided on a probabilistic basis, and these retrievals will improve with time through incorporating more precipitation data and polarimetric observables when available. It has also been shown that precipitation must be treated differently according to the region and the season.

- A tomographic approach to solve the ambiguity between intensity and extension that appears due to the integrated nature of the observable has been proposed. Even though ancillary information would be needed in order to improve its performance, it has been proven that it can provide valuable information for the relative positioning of the precipitation cells, in terms of the distance to the RO's tangent point.
- The need for improving the characterization of heavy rain events has been shown with two examples that have used the collocated thermodynamic RO retrievals along with actual precipitation information. An obvious difference has been observed comparing the RO products with NWP model outputs when heavy rain is present with respect to when it is not. It has also been shown how the refractivity profiles exhibit different features under heavy rain conditions.
- The ionosphere contribution to the $\Delta\Phi$ observable has been identified as a potential threat to the characterization of precipitation, and hence a calibration exercise must be addressed when actual data comes.

FUTURE WORK

The perspectives for this field of research mostly depend on whether the space mission is a success or not. If the ability to provide vertical precipitation information is proven, a wide range of opportunities will open up. Two main paths are then to be explored. On the one hand, Pol-RO data assimilation for weather prediction applications has to be addressed. Containing precipitation information, it has the potential to have an important impact on the assimilation of the RO thermodynamic products. Hence investigation in this direction will be needed.

On the other hand, Pol-RO data will potentially have a large impact on precipitation research. Thermodynamic characterization of heavy rain events will improve with the Pol-RO data, thus complementing for the precipitation missions. Understanding the mechanisms that lead to heavy precipitation is an active field of research right now, and could benefit from Pol-RO data.

Additionally, polarimetric data could be used in ionospheric research. Results from this research have shown how the ionosphere induces a depolarization of the signal that interferes with the precipitation signature. While isolating the precipitation signature is the main objective for this mission, valuable ionospheric information will be obtained as well, especially at higher altitude RO measurements.

Part IV

APPENDIX

A

LOOK UP TABLES FOR POLARIMETRIC OBSERVABLES

This appendix contains the LUTs generated for Section 5.1. The followed procedure is explained in Section 5.1.2.1.

A.1 COMPLETE LUTS

The full regional LUTs are shown here. The ones that relate the $\langle R \rangle$ with the $\Delta\Phi^{\text{trop}}$ are the following:

- Figure A.1 contains all the regional LUTs for the 5th percentile
- Figure A.2 contains all the regional LUTs for the 25th percentile
- Figure A.3 contains all the regional LUTs for the 50th percentile

The ones that relate the R_{max} with the $\Delta\Phi^{\text{trop}}$ are the following:

- Figure A.4 contains all the regional LUTs for the 5th percentile
- Figure A.5 contains all the regional LUTs for the 25th percentile
- Figure A.6 contains all the regional LUTs for the 50th percentile

A.2 DIFFERENCES AMONG LUTS

Here there are shown the differences among the LUTs, as is described in Section 5.1.2.1. The figures showing the mean values of the differences of $\langle R \rangle$ LUTs are the following:

- Figure A.7 contains the mean differences among all the regional LUTs for the 5th percentile
- Figure A.8 contains the mean differences among all the regional LUTs for the 25th percentile

- Figure A.9 contains the mean differences among all the regional LUTs for the 50th percentile

The figures showing the mean values of the differences of R_{max} LUTs are the following:

- Figure A.10 contains the mean differences among all the regional LUTs for the 5th percentile
- Figure A.11 contains the mean differences among all the regional LUTs for the 25th percentile
- Figure A.12 contains the mean differences among all the regional LUTs for the 50th percentile

The figures showing the maximum values of the differences of $\langle R \rangle$ LUTs are the following:

- Figure A.13 contains the maximum differences among all the regional LUTs for the 5th percentile
- Figure A.14 contains the maximum differences among all the regional LUTs for the 25th percentile
- Figure A.15 contains the maximum differences among all the regional LUTs for the 50th percentile

The figures showing the maximum values of the differences of R_{max} LUTs are the following:

- Figure A.16 contains the maximum differences among all the regional LUTs for the 5th percentile
- Figure A.17 contains the maximum differences among all the regional LUTs for the 25th percentile
- Figure A.18 contains the maximum differences among all the regional LUTs for the 50th percentile

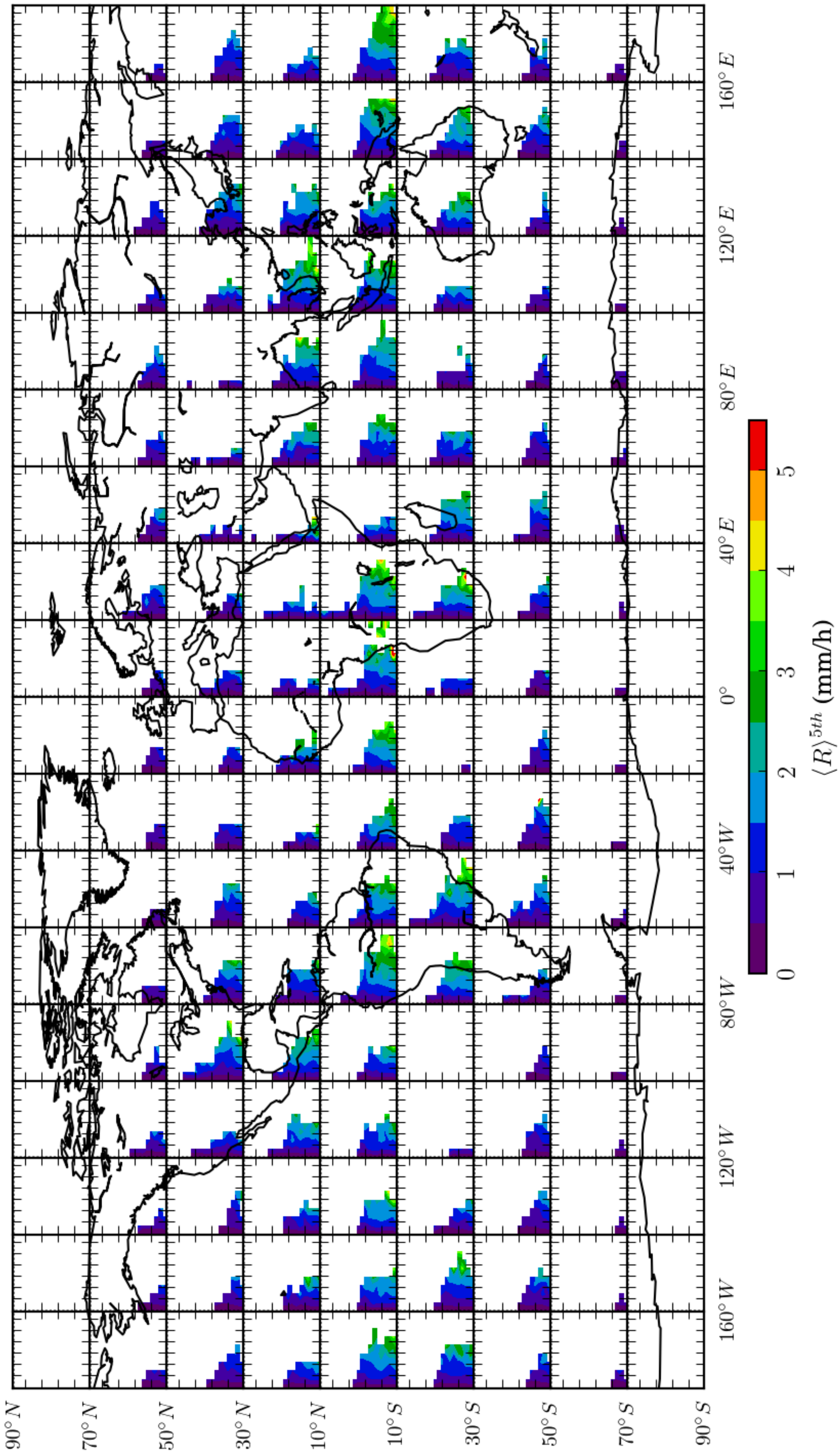

Figure A.1: Regional LUTs for $\langle R \rangle$; 5th percentile

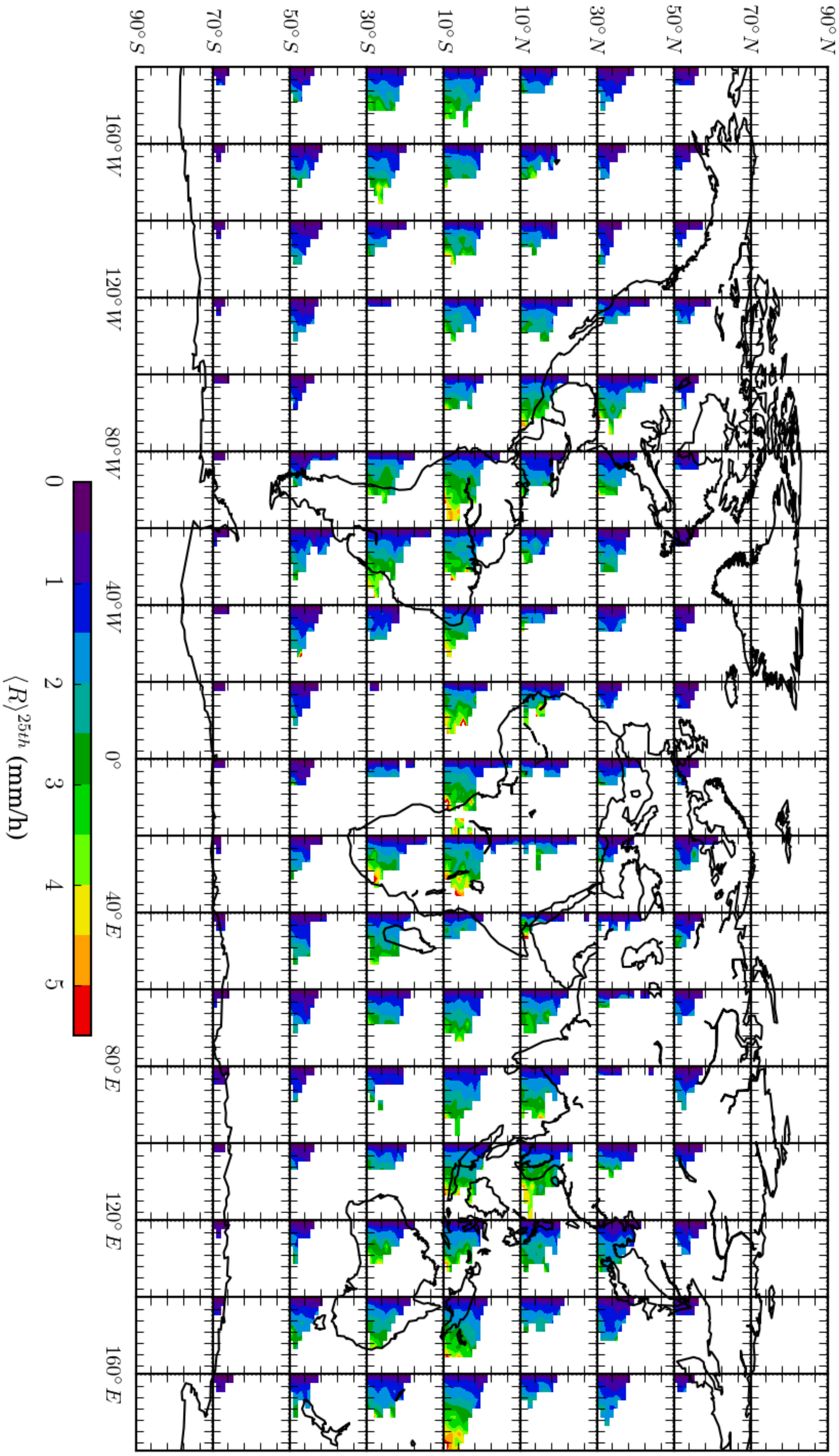

Figure A.2: Regional LUTs for $\langle R \rangle$; 25th percentile

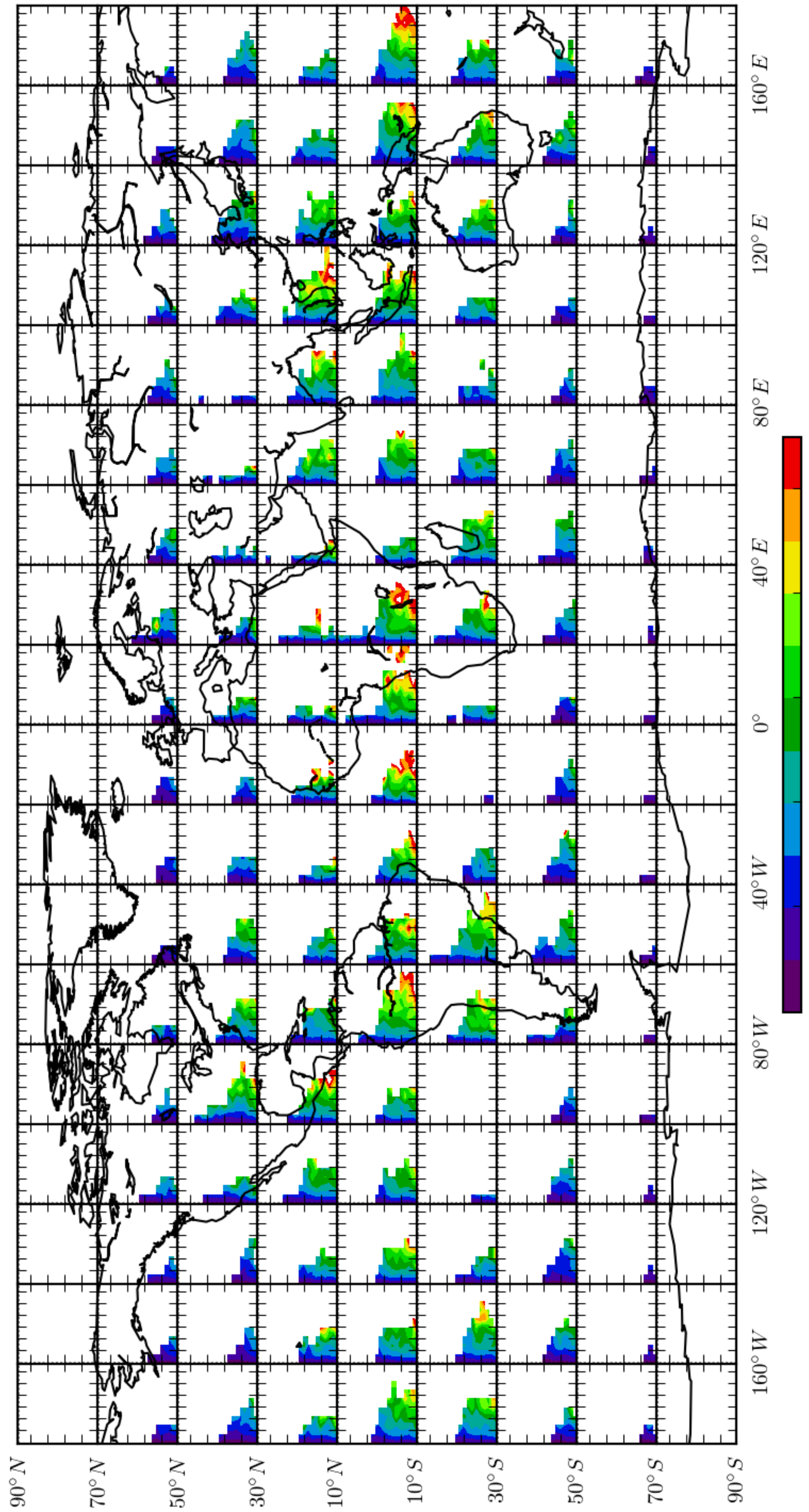

Figure A.3: Regional LUTs for $\langle R \rangle$; 50th percentile

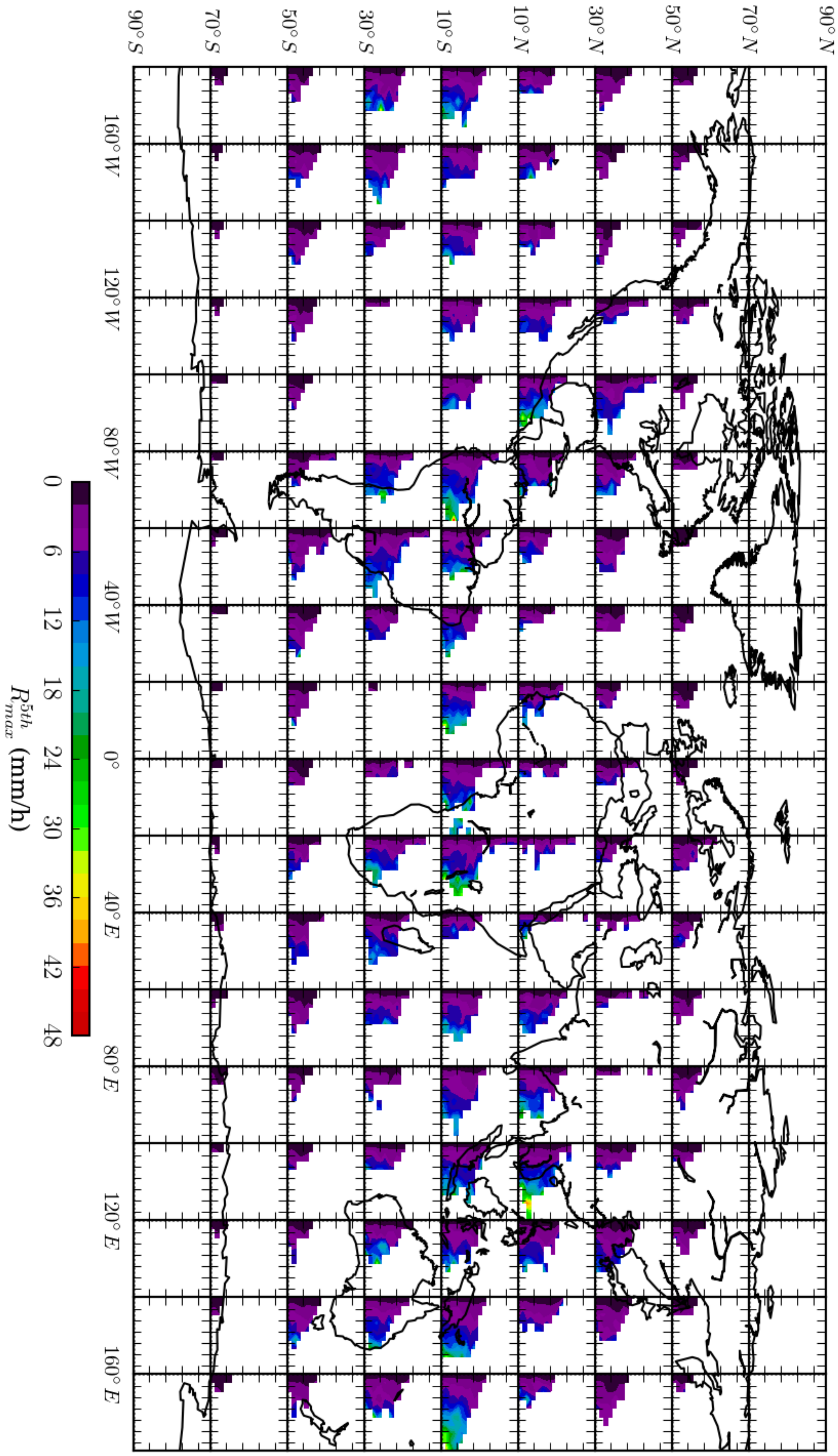

Figure A.4: Regional LUTs for R_{max}; 5th percentile

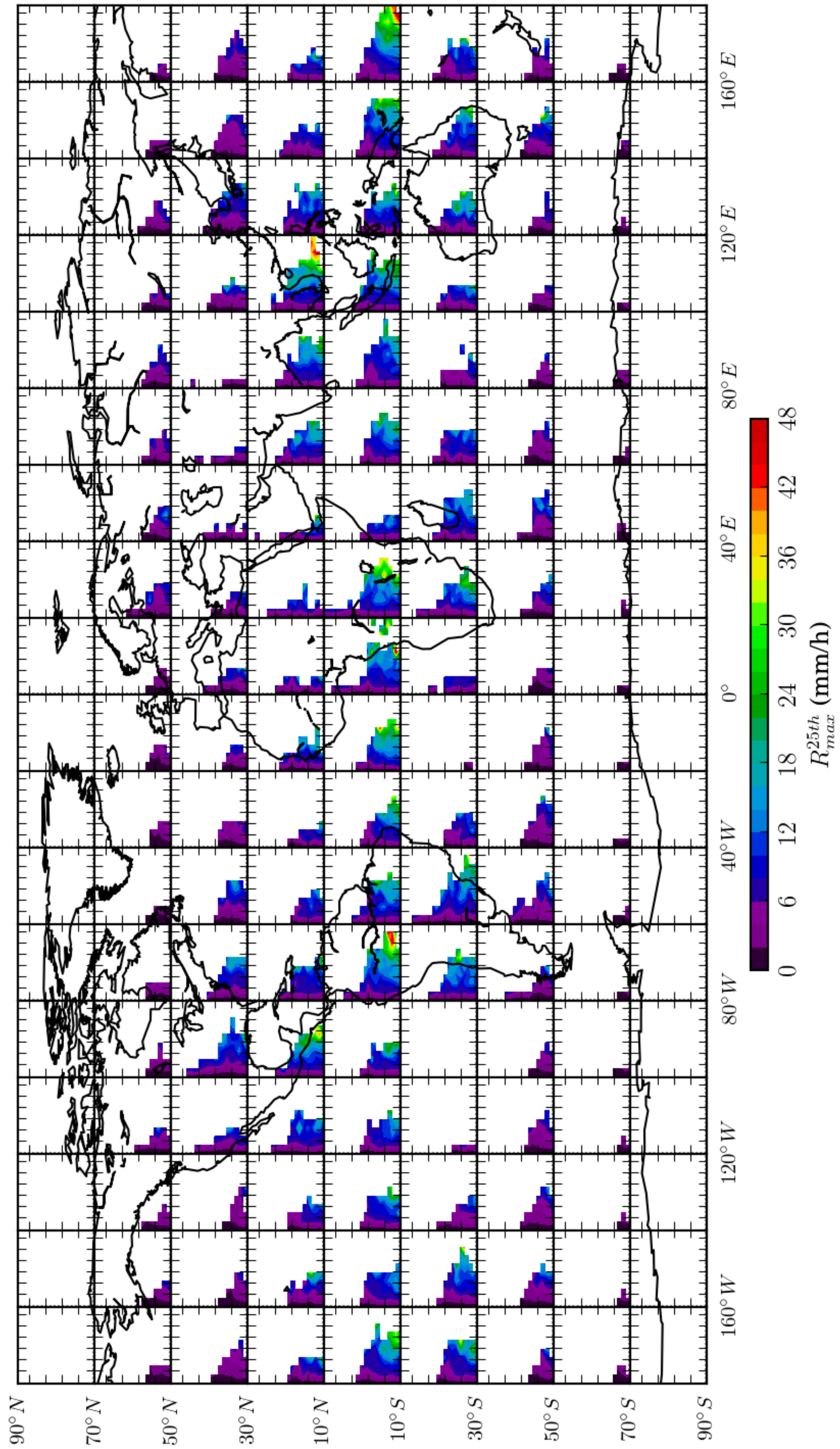

Figure A.5: Regional LUTs for $R_{\max}$; 25th percentile

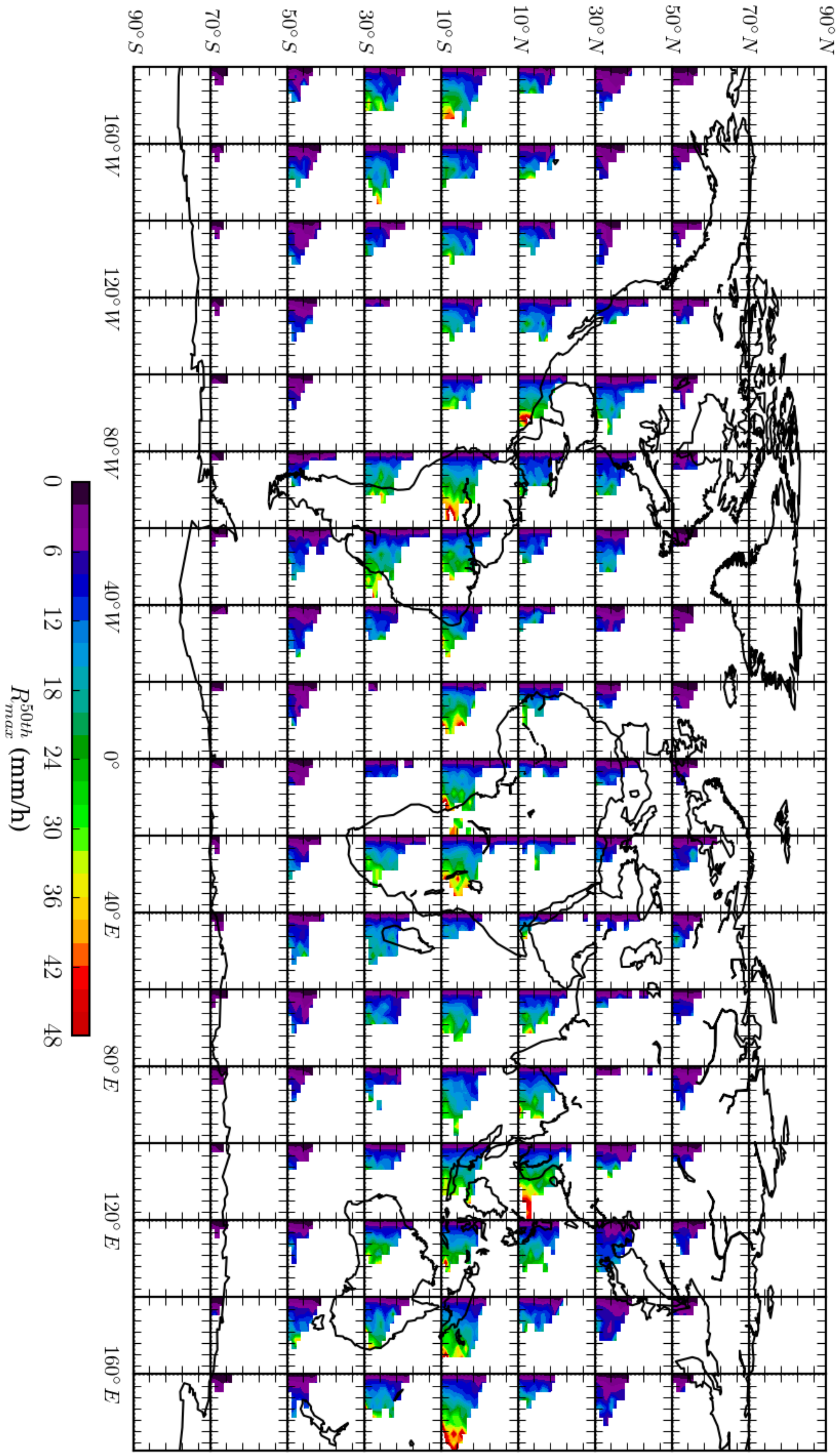

Figure A.6: Regional LUTs for R_{max}; 50th percentile

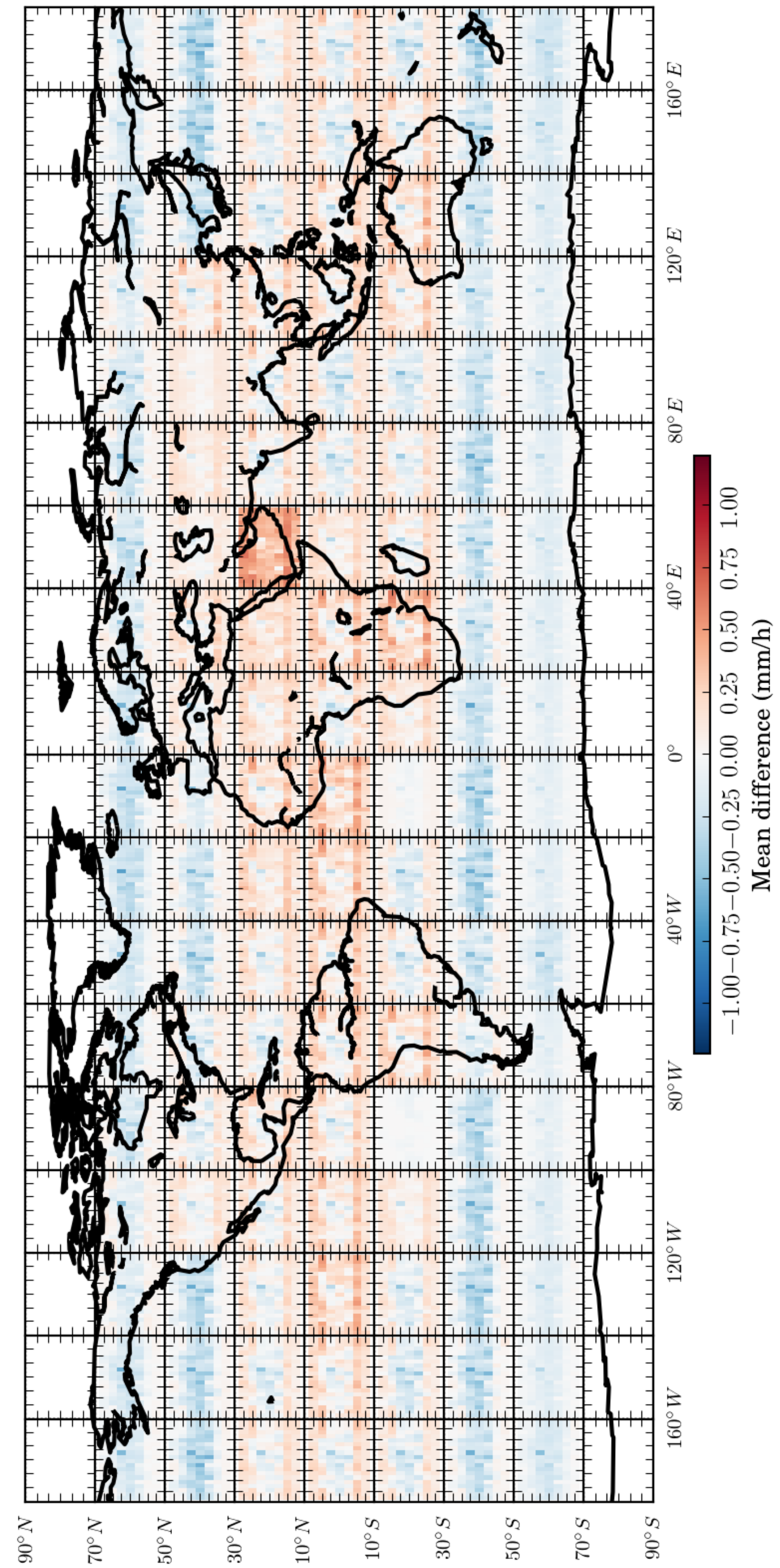

Figure A.7: Mean differences among regional LUTs for $\langle R \rangle$; 5th percentile

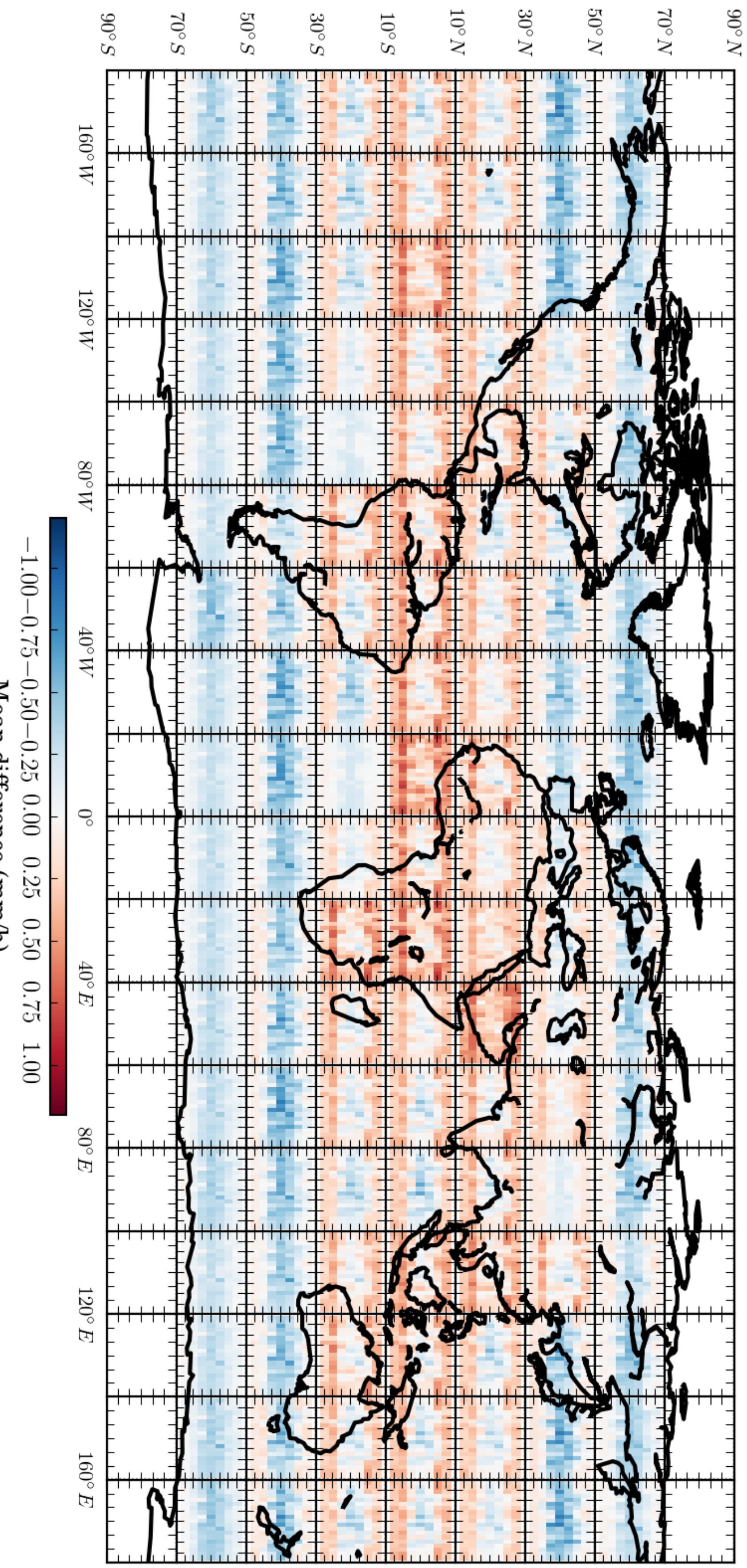

Figure A.8: Mean differences among regional LUTs for $\langle R \rangle$; 25th percentile

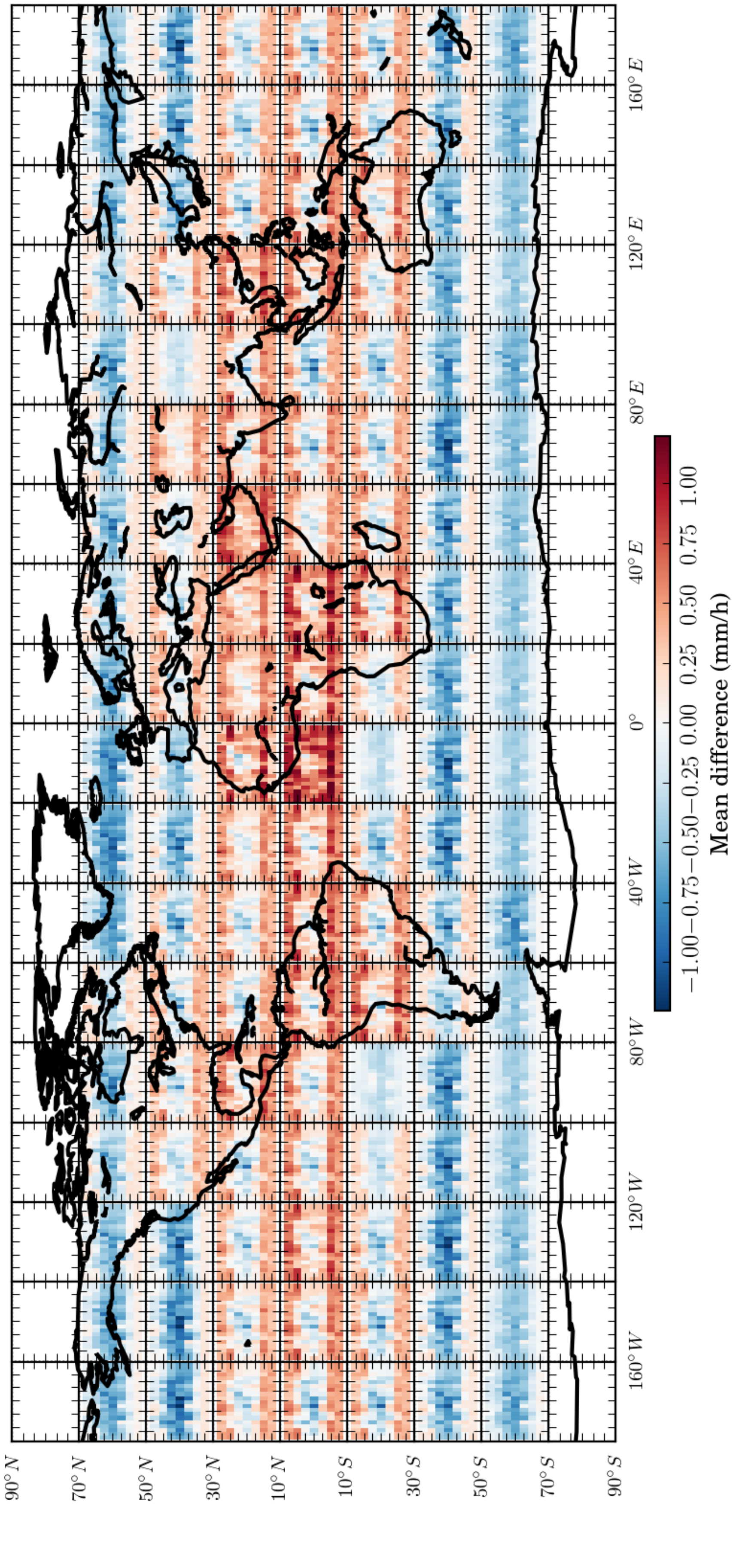

Figure A.9: Mean differences among regional LUTs for $\langle R \rangle$; 50th percentile

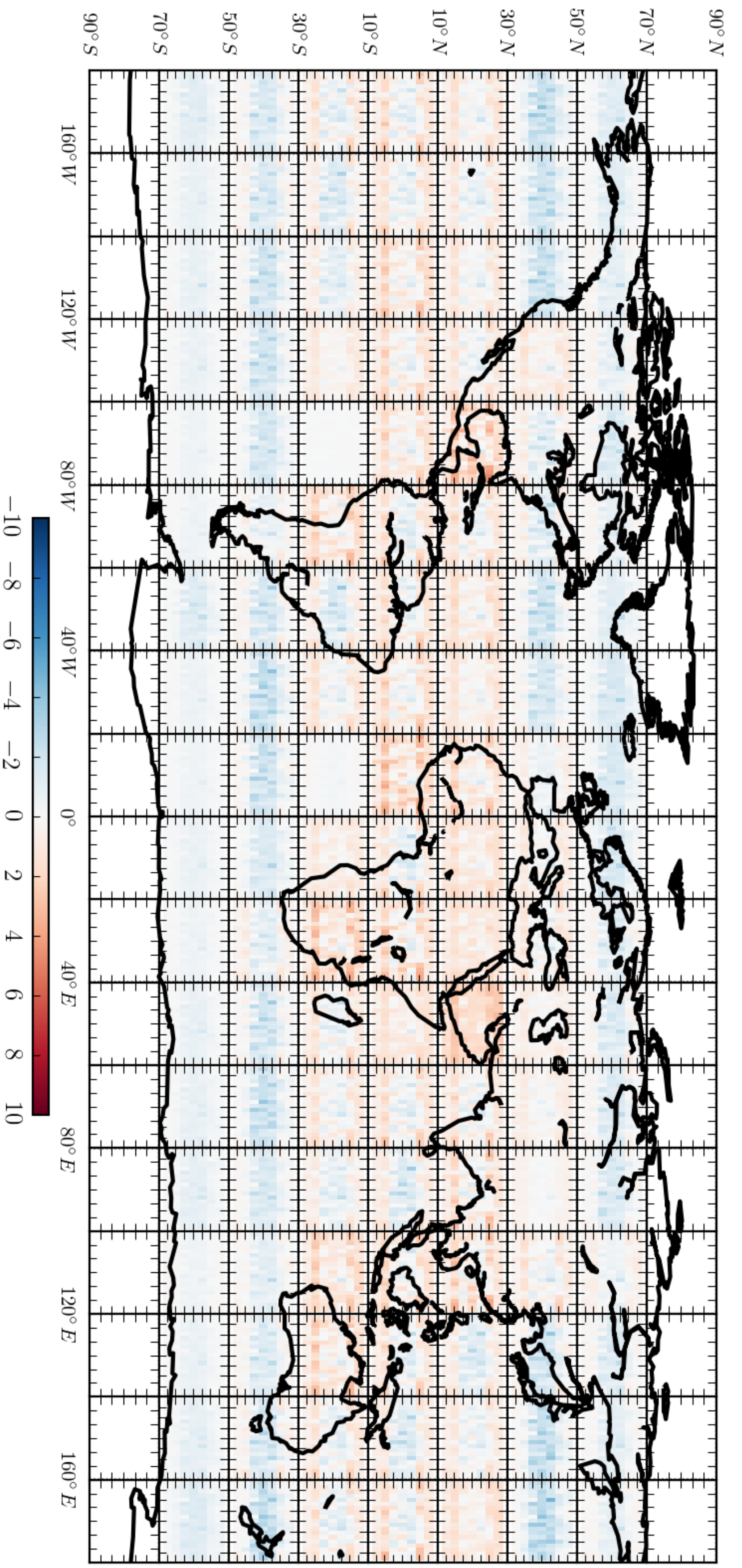

Figure A.10: Mean differences among regional LUTs for R_{max}; 5th percentile

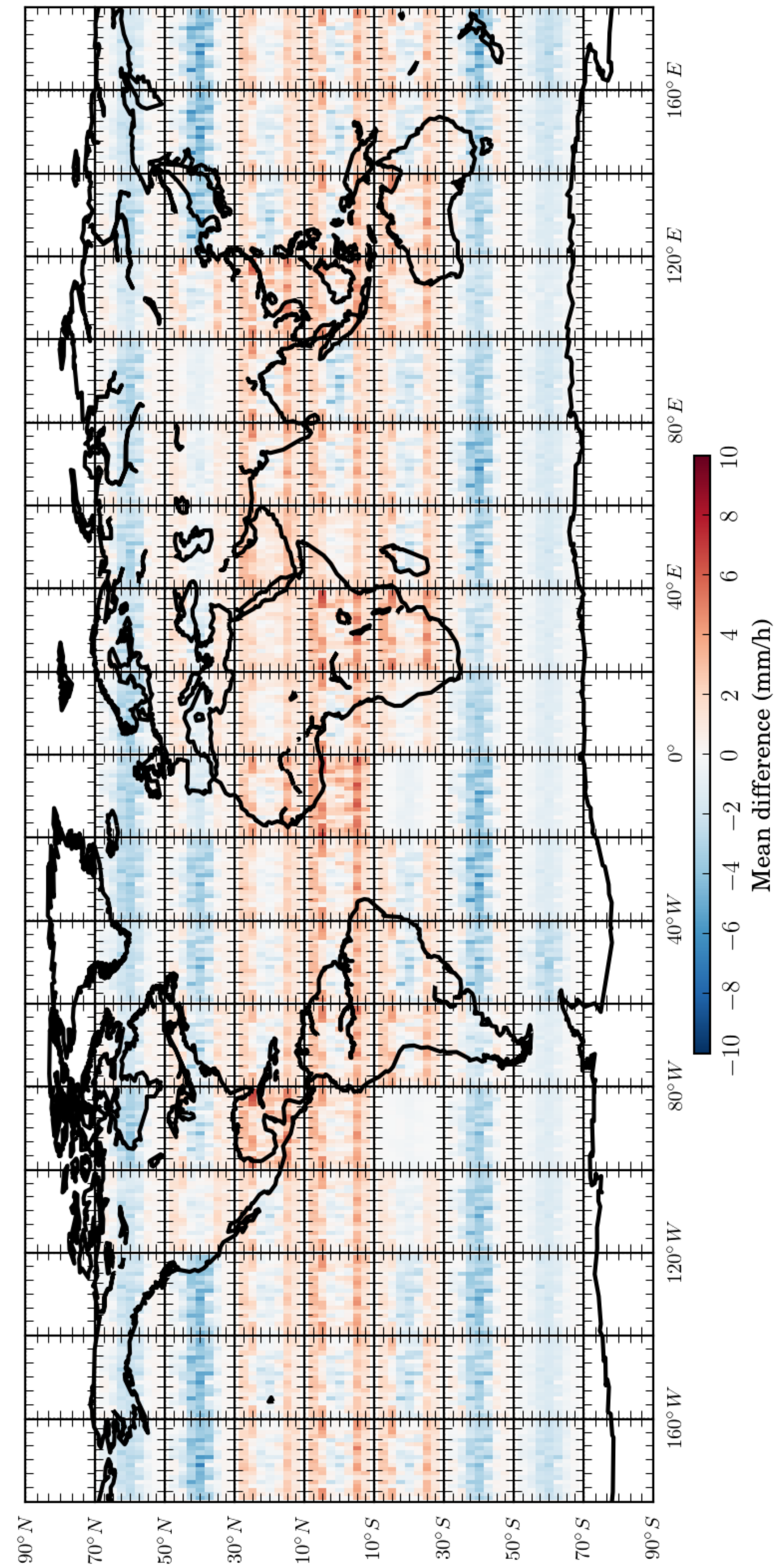

Figure A.11: Mean differences among regional LUTs for $R_{\max}$; 25th percentile

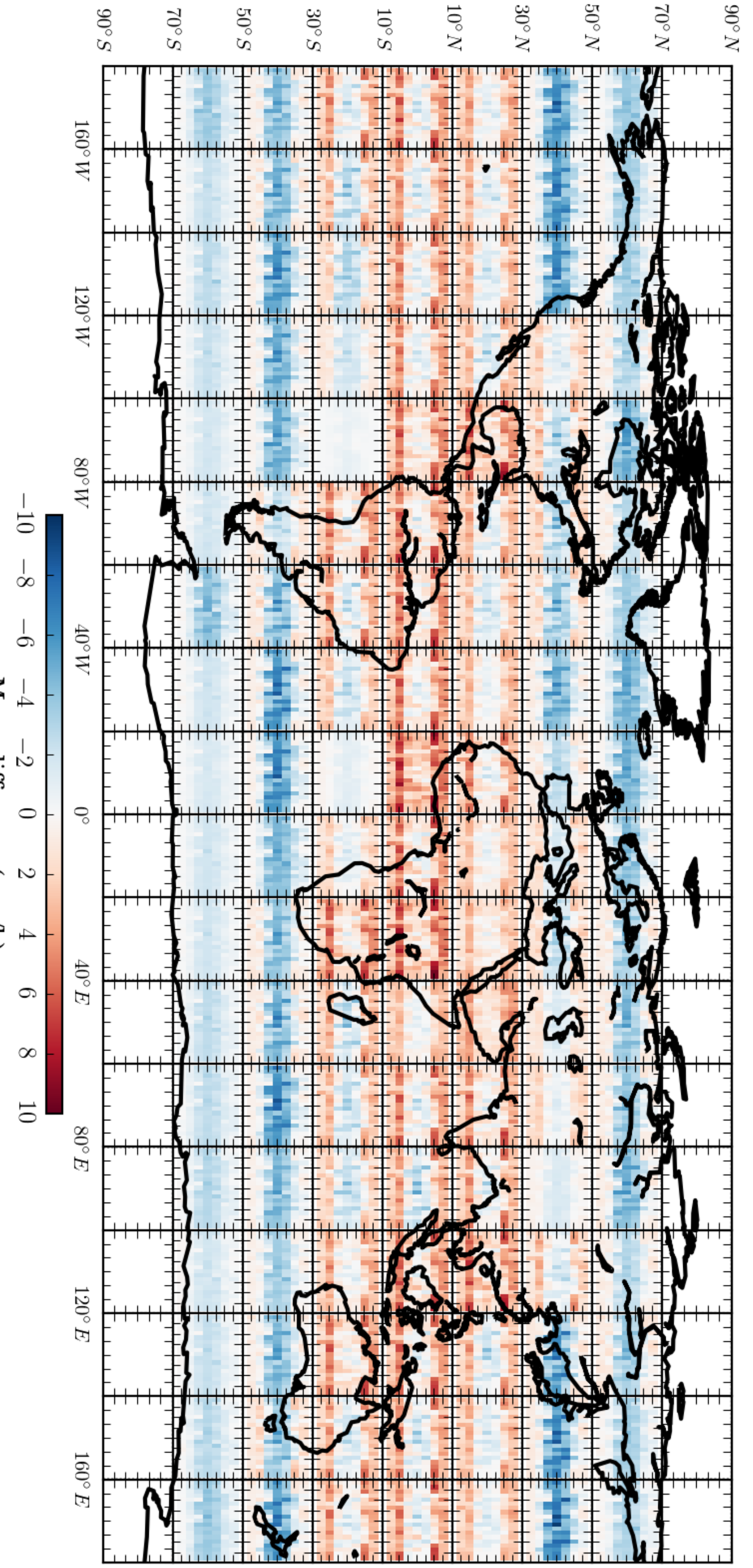

Figure A.12: Mean differences among regional LUTs for R_{max}; 50th percentile

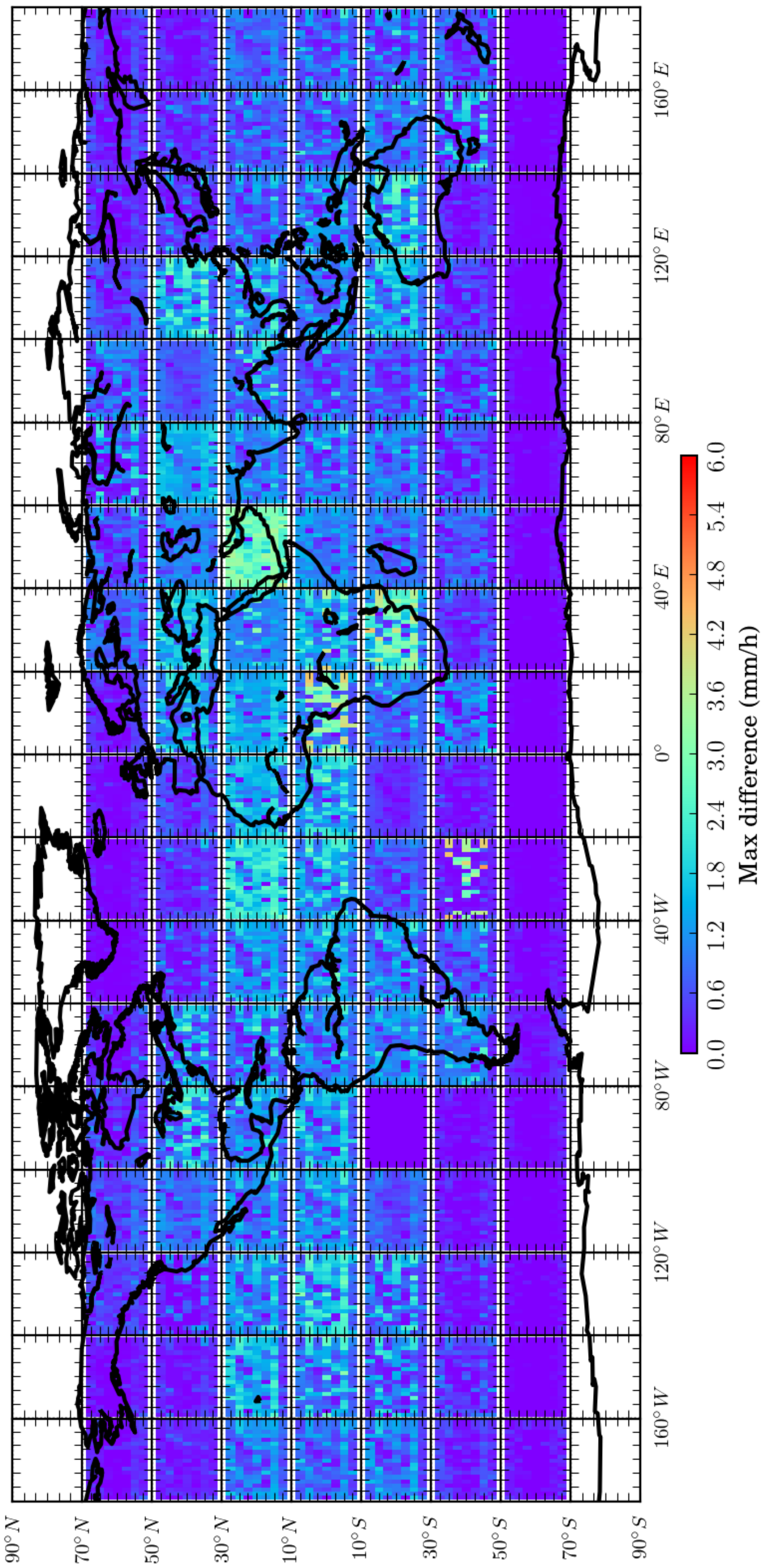

Figure A.13: Maximum differences among regional LUTs for $\langle R \rangle$; 5th percentile

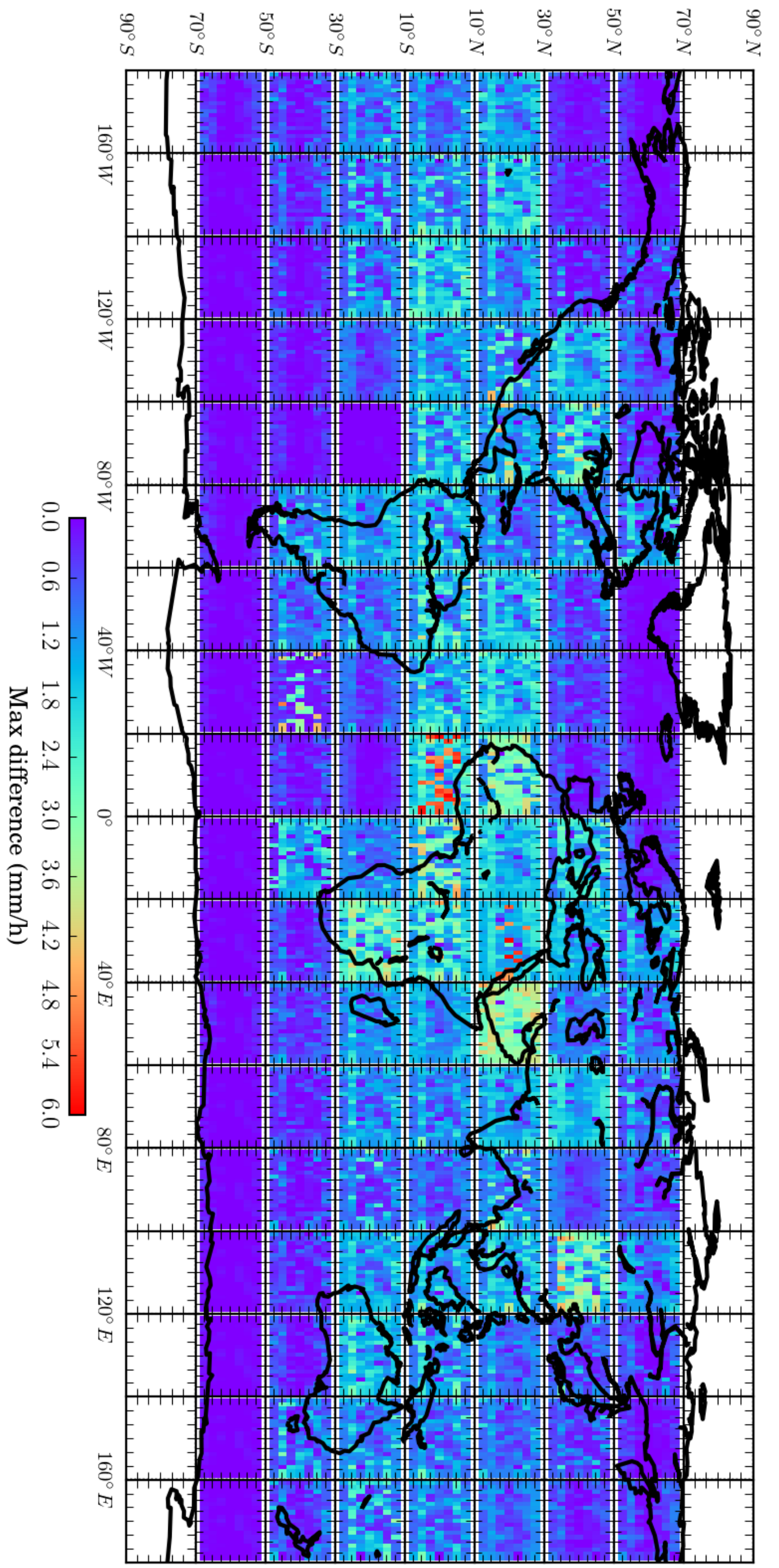

Figure A.14: Maximum differences among regional LUTs for $\langle R \rangle$; 25th percentile

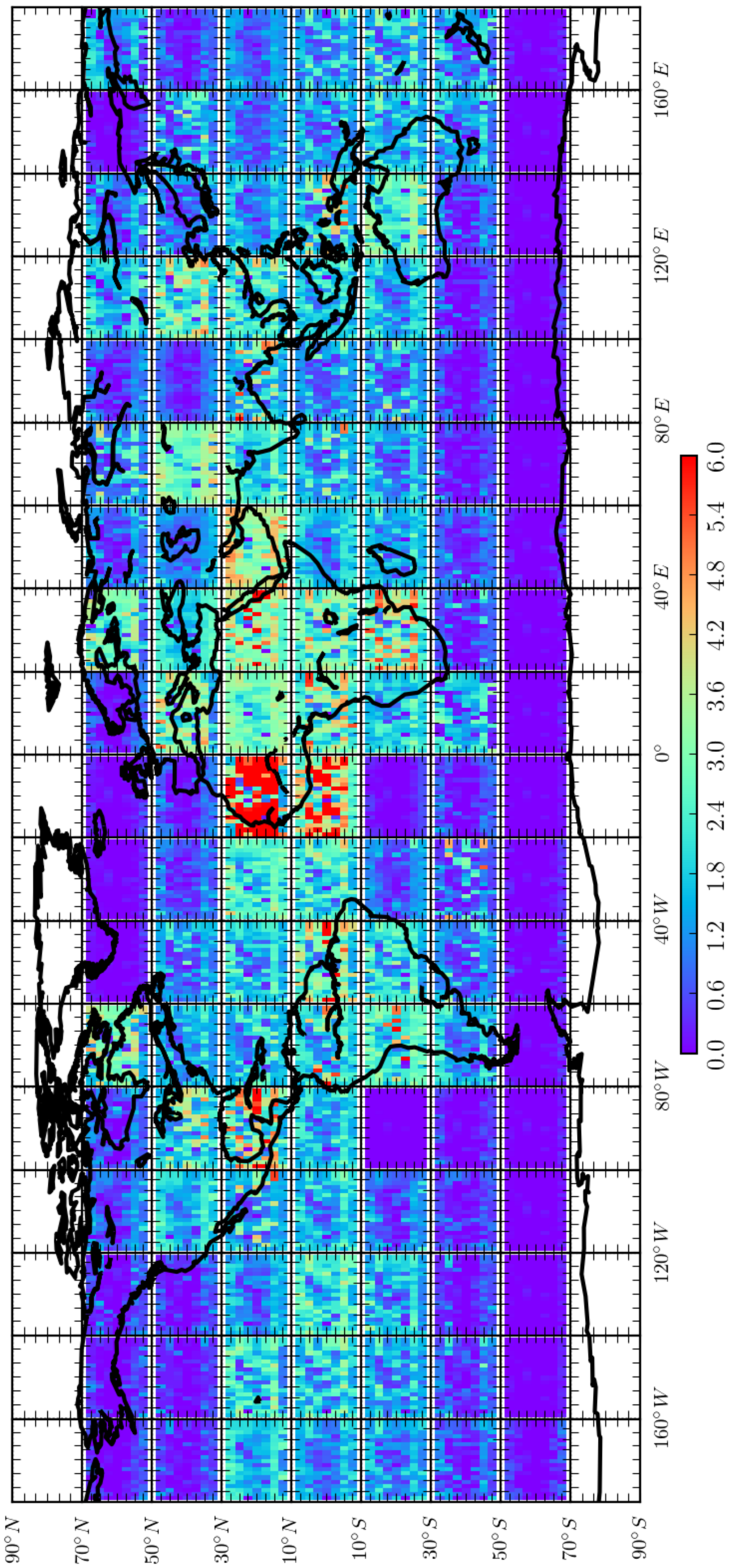

Figure A.15: Maximum differences among regional LUTs for $\langle R \rangle$; 50th percentile

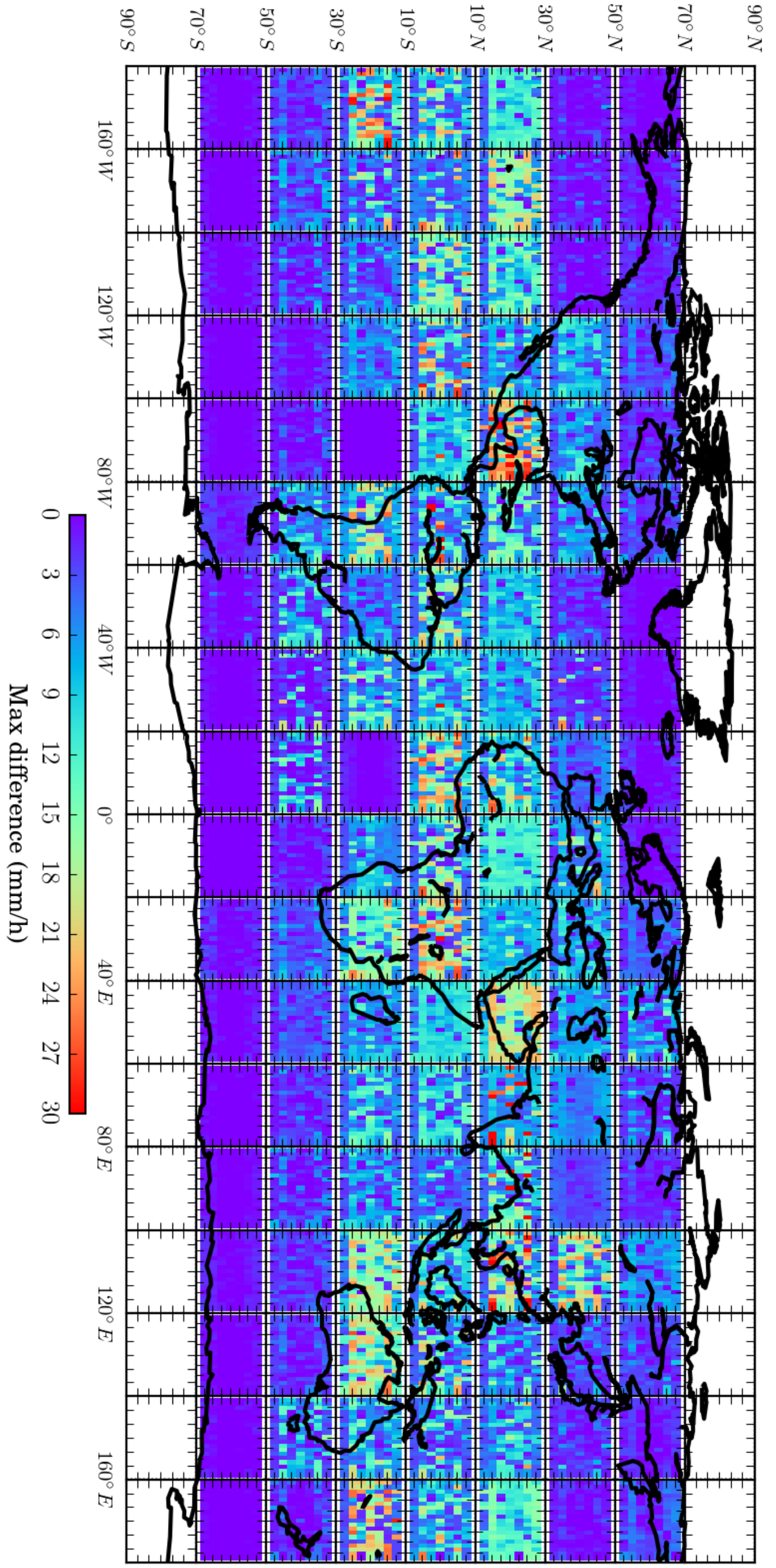

Figure A.16: Maximum differences among regional LUTs for R_{max}; 5th percentile

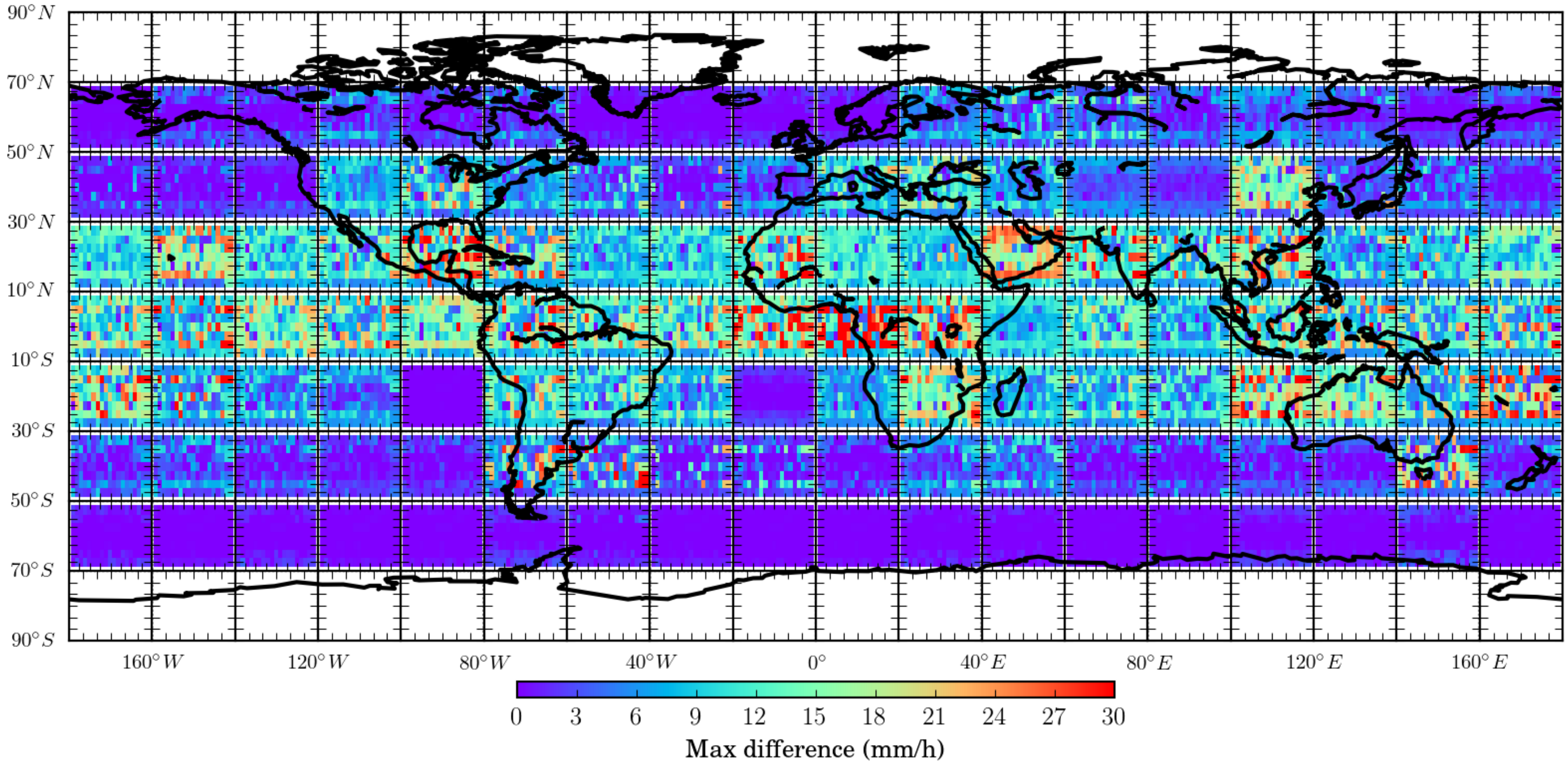

Figure A.17: Maximum differences among regional LUTs for $R_{\max}$; 25th percentile

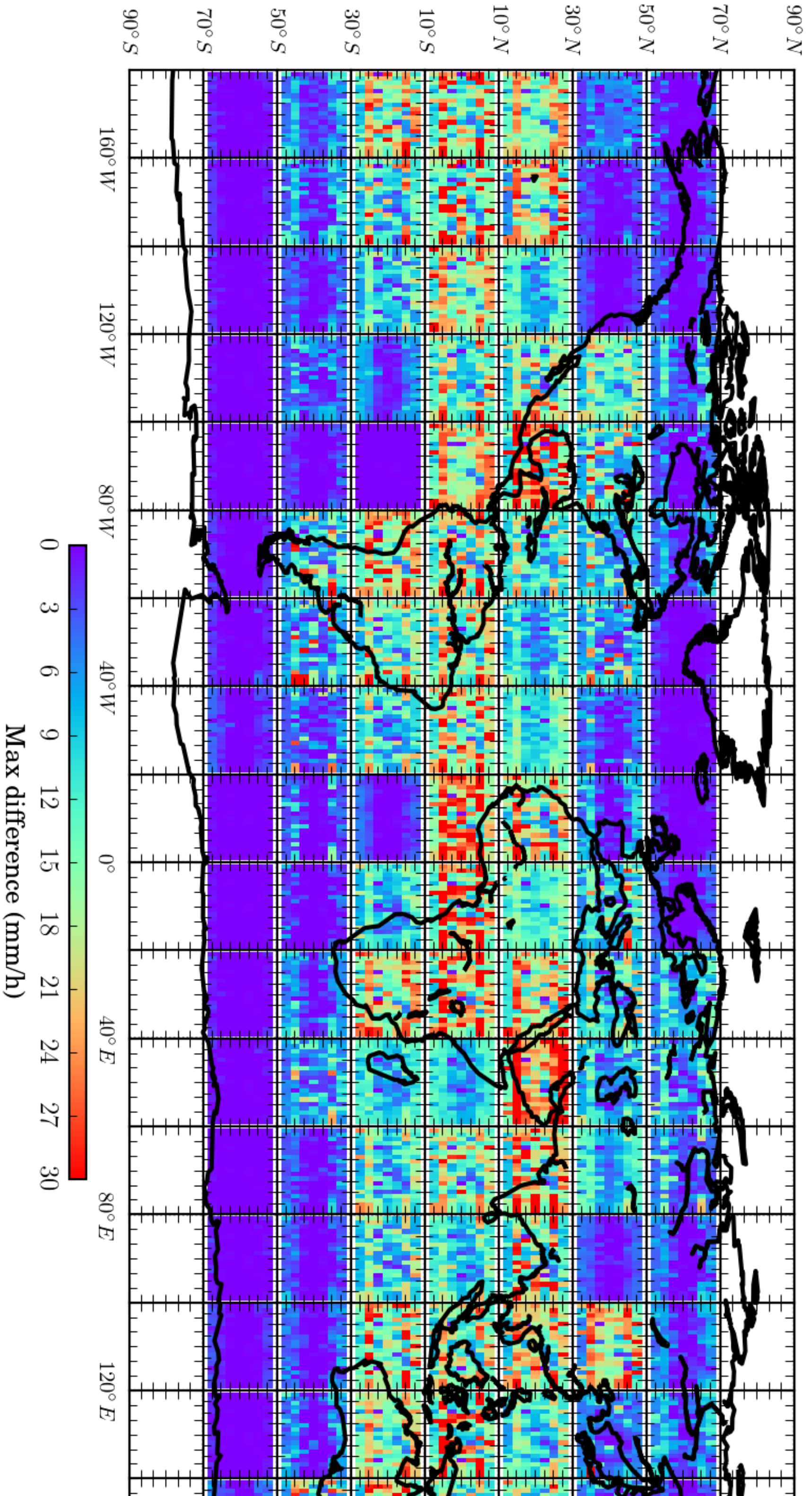

Figure A.18: Maximum differences among regional LUTs for $R_{\max}$; 50th percentile

BIBLIOGRAPHY

Ahmad, B. and Tyler, G.L. Systematic errors in atmospheric profiles obtained from Abelian inversion of radio occultation data: Effects of large-scale horizontal gradients. *J. Geophys. Res.*, 104(D4):3971–3992, 1999. doi: 10.1029/1998JD200102.

Aminou, D.M. MSG's SEVIRI Instrument. *ESA Bulletin*, 111(August):15–17, 2002.

An, H., Yan, W., Huang, Y., Ai, W., Wang, Y., Zhao, X. and Huang, X. GNSS Measurement of Rain Rate by Polarimetric Phase Shift: Theoretical Analysis. *Atmosphere*, 7(8):101, 2016. doi: 10.3390/atmos7080101.

Anthes, R.A. Exploring Earth's atmosphere with radio occultation: Contributions to weather, climate and space weather. *Atmospheric Measurement Techniques*, 4(6): 1077–1103, 2011. doi: 10.5194/amt-4-1077-2011.

Anthes, R.A. et al. The COSMIC/Formosat-3 mission: Early results. *Bulletin of the American Meteorological Society*, 89(3):313–333, 2008. doi: 10.1175/BAMS-89-3-313.

Ao, C.O., Meehan, T.K., Hajj, G.A. and Mannucci, A.J. Lower troposphere refractivity bias in GPS occultation retrievals. *Journal of Geophysical Research*, 108(D18): 1–16, 2003. doi: 10.1029/2002JD003216.

Ao, C.O., Hajj, G.A., Meehan, T.K., Dong, D., Iijima, B.A., Mannucci, A.J. and Kursinski, E.R. Rising and setting GPS occultations by use of open-loop tracking. *Journal of Geophysical Research Atmospheres*, 114(4):1–15, 2009. doi: 10.1029/2008JD010483.

Ao, C.O., Waliser, D.E., Chan, S.K., Li, J.L., Tian, B., Xie, F. and Mannucci, A.J. Planetary boundary layer heights from GPS radio occultation refractivity and humidity profiles. *Journal of Geophysical Research Atmospheres*, 117(16):1–18, 2012. doi: 10.1029/2012JD017598.

Aparicio, J.M. and Deblonde, G. Impact of the assimilation of CHAMP refractivity profiles on Environment Canada global forecasts. *Monthly Weather Review*, 136: 257–275, 2008. doi: 10.1175/2007MWR1951.1.

Aparicio, J.M. and Laroche, S. Estimation of the added value of the absolute calibration of GPS Radio Occultation data for Numerical Weather Prediction. *Monthly Weather Review*, 143:1259–1274, 2014. doi: 10.1175/MWR-D-14-00153.1.

Aparicio, J.M. and Rius, A. A raytracing inversion procedure for the extraction of the atmospheric refractivity from GNSS travel-time data. *Physics and Chemistry of the Earth, Parts A/B/C*, 29(2-3):213–224, jan 2004. doi: 10.1016/j.pce.2004.01.008.

Aparicio, J.M., Deblonde, G., Garand, L. and Laroche, S. Signature of the atmospheric compressibility factor in COSMIC, CHAMP, and GRACE radio occultation data. *Journal of Geophysical Research: Atmospheres*, 114(D16114):1–10, 2009. doi: 10.1029/2008JD011156.

Ashley, S.T. and Ashley, W.S. Flood fatalities in the United States. *Journal of Applied Meteorology and Climatology*, 47(3):805–818, 2008. doi: 10.1175/2007JAMC1611.1.

Aumann, H.H. et al. AIRS / AMSU / HSB on the Aqua Mission : Design, Science Objectives, Data Products, and Processing Systems. *IEEE Transactions on Geoscience and Remote Sensing*, 41(2):253–264, 2003. doi: 10.1109/TGRS.2002.808356.

Bailey, M. and Hallett, J. A Comprehensive Habit Diagram for Atmospheric Ice Crystals: Confirmation from the Laboratory, AIRS II, and Other Field Studies. *Journal of Atmospheric Sciences*, 66(9):2888–2899, 2009. doi: 10.1175/2009JAS2883.1.

Beard, K.V. and Chuang, C. A new model for the equilibrium shape of raindrops. *Journal of the Atmospheric sciences*, 44(11):1509–1524, 1987. doi: dx.doi.org/10.1175/1520-0469(1987)044<1509:ANMFTE>2.0.CO;2.

Beard, K.V., Bringi, V.N. and Thurai, M. A new understanding of raindrop shape. *Atmospheric Research*, 97(4):396–415, 2010. doi: 10.1016/j.atmosres.2010.02.001.

Bech, J., Vilaclara, E., Pineda, N., Rigo, T., Lopez, J., O'Hora, F., Lorente, J., Sempere, D. and Fabregas, F.X. The weather radar network of the Catalan Meteorological Service: description and applications. In *Proceedings of ERAD*, volume 2, pages 416–420, 2004.

Bevis, M., Businger, S., Herring, T.A., Rocken, C., Anthes, R.A. and Ware, R.H. GPS Meteorology: Remote Sensing of Atmospheric Water Vapor Using the Global Positioning System. *Journal of Geophysical Research*, 97(D14):15787, 1992. doi: 10.1029/92JD01517.

Beyerle, G., Hocke, K., Wickert, J., Schmidt, T., Marquardt, C. and Reigber, C. GPS radio occultations with CHAMP: A radio holographic analysis of GPS signal propagation in the troposphere and surface reflections. *Journal of Geophysical Research Atmospheres*, 107(24):1–14, 2002. doi: 10.1029/2001JD001402.

Bilitza, D., McKinnell, L.A., Reinisch, B. and Fuller-Rowell, T. The international reference ionosphere today and in the future. *Journal of Geodesy*, 85(12):909–920, 2011. doi: 10.1007/s00190-010-0427-x.

Biondi, R., Randel, W.J., Ho, S.P., Neubert, T. and Syndergaard, S. Thermal structure of intense convective clouds derived from GPS radio occultations. *Atmospheric Chemistry and Physics*, 12(12):5309–5318, 2012. doi: 10.5194/acp-12-5309-2012.

Biondi, R., Ho, S.P., Randel, W.J., Syndergaard, S. and Neubert, T. Tropical cyclone cloud-top height and vertical temperature structure detection using GPS radio occultation measurements. *Journal of Geophysical Research: Atmospheres*, 118(11): 5247–5259, 2013. doi: 10.1002/jgrd.50448.

Black, R.A. and Hallett, J. Rain Rate and Water Content in Hurricanes Compared with Summer Rain in Miami, Florida. *Journal of Applied Meteorology and Climatology*, 51(12):2218–2235, dec 2012. doi: 10.1175/JAMC-D-11-0144.1.

Blewitt, G. Carrier phase ambiguity resolution for the Global Positioning System applied to geodetic baselines up to 2000 km. *Journal of Geophysical Research*, 94 (B8):10187–10203, 1989. doi: 10.1029/JB094iB08p10187.

Boerner, W.M. *Basic concepts in radar polarimetry*. ESA PolSARpro Documentation, 2007. doi: earth.esa.int/documents/653194/656796.

Bohren, C.F. and Albrecht, B.A. *Atmospheric Thermodynamics*. Oxford University Press, New York, NY, USA, 1998. ISBN 978-0-19-509904-1.

Bohren, C.F. and Huffman, D.R. *Absorption and scattering of light by small particles*. John WIley & Sons, Inc., 1983. ISBN 0-471-29340-7. doi: 10.1002/9783527618156.

Bréon, F.M. and Dubrulle, B. Horizontally Oriented Plates in Clouds. *Journal of the Atmospheric Sciences*, 61:2888–2898, 2004. doi: 10.1175/JAS-3309.1.

Bringi, V.N. and Chandrasekar, V. *Polarimetric doppler weather radar; principles and applications*. Cambridge University Press, 2001. ISBN 0511035454.

Buontempo, C., Jupp, A.M. and Rennie, M.P. Operational NWP assimilation of GPS radio occultation data. *Atmospheric Science Letters*, 9:129–133, 2008. doi: 10.1002/asl.173.

Cardellach, E. *Sea surface determination using GNSS reflected signals*. PhD thesis, 2002.

Cardellach, E., Ao, C.O., de la Torre-Juárez, M. and Hajj, G.A. Carrier phase delay altimetry with GPS-reflection/occultation interferometry from low Earth orbiters. *Geophysical Research Letters*, 31(10):L10402, 2004. doi: 10.1029/2004GL019775.

Cardellach, E., Fabra, F., Nogués-Correig, O., Oliveras, S., Ribó, S. and Rius, A. GNSS-R ground-based and airborne campaigns for ocean, land, ice, and snow techniques: Application to the GOLD-RTR data sets. *Radio Science*, 46(6):n/a–n/a, dec 2011. doi: 10.1029/2011RS004683.

Cardellach, E. et al. Sensitivity of PAZ LEO Polarimetric GNSS Radio-Occultation Experiment to Precipitation Events. *IEEE Transactions on Geoscience and Remote Sensing*, 53(1):190–206, 2014. doi: 10.1109/TGRS.2014.2320309.

Cardellach, E., Padullés, R., Tomás, S., Turk, F.J., Ao, C.O. and de la Torre-Juárez, M. Probability of intense precipitation in GNSS radio-occultation thermodynamic profiles derived from their polarimetric signatures. *submitted to Quarterly Journal of the Royal Meteorological Society*, 2017.

Cardinali, C. and Healy, S.B. Impact of GPS radio occultation measurements in the ECMWF system using adjoint-based diagnostics. *Quarterly Journal of the Royal Meteorological Society*, 140(684):2315–2320, 2014. doi: 10.1002/qj.2300.

Carey, L.D., Niu, J., Yang, P., Kankiewicz, J.A., Larson, V.E. and Vonder Haar, T.H. The vertical profile of liquid and ice water content in midlatitude mixed-phase altocumulus clouds. *Journal of Applied Meteorology and Climatology*, 47:2487–2495, 2008. doi: 10.1175/2008JAMC1885.1.

Carey, L.D., Petersen, W.A. and Deierling, W. Radar Differential Phase Signatures of Ice Orientation for the Prediction of Lightning Initiation and Cessation. In *34th Conference on Radar Meteorology*, Williamsburg, VA, 2009. Amer. Meteor. Soc.

Casas, M.C., Codina, B., Redaño, A. and Lorente, J. A methodology to classify extreme rainfall events in the western mediterranean area. *Theoretical and Applied Climatology*, 77(3-4):139–150, 2004. doi: 10.1007/s00704-003-0003-x.

Caylor, I.J. and Chandrasekar, V. Time-varying ice crystal orientation in thunderstorms observed with multiparameter radar. *IEEE Transactions on Geoscience and Remote Sensing*, 34(4):847–858, 1996. doi: 10.1109/36.508402.

Chandrasekar, V., Bringi, V.N., Balakrishnan, N. and Zrnić, D.S. Error Structure of Multiparameter Radar and Surface Measurements of Rainfall. Part III: Specific Differential Phase. *Journal of Atmospheric and Oceanic Technology*, 7:621–629, 1990. doi: 10.1175/1520-0426(1990)007<0621:ESOMRA>2.0.CO;2.

Chen, T., Rossow, W.B. and Zhang, Y. Radiative effects of cloud-type variations. *Journal of Climate*, 13(1):264–286, 2000. doi: 10.1175/1520-0442(2000)013<0264:REOCTV>2.0.CO;2.

Clark, P., Roberts, N., Lean, H., Ballard, S.P. and Charlton-Perez, C. Convection-permitting models: a step-change in rainfall forecasting. *Meteorological Applications*, 23:165–181, 2016. doi: 10.1002/met.1538.

Cotton, R.J., Field, P.R., Ulanowski, Z., Kaye, P.H., Hirst, E., Greenaway, R.S., Crawford, I., Crosier, J. and Dorsey, J. The effective density of small ice particles obtained from in situ aircraft observations of mid-latitude cirrus. *Quarterly Journal of the Royal Meteorological Society*, 139(676):1923–1934, oct 2013. doi: 10.1002/qj.2058.

Cucurull, L. *The use of Global Navigation Satellite Systems (GNSS) signals in Numerical Weather Prediction (NWP)*. PhD thesis, Universitat de Barcelona, 2001.

Cucurull, L. and Derber, J.C. Operational Implementation of COSMIC Observations into NCEP's Global Data Assimilation System. *Weather and Forecasting*, 23(4):702–711, aug 2008. doi: 10.1175/2008WAF2007070.1.

Cucurull, L., Derber, J.C., Treadon, R. and Purser, R.J. Preliminary Impact Studies Using Global Positioning System Radio Occultation Profiles at NCEP. *Monthly Weather Review*, 136(6):1865–1877, 2008. doi: 10.1175/2007MWR2260.1.

Cucurull, L., Anthes, R.A. and Tsao, L.L. Radio occultation observations as anchor observations in numerical weather prediction models and associated reduction of bias corrections in microwave and infrared satellite observations. *Journal of Atmospheric and Oceanic Technology*, 31(1):20–32, 2014. doi: 10.1175/JTECH-D-13-00059.1.

Culverwell, I.D., Lewis, H.W., Offiler, D., Marquardt, C. and Burrows, C.P. The radio occultation processing package, ROPP. *Atmospheric Measurement Techniques*, 8:1887–1899, 2015. doi: 10.5194/amt-8-1887-2015.

Davies, T., Cullen, M.J.P., Malcolm, A.J., Mawson, M.H., Staniforth, A., White, A.A. and Wood, N. A new dynamical core for the Met Office's global and regional modelling of the atmosphere. *Quarterly Journal of the Royal Meteorological Society*, 131(608):1759–1782, 2005. doi: 10.1256/qj.04.101.

Delanoë, J. and Hogan, R.J. Combined CloudSat-CALIPSO-MODIS retrievals of the properties of ice clouds. *Journal of Geophysical Research*, 115:D00H29, jul 2010. doi: 10.1029/2009JD012346.

Delanoë, J., Protat, A., Testud, J., Bouniol, D., Heymsfield, A.J., Bansemer, A., Brown, P.R. and Forbes, R.M. Statistical properties of the normalized ice particle size distribution. *Journal of Geophysical Research*, 110(D10):D10201, 2005. doi: 10.1029/2004JD005405.

Delanoë, J., Heymsfield, A.J., Protat, A., Bansemer, A. and Hogan, R.J. Normalized particle size distribution for remote sensing application. *Journal of Geophysical Research: Atmospheres*, 119:4204–4227, 2014. doi: 10.1002/2013JD020700.

Deschamps, G.A. Techniques for Handling Elliptically Polarized Waves with Special Reference to Antennas: Part II-Geometrical Representation of the Polarization of a Plane Electromagnetic Wave. *Proceedings of the IRE*, 39(5):540–544, 1951. doi: 10.1109/JRPROC.1951.233136.

Dolan, B., Rutledge, S.A., Lim, S., Chandrasekar, V. and Thurai, M. A robust C-band hydrometeor identification algorithm and application to a long-term polarimetric radar dataset. *Journal of Applied Meteorology and Climatology*, 52(9):2162–2186, 2013. doi: 10.1175/JAMC-D-12-0275.1.

Draine, B.T. The discrete-dipole approximation and its application to interstellar graphite grains. *The Astrophysical Journal*, 1988. doi: 10.1086/166795.

Draine, B.T. and Flatau, P.J. Discrete-dipole approximation for scattering calculations. *Journal of the Optical Society of America A*, 11(4):1491, apr 1994. doi: 10.1364/JOSAA.11.001491.

Draine, B.T. and Flatau, P.J. User Guide for the Discrete Dipole Approximation Code DDSCAT 7.3. *arXiv preprint*, 3(1994), 2013.

Ducrocq, V. et al. HyMeX-SOP1, the field campaign dedicated to heavy precipitation and flash flooding in the northwestern Mediterranean. *Bulletin of the American Meteorological Society*, 95(July):1083–1100, 2014. doi: 10.1175/BAMS-D-12-00244.1.

ECMWF. ECMWF TOGA 2.5 degree Global Surface and Upper Air Analyses. *Research Data Archive at the National Center for Atmospheric Research, Computational and Information Systems Laboratory*, 1990.

Emanuel, K.A. *Atmospheric convection*. Oxford University Press, 1994. ISBN 9780195066302.

Eyre, J. Assimilation of Radio Occultation measurements into a numerical weather prediction system. *ECMWF Technical Memoranda*, 199, 1994.

Fischbach, F.F. Atmospheric pressure and temperature below 24 km using satellite measurements of atmospheric light refraction from given stars. In *American meteorological society, annual meeting 45th*, New York, NY, USA, 1965.

Fjeldbo, G. and Eshleman, V.R. The Bistatic Radar-Occultation Method for the Study of Planetary Atmospheres. *Journal of Geophysical Research*, 70(13):3217–3225, 1965. doi: 10.1029/JZ070i013p03217.

Fjeldbo, G. and Eshleman, V.R. Atmosphere of Venus as studied with the Mariner 5 dual radio-frequency occultation experiment. *Radio Science*, 4(10):879–897, 1969. doi: 10.1029/RS004i010p00879.

Fjeldbo, G., Eshleman, V.R., Garriot, O.K. and Smith, F.L. The Two-Frequency Bistatic Radar-Occultation Method for the Study of Planetary Ionospheres. *Journal of Geophysical Research*, 70(15):3701–3710, 1965. doi: 10.1029/JZ070i015p03701.

Fjeldbo, G., Kliore, A. and Eshleman, V.R. The Neutral Atmosphere of Venus as Studied with the Mariner V Radio Occultation Experiments. *The Astronomical Journal*, 76(2), 1971. doi: 10.1086/111096.

Fletcher, J.O. Early Developments of Weather Radar during World War II. In Atlas, D., editor, *Radar in Meteorology*. American Meteorological Society, Boston, 1990. ISBN 978-0-933876-86-6. doi: 10.1007/978-1-935704-15-7.

Foelsche, U., Syndergaard, S., Fritzer, J. and Kirchengast, G. Errors in GNSS radio occultation data: Relevance of the measurement geometry and obliquity of profiles. *Atmospheric Measurement Techniques*, 4(2):189–199, 2011. doi: 10.5194/amt-4-189-2011.

Fridlind, A.M., Ackerman, A.S., Grandin, A., Dezitter, F., Weber, M., Strapp, J.W., Korolev, A.V. and Williams, C.R. High ice water content at low radar reflectivity near deep convection - Part 1: Consistency of in situ and remote-sensing observations with stratiform rain column simulations. *Atmospheric Chemistry and Physics*, 15(20):11713–11728, 2015. doi: 10.5194/acp-15-11713-2015.

Garrison, J.L., Katzberg, S.J. and Hill, M.I. Effect of sea roughness on bistatically scattered range coded signals from the Global Positioning System. *Geophysical Research Letters*, 25(13):2257, 1998. doi: 10.1029/98GL51615.

Gorbunov, M.E. Canonical transform method for processing radio occultation data in the lower troposphere. *Radio Science*, 37(5):1–9, 2002. doi: 10.1029/2000RS002592.

Gorbunov, M.E. and Sokolovskiy, S.V. Remote sensing of refractivity from space for global observations of atmospheric parameters. Technical report, Max-Planck Institut fur Meteorologie, Hamburg, 1993.

Haase, J.S., Murphy, B.J., Muradyan, P., Nievinski, F.G., Larson, K.M., Garrison, J.L. and Wang, K.N. First results from an airborne GPS radio occultation system for atmospheric profiling. *Geophysical Research Letters*, 40:1759–1765, 2014. doi: 10.1002/2013GL058681.

Hagen, M. and Yuter, S.E. Relations between radar reflectivity, liquid-water content, and rainfall rate during the MAP SOP. *Quarterly Journal of the Royal Meteorological Society*, 129(588):477–493, jan 2003. doi: 10.1256/qj.02.23.

Hajj, G.A., Kursinski, E.R., Romans, L.J., Bertiger, W.I. and Leroy, S.S. A Technical Description of Atmospheric Sounding By Gps occultation. *Journal of Atmospheric and solar-terrestrial physics*, 64:451–469, 2002. doi: 10.1016/S1364-6826(01)00114-6.

Hajj, G.A., Ao, C.O., Iijima, B.A., Kuang, D., Kursinski, E.R., Mannucci, A.J., Meehan, T.K., Romans, L.J., de la Torre-Juárez, M. and Yunck, T.P. CHAMP and SAC-C atmospheric occultation results and intercomparisons. *Journal of Geophysical Research*, 109(D6):1–24, 2004. doi: 10.1029/2003JD003909.

Hansen, P.C. The truncated svd as a method for regularization. *BIT Numerical Mathematics*, 27(4):534–553, 1987. doi: 10.1007/BF01937276.

Hartmann, D.L., Ramanathan, V., Berroir, A. and Hunt, G.E. Earth Radiation Budget data and climate research. *Reviews of Geophysics*, 24(2):439–468, 1986. doi: 10.1029/RG024i002p00439.

Healy, S.B. Forecast impact experiment with a constellation of GPS radio occultation receivers. *Atmospheric Science Letters*, 9:111–118, 2008. doi: 10.1002/asl.169.

Healy, S.B. Refractivity coefficients used in the assimilation of GPS radio occultation measurements. *Journal of Geophysical Research Atmospheres*, 116(1):1–10, 2011. doi: 10.1029/2010JD014013.

Healy, S.B. and Eyre, J.R. Retrieving temperature, water vapour and surface pressure information from refractive index profiles derived by radio occultation: A simulation study. *Quarterly Journal of the Royal Meteorological Society*, 126:1661–1683, 2000. doi: 10.1002/qj.49712656606.

Healy, S.B., Haase, J.S. and Lesne, O. Abel transform inversion of radio occultation measurements made with a receiver inside the Earth's atmosphere. *Annales Geophysicae*, 20:1253–1256, 2002.

Healy, S.B., Jupp, A.M. and Marquardt, C. Forecast impact experiment with GPS radio occultation measurements. *Geophysical Research Letters*, 32(3):L03804, 2005. doi: 10.1029/2004GL020806.

Hegarty, C.J. and Chatre, E. Evolution of the Global Navigation SatelliteSystem (GNSS). *Proceedings of the IEEE*, 96(12):1902–1917, 2008. doi: 10.1109/JPROC.2008.2006090.

Herman, G.T. *Image Reconstruction from Projections: Fundamentals of Computerized Tomography*. Springer, 2n ed, edition, 2009. ISBN 978-1-85233-617-2.

Heymsfield, A.J., Bansemer, A., Field, P.R., Durden, S.L., Stith, J.L., Dye, J.E., Hall, W. and Grainger, C.A. Observations and Parameterizations of Particle Size Distributions in Deep Tropical Cirrus and Stratiform Precipitating Clouds: Results from In Situ Observations in TRMM Field Campaigns. *Journal of the Atmospheric Sciences*, 59, 2002a.

Heymsfield, A.J., Lewis, S., Bansemer, A., Iaquinta, J., Miloshevich, L.M., Kajikawa, M., Twohy, C.H. and Poellot, M.R. A general approach for deriving the properties of cirrus and stratiform ice cloud particles. *Journal of the Atmospheric Sciences*, 2002b.

Hirakata, M., Okamoto, H., Hagihara, Y., Hayasaka, T. and Oki, R. Comparison of Global and Seasonal Characteristics of Cloud Phase and Horizontal Ice Plates Derived from CALIPSO with MODIS and ECMWF. *Journal of Atmospheric and Oceanic Technology*, aug 2014. doi: 10.1175/JTECH-D-13-00245.1.

Holloway, C.E. and Neelin, J.D. Moisture Vertical Structure, Column Water Vapor, and Tropical Deep Convection. *Journal of the Atmospheric Sciences*, 66(6):1665–1683, 2009. doi: 10.1175/2008JAS2806.1.

Hong, G., Yang, P., Baum, B.A. and Heymsfield, A.J. Relationship between ice water content and equivalent radar reflectivity for clouds consisting of nonspherical ice particles. *Journal of Geophysical Research*, 113(D20):D20205, oct 2008. doi: 10.1029/2008JD009890.

Hong, Y. and Liu, G. The characteristics of ice cloud properties derived from CloudSat and CALIPSO measurements. *Journal of Climate*, 28(9):3880–3901, 2015. doi: 10.1175/JCLI-D-14-00666.1.

Hou, A.Y., Kakar, R.K., Neeck, S., Azarbarzin, A.A., Kummerow, C.D., Kojima, M., Oki, R., Nakamura, K. and Iguchi, T. The global precipitation measurement mission. *Bulletin of the American Meteorological Society*, 95(5):701–722, 2014. doi: 10.1175/BAMS-D-13-00164.1.

Howard, H.T. et al. Mercury: results on mass, radius, ionosphere, and atmosphere from mariner 10 dual-frequency radio signals. *Science*, 185(4146):179–180, 1974. doi: 10.1126/science.185.4146.179.

Hubbert, J.C., Ellis, S.M., Chang, W.Y., Rutledge, S. and Dixon, M. Modeling and interpretation of S-band ice crystal depolarization signatures from data obtained by simultaneously transmitting horizontally and vertically polarized fields. *Journal of Applied Meteorology and Climatology*, 53(6):1659–1677, 2014. doi: 10.1175/JAMC-D-13-0158.1.

Humliĉek, J. Polarized light and ellipsometry. In Tompkins, H.G. and Irene, E.A., editors, *Handbook of ellipsometry*, chapter 1. William Andrew, Inc., 2004. ISBN 0-8155-1499-9.

Iwai, K. Three-Dimensional Structures of Natural Snow Crystals Shown by Stereo-Photomicrographs. *Atmospheric Research*, 24:137–147, 1989. doi: 10.1016/0169-8095(89)90042-2.

Jackson, J.D. *Classical Electrodynamics*. John WIley & Sons, Inc., New York, NY, USA, 1998.

Jensen, A.S., Lohmann, M.S., Benzon, H.H. and Nielsen, A.S. Full spectrum inversion of radio occultation signals. *Radio Science*, 38(3):1–15, 2003. doi: 10.1029/2002RS002763.

Jensen, A.S., Lohmann, M.S., Nielsen, A.S. and Benzon, H.H. Geometrical optics phase matching of radio occultation signals. *Radio Science*, 39(3):1–8, 2004. doi: 10.1029/2003RS002899.

Jin, S., Cardellach, E. and Xie, F. *GNSS Remote Sensing: Theory, Methods and Applications*, volume 19. Springer, 2014. ISBN 978-94-007-7481-0. doi: 10.1007/978-94-007-7482-7.

Junyent, F. and Chandrasekar, V. An examination of precipitation using CSU - CHILL dual-wavelength, dual-polarization radar observations. *Journal of Atmospheric and Oceanic Technology*, 33(2):313–329, 2016. doi: 10.1175/JTECH-D-14-00229.1.

Kaplan, E.D. and Hegarty, C.J. *Understanding GPS: principles and applications*. Artech house, inc., Norwood, MA, 2nd ed. edition, 2006. ISBN 1-58053-894-0.

Kendon, E.J., Roberts, N.M., Senior, C.A. and Roberts, M.J. Realism of rainfall in a very high-resolution regional climate model. *Journal of Climate*, 25(17):5791–5806, 2012. doi: 10.1175/JCLI-D-11-00562.1.

Kennedy, P.C. and Rutledge, S.A. S-Band Dual-Polarization Radar Observations of Winter Storms. *Journal of Applied Meteorology and Climatology*, 50(4):844–858, apr 2011. doi: 10.1175/2010JAMC2558.1.

Kliore, A. Some remarks on meteorological measurements with occultation satellites. In *Proceedings of Open Meetings of Working Groups of the Eleventh Plenary Meeting of COSPAR*, Tokyo, 1969.

Kliore, A., Cain, D.L., Levy, G.S., Eshleman, V.R., Fjeldbo, G. and Drake, F.D. Occultation Experiment: Results of the First Direct Measurement of Mars's Atmosphere and Ionosphere. *Science*, 149(3689):1243–8, 1965. doi: 10.1126/science.149.3689.1243.

Kummerow, C.D., Barnes, W., Kozu, T., Shiue, J. and Simpson, J. The tropical rainfall measuring mission(TRMM) sensor package. *Journal of Atmospheric and Oceanic Technology*, 15(3):809–817, 1998. doi: 10.1175/1520-0426(1998)015<0809:TTRMMT>2.0.CO;2.

Kunkel, K.E. et al. Monitoring and understanding trends in extreme storms: State of knowledge. *Bulletin of the American Meteorological Society*, 94(4):499–514, 2013. doi: 10.1175/BAMS-D-11-00262.1.

Kuo, Y.H., Schreiner, W.S., Wang, J.K., Rossiter, D.L. and Zhang, Y. Comparison of GPS radio occultation soundings with radiosondes. *Geophysical Research Letters*, 32(5):1–4, 2005. doi: 10.1029/2004GL021443.

Kursinski, E.R. and Hajj, G.a. A comparison of water vapor derived from GPS occultations and global weather analyses. *Journal of Geophysical Research*, 106(D1):1113, 2001. doi: 10.1029/2000JD900421.

Kursinski, E.R. et al. Initial results of radio occultation observations of Earth's atmosphere using the Global Positioning System. *Science*, 271(5252):1107–1110, 1996. doi: 10.1126/science.271.5252.1107.

Kursinski, E.R., Hajj, G.A., Schofield, J.T., Linfield, R.P. and Hardy, K.R. Observing Earth's atmosphere with radio occultation measurements using the Global Positioning System. *Journal of Geophysical Research*, 102(97):23429–23465, 1997. doi: 10.1029/97JD01569.

Kursinski, E.R., Hajj, G.A., Leroy, S.S. and Herman, B.M. The GPS radio occultation technique. *Terrestrial, Atmospheric and Oceanic Sciences*, 11(1):53–114, 2000. doi: 10.3319/TAO.2000.11.1.53(COSMIC).

Lackner, B.C., Steiner, A.K., Kirchengast, G. and Hegerl, G.C. Atmospheric climate change detection by radio occultation data using a fingerprinting method. *Journal of Climate*, 24(20):5275–5291, 2011. doi: 10.1175/2011JCLI3966.1.

Ladstädter, F., Steiner, A.K., Schwärz, M. and Kirchengast, G. Climate intercomparison of GPS radio occultation, RS90/92 radiosondes and GRUAN from 2002 to 2013. *Atmospheric Measurement Techniques*, 8(4):1819–1834, 2015. doi: 10.5194/amt-8-1819-2015.

Larsen, G.B., Syndergaard, S., Høeg, P. and Sørensen, M.B. Single frequency processing of Orsted GPS radio occultation measurements. *GPS Solutions*, 9(2):144–155, 2005. doi: 10.1007/s10291-005-0142-x.

Larson, K.M., Braun, J.J., Small, E.E., Zavorotny, V.U., Gutmann, E.D. and Bilich, A.L. GPS Multipath and Its Relation to Near-Surface Soil Moisture Content. *Journal of Selected Topics In Applied Earth Observations And Remote Sensing*, 3(1):91–99, 2010.

Larson, K.M., Löfgren, J.S. and Haas, R. Coastal sea level measurements using a single geodetic GPS receiver. *Advances in Space Research*, 51(8):1301–1310, 2013. doi: 10.1016/j.asr.2012.04.017.

L'Ecuyer, T. and Jiang, J.H. Touring the atmosphere aboard the A-Train. *Physics Today*, 63(7):36–41, 2010. doi: 10.1063/1.3463626.

Leick, A. *GPS satellite surveying*. John WIley & Sons, Inc., 2nd ed. edition, 1995. ISBN 0-471-30626-6.

Leinonen, J. *Impact of the microstructure of precipitation and hydrometeors on multi-frequency radar observations*. PhD thesis, Aalto University, 2013.

Leinonen, J. High-level interface to T-matrix scattering calculations: architecture, capabilities and limitations. *Opt. Express*, 22(2):1655–1660, 2014. doi: 10.1364/OE.22.001655.

Leinonen, J. and Moisseev, D. What do triple-frequency radar signatures reveal about aggregate snowflakes ? *Journal of Geophysical Research: Atmospheres*, 120: 229–239, 2015. doi: 10.1002/2014JD022072.

Leinonen, J. and Szyrmer, W. Radar signatures of snowflake riming : A modeling study. *Earth and Space Science*, 2(8):346–358, 2015. doi: 10.1002/2015EA000102.

Li, J.L., Waliser, D.E., Stephens, G.L. and Lee, S. Characterizing and Understanding Cloud Ice and Radiation Budget Biases in Global Climate Models and Reanalysis. *Meteorological monographs*, Chapter 13:1–20, 2016. doi: 10.1175/AMSMONOGRAPHS-D-15-0007.1.

Libbrecht, K.G. The physics of snow crystals. *Reports on Progress in Physics*, 68: 855–895, 2005. doi: 10.1088/0034-4885/68/4/R03.

Liebe, H.J., Hufford, G.A. and Manabe, T. A model for the complex permittivity of water at frequencies below 1 THz. *International Journal of Infrared and Millimeter Waves*, 12(7):659–675, 1991. doi: 10.1007/BF01008897.

Lilly, D.K. Numerical prediction of thunderstorms - has its time come? *Quarterly Journal of the Royal Meteorological Society*, 116(494):779–798, 1990. doi: 10.1002/qj.49711649402.

Liu, G. A Database of Microwave Single-Scattering Properties for Nonspherical Ice Particles. *Bulletin of the American Meteorological Society*, 89(10):1563–1570, oct 2008. doi: 10.1175/2008BAMS2486.1.

Liu, H., Zou, X., Shao, H., Anthes, R.A., Tseng, J.C. and Wang, B. Impact of 837 GPS/MET bending angle profiles on assimilation and forecasts for the period June 20-30, 1995. *Journal of Geophysical Research*, 106(D23):771–786, 2001. doi: 10.1029/2001JD000345.

Liu, H., Anderson, J. and Kuo, Y.H. Improved Analyses and Forecasts of Hurricane Ernesto's Genesis Using Radio Occultation Data in an Ensemble Filter Assimilation System. *Monthly Weather Review*, 140(1):151–166, 2011. doi: 10.1175/MWR-D-11-00024.1.

Lorente, J. and Redaño, A. Rainfall Rate Distribution in a Local Scale : The Case of Barcelona City. *Theoretical and Applied Climatology*, 41:23–32, 1990. doi: doi: 10.1007/BF00866199.

Luntama, J.P., Kirchengast, G., Borsche, M., Foelsche, U., Steiner, A.K., Healy, S.B., Von Engeln, A., O'Clerigh, E. and Marquardt, C. Prospects of the EPS GRAS mission for operational atmospheric applications. *Bulletin of the American Meteorological Society*, 89(12):1863–1875, 2008. doi: 10.1175/2008BAMS2399.1.

Marshall, J.S. and Palmer, W.M.K. The distribution of raindrops with size. *Journal of meteorology*, 5(4):165–166, 1948.

Martín-Neira, M., Caparrini, M., Font-Rossello, J., Lannelongue, S. and Vallmitjana, C.S. The paris concept: an experimental demonstration of sea surface altimetry using gps reflected signals. *IEEE Transactions on Geoscience and Remote Sensing*, 39 (1):142–150, 2001. doi: 10.1109/36.898676.

May, P.T., Jameson, A.R., Keenan, T.D. and Johnston, P.E. A Comparison between Polarimetric Radar and Wind Profiler Observations of Precipitation in Tropical Showers. *Journal of Applied Meteorology*, 40(10):1702–1717, 2001. doi: 10.1175/1520-0450(2001)040<1702:ACBPRA>2.0.CO;2.

Melbourne, W.G., Davis, E.S., Duncan, C.B., Hajj, G.a., Hardy, K.R., Kursinski, E.R., Meehan, T.K., Young, L.E. and Yunck, T.P. The application of spaceborne GPS to atmospheric limb sounding and global change monitoring. *JPL Publication*, 94-18:158, 1994.

Mishchenko, M.I., Travis, L.D. and Mackowski, D.W. T-matrix computations of light scattering by nonspherical particles: A review. *Journal of Quantitative Spectroscopy and Radiative Transfer*, 55(5):535–575, 1996.

Mishchenko, M.I., Travis, L.D. and Lacis, A.A. *Scattering, Absorption, and Emmision of Light by Small Particles*. Cambridge university press, 2002. ISBN 0-521-78252X.

Morrison, H., Thompson, G. and Tatarskii, V. Impact of Cloud Microphysics on the Development of Trailing Stratiform Precipitation in a Simulated Squall Line: Comparison of One- and Two-Moment Schemes. *Monthly Weather Review*, 137(3):991–1007, 2009. doi: 10.1175/2008MWR2556.1.

Mostert, S. and Koekemoer, J.A. The science and engineering payloads and experiments on sunsat. *Acta Astronautica*, 41(4-10):401–411, 1997. doi: 10.1016/S0094-5765(98)00095-2.

Navstar GPS. Interface Specification IS-GPS-200H, 2013a.

Navstar GPS. Interface Specification IS-GPS-800D. *Navstar GPS Space Segment/User Segment L1C Interface*, page 127, 2013b.

Neelin, J.D., Peters, O. and Hales, K. The Transition to Strong Convection. *Journal of the Atmospheric Sciences*, 66(8):2367–2384, 2009. doi: 10.1175/2009JAS2962.1.

Neiman, P.J., Ralph, F.M., Wick, G.A., Lundquist, J.D. and Dettinger, M.D. Meteorological Characteristics and Overland Precipitation Impacts of Atmospheric Rivers Affecting the West Coast of North America Based on Eight Years of SSM/I Satellite Observations. *Journal of Hydrometeorology*, 9(1):22–47, 2008. doi: 10.1175/2007JHM855.1.

NOAA/NCEP, C.E.M. The GFS Atmospheric Model. *NOAA/NCEP/Environmental Modeling Center Office Note*, 442:14, 2003.

Noel, V. and Chepfer, H. A global view of horizontally oriented crystals in ice clouds from Cloud-Aerosol Lidar and Infrared Pathfinder Satellite Observation (CALIPSO). *Journal of Geophysical Research*, 115(D00H23), may 2010. doi: 10.1029/2009JD012365.

Noel, V., Chepfer, H., Haeffelin, M. and Morille, Y. Classification of Ice Crystal Shapes in Midlatitude Ice Clouds from Three Years of Lidar Observations over the SIRTA Observatory. *Journal of the Atmospheric Sciences*, 63:2978–2991, 2006. doi: 10.1175/JAS3767.1.

Oguchi, T. Electromagnetic wave propagation and scattering in rain and other hydrometeors. *Proceedings of the IEEE*, 71(9):1029–1078, 1983. doi: 10.1109/PROC.1983.12724.

Padullés, R., Cardellach, E., de la Torre-Juárez, M., Tomás, S., Turk, F.J., Oliveras, S., Ao, C.O. and Rius, A. Atmospheric polarimetric effects on GNSS Radio Occultations: the ROHP-PAZ field campaign. *Atmospheric Chemistry and Physics*, 2(16): 635–649, 2016a. doi: 10.5194/acp-16-635-2016.

Padullés, R., Cardellach, E. and Rius, A. Untangling rain structure from polarimetric GNSS Radio Occultation observables: a 2D tomographic approach. *European Journal of Remote Sensing*, 49:571–585, 2016b. doi: 10.5721/EuJRS20164930.

Peng, G.S., de la Torre-Juárez, M., Farley, R.W. and Wessel, J.E. Impacts of upper tropospheric clouds on GPS radio refractivity. In *Aerospace Conference IEEE*, pages 0–5, 2006. ISBN 0-7803-9545-X. doi: 10.1109/AERO.2006.1655899.

Phinney, R.A. and Anderson, D.L. On the radio occultation method for studying planetary atmospheres. *Journal of Geophysical Research*, 73(5):1819–1827, 1968. doi: 10.1029/JA073i005p01819.

Prein, A.F. et al. A review on regional convection-permitting climate modeling: Demonstrations, prospects, and challenges. *Reviews of Geophysics*, 53(2):323–361, 2015. doi: 10.1002/2014RG000475.

Pruppacher, H.R. and Beard, K.V. A wind tunnel investigation of the internal circulation and shape of water drops falling at terminal velocity in air. *Quarterly Journal of the Royal Meteorological Society*, 96:247–256, 1970. doi: 10.1002/qj.49709640807.

Pruppacher, H.R. and Klett, J.D. *Microphysics of clouds and precipitation*. Kluwer Academic Publishers, 2n edition edition, 1997. ISBN 0-7923-4211-9.

Ralph, F.M., Sukovich, E., Reynolds, D., Dettinger, M., Weagle, S., Clark, W. and Neiman, P.J. Assessment of Extreme Quantitative Precipitation Forecasts and Development of Regional Extreme Event Thresholds Using Data from HMT-2006 and COOP Observers. *Journal of Hydrometeorology*, 11(6):1286–1304, 2010. doi: 10.1175/2010JHM1232.1.

Rangaswamy, S. Recovery of Atmospheric Parameters from the Apollo/Soyuz-ATS-F Radio Occultation Data. *Geophysical Research Letters*, 3(8):483–486, 1976. doi: 10.1029/GL003i008p00483.

Rasmussen, R. and Heymsfield, A.J. Melting and Shedding of Graupel and Hail. Part I: Model Physics. *Journal of Atmospheric Sciences*, 44(19):2754–2763, 1987. doi: 10.1175/1520-0469(1987)044<2754:MASOGA>2.0.CO;2.

Rayleigh, L. On the scattering of light by small particles. *Phil. Mag.*, 41(275):447–454, 1871. doi: 10.1080/14786447108640507.

Rennie, M.P. The impact of GPS radio occultation assimilation at the Met Office. *Quarterly Journal of the Royal Meteorological Society*, 136(646):116–131, 2010. doi: 10.1002/qj.521.

Richardson, L.F. *Weather prediction by numerical process*. Cambridge University Press, 1920. ISBN 978-0-521-68044-8.

Rieckh, T., Scherllin-Pirscher, B., Ladstädter, F. and Foelsche, U. Characteristics of tropopause parameters as observed with GPS radio occultation. *Atmospheric Measurement Techniques*, 7(11):3947–3958, 2014. doi: 10.5194/amt-7-3947-2014.

Rocken, C. et al. Analysis and validation of GPS/MET data in the neutral atmosphere. *Journal of Geophysical Research*, 102(D25):29,849–29,866, 1997. doi: 10.1029/97JD02400.

Rodriguez-Alvarez, N. et al. Land geophysical parameters retrieval using the interference pattern GNSS-R technique. *IEEE Transactions on Geoscience and Remote Sensing*, 49:71–84, 2011. doi: 10.1109/TGRS.2010.2049023.

Rosenfeld, D. and Ulbrich, C.W. Cloud Microphysical Properties, Processes, and Rainfall Estimation Opportunities. In Wakimoto, R.M. and Srivastava, R., editors, *Radar and Atmospheric Science: A Collection of Essays in Honor of David Atlas*, pages 237–258. American Meteorological Society, 2003. ISBN 978-1-878220-36-3. doi: 10.1007/978-1-878220-36-3_10.

Rossow, W.B. and Zhang, Y. Calculation of Surface and Top of Atmosphere Radiative Fluxes From Physical Quantities Based on Isccp Data Sets 2. Validation and first results. *Journal of Geophysical Research Atmospheres*, 100(D1):1167–1197, 1995. doi: 10.1029/94JD02746.

Ryzhkov, A.V. and Zrnić, D.S. Assessment of rainfall measurement that uses specific differential phase. *Journal of Applied Meteorology*, 35:2080–2090, 1996. doi: 10.1175/1520-0450(1996)035<2080:AORMTU>2.0.CO;2.

Ryzhkov, A.V., Pinsky, M., Pokrovsky, A. and Khain, A. Polarimetric radar observation operator for a cloud model with spectral microphysics. *Journal of Applied Meteorology and Climatology*, 50(4):873–894, 2011. doi: 10.1175/2010JAMC2363.1.

Ryzhkov, A.V., Kumjian, M.R., Ganson, S.M. and Khain, A.P. Polarimetric radar characteristics of melting hail. Part I: Theoretical simulations using spectral microphysical modeling. *Journal of Applied Meteorology and Climatology*, 52(12):2849–2870, 2013. doi: 10.1175/JAMC-D-13-073.1.

Schiro, K.A., Neelin, J.D., Adams, D.K. and Lintner, B.R. Deep Convection and Column Water Vapor over Tropical Land vs. Tropical Ocean: A comparison between the Amazon and the Tropical Western Pacific. *Journal of the Atmospheric Sciences*, 73:4043–4063, 2016. doi: 10.1175/JAS-D-16-0119.1.

Schmidt, T., Wickert, J., Heise, S., Flechtner, F., Fagiolini, E., Schwarz, G., Zenner, L. and Gruber, T. Comparison of ECMWF analyses with GPS radio occultations from CHAMP. *Annales Geophysicae*, 26:3225–3234, 2008. doi: 10.5194/angeo-26-3225-2008.

Schmidt, T., Wickert, J. and Haser, A. Variability of the upper troposphere and lower stratosphere observed with GPS radio occultation bending angles and temperatures. *Advances in Space Research*, 46(2):150–161, 2010. doi: 10.1016/j.asr.2010.01.021.

Schneider, S. Cloudiness as a Global Climatic Feedback Mechanism: The Effects on the Radiation Balance and Surface Temperature of Variations in Cloudiness. *Journal of the Atmospheric Sciences*, 29:1413–1422, 1972. doi: 10.1175/1520-0469(1972)029<1413:CAAGCF>2.0.CO;2.

Schreiner, W.S., Sokolovskiy, S.V., Rocken, C. and Hunt, D.C. Analysis and validation of GPS/MET radio occultation data in the ionosphere. *Radio Science*, 34(4):949–966, 1999. doi: 10.1029/1999RS900034.

Schreiner, W.S., Sokolovskiy, S.V., Hunt, D.C., Rocken, C. and Kuo, Y.H. Analysis of GPS radio occultation data from the FORMOSAT-3/COSMIC and Metop/GRAS missions at CDAAC. *Atmospheric Measurement Techniques*, 4(10):2255–2272, 2011. doi: 10.5194/amt-4-2255-2011.

Segre, S.E. A review of plasma polarimetry - theory and methods. *Plasma Physics and Controlled Fusion*, 41(2):R57–R100, 1999. doi: 10.1088/0741-3335/41/2/001.

Simpson, J., Kummerow, C., Tao, W.K. and Adler, R.F. On the Tropical Rainfall Measuring Mission (TRMM). *Meteorology and Atmospheric Physics*, 60(1-3):19–36, 1996. doi: 10.1007/BF01029783.

Smith, A.B. and Katz, R.W. US billion-dollar weather and climate disasters: Data sources, trends, accuracy and biases. *Natural Hazards*, 67(2):387–410, 2013. doi: 10.1007/s11069-013-0566-5.

Smith, A.B. and Matthews, J.L. Quantifying uncertainty and variable sensitivity within the US billion-dollar weather and climate disaster cost estimates. *Natural Hazards*, 77(3):1829–1851, 2015. doi: 10.1007/s11069-015-1678-x.

Sokolovskiy, S.V. Tracking Tropospheric Radio Occultation Singals from Low Earth Orbit. *Radio Science*, 36(3):483–498, 2001. doi: 10.1029/1999RS002305.

Sokolovskiy, S.V. Effect of superrefraction on inversions of radio occultation signals in the lower troposphere. *Radio Science*, 38(3):1–14, 2003. doi: 10.1029/2002RS002728.

Steiner, A.K., Lackner, B.C., Ladstädter, F., Scherllin-Pirscher, B., Foelsche, U. and Kirchengast, G. GPS radio occultation for climate monitoring and change detection. *Radio Science*, 46(6):1–17, 2011. doi: 10.1029/2010RS004614.

Steiner, M., Smith, J.A. and Uijlenhoet, R. A Microphysical Interpretation of Radar Reflectivity - Rain Rate Relationships. *Journal of the Atmospheric Sciences*, 61(10):1114–1131, 2004. doi: 10.1175/1520-0469(2004)061<1114:AMIORR>2.0.CO;2.

Stephens, G.L. Cloud feedback in the climate system: a critical review. *Journal of Climate*, 18:237–273, 2005. doi: 10.1175/JCLI-3243.1.

Stephens, G.L. et al. The cloudsat mission and the A-Train: A new dimension of space-based observations of clouds and precipitation. *Bulletin of the American Meteorological Society*, 83(12):1771–1790+1742, 2002. doi: 10.1175/BAMS-83-12-1771.

Stephens, G.L. et al. CloudSat mission: Performance and early science after the first year of operation. *Journal of Geophysical Research Atmospheres*, 113(8):1–18, 2008. doi: 10.1029/2008JD009982.

Straka, J.M. *Cloud and precipitation microphysics: principles and parameterizations*. Cambridge University Press, 2009. ISBN 978-0-521-88338-2.

Straka, J.M., Zrnić, D.S. and Ryzhkov, A.V. Bulk Hydrometeor Classification and Quantification Using Polarimetric Radar Data: Synthesis of Relations. *Journal of Applied Meteorology*, 39(8):1341–1372, 2000. doi: 10.1175/1520-0450(2000)039<1341:BHCAQU>2.0.CO;2.

Strangeways, I. *Precipitation: Theory, measurement and distribution*. Cambridge university press, New York, NY, USA, 2006. ISBN 978-0-521-85117-6.

Sukovich, E.M., Ralph, F.M., Barthold, F.E., Reynolds, D.W. and Novak, D.R. Extreme Quantitative Precipitation Forecast Performance at the Weather Prediction Center from 2001 to 2011. *Wea. Forecasting*, 29(4):894–911, 2014. doi: 10.1175/WAF-D-13-00061.1.

Sun, B., Reale, A., Seidel, D.J. and Hunt, D.C. Comparing radiosonde and COSMIC atmospheric profile data to quantify differences among radiosonde types and the effects of imperfect collocation on comparison statistics. *Journal of Geophysical Research Atmospheres*, 115(23):1–16, 2010. doi: 10.1029/2010JD014457.

Susskind, J., Barnet, C.D. and Blaisdell, J.M. Retrieval of Atmospheric and Surface Parameters From AIRS / AMSU / HSB Data in the Presence of Clouds. *IEEE Transactions on Geoscience and Remote Sensing*, 41(2):390–409, 2003. doi: 10.1109/TGRS.2002.808236.

Syndergaard, S., Flittner, D.E., Kursinski, E.R. and Herman, B.M. Simulating the Influence of Horizontal Gradients on Refractivity Profiles from Radio Occultations. In *OIST-4 Proceedings, 4'th Oersted International Science Team Conference*, pages 245–250, 2003.

Tapiador, F.J. et al. Global precipitation measurement: Methods, datasets and applications. *Atmospheric Research*, 104-105:70–97, 2012. doi: 10.1016/j.atmosres.2011.10.021.

Tarantola, A. *Inverse problem theory and methods for model parameter estimation*. Society for Industrial and Applied Mathematics, 2005. ISBN 0898715725.

Testud, J., Bouar, E.L., Obligis, E. and Ali-Mehenni, M. The rain profiling algorithm applied to polarimetric weather radar. *Journal of Atmospheric and Oceanic Technology*, 17(3):332–356, 2000. doi: 10.1175/1520-0426(2000)017<0332:TRPAAT>2.0.CO;2.

Testud, J., Oury, S., Black, R.A., Amayenc, P. and Dou, X. The concept of "normalized" distribution to describe raindrop spectra: A tool for cloud physics and cloud remote sensing. *Journal of Applied meteorology*, 40:1118 – 1140, 2001. doi: 10.1175/1520-0450(2001)040%3C1118:TCONDT%3E2.0.CO;2.

Thébault, E. et al. International Geomagnetic Reference Field: the 12th generation. *Earth, Planets and Space*, 67(1):79, 2015. doi: 10.1186/s40623-015-0228-9.

Thurai, M., Szakáll, M., Bringi, V.N., Beard, K.V., Mitra, S.K. and Borrmann, S. Drop shapes and axis ratio distributions: Comparison between 2D video disdrometer and wind-tunnel measurements. *Journal of Atmospheric and Oceanic Technology*, 26 (7):1427–1432, 2009. doi: 10.1175/2009JTECHA1244.1.

Thurai, M., Bringi, V.N., Manic, A.B., Šekeljic, N.J. and Notaroš, B.M. Investigating raindrop shapes, oscillation modes, and implications for radio wave propagation. *Radio Science*, 49(10):921–932, 2014. doi: 10.1002/2014RS005503.

Thurai, M., Chobanyan, E., Notaroš, B.M. and Bringi, V.N. Large raindrops against melting hail: calculation of specific differential attenuation, phase and reflectivity. *Electronics Letters*, 51(15):1140–1142, 2015. doi: 10.1049/el.2015.1564.

Tomás, S., Cardellach, E. and Padullés, R. Characterization of the systematic errors of the Polarimetric Radio Occultation observables: identification and separability. 2017.

Tyynelä, J., Leinonen, J., Westbrook, C.D., Moisseev, D. and Nousiainen, T. Applicability of the Rayleigh-Gans approximation for scattering by snowflakes at microwave frequencies in vertical incidence. *Journal of Geophysical Research: Atmospheres*, 118(4):1826–1839, feb 2013. doi: 10.1002/jgrd.50167.

Ulbrich, C.W. Natural Variations in the Analytical Form of the Raindrop Size Distribution. *Journal of Climate and Applied Meteorology*, 22(10):1764–1775, 1983. doi: 10.1175/1520-0450(1983)022<1764:NVITAF>2.0.CO;2.

Uppala, S.M. et al. The ERA-40 re-analysis. *Quarterly Journal of the Royal Meteorological Society*, 131(612):2961–3012, 2005. doi: 10.1256/qj.04.176.

Van Weverberg, K., Goudenhoofdt, E., Blahak, U., Brisson, E., Demuzere, M., Marbaix, P. and van Ypersele, J.P. Comparison of one-moment and two-moment bulk microphysics for high-resolution climate simulations of intense precipitation. *Atmospheric Research*, 147-148:145–161, 2014. doi: 10.1016/j.atmosres.2014.05.012.

Vergados, P., Mannucci, A.J. and Su, H. A validation study for GPS radio occultation data with moist thermodynamic structure of tropical cyclones. *Journal of Geophysical Research: Atmospheres*, 118(July):1–13, aug 2013. doi: 10.1002/jgrd.50698.

Vergados, P., Luo, Z.J., Emanuel, K. and Mannucci, A.J. Observational tests of hurricane intensity estimations using GPS radio occultations. *Journal of Geophysical Research: Atmospheres*, 119:1936–1948, 2014. doi: 10.1002/2013JD020934.

Von Engeln, A., Healy, S., Marquardt, C., Andres, Y. and Sancho, F. Validation of operational GRAS radio occultation data. *Geophysical Research Letters*, 36(17):2–5, 2009. doi: 10.1029/2009GL039968.

Von Engeln, A., Andres, Y., Marquardt, C. and Sancho, F. GRAS radio occultation on-board of Metop. *Advances in Space Research*, 47(2):336–347, 2011. doi: 10.1016/j.asr.2010.07.028.

Vorob'ev, V.V. and Krasil'nikova, T.G. Estimation of the accuracy of the atmospheric refractive index recovery from Doppler shift measurements at frequencies used in the NAVSTAR system. *Physics of Atmosphere an Ocean*, 23:602–609, 1994.

Walpole, R.E., Myers, R.H., Myers, S.L. and Ye, K. *Probability and Statistics for Engineers and Scientists*. Prentice Hall, Boston, 9th edition, 2012. ISBN 978-0-321-63911-1.

Wang, B.R., Liu, X.Y. and Wang, J.K. Assessment of COSMIC radio occultation retrieval product using global radiosonde data. *Atmospheric Measurement Techniques*, 6(4):1073–1083, 2013. doi: 10.5194/amt-6-1073-2013.

Wang, P.K. *Physics and dynamics of clouds and precipitation*. Cambridge university press, 2013. ISBN 978-1-107-00556-3.

Ware, R.H. GPS sounding of the Earth's atmosphere. *GPS world*, 56-57, 1992.

Ware, R.H. et al. GPS sounding of the atmosphere from low earth orbit: Preliminary results. *Bulletin of the American Meteorological Society*, 77(1):19–40, 1996. doi: 10.1175/1520-0477(1996)077<0019:GSOTAF>2.0.CO;2.

Waterman, P. Matrix formulation of electromagnetic scattering. *Proceedings of the IEEE*, 53(8):805–812, 1965. doi: 10.1109/PROC.1965.4058.

Wickert, J. et al. Atmosphere sounding by GPS radio occultation: First results from CHAMP. *Geophysical Research Letters*, 28(17):3263–3266, 2001. doi: 10.1029/2001GL013117.

Wickert, J., Beyerle, G., König, R., Heise, S., Grunwaldt, L., Michalak, G., Reigber, C. and Schmidt, T. GPS radio occultation with CHAMP and GRACE: A first look at a new and promising satellite configuration for global atmospheric sounding. *Annales Geophysicae*, 23(3):653–658, 2005. doi: 10.5194/angeo-23-653-2005.

Wielicki, B.A., Harrison, E.F., Cess, R.D., King, M.D. and Randall, D.A. Mission to Planet Earth: Role of Clouds and Radiation in Climate. *Bulletin of the American Meteorological Society*, 76(11):2125–2153, 1995. doi: 10.1175/1520-0477(1995)076<2125:MTPERO>2.0.CO;2.

Williams, C.R. et al. Describing the Shape of Raindrop Size Distributions Using Uncorrelated Raindrop Mass Spectrum Parameters. *Journal of Applied Meteorology and Climatology*, 53(5):1282–1296, may 2014. doi: 10.1175/JAMC-D-13-076.1.

Winker, D.M. et al. The Calipso Mission: A Global 3D View of Aerosols and Clouds. *Bulletin of the American Meteorological Society*, 91(9):1211–1229, 2010. doi: 10.1175/2010BAMS3009.1.

Wulfmeyer, V., Hardesty, R.M., Turner, D.D., Behrendt, A., Cadeddu, M.P., Di Girolamo, P., Schlüssel, P., Baelen, J.V. and Zus, F. A review of the remote sensing of lower tropospheric thermodynamic profiles and its indispensable role for the understanding and the simulation of water and energy cycles. *Reviews of Geophysics*, 53:819–895, 2015. doi: 10.1002/2014RG000476.

Xie, F., Syndergaard, S., Kursinski, E.R. and Herman, B.M. An approach for retrieving marine boundary layer refractivity from GPS occultation data in the presence of superrefraction. *Journal of Atmospheric and Oceanic Technology*, 23(12):1629–1644, 2006. doi: 10.1175/JTECH1996.1.

Xie, F., Wu, D.L., Ao, C.O., Kursinski, E.R., Mannucci, A.J. and Syndergaard, S. Super-refraction effects on GPS radio occultation refractivity in marine boundary layers. *Geophysical Research Letters*, 37(11):1–5, 2010. doi: 10.1029/2010GL043299.

Xie, F., Wu, D.L., Ao, C.O., Mannucci, A.J. and Kursinski, E.R. Advances and limitations of atmospheric boundary layer observations with GPS occultation over southeast Pacific Ocean. *Atmospheric Chemistry and Physics*, 12(2):903–918, 2012. doi: 10.5194/acp-12-903-2012.

Yoshida, R., Okamoto, H., Hagihara, Y. and Ishimoto, H. Global analysis of cloud phase and ice crystal orientation from Cloud-Aerosol Lidar and Infrared

Pathfinder Satellite Observation (CALIPSO) data using attenuated backscattering and depolarization ratio. *Journal of Geophysical Research Atmospheres*, 115(16):1–12, 2010. doi: 10.1029/2009JD012334.

Yunck, T.P., Lindal, G.F. and Liu, C.H. The role of GPS in precise Earth observation. In *IEEE PLANS '88.,Position Location and Navigation Symposium, Record. 'Navigation into the 21st Century'.*, pages 251–258, 1988. doi: 10.1109/PLANS.1988.195491.

Yurkin, M.A. and Hoekstra, A.G. The discrete-dipole-approximation code ADDA: Capabilities and known limitations. *Journal of Quantitative Spectroscopy and Radiative Transfer*, 112(13):2234–2247, 2011. doi: 10.1016/j.jqsrt.2011.01.031.

Zavorotny, V.U. and Voronovich, A.G. Scattering of GPS signals from the ocean with wind remote sensing application. *IEEE Transactions on Geoscience and Remote Sensing*, 38(2 II):951–964, 2000. doi: 10.1109/36.841977.

Zhang, J., Crocker, N.A., Carter, T.A., Kubota, S. and Peebles, W.A. Interaction between Faraday rotation and Cotton-Mouton effects in polarimetry modeling for NSTX. *Review of Scientific Instruments*, 81:3–6, 2010. doi: 10.1063/1.3479042.

Zhou, C., Yang, P., Dessler, A.E. and Liang, F. Statistical properties of horizontally oriented plates in optically thick clouds from satellite observations. *IEEE Geoscience and Remote Sensing Letters*, 10(5):986–990, 2013. doi: 10.1109/LGRS.2012.2227451.